Francisco Guillermo Leonardo Briones Castillo

Microstructural, mechanical and tribological characterizations of copper and copper-Al_2O_3 composites obtained by Spark Plasma Sintering

SÃO PAULO

2023

Francisco Guillermo Leonardo Briones Castillo

Microstructural, mechanical and tribological characterizations of copper and copper-Al_2O_3 composites obtained by Spark Plasma Sintering

Revised Edition

Thesis submitted to Escola Politécnica of the University of São Paulo to obtain the degree of Doctor of Science.

Area: Manufacturing and Design - Mechanical Engineering

Supervisor: Prof. Dr. Izabel Fernanda Machado

Co-Supervisor: Prof. Dr. Vanessa Seriacopi

SÃO PAULO

2023

Este exemplar foi revisado e corrigido em relação à versão original, sob responsabilidade única do autor e com a anuência de seu orientador.

São Paulo, 13 de 04 de 2023

Assinatura do autor: 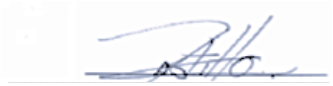

Assinatura do orientador: _ gov.br Documento assinado digitalmente IZABEL FERNANDA MACHADO Data: 13/04/2023 11:22:54-0300 Verifique em https://validar.iti.gov.br

Catalogação-na-publicação

Briones, Francisco

Microstructural, mechanical and tribological characterizations of copper and copper-Al_2O_3 composites obtained by Spark Plasma Sintering / F. Briones –- versão corr. –São Paulo, 2023

191 p.

Tese (Doutorado) – Escola Politécnica da Universidade de São Paulo. Departamento de Engenharia Mecatrônica e de Sistemas Mecânicos.

1.Cobre 2.SPS 3.Influência da rota de aplicação de pressão 4.Al_2O_3 5.Ensaio de riscamento. I. Universidade de São Paulo. Escola Politécnica. Departamento de Engenharia Mecatrônica e de Sistemas Mecânicos II.t.

To my beloved wife Vivian for her help, patience, support and motivation to finish this great challenge.

ACKNOWLEDGMENTS

I want to thank my supervisor, Prof. Dr. Izabel Fernanda Machado, for providing me with excellent discussions, patience, and support during my Ph.D. I value every professional and life advice essential for my academic and personal development.

My most sincere thanks, admiration and affection to my Co-supervisor, Prof. Dr. Vanessa Seriacopi, for her patience and unconditional support during my Ph.D. stage.

Prof. Dr. Carola Martínez is recognized for her valuable help and suggestions from my engineering training.

In addition, I want to thank the Pontifícia Universidad Católica de Valparaíso (PUCV) and the Escuela Ingeniería Mecánica, which supported me professionally and financially in carrying out my doctorate outside of Chile. I wish to express special recognition to Prof. Dr. José Luis Valin for his constant support from the initial stage of my doctorate, which allowed my academic development.

I would like to thank the Agencia Nacional de Investigación y Desarrollo (ANID) for the financial support through its Becas-Chile Ph.D. program.

In addition, thanks to the Department of Metallurgical Engineering and Materials PMT-EPUSP for carrying out the analysis by scanning electron microscopy. I wish to express special recognition to Dr. Dany Centeno for his unconditional support and friendship, which contributed to improving the polishing processes and microstructural characterization of all the samples in this work.

I would like to dedicate special thanks to Prof. Douglas Gouvea for helping with providing the alumina particles, and conducting explanations and discussions during my Ph.D.

Also, I wish to thank Prof. Dr. Amilton Sinatora, Prof. Dr. Roberto M. Souza and Dr. Francisco J. Profito, for their teachings in the disciplines of tribology. Also, thanks to Dr. Newton K. Fukumasu for his support in the deposition of silver on Al_2O_3 particles.

I thank all my colleagues, friends, and technicians from the Surface Phenomena Laboratory (LFS)-EPUSP, for being there to help and support me every day during my Ph.D. Thank my family for the love they give me every day and there was no day that I did not think of them during my stay here in Brazil.

Last but not least, to my wife Vivian for her unconditional love and support in facing life's challenges.

Since you are not experienced in things of the world, all things that are a bit difficult seem impossible to you. Trust in time; it usually provides a sweet way out of many bitter challenges."

(Miguel de Cervantes Saavedra, Don Quixote)

ABSTRACT

The Spark Plasma Sintering (SPS) technique is employed to obtain superior tribological responses in copper and Cu-Al_2O_3 composites. Thus, the modification at the interface between copper and Al_2O_3 is a powerful method to improve the mechanical properties and resistance to abrasive wear of copper, applied in mechanical and electrical systems. This thesis addresses the effect of microstructural features and the addition of Al_2O_3 particles on the tribological performance of copper sintered using the SPS technique. The first part of this study consisted of the consolidation of copper at 650 ºC and different routes of pressure applied during the holding time and heating. The pressures reached 50, 65 and 110 MPa. The result presented different characteristics, such as densification, porosity distribution, grain size, and mechanical properties. The main objective of the first part of the study was to select the best sintering parameters, based on the density and hardness results, to sinter the Cu-Al_2O_3 composites. The second part of the study was the modification of the interfaces between copper and Al_2O_3 particles from an exploratory point of view. Finally, mixtures of copper-based composites were evaluated using different Al_2O_3 addition methods, which were: i) mixture of Al_2O_3 particles to copper powder as received; ii) coating process, in which silver was deposited on Al_2O_3 particles using a pulsed direct current magnetron (PDCMS) and iii) mechanical-chemical coating of the surface of Al_2O_3 particles with silver using the electroless technique. Samples characterizations were analyzed by SEM, energy dispersive spectroscopy (EDS), and X-ray diffraction (XRD). The hardness and elastic modulus of the samples were determined using instrumented indentation tests and Vickers microhardness. The abrasive micro-mechanisms were evaluated from a simplified abrasion study, considering a single abrasive particle. The scratch tests were conducted using two different abrasive geometries, applying constant normal loads. The worn surfaces were analyzed utilizing 3D profilometry, SEM, and FEGSEM. The results showed the versatility of the SPS for manufacturing samples with different microstructural characteristics, allowing to obtain materials with varying apparent coefficients of friction (COF) and abrasive wear mechanisms. Adding Al_2O_3 particles increased the wear resistance and hardness with respect to copper. The main results of the scratch tests have shown changes in the local micro-scale COF, which were related to the methods of modifying the surface of the Al_2O_3 particles, which resulted in changes in the porosity, particle distribution, and the interfaces between copper/Al_2O_3. The influence of Al_2O_3 surface changes was predominant in local wear behavior. Consequently, the local penetration depth and volume removed decreased, and the specific frictional energy increased. Also, the local COF decreased due to the Al_2O_3 particles during scratching and raised in the presence of pores. The transitions of the micro-mechanisms were marked as a function of the normal loads applied for each sintered composite. Therefore, this research contributed to developing a methodology to evaluate the SPS new sintering routes, the addition of alumina and alumina-modified interfaces in the densification, and the tribological performance of copper and copper composites.

Keywords: Copper, SPS, Pressure application route influence, Al_2O_3, Scratch test.

RESUMO

A sinterização por *Spark Plasma (SPS)* é empregada para obter respostas tribológicas superiores em cobre e compósitos de Cu-Al_2O_3. Neste contexto, a modificação na interface entre cobre e Al_2O_3 é um método para melhorar as propriedades mecânicas e a resistência ao desgaste abrasivo do cobre, aplicado em sistemas mecânicos e elétricos. Esta tese aborda o efeito das características microestruturais e da adição de partículas de Al_2O_3 no desempenho tribológico do cobre sinterizado pela técnica *Spark Plasma Sintering*. A primeira parte da tese consistiu na consolidação do cobre por SPS a 650 ºC e diferentes rotas de pressão aplicadas durante o tempo de patamar e de aquecimento. As pressões alcançaram valores de 50, 65 e 110 MPa. Os resultados mostraram diferentes características, como densificação, distribuição dos poros, tamanho de grão e propriedades mecânicas. O principal objetivo da primeira parte do estudo foi selecionar os melhores parâmetros de sinterização, com base nos resultados de densidade e dureza, para sinterizar os compósitos Cu-Al_2O_3. A segunda parte foi a modificação das interfaces entre partículas de cobre e Al_2O_3 de modo exploratório. Por fim, a fabricação de compósitos à base de cobre foi avaliada usando métodos de adição de Al_2O_3: i) mistura de partículas de Al_2O_3 em pó de cobre como recebido; ii) processo de revestimento, no qual a deposição de prata sobre partículas de Al_2O_3 foi realizada por um magnéton pulsado de corrente contínua (PDCMS) e iii) revestimento mecânico-químico da superfície de partículas de Al_2O_3 com prata usando eletrodeposição. As caracterizações das amostras foram feitas por MEV, espectroscopia de energia dispersiva de raios X (EDS) e difração de raios X (XRD). A dureza e o módulo de elasticidade das amostras foram determinados por ensaios de indentação instrumentada e microdureza Vickers. A avaliação dos micro-mecanismos abrasivos foi realizada considerando o efeito de abrasivo único. Os ensaios de riscamento foram conduzidos por meio de duas geometrias abrasivas, aplicando-se cargas normais constantes. As superfícies desgastadas foram analisadas utilizando perfilometria 3D, MEV e FEG/MEV. Os resultados mostraram a versatilidade da técnica SPS para a fabricação de amostras com distintas microestruturas, o que permite a obtenção de materiais com diferentes respostas de coeficientes de atrito (COF) aparente e mecanismos de desgaste abrasivo. A adição de partículas de Al_2O_3 aumentou a resistência ao desgaste e dureza em relação ao cobre. Os resultados tribológicos indicaram efeitos locais no COF em micro-escala que foram relacionados aos métodos de modificação da superfície das partículas de Al_2O_3, o que resultou em mudanças na distribuição de partículas e poros e nas interfaces entre cobre/Al_2O_3. As mudanças de superfície de Al_2O_3 foram predominantes no desgaste local. Em consequência, a profundidade e o volume removido diminuíram e a energia específica de atrito aumentou. O COF local diminuiu devido às partículas de Al_2O_3 e aumentou em regiões de poros. As transições dos micro-mecanismos foram marcadas em função das cargas normais para cada compósito. Portanto, esta pesquisa contribuiu para o desenvolvimento de uma metodologia para avaliar novas rotas de sinterização por SPS, a adição de alumina e interfaces modificadas na densificação, bem como o desempenho tribológico de cobre e seus compósitos.

Palavras-chaves: Cobre, SPS, Influência da rota de aplicação de pressão, Al_2O_3, Ensaio de riscamento.

LIST OF FIGURES

LIST OF TABLES

NOMENCLATURE

a	radius of the tip projected with respect to the surface
A	The projected contact area between the tip and the sample surface
A_1+A_2	Area of the pile-up sum for the case of meso-scale tests
A_v	Area of the groove for the case of meso-scale tests
$A_v-(A_1+A_2)$	Area of material removal
h_r	Residual penetration depth
h_p	Penetration depth in-situ
D_p	Degree of penetration
E	Elastic modulus
E_i	Elastic modulus of the indenter
E_v	Elastic modulus of the material
E_r	Reduced modulus
S_e	Specific energy (frictional parcel)
f	Interfacial shear strength / yield stress ratio
F_{ab}	Material removal factor due to abrasion
F_n	normal force
$F_{critical}$	Critical value for the ANOVA, based on a significance level (F- distribution)
F_t	Tangential force
h_s	Pile-up height (micro-scale)
H	Heating
HT	Holding time
H_H	Indentation hardness
H_{def}	Hardness of the deformed material by the abrasion effect
W_r	Scratch width
n	Strain-hardening exponent
N	Pressure exponent
P-h	Load-displacement curve
R	Tip radius (Abrasive tip radius)
L	Scratch length or sliding distance
S_a	Arithmetic Mean Height – Average Roughness
S_q	Sum of squares

D_F	Degrees of freedom
M_Q	Mean square
F/P_value	Indicate in case the null hypothesis is sustained at the 5% significance level
p	significance level; p<5% (ANOVA)
V	Removed volume due to the abrasive action
V_{pu}	Pile-up volume
V_T	Total volume
W	Normal load
θ	Attack angle
θ_c	Critical attack angle
ρ	Material density
$\bar{\bar{\sigma}}_y$	Yield stress
μ_a	Coefficient of friction of adhesion
μ_p	Coefficient of friction of ploughing
ν	Poisson ratio
ν_i	Poisson ratio of the indenter
ν_s	Poisson ratio of the indented surface

ABBREVIATIONS

Al_2O_3	Alumina
ASM	American Society for Metals
ASTM	American Society for Testing and Materials
ANOVA	Analysis of Variance
BSE	Backscattered electrons
DRX	X-ray Diffraction
COF	Coefficient of friction apparent (F_t/F_n)
Cu	Copper
Cu-Al_2O_3	Copper matrix composite reinforced with Al_2O_3 particles
DF	Degrees of freedom
EBSD	Electron Backscatter Diffraction
FEGSEM	Field Emission Gun Scanning Electron Microscope
EDS	Energy Dispersive X-Ray Spectroscopy
LCT	Technological Characterization Laboratory
LFS	Surface Phenomena Laboratory
LPC	Ceramic Processes Laboratory
MQ	Mean square
SQ	Sum of squares
SEM	Scanning Electron Microscopy
SPS	Spark Plasma Sintering. Also called as: FAST, PECS, PAS e PECS
SPM	Scanning Probe Microscopy
SD	Standard deviation
HP	Hot Pressing
HIP	Hot Isostatic Pressing
PM	Powder Metallurgy
PMT	Metallurgical and Materials Engineering Department
SM	Microwave Sintering
LPC	Ceramic Processes Laboratory

SUMMARY

1 INTRODUCTION

Copper is widely used in different applications due to its excellent electrical-thermal conductivity, ductility, and corrosion resistance (ASM INTERNATIONAL, 2001; ZHOU et al., 2019a, 2019b; ZHU et al., 2020). These advantages are the driving force for new and challenging applications of copper as a high-performance material adopted in mechanical and electrical systems such as friction plates (KOVALCHENKO; FUSHCHICH; DANYLUK, 2012), brake pads (XIAO et al., 2018), welding electrodes (SAMAL; PARIHAR; CHAIRA, 2013) and electronic contact devices (LI et al., 2020). Unfortunately, low mechanical strength and wear resistance limit the performance of copper. Therefore, it is essential to evaluate different solutions to develop materials with high thermal conductivity and other excellent wide-ranging properties, such as improved wear resistance, a significant increase in hardness, and reduced plastic deformations on contact during the sliding of surfaces in mechanical applications.

Among many possibilities for combining materials, metal matrix composites (MMC) are prospective to improve copper performance. The MMCs consist of a minimum of two constituents; a matrix (metal or alloys) and the second constituent is a reinforcement, such as whiskers, particles, or fibers made of ceramics, solid lubricants, or organic composite, obtaining a unique combination of ductility, toughness, high strength and elastic modulus (MAZUMDAR, 2002).

The leading advanced processing routes for large-scale composite manufacturing are liquid-state and solid-state (KUMAR et al., 2020). In the solid state, a considerable amount of work has been devoted to powder metallurgy (PM) (BOIDI et al., 2021; MACHADO et al., 2021a; MARTÍNEZ et al., 2020b; ZHOU et al., 2019a). PM methods allow manufacturing components from powders with a high degree of freedom, such as chemical composition, particle morphology, size, and volume fraction. In addition, PM allows the mixing of different materials to obtain a wide range of properties and functionalities (CAVALIERE, 2019).

One of the techniques used in PM to manufacture composites is Spark Plasma Sintering (SPS). This non-conventional technique is characterized by the heating due to Joule effect and uniaxial pressure-assisted system. The main advantage of SPS compared to other conventional sintering techniques, such as Hot Pressing (HP), Hot Isostatic Pressing (HIP), and Microwave Sintering (SM), is the high heating rate of up to 1000 ºC/min, which can be easily achieved by applying electrical current (MUNIR; ANSELMI-TAMBURINI; OHYANAGI, 2006). Additionally, SPS exhibits greater flexibility in sintering parameters, i.e., lower sintering

temperature, shorter dwell times and pressure variation during sintering, to provide better ways to combine characteristics, e.g., microstructural, mechanical, and tribological performances of composites (DASH; RAY; CHAIRA, 2012; PELLIZZARI; CIPOLLONI, 2017; ZHAO; BAO; YI, 2021).

Regarding tribological performance, the increased wear resistance of copper matrix composites can be achieved using ceramic particles due to their high hardness. These particles support high normal loads, as well as in deformation/damage processes. In addition, the particles hinder plastic flow and restrict crack propagation. The ceramic materials, such as WC, SiC, TiB_2, B_4C, ZrO_2, and Al_2O_3, were presented in the literature to improve the hardness and wear resistance of copper matrix composites manufactured by SPS. However, composites with self-lubricating particles (solid lubricants) are also added to reduce the friction coefficient and increase wear resistance in long-term sliding systems. The leading solid lubricants used in copper matrix composites and processed by PM are graphite, MoS_2, WS_2, CNT, and graphene (XIAO; ZHANG; ZHANG, 2018).

In abrasive conditions, the response of composites is related to hardness and the ability to activate wear mechanisms depending on the system. The wear will depend on the porosity and grain size of sintered copper. In composites, the size and network of the particles have a direct relationship with the adhesion area with the matrix. The copper matrix must support the hard particles to prevent detachment and premature fracture. To avoid this detachment, the interface (adhesion) between the constituents is essential to support loads and reduce the penetration depth (GAHR, 1998). Another critical factor is the mean free path of the particles or clustering of particles that act as an obstacle for the abrasive and prevent it from causing a high plastic deformation affecting the toughness of the composites. Therefore, abrasive wear from hard particles is initially characterized by plastic deformation and fracture at the surfaces in contact (FUTAMI et al., 2009; HOKKIRIGAWA; KATO, 1988).

Evaluation of abrasive wear has been investigated using the scratch test, which has been used to evaluate material removal with different surface and microstructural features (ZHANG et al., 2020; ZUM GAHR, 1987). This test is an advantageous alternative to characterize, in a simplified way, the tribological performance and the mechanisms of abrasive wear, considering a single abrasive event. Also, the scratch test can help evaluate the severity of material removal from different geometric parameters, such as angle of attack (θ), degree of penetration (D_p), and material removal factor (F_{ab}) that depend on the properties of the material and characteristics of the system. Finally, the advantage of using the scratch test is determining the

specific energy (S_e), in which the frictional parcel can be related to both the scratch force to generate the groove and the volume of material removed from the surface of the material.

In this context, microstructural design is an alternative to improve both the mechanical properties and wear resistance of copper and its composites. In this sense, the versatility of SPS allows microstructural control by optimizing the sintering parameters. It is worth mentioning that there is still no understanding of the effect of pressure during the SPS process on the microstructure, hardness, and, consequently, tribological performance of copper.

Considering the above described, there is a gap in the literature in three crucial aspects:

1. The effect of the quantity, size, and shape (morphology) of the pores and grain size control on the tribological performance of sintered copper during the scratch tests.
2. The effect of different mechanical-chemical methods in the adding of hard particles (without changes in particle size) on the microstructure and interfaces (Cu-Al_2O_3) in metal matrix composites
3. The effect of adding hard particles on the ability to withstand loads and the abrasion mechanisms found during scratch tests using a micro-scale.

To address these issues, the present work studied the influence of the applied pressure rate during SPS holding time and heating on the evolution of porosity, grain size, and mechanical properties of copper sintered. To study copper composites, the addition of alumina (Al_2O_3) as a hard particle in the copper matrix was selected because it is widely used and offers good wear resistance and low density, which makes it particularly advantageous in applications in electrical contact devices and components in the automotive field (HAN et al., 2017; RAJKOVIC et al., 2012). Moreover, Al_2O_3 particles maintain microstructural stability with stable mechanical properties at high temperatures (SCHULTZ; FERGUSON; ROHATGI, 2011).

1.1 Objectives and Motivation

This work highlights the characteristics of the SPS technique that allow control over the sintering parameters to enhance the performance of copper, improving its mechanical and tribological performance. Furthermore, considering the microstructural evolution of sintered copper is essential to optimize Cu-Al_2O_3 composite manufacturing processes. Therefore, the general objective of this work is to understand the effect of pressure during holding time and heating in the copper sintering process. In addition, the influence of different methods of addition of Al_2O_3 in copper to determine the abrasive micro-mechanisms in copper and Cu-Al_2O_3, which present combinations of mechanical properties of the matrix and its reinforcement particles. Therefore, this study is focused on promoting an advance toward developing copper matrix composites and understanding the micro-mechanisms of abrasive wear.

Taking this into account, the specific objectives of this work were as follows.

1.1.1 Specific objectives

1. To obtain copper samples from different sintering pressure routes applied during holding time and heating SPS to assess different microstructural characteristics and their effect on densification and hardness.
2. To study the effect of different mechanical-chemical methods of adding Al_2O_3 particles on the microstructure, hardness, and elastic modulus.
3. To analyze the effect of the normal load on different friction levels and penetration depth of the sintered samples through the scratch tests.
4. To evaluate the microstructural evolution of sintered copper and the addition of Al_2O_3 particles using different methods in the characterizations of abrasive micro-mechanisms, and specific energy through scratch tests in meso and micro-scale.

A schematic flow is presented in Figure 1, summarizing the scope and goals of this work.

Figure 1- Stages and scope of each step of the present work.

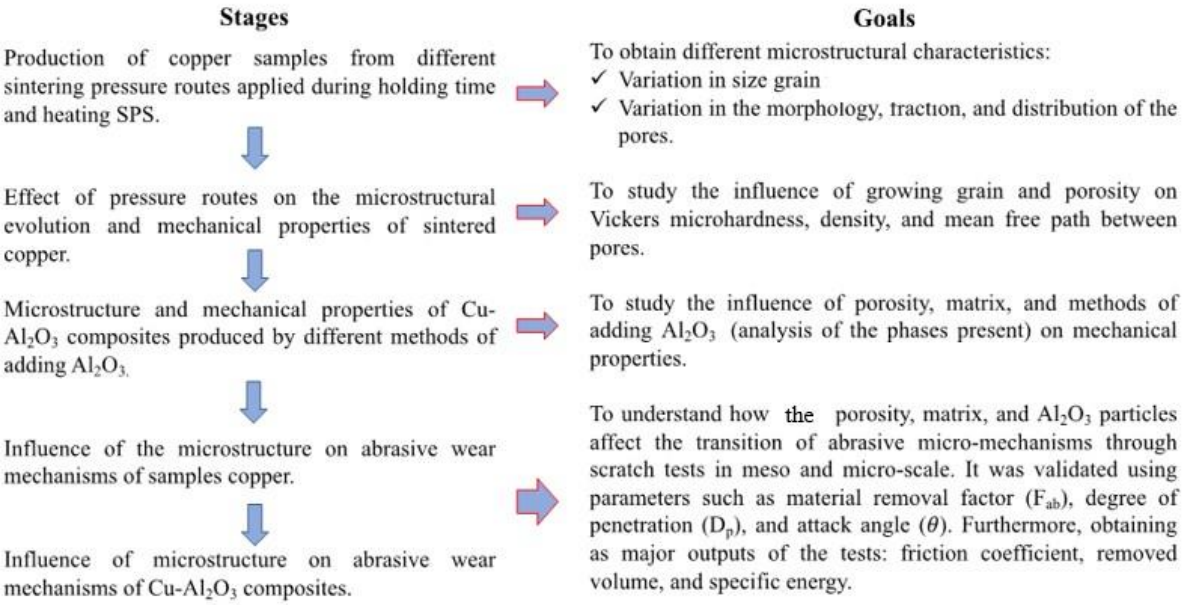

2 LITERATURE REVIEW

This chapter is divided into three groups. First, fundamental concepts of powder metallurgy regarding solid-state sintering and the SPS technique are addressed. The following section describes SPS parameters effects on the microstructure and mechanical properties of metal matrix composites. Lastly, the concepts of abrasive wear and removal mechanisms in metallic and composite materials are reviewed considering the single-abrasive scratch tests.

2.1 Powder Metallurgy

Powder metallurgy (PM) is a process for manufacturing components from powders, which combines compacting techniques with subsequent densification processes (sintering) (DAVIS, 1998). Compacting and densification processes aim to obtain a finished or semi-finished product (near net shape) (GERMAN, 2005). Metal hot isostatic pressing and powder forging are types of powder densification techniques. The widely used PM process to produce industrial parts is compaction and sintering (*press and sinter*) (CAPUS, 2005). In the powder metallurgy technique, materials generally remain in the solid-state. However, the different powders mixtures, compacting and sintering processes to control or minimize the porosity of the material are also important to control microstructural features (HÖGANÄS; SWEDEN; PUBLICATIONS, 2012). On the other hand, it is possible to manufacture components with different degrees of porosity, such as metal foams, micro-porous materials (WANG et al., 2015) or to reach full densification, as mentioned, and to achieve mechanical properties close to or superior to materials manufactured by forming (DAVIS, 1998).

2.1.1 Solid-State Sintering

Solid-state sintering is part of the PM process and is thermally activated at temperatures below the melting point of the powder. During sintering, the mass transport has been driven (diffusion) by minimizing total free energy by decreasing surface area (since surfaces always bring extra or excess energy). Therefore, greater surface energy results in a better potential for sintering to occur (driving force) (NOWACKI; KLIMEK, 1993; BARSOUM, 2002). When the

diffusion of the atoms is high enough, simultaneous processes begin to occur: sintering, coalescence, and grain growth; these processes are usually denominated “coarsening” (PORTER; EASTERLING; SHERIF, 2009).

The formation of a neck between two particles is shown in Figure 2. This generates densification and shrinkage since, as the sintering process progresses, the grain boundary (neck) forms and grows, decreasing the volume of the pores until they remain isolated, as will be represented later. Moreover, and simultaneously, when the neck is formed, grain growth also initiates (also driving forces are interface energy) (CASTRO, 2013). In addition to thermodynamics in the process, sintering kinetics indicates how fast sintering occurs and what is the path of the atoms; consequently, both factors control the final microstructure of the sintered sample (CAVALIERE, 2019). For example, Figure 3 shows a schematic representation of a neck between two particles, idealized as two spheres, establishing different sources of the material (atoms) to move towards the neck using different paths, which can be: from the surface, from the grain boundary, or the bulk. Thus, the transport mechanisms listed in Figure 3 can be established. For example, if the material moves from the grain boundary or bulk to the neck, high densification should be seen during sintering (elimination of pores).

Figure 2 - a) SEM images showing tungsten sintered through SPS with particle sizes of 1 μm, 40 MPa at different temperatures. The white arrows mark the sinter necks, and the red arrow marks the interconnected pores and b) an idealized geometry of a powder compact on sintering (the initial stage of sintering: contact between adjacent particles).

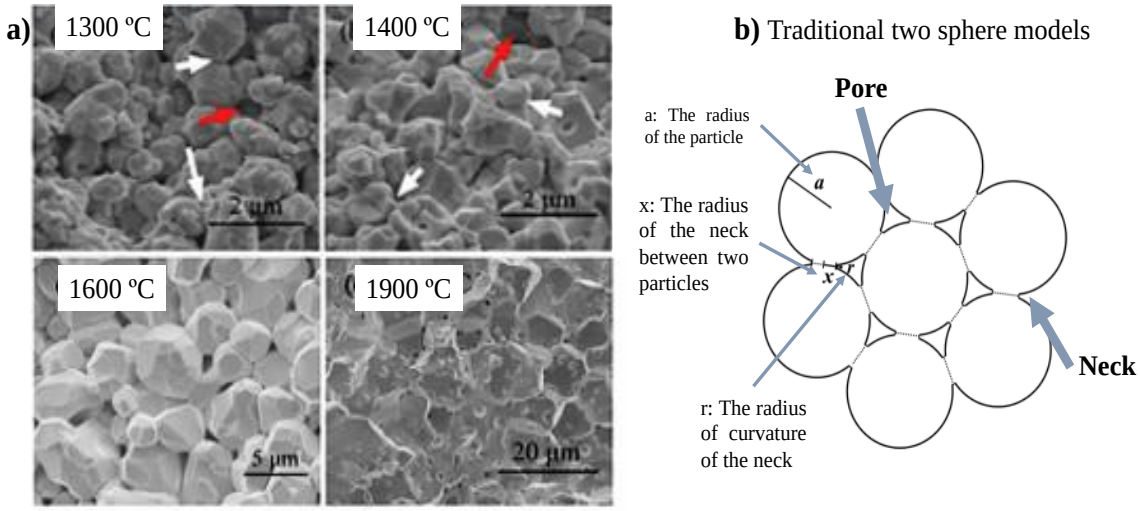

Source: Adapted from (BORDIA; KANG; OLEVSKY, 2017; DENG et al., 2020).

Figure 3 - illustration of the sintering mechanisms in a two particles array. The numbers represent the different mechanisms and sources of material. (a) Radii of curvature at the particle surface R and the neck surface ρ-X and (b) mass transport mechanisms responsible for neck growth.

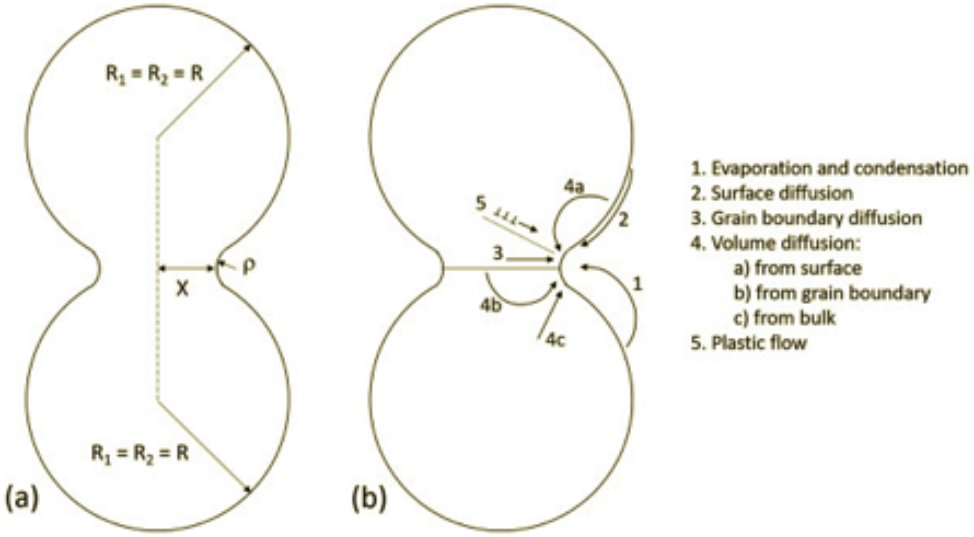

Source: Adapted from (CAVALIERE, 2019).

2.1.2 Spark Plasma Sintering (SPS)

There are different sintering techniques, such as conventional sintering, microwave sintering (SM), hot pressing (HP), hot isostatic pressing (HIP), and spark plasma sintering (SPS). Among them, SPS is one of the most modern, high-tech, and high-speed sintering processes. SPS sintering is a head treatment that has stimulated worldwide interest due to the rapid consolidation of powders. Additionally, SPS achieves high heating rates (10-1000 ºC/min), shorter holding times, and full densification in a few minutes at lower temperatures than conventional sintering techniques. Therefore, grain growth is hindered. It is well-known that SPS is an advanced processing technology to produce homogenous, highly dense, nano-structural sintered compact, composite materials, functionally graded materials (FGMs), fine ceramics, wear-resistant materials, thermoelectric semiconductors, and biomaterials (BORDIA; KANG; OLEVSKY, 2017).

Figure 4 presents a simplified schematic of the SPS process. The powders are placed in a die, usually made of high-density graphite, and heated by passing an electrical current (Joule effect), normally pulsed D.C., through the matrix and sample. At the same time, pressure is applied to the powder. Both parameters (electrical current and pressure) are adjusted during the process. A low vacuum chamber (atmosphere) and a water-cooling system are parts of the methods to avoid oxidation.

Figure 4 - a) Schematic representation of the SPS system and b) the die and graphite punches of the SPS during the copper sintering at 750 ºC.

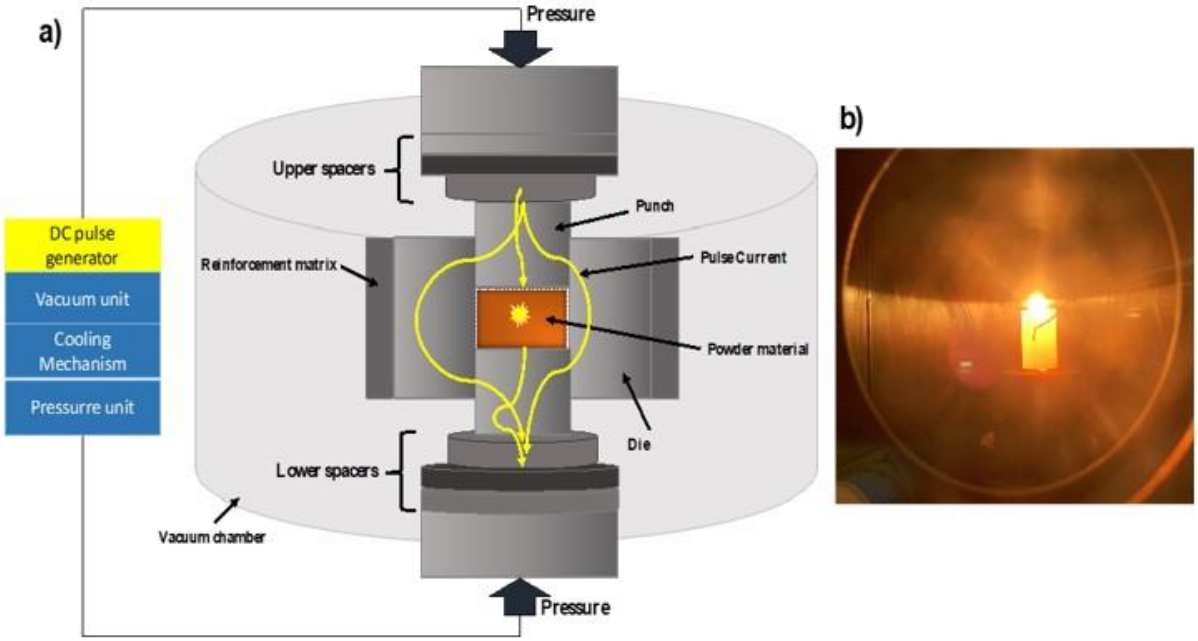

Source: Author.

Figure 5 presents the direction of the current flow. Spark discharge into a gap or contact area between particles, or contamination, generates a high-temperature spot area (discharge column) (TOKITA et al., 2013). When the spark is generated in gaps or contact points between particles, the local heat generated in the discharge column causes a punctual increase in temperature, reaching more than 1000 ºC in a few seconds; these high punctual temperatures lead to evaporation and melting from the surface of the particles. These molten regions absorb each other through electron flow (ON time) and vacuum generation (OFF time), eventually forming the necks between the particles. Furthermore, the applied pressure in SPS results in better contact between powder particles and changes the amount of those contacts. It promotes existing densification mechanisms or activates new mechanisms, such as plastic deformation and grain boundary slip (SAHEB et al., 2012).

Figure 5 - Neck formation between particles: electric current passes through the particles in the SPS process.

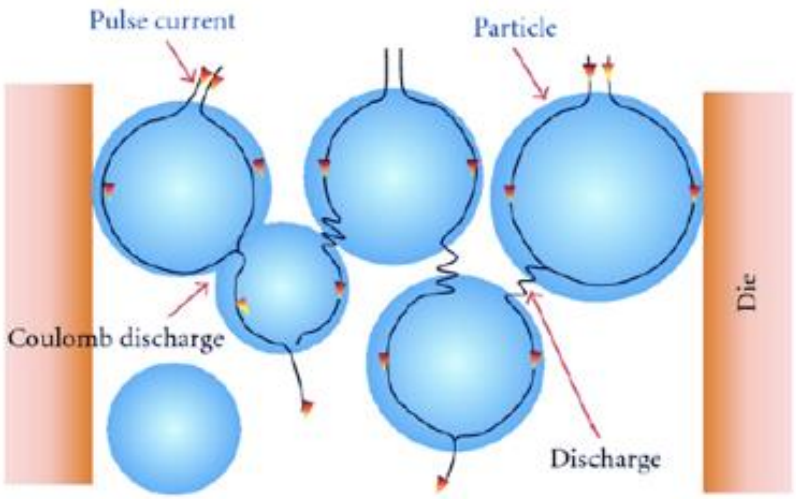

Source: Adapted from (SAHEB et al., 2012).

The main SPS sintering parameters are: temperature, dwell time, and pressure, which have been the subject of extensive research in copper sintering. Temperature and dwell time are parameters in all sintering processes, but the pressure-assisted system is complementary at SPS.

The classical theory of the sintering process is divided into three stages (German, 1996), schematized in Figure 6. In the first stage of sintering, the central phenomenon is the formation and growth of the bond between adjacent particles and the growth of the neck. The most significant porosity reduction (shrinkage) occurs in the intermediate stage and promotes extensive densification. In the final step, the densification rate slows down significantly while coarsening increases. Therefore, the evolution of the microstructure is controlled by the interaction between the pores and the grain boundaries. During the intermediate and final stages, the microstructure is represented as channel-like interconnected porosity along the grain boundaries towards isolated pores and closed porosity. In addition, the mechanisms that contribute to densification in the intermediate and final stages of the sintering process are grain boundary diffusion and volume diffusion: diffusion is from the grain boundary to the pore surface (Figure 3 mass transport mechanism number 3 and 4b, respectively) (MUNIR; ANSELMI-TAMBURINI; OHYANAGI, 2006; SONG; LIU; ZHANG, 2006; GRAPHENE et al., 2009).

Figure 6 - The three stages of sintering.

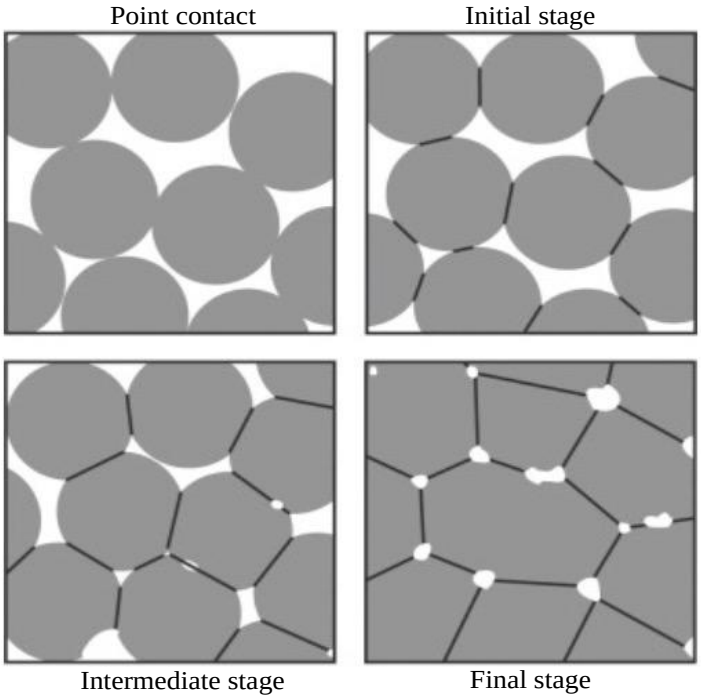

Source: Adapted from (R.M. GERMAN, 1996)

The densification mechanisms in SPS are influenced by electric fields and/or currents, changes in the heating rate, and the effects of applied pressures on ceramic and metallic materials. Electric fields affect the electro-transport. Therefore, the transfer of material might play a role in controlling and/or modifying the kinetics and mechanisms of the sintering process. Nevertheless, it is known in the literature that high heating rates benefit densification behaviors in numerous material systems (GERMAN, 2005; MUNIR; ANSELMI-TAMBURINI; OHYANAGI, 2006). Densification is also favored by external compression pressure. In this case, the process is called "pressure-assisted sintering." However, the pressures used in SPS are less than 200 MPa due to the necessity to use conductive dies (graphite). This limitation opens an opportunity to study the effects of pressure on densification behavior.

The pressure generates shear stresses to reorganize powders through pore collapse in agglomerates or non-ideal packing, cleans surfaces by shearing removal of oxides and other surface contaminations, and generates a plastic flow of the porous media in the later stages of densification. As densification proceeds, the neck size increases, while through plastic or diffusional flow stress accommodation mechanisms and the stress level is reduced. Once the final stage of sintering is achieved, the close of porosity occurs, and the "effective" stress is reduced by the gas pressure occurring in closed pores. The densification rate will change as the

adequate pressure decreases with the increasing density levels. The densification is rate-independent at stress levels above the temperature-compensated yield stresses. As the pressure levels diminish with higher density and grain growth, the pressure effects become dominated by rate-dependent creep and/or diffusion mechanisms (CASTRO, 2013). To understand the effect of pressure on density, Figure 7 presents a compressibility diagram for copper by conventional sintering.

Figure 7 - a) Effect of compaction pressures on the green and sintered density of the copper and b) Effect of compaction pressure on the size and shape of pores (schematic representation).

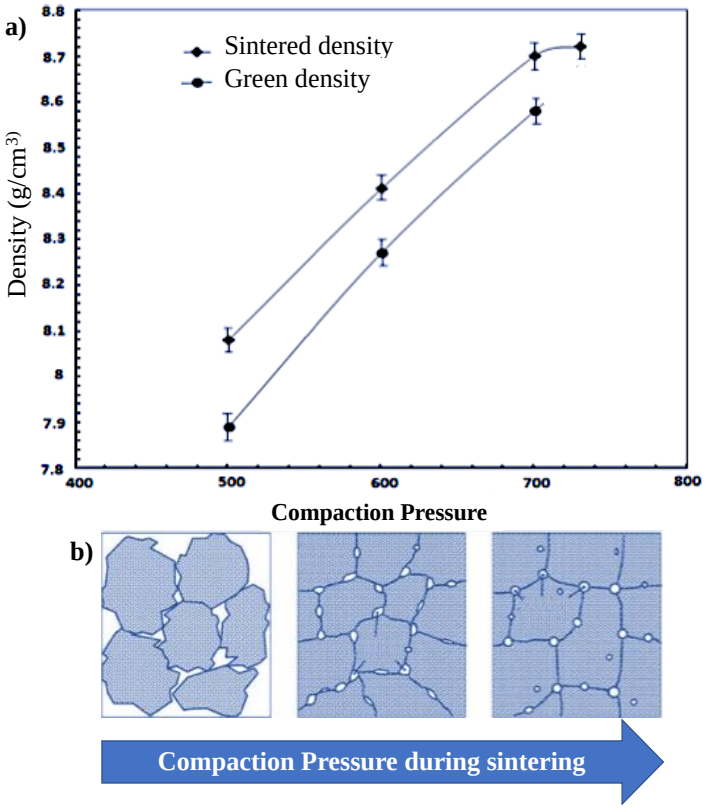

Source: Adapted from (DIXIT; SRIVASTAVA, 2018).

The increase in compaction pressure influences the density (green) and the work hardening of the green compact. Figure 7a confirms that green and sintered density increase with increasing compaction pressure. Compaction pressure also influences the size and shape of the pores; therefore, when porosity is high, the pores are interconnected (GOODALL, 2013). When the compaction pressure increases, the pores lose connectivity, becoming isolated, smaller, and more regularly shaped (rounded). An example is presented in Figure 7b.

Small particles have a higher specific surface area than powders with large particles, resulting in more friction between the particles and less plastic deformation during pressing

(since the applied force is divided by an area of a larger surface). Figure 8 shows of pressure (green compact) of these parameters for sintered titanium. For a constant compaction pressure, the density decreases along with the increase in the size of the particles.

Figure 8 - Density as a function of compaction pressure and particle size.

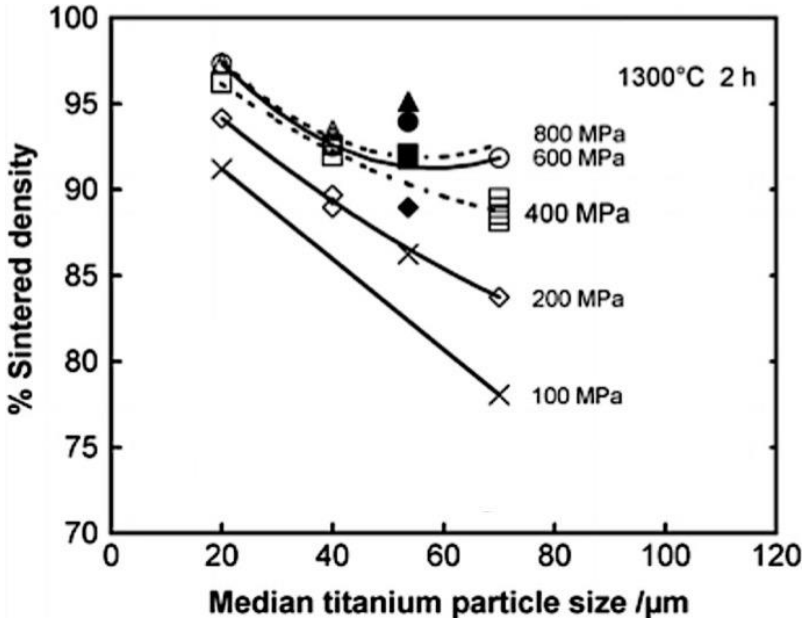

Source: Adapted from (ROBERTSON; SCHAFFER 2009).

Other works have shown that the SPS mechanical pressure-assisted system is beneficial in achieving theoretical density in metallic materials, the strength improvement being related to grain size control and low volume fraction of porosity (WEGNER et al., 2013; WEN et al., 2011). For example, ZHANG et al., (2008) sintered copper powder (1 μm) at 800 ºC, varying the pressure from 0 to 50 MPa and a holding time of 6 minutes (Figure 9). The authors observed that at an initial sintering pressure of 1 MPa up to a maximum pressure of 50 MPa during the holding time, the relative density increased considerably from 74 to 98%, and grain growth was hindered (from 5.6 to 6.4 μm). Furthermore, the relationship between the relative densities and the holding time from 3 to 15 min at a constant pressure of 50 MPa showed a difference in the relative density from 96.76% to 98.71%, respectively. However, the maximum applied pressure must be greater than 25 MPa. Copper powder compacts showed poor results at pressures below 25 MPa.

Figure 9 - Effect of holding pressure on relative density and average grain size (T = 800 °C; holding time = 6 min; rate heating= 80 ºC/min).

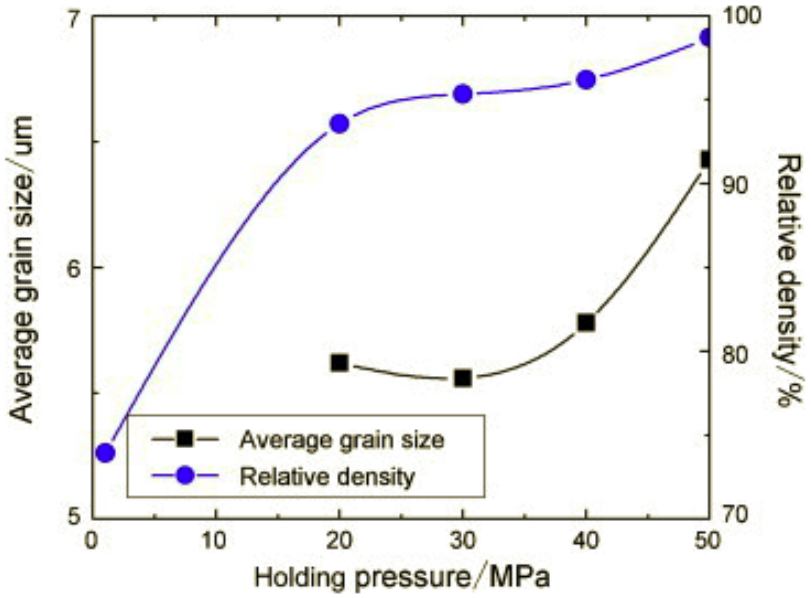

Source: (ZHANG et al., 2008b).

From a mechanistic point of view, sintering proceeds by evaporation–condensation, surface diffusion, grain boundary diffusion, volume diffusion, plastic deformation, or creep (if pressure is applied). Only grain boundary diffusion, volume diffusion densification, and plastic deformation/creep lead to shrinkage/densification. Remarkably, pressures during SPS directly cause time-dependent deformation mechanisms such as creep (COBLE, 1970). Creep equations describing the deformation of dense materials at high temperatures were adapted for the intermediate and final stage of sintering by transforming the creep rate into a densification rate, considering the sintering body's porous nature. Therefore, this mechanical description helps to identify the main mechanisms during SPS.

According to the study of TRAPP et al., (2020), the densification mechanisms of copper powder sintered by SPS also show a linear dependence between pressure and densification rate, as shown in Figure 10.

Figure 10 - Dependence of the densification rate on applied external pressure for the same copper powder at T = 500 ºC. The value for the lower pressure of P = 10 MPa. (N: pressure exponent. n increases with increasing sintering pressure).

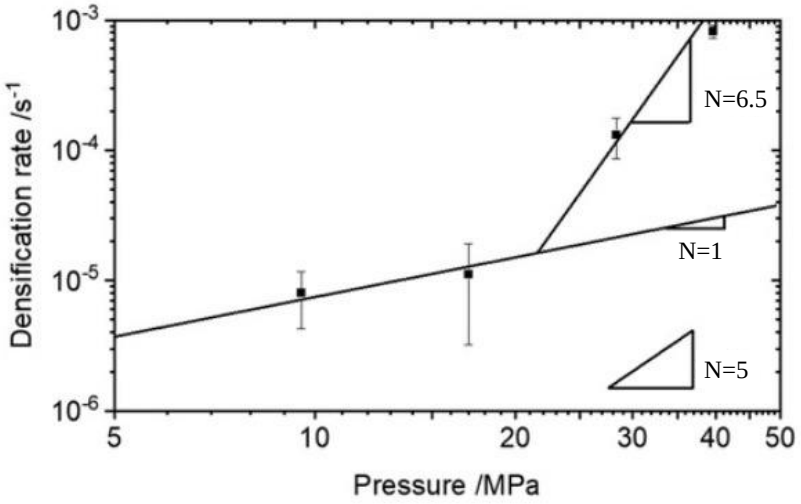

Source: (TRAPP et al., 2020).

From the experimental results, the authors observe a localized plastic deformation (extrusion-like) of the material near the grain boundary during sintering (Figure 11). This occurs in polycrystalline copper powders at low temperatures of T<700 ºC. An explanation may be related to the initially - for small relative neck radii - the transport of material along the contact grain boundary to the neck surface is significantly enhanced by the application of the pressure. At the same time, the rearrangement of the atoms from the grain boundary by surface diffusion is not altered by the pressure (TRAPP et al., 2020).

Figure 11- The grain boundary diffusion accelerated by the mechanical pressure is faster than surface diffusion, suppressing the energetically favorable rearrangement of the atoms on the neck surface in (a) monocrystalline and (b) polycrystalline materials.

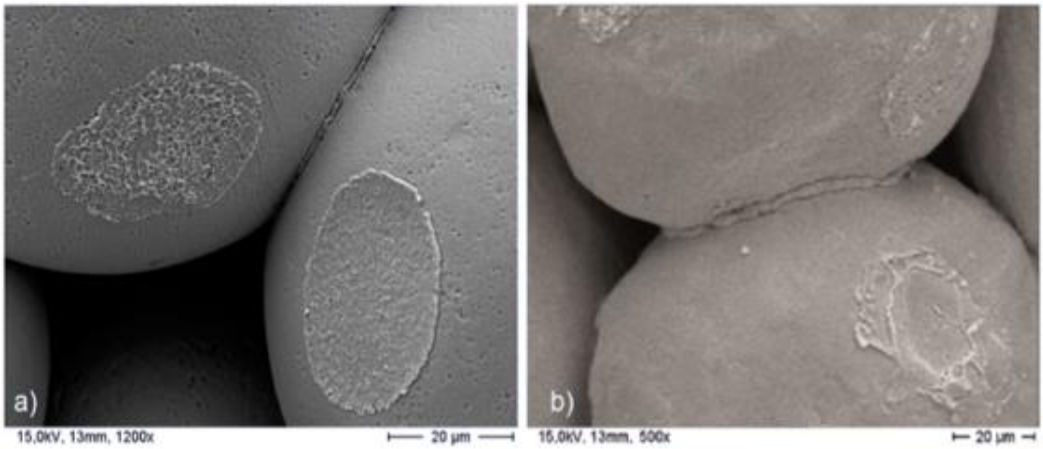

Source: (TRAPP et al., 2020).

In conclusion, pressure and temperature are the most studied parameters for optimizing sintering results using the SPS technique. Specifically, the advantage of applying high pressure is homogeneously distributing stresses and improving contact points between particles within the sintered sample, inhibiting grain growth and achieving high densification.

2.2 Effect of porosity and grain size on the mechanical properties of sintered materials

A considerable number of studies has focused on how porosity affects the mechanical properties of sintered materials (HAYNES, 1991; Y.E.; LI; EADIE, 2001; CHAWLA; DENG, 2005; YALCIN, 2009; KULECKI et al., 2016). In this context, Gibson. & Ashby proposed **eq. (1)** to estimate the mechanical properties (elastic modulus) of a porous material and can be modeled considering the mechanisms by which pores deform and fail (LORNA J. GIBSON AND MICHAEL F. ASHBY, 1999).

$$\boldsymbol{\sigma_{p1}^{*} * \sigma_{us} = C_2 \rho^{*} * \rho_s^{\frac{3}{2}}} \quad \textbf{(1)}$$

Where ρ^* and σ_{p1}^* are the apparent density and ultimate stress of the sintered material, σ_{us} and ρ_s are for the bulk density. C_2 is a constant related to the geometry of the pore. In addition, the material has Young's modulus E_p that can be predicted using the Nielsen equation **eq.(2)** (NIELSEN, 1983), expressed as:

$$\boldsymbol{E_p = E_s * \left[\frac{\left(1 - \frac{P(x)}{100}\right)^2}{1 + \left(\frac{1}{F_f} - 1\right)\frac{P(x)}{100}} \right]} \quad \textbf{(2)}$$

Where E_s is Young's modulus for the bulk material, P(x) is the percentage of total porosity of the sample, and F_f is the shape factor calculated from the image analysis results. Although the results of the different methods are estimates of the mechanical properties, they can offer good results and be a quick and straightforward solution for predicting sintered materials.

Figure 12 shows a schematic graph of the increase in mechanical properties with sintered density. According to this Figure, the route used to densify is less relevant than the density itself (BEISS, 2003; HÓGANAS AB, 2004). However, the sintering time and temperature affect the shape and size of the pores and, therefore, the mechanical properties of the sintered material (HAYNES, 1991; DOBRZANSKI et al., 2007).

Figure 12 - Increase the mechanical properties of sintered material with sintered density (Schematically).

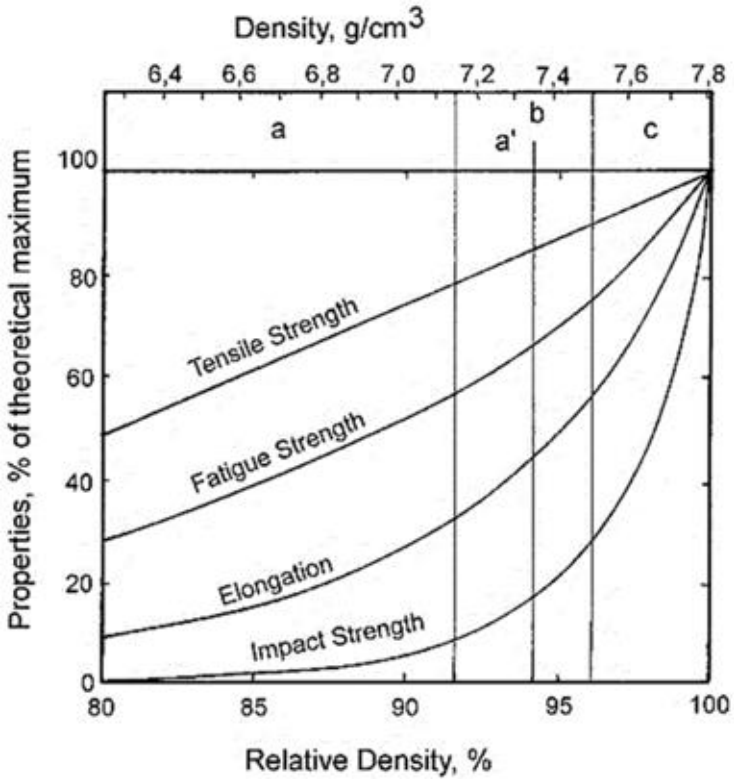

* Letters inside the graph indicate common processing routes with density ranges: a = press and sinter, a' = hot pressing, b = pressing + pre-sintering, re-pressing, and sintering, c = powder forging.

Source: Adapted from (BEISS, 2003; HÓGANAS AB, 2004).

2.3 SPSed copper and copper composites

Temperature and pressure are the main parameters for the sintering of materials. Table 1 presents some results from the literature on sintering parameters used in copper and SPSed copper-based composites. From this literature review, sintering parameters can be defined to adequately optimize the sintering parameters with high densification and little grain growth.

Table 1- Related works on copper sintering parameters and copper-based materials.

Matrix	Reinforcements		Sintering parameters SPS			Reference
	Particles	Percentage	Temperature (ºC)	Pressure (MPa)	Holding time (min)	
Copper	-	-	350-800	50	6	(ZHAOHUI et al., 2008)
Copper	-	-	800	50	15	(ZHANG et al., 2008b)
Copper	-	-	450-800	50	10	(ZHANG et al., 2008a)
Copper	-	-	600-800	100	6	(RITASALO et al., 2010)
Copper	-	-	300-472-567	60	5	(DIOUF; MOLINARI, 2012)
Copper	-	-	650	100	-	(MONNIER et al., 2015)
Copper	-	-	500-1000	50	5	(ZHU et al., 2017a)
Copper	Al_2O_3	30 wt.%	1350	30	10	(SHI et al., 2018)
Copper	Al_2O_3	5 wt.%	850	40	5	(PAN et al., 2019)
Copper	Al_2O_3	0.5-20 wt.%	800-1000	50-100	6	(RITASALO et al., 2011)
Copper	Al_2O_3	0.2-0.7 wt.%	860	45	20	(FU et al., 2019)
Copper	Al_2O_3	0.5-1-1.5 vol.%	900	30	5	(TAN et al., 2020)
Copper	Al_2O_3	1-3-5 vol.%	1050	30	15	(STROJNY-NĘDZA; PIETRZAK; WĘGLEWSKI, 2016)
Copper	TiB2	0.5wt.%	950	60	15	(PELLIZZARI; CIPOLLONI, 2017)
Copper	SiC	2-4 vol.%	750	70	6	(AKBARPOUR; ALIPOUR, 2017)
Copper	Graphene	0.1-0.2-0.3wt.%	600	35	5	(SHAO et al., 2019; TAN et al., 2020)

Source: Author.

The copper sintering via SPS is usually conducted at a temperature ranging from 600 to 1050 °C, holding times between 5 to 20 minutes, and pressures varying from 30 to 150 MPa (see Table 1). It is worth noticing that SPS does not need a pre-compaction.

The increase in sintering temperature also leads to a straightforward increase in density. However, rapid grain growth occurs during the sintering process. The lower sintering

temperatures of SPS and the pressure-assisted system in the final stage of the sintering process allow the theoretical density and, consequently, a low pore volume fraction to be achieved (DOBRZAŃSKI et al., 2007). ZHU et al., (2017a) reported that copper sintered at 800 and 1000 ºC via SPS presented grain sizes of from 0.56 to 0.96 μm, respectively, at the pressure of 50 MPa. Above 1000 ºC, the samples showed significant grain growth (2.9 um), as shown in Figure 13.

Figure 13 - Measured density of samples sintered at different temperatures and EBSD investigations of the SPS samples: maps showing the microstructure of samples sintered: inverse pole Figure (IPF) coloring, based on the sample normal direction, superposed on a band contrast map.

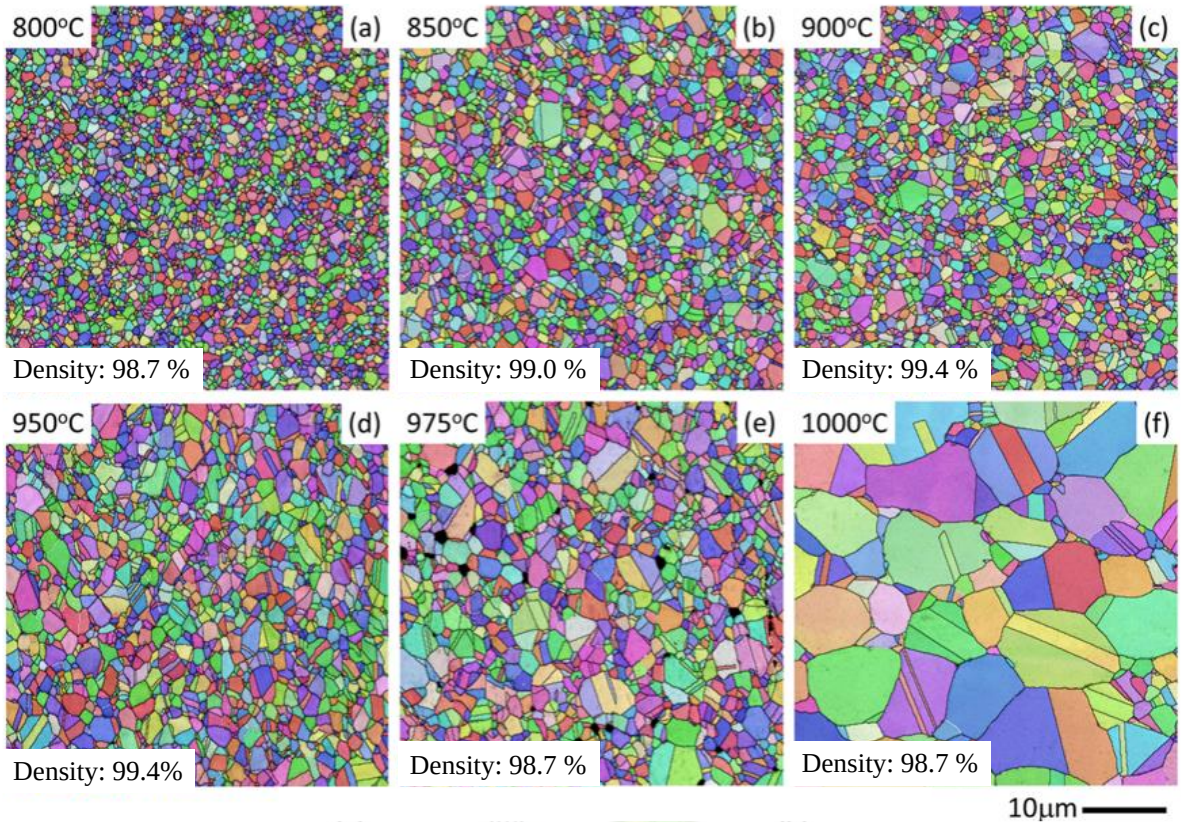

Source: Adapted from (ZHU et al., 2017a).

ZHANG et al., (2008a) have shown that the SPS sintering temperature of copper powders must be below 750 °C (at 50 MPa) to avoid significant grain growth since at 800 °C, the grains grow about three times (Figure 14).

Figure 14 - Microstructures of the bulk copper at sintering temperatures of (a) 450 °C, (b) 600 °C, (c) 750 °C and (d) 800 °C.

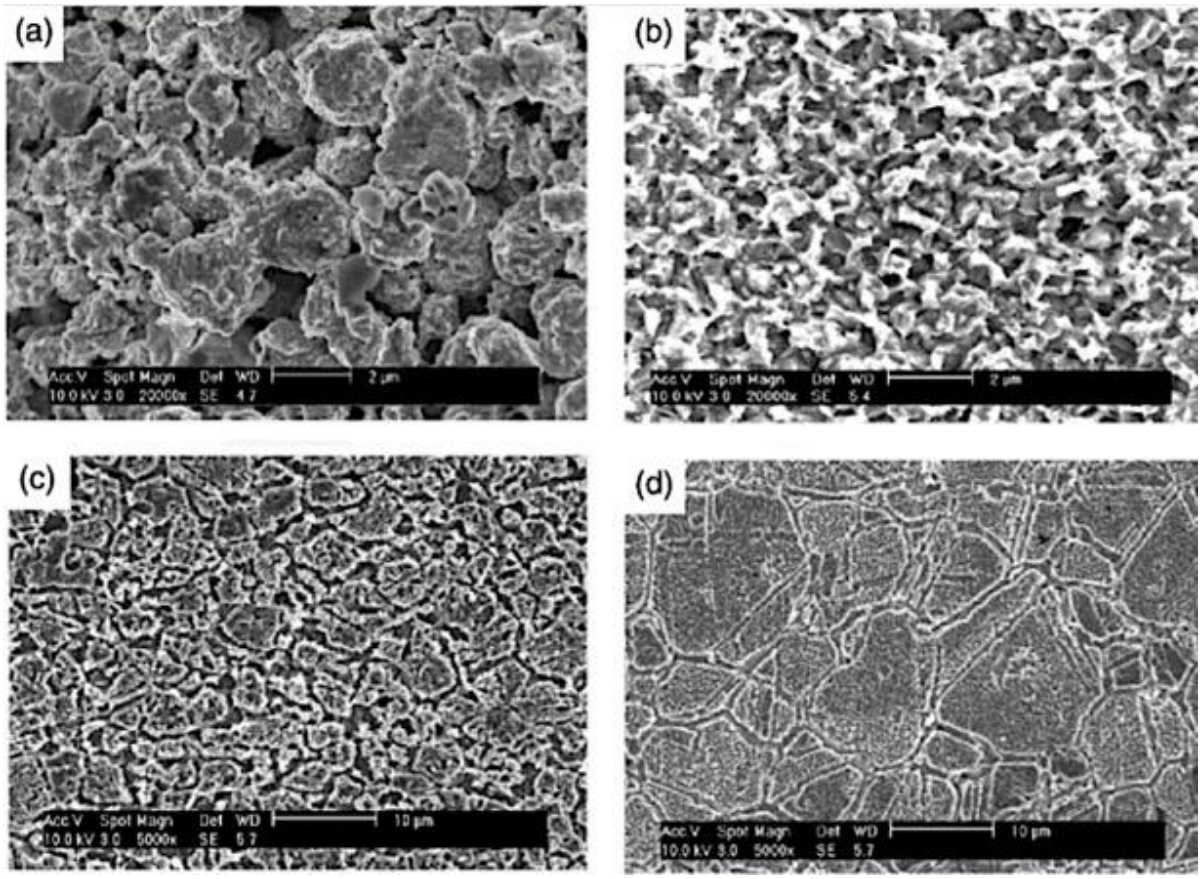

Source: (ZHANG et al., 2008a).

For the case of copper sintered by SPS, the microstructural contribution to the hardness increase can be assigned to the reduction in porosity and the high rate of densification. In addition, grain size retention in copper after sintering could also contribute to high hardness. For example, RITASALO et al., (2010) reported the hardness of SPS sintering of copper powder of size 410 nm sintered at different temperatures at 100 MPa with 6 minutes of holding time. Its hardness value ranges from 1.02 GPa to 1.24 GPa. Moreover, the increase in temperature to 900 ºC caused an increase in grain size twice the size of the starting powders. Therefore, the sintering temperature directly affects the relationship between hardness and microstructure (Figure 15).

Figure 15 - Grain sizes, microhardness, and densities of the copper.

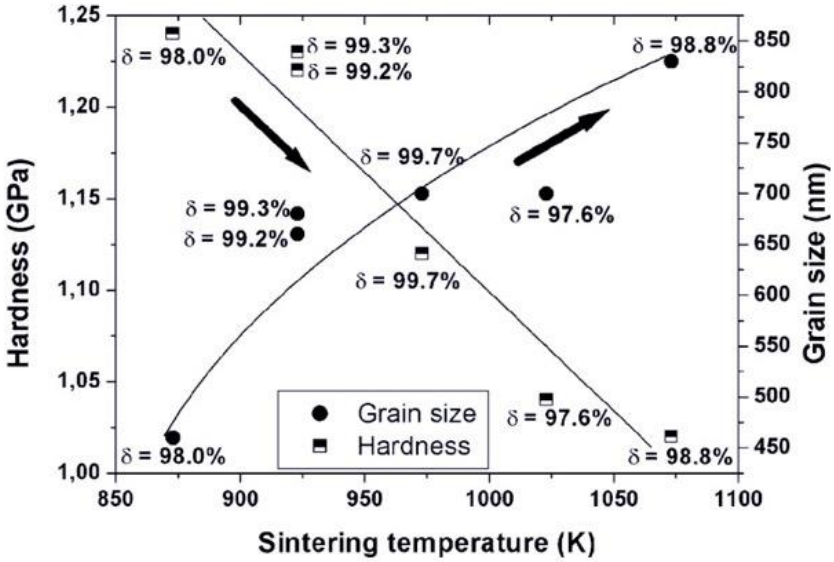

Source: Adapted from (RITASALO et al., 2010)

A. WIJAYA et al., (2021) developed some characterization methods to understand the impact of pore morphology on the elastic behavior of sintered copper. Figure 16 represents of the effect pores on the elastic modulus of sintered copper. It can be seen that the elastic modulus falls sharply with increasing porosity. However, the results of the elastic modulus from nanoindentation and FEM (Finite Element Method) simulation provide a good agreement with the curves presented in Figure 16.

Figure 16 - (a) Elastic modulus as a function of the mean porosity P. Experimental nanoindentation data of sample with 36.1 ± 1.7, 31.2 ± 4.8 and 55.0 ± 4.15 are compared with modeled data using FEM simulations. The FEM simulations use the segmented 3D morphology as input. The grain morphology of copper is not incorporated into modeling.

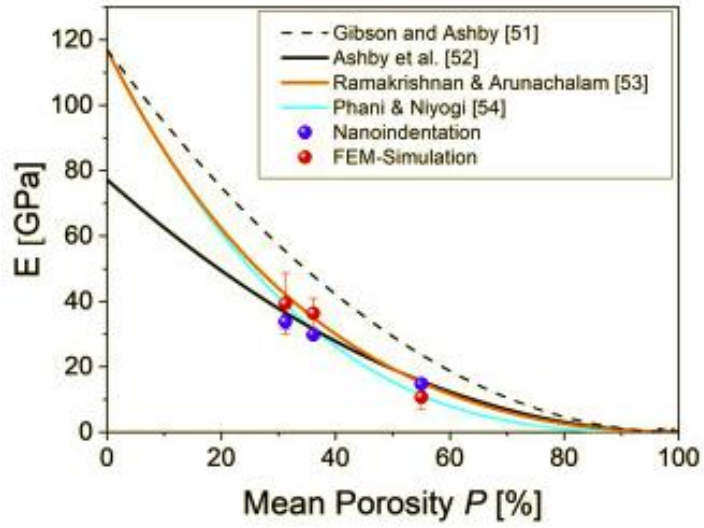

Source: Adapted from (A. WIJAYA et al., 2021).

On the other hand, the strenght is determined by other microstructural features (for instance, grain size, pore morphology and bulk anisotropy), but porosity could be the key variable that controls the elastic modulus, in particular for the sintered copper.

BORKAR and BANERJEE, (2014) studied the influence of sintering parameters on the microstructure and mechanical properties of nickel (Figure 17). The results showed that increasing the pressure from 50 to 80 MPa reduces the yield stress and elongation by 11% and 9%, respectively. Furthermore, the results indicate no significant effect of pressure on the tensile yield strength or ductility for the nickel. However, the authors assume that the selected SPS parameters (80 MPa and 850 ºC) present a better compromise between density and mechanical properties.

Figure 17 - The stress-strain curves of SPS processed pure nickel at 1000 °C for 50, 65, and 80 MPa pressures obtained from the tensile test. It also indicates the average grain size/relative density measurements of SPS sintered pure nickel.

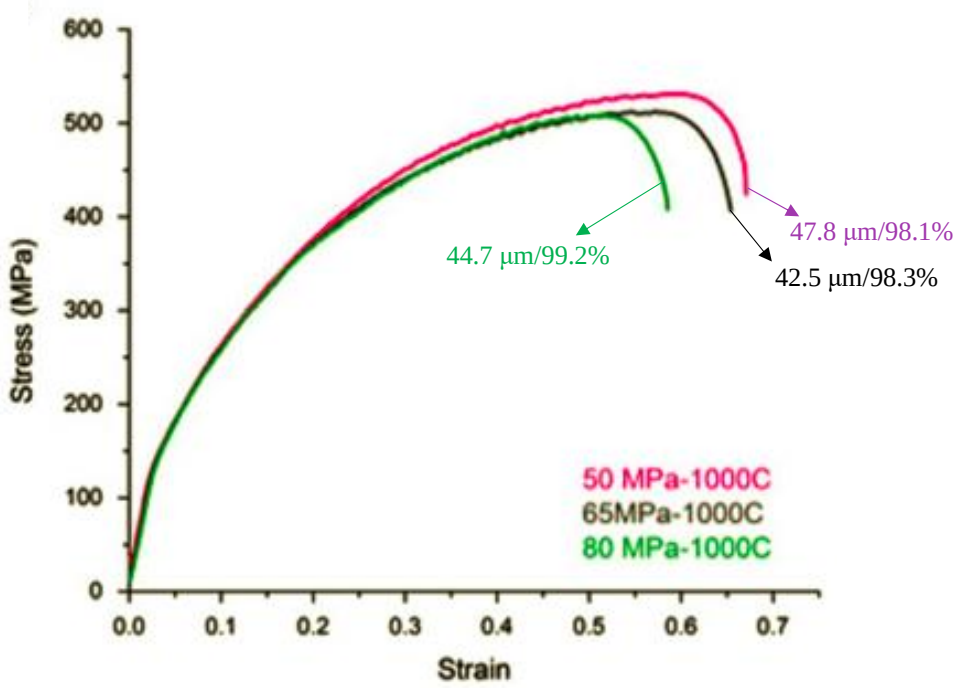

Source: Adapted from (BORKAR; BANERJEE, 2014).

2.3.1 Metal Matrix Composites

Metal matrix composites (MMC) can be defined as materials consisting of at least two distinct phases with different chemical compositions and physical properties, for instance, a ceramic reinforcement in a metal matrix. Cu, Al, Mg, Ti, Co, Ni, Be, and Ag matrices have been studied (JAYALAKSHMI; GUPTA, 2015). The metal matrix is a continuous phase that is ductile and chemically stable. It has good thermal/electrical conductivity, and mechanical and tribological properties are enhanced when mechanical reinforcement is added.

In MMC, the reinforcement is a load-bearing phase due to its high Young's modulus (stiffness) and mechanical resistance properties. Therefore, the reinforcement is usually a ceramic material added as fibers, short fibers, or particles of oxides, carbides, nitrides, and borides such as SiC, Al_2O_3, B_4C, TiB_2, TiB, TiC, TiN, TiCN, and graphite (CHAWLA; DENG, 2005). The first requirement for a composite is a superior performance reached based on a homogeneous distribution of reinforcement.

In addition, an essential characteristic of particle size distribution, it is widely recognized that the size distribution of particles in a mixture significantly impacts the packing efficiency and influences the pore size and shape, shrinkage, and microstructure. Particle distribution homogeneity allows transferring shear stresses, supporting high normal loads, as well as in deformation/damage since hard particles retain the flow and restrict the propagation of cracks (FOGAGNOLO et al., 2003). Therefore, there is a critical value of the matrix-reinforcement particle size and morphology ratio.

Soft particles in MMC are the main ones responsible for the densification of the composite. However, RAZAVI-TOUSI; YAZDANI-RAD; MANAFI, (2011) showed the volume fraction of the hard particles could affect the densification (Figure 18) since hard particles agglomerate and make it difficult to close the pores. In this case, the clustering of the reinforcing particles affects the mechanical properties of the composite.

Another relevant characteristic of the mixture is the particle size; it is widely recognized that the size distribution of particles in a mixture significantly impacts the packing efficiency, which in turn influences the pore size and shape, shrinkage, and microstructure development. Furthermore, the work by RAZAVI-TOUSI; YAZDANI-RAD; MANAFI, (2011) schematically showed different types of pores and particle configurations that cause changes in densification (Figure 18). A good dispersion can contribute to densification because the soft particles are the main ones responsible for the densification of the composite. When hard particles agglomerate, it is difficult to close the pores formed between them, leaving them with

high residual porosity due to the generation of new pores between the reinforcement particles (ABD-ELWAHED; WAGIH; NAJJAR, 2020).

Figure 18 - Different pores formed between initial particles; type 1: between matrix particles, type 2: between matrix and reinforcement particles, and type 3: between reinforcement particles. (a) Reinforcement and matrix particles of the same size, (b) nano-reinforcement, and (c) ball-milled mixture.

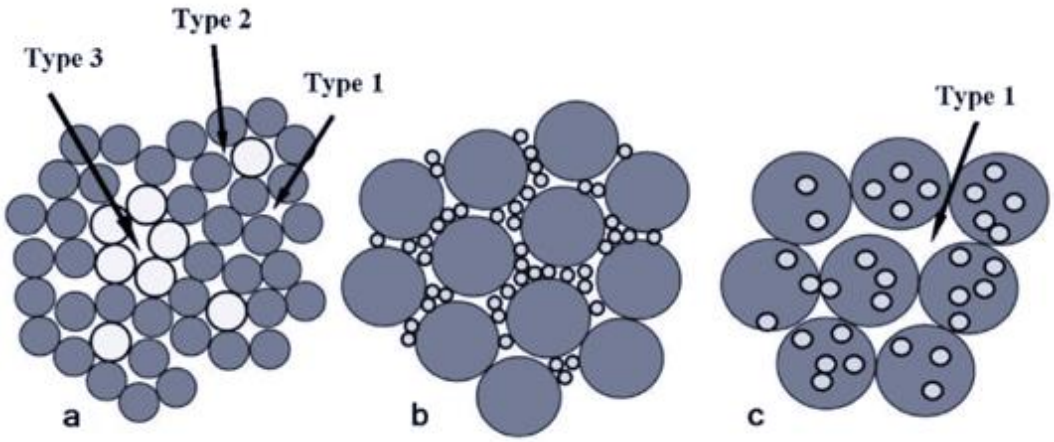

Source: (RAZAVI-TOUSI; YAZDANI-RAD; MANAFI, 2011).

2.3.2 Particle addition methods in copper base composites.

The mixture is the most critical step, where the objective is to achieve a uniform distribution of particles in the matrix. The mixture can be performed in grinding high energy system, tubular, ultrasound, and wet or dry mixing. Therefore, a good mixture directly affects the results of the mechanical properties (SADOUN; MESELHY; ABDALLAH, 2021).

For the manufacture of composites, there are different techniques. Mainly, two types of composite manufacturing techniques are reported in the literature: Cu-Al_2O_3, which are in-situ and ex-situ (SADOUN et al., 2020b). The ex-situ technique is performed by milling or mixing Cu with Al_2O_3 particles. The in-situ technique is performed through two main techniques, mechanochemical and thermochemical techniques. Mechanochemical techniques are achieved through two different ways of producing composite Cu-Al_2O_3. The first form is carried out by adding Cu to an aqueous aluminum nitrate solution. The second way is carried out by adding Cu to an aqueous solution of ammonium hydroxide and aluminum nitrate. Generally, in the two mechanochemical techniques, the mixture is heated in the air and is reduced by H_2; to turn it into Al_2O_3 and CuO powder oxides (SHEHATA et al., 2009). The manufacturing of composites Cu-Al_2O_3 using thermochemical techniques is performed in two ways. First, a route consisted

of adding a specific amount of CuO to an aqueous aluminum nitrate solution. The other route involves mixing CuO and aluminum nitrate in adequate amounts of ammonium hydroxide. In the two routes, the mixtures are heated at 850 ° C and are reduced in H_2 (atmosphere) at 970 ° C for 1.5 h until obtaining the final structure (JENA et al., 2004),

Figure 19 shows that the presence and good dispersion of Al_2O_3 particles in a copper matrix improve the hardness of the composite. In addition, due to the high hardness and thermal stability, Al_2O_3 phase transformations do not occur during processing. Thus, alumina prevents dislocation motion and slows grain growth rate even close to the melting point of the copper matrix, where other strengthening mechanisms, such as precipitation hardening or solid solution hardening, quickly lose their effectiveness (HAN et al., 2015; RAJKOVIC; BOZIC; JOVANOVIC, 2008; SHI et al., 2018).

Figure 19 - a) Cu–5 wt.% Al_2O_3; Milling time: 20 h, 800 ºC, 1 h, 35 MPa (ex – situ), b) Cu–8 wt.% Al_2O_3, c) Cu–7 wt.% Al_2O_3; 700 ºC, 5 min, 50 MPa (in-situ: mechanochemical) and d) Cu–70 wt.% Al_2O_3; 1350 ºC, 10 min, 30 MPa, (in-situ: thermochemical).

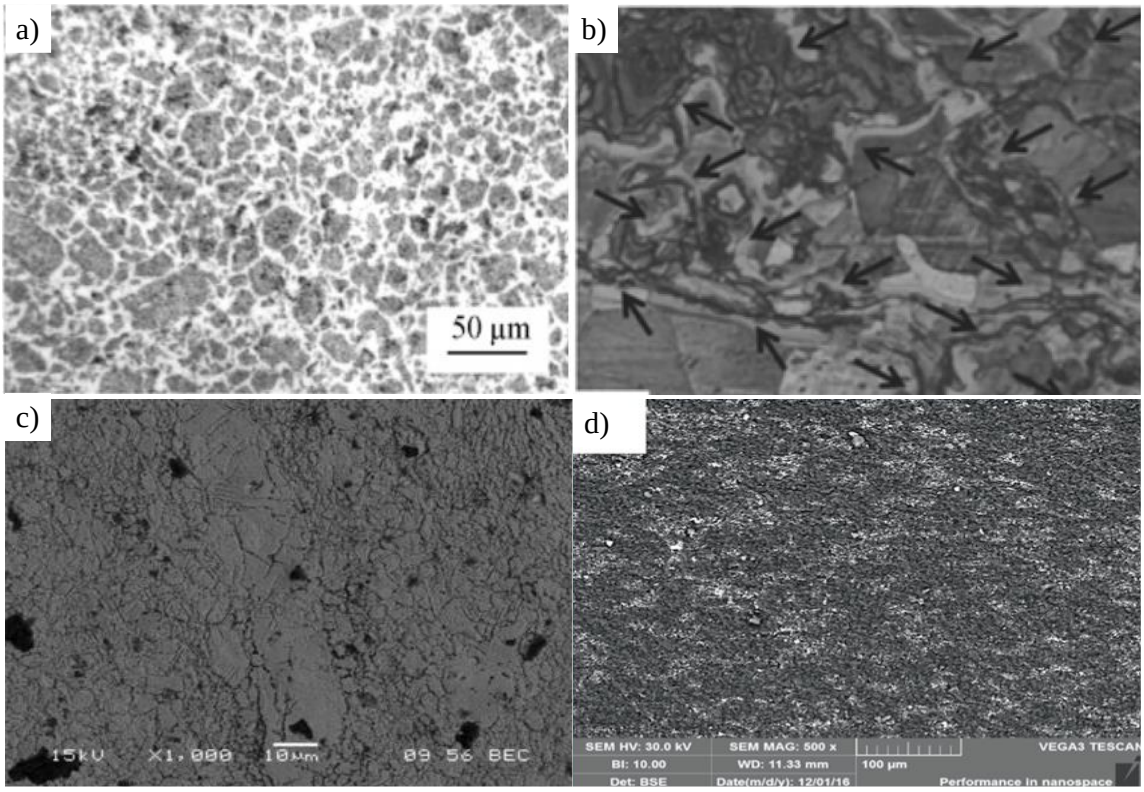

Source: Adapted from (HAN et al., 2015; RAJKOVIC; BOZIC; JOVANOVIC, 2008; SHI et al., 2018).

The in-situ and ex-situ manufacturing techniques can be complemented with coating techniques on the Al_2O_3 particles, which can be carried out by the coating method of Electroless plating. Electroless plating is a highly efficient method to modify the interface between copper and Al_2O_3; there is no limit to the shape and size of the particles for Electroless plating to achieve a uniform and dense deposition. Electroless plating is a mechanical-chemical technique that is carried out by adding Al_2O_3 particles to an aqueous solution of ammonium hydroxide and silver nitrate, in which the silver particles are deposited on the surface of the Al_2O_3 particles and modifies the interface between Al_2O_3 and copper during sintering (GÜLER et al., 2020; SADOUN et al., 2020b; SADOUN; MESELHY; ABDALLAH, 2021).

In the literature, different elements have been used to coat ceramic particles, such as Ag, Ni, Fe, Cr, and Zn, which are called effective sintering additives and can improve the density of sintered composites without drastically decreasing thermal and electrical conductivity. Silver is an effective additive that can enhance the sinterability of composites during sintering (LI et al., 2019). Silver particles are attracting more attention due to their antimicrobial properties in the healthcare industry. In addition, silver inhibits SARS-CoV-2 and has been studied due to its bactericide properties (GÜLER et al., 2020; SADOUN et al., 2020b). Figure 20 shows the microstructure of synthesized Cu–Al_2O_3 composites containing different content of coated Al_2O_3 particles. This figure reflects the homogenous microstructure of the powders and composites sintered without observation of agglomerations and microvoids. Moreover, the figure shows grain refinement with increasing Al_2O_3 content.

Figure 20 - SEM images of the composite powders of a) Cu-5 wt. %Al_2O_3 without coating, b) Cu-5 wt. % Al_2O_3 with coating, c) Cu-10 wt. % Al_2O_3 composite with coating and d) larger magnification for composite with 10% Al_2O_3.

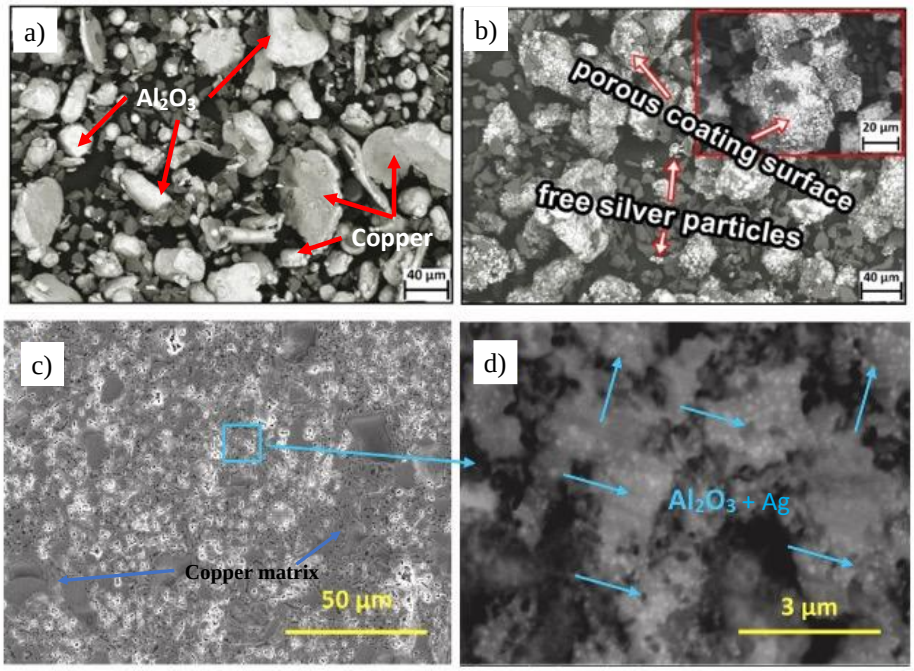

Source: Adapted from (GÜLER et al., 2020) (SADOUN et al., 2020b) (SADOUN; MESELHY; ABDALLAH, 2021).

Surface modification is widely adopted as a viable solution for metal matrix composites. Various coatings can be manufactured using different techniques, and it has been applied on multiple substrates, which results in other characteristics. Hard protective coatings may consist of various compositions. However, based on the hardness and the resistance to wear, some frequently used elements are Ag, Ti, Ni, carbides, Zr, B, and Diamond Like Carbon (DLC). The deposition methods such as Chemical Vapor Deposition (CVD), Physical Vapor Deposition (PVD) as well as the cutting-edge coating hybrid-deposition methods, such as Pulsed DC Magnetron Sputtering (PDCMS), High Power impulse (HiPIMS) and Arc Ion Plating (AIP) (AL-ASADI; AL-TAMEEMI, 2022). However, these deposition methods are rarely used for the coating of particles (ceramics) for the manufacture of sintered composites.

Surface coating methods can be classified according to Figure 21.

Figure 21 - Surface modification techniques.

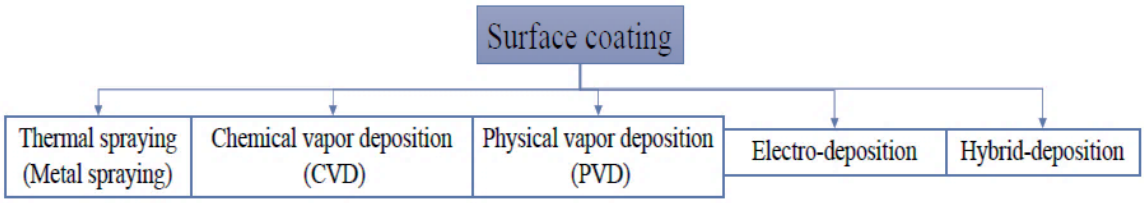

Source: Adapted from (AL-ASADI; AL-TAMEEMI, 2022).

CHE et al., (2015) sintered Cu-diamond composites by coating the diamond particles with Ti using the PVD technique to improve the interfacial bond between the diamond particles and the Cu matrix. The diamond particle with a non-uniform layer of Ti is presented in Figure 22.

Figure 22 - SEM images of Ti-coated layer on the surface of diamond particle.

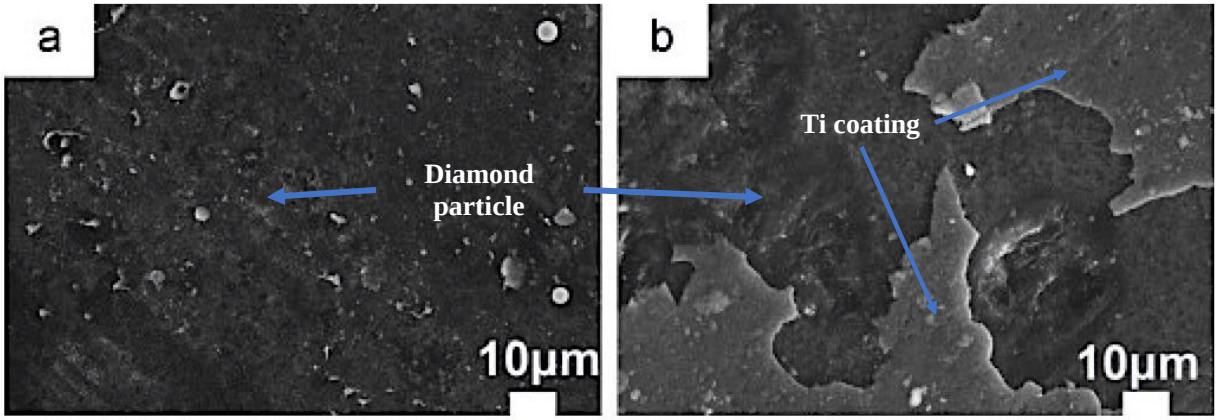

Source: Adapted from (CHE et al., 2015).

2.4 Abrasive Wear

In the literature, there are studies on the wear mechanisms, elastic-plastic deformations, abrasion depth, characteristics of the interface between the constituents, and the sliding contact properties of copper and copper-based MMCs (PÖHL; MOHR; THEISEN, 2017; XIAO et al., 2013). However, the abrasive wear occurrence related to micro-mechanisms and geometric parameters of abrasives for copper still needs to be improved. Therefore, it is significant to investigate the scratch behavior of copper and copper-based composites by detecting the effects of normal loads, microstructure, and mechanical reinforcement content.

The ASTM G40, (2015) standard defines abrasive wear as the loss or displacement of mass resulting from the interaction between particles or hard asperities that are forced against a surface along which they move. As described by GAHR, (1981), abrasive wear can be defined

as the loss of matter due to the relative movement of two surfaces due to the action of hard asperities on one of the surfaces, free abrasive particles between the two surfaces, or abrasive particles embedded on the surfaces. These hard particles can come from the material in process, fragments from the wear process, or even contamination by an external environment (GAHR, 1987). According to BURWELL, (1957), the wear mode is determined by the dynamics of the particles on the contact surfaces. Also, abrasion resistance is not an intrinsic property of the material but comes from the tribological system. Therefore, the abrasive wear process can be considered complex, and the most important factors influencing the amount of abrasive wear are shown in Figure 23.

Figure 23 - Influence of various parameters on abrasive wear performance of composite materials.

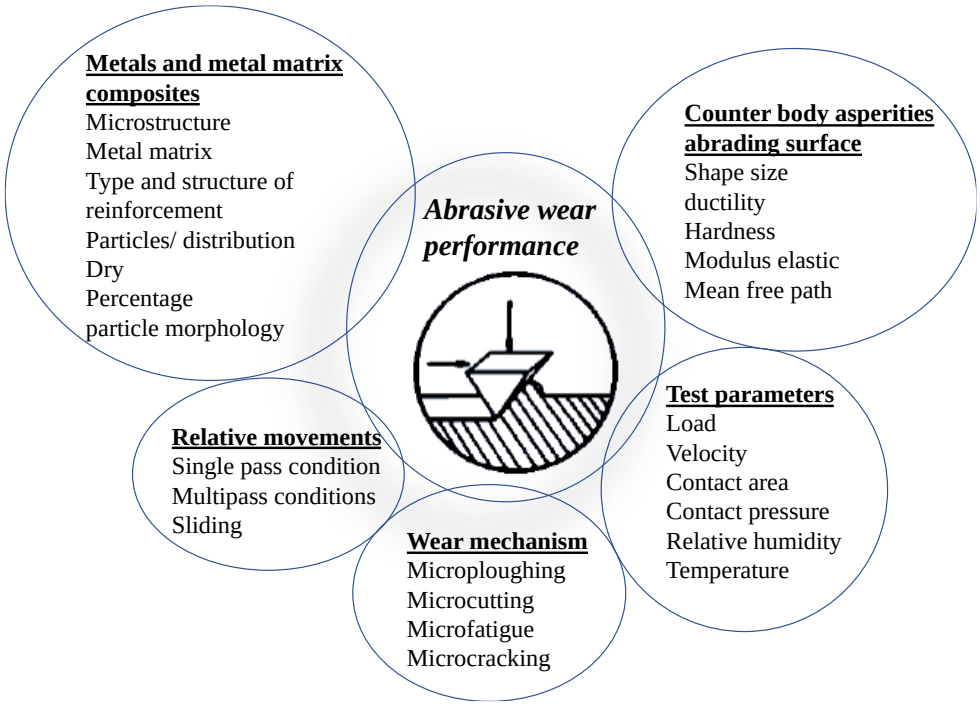

Source: Adapted from (HUTCHINGS; SHIPWAY, 2017).

Additionally, abrasive wear can be classified in two ways: two-body abrasion (Figure 24a) and three-body abrasion (Figure 24b). In this context, the sample is considered the first body, the counter body the second, and the abrasive the third. Two-body wear occurs when hard asperities or abrasive particles are rigidly attached to the counter-body, generating grooves/scratches on the surface of the specimen during movement. In three-body wear, the abrasive particles are free, thus allowing rolling and/or sliding with the sample and the counter-body.

Figure 24 - Wear modes a) with fixed abrasive and b) loose abrasive.

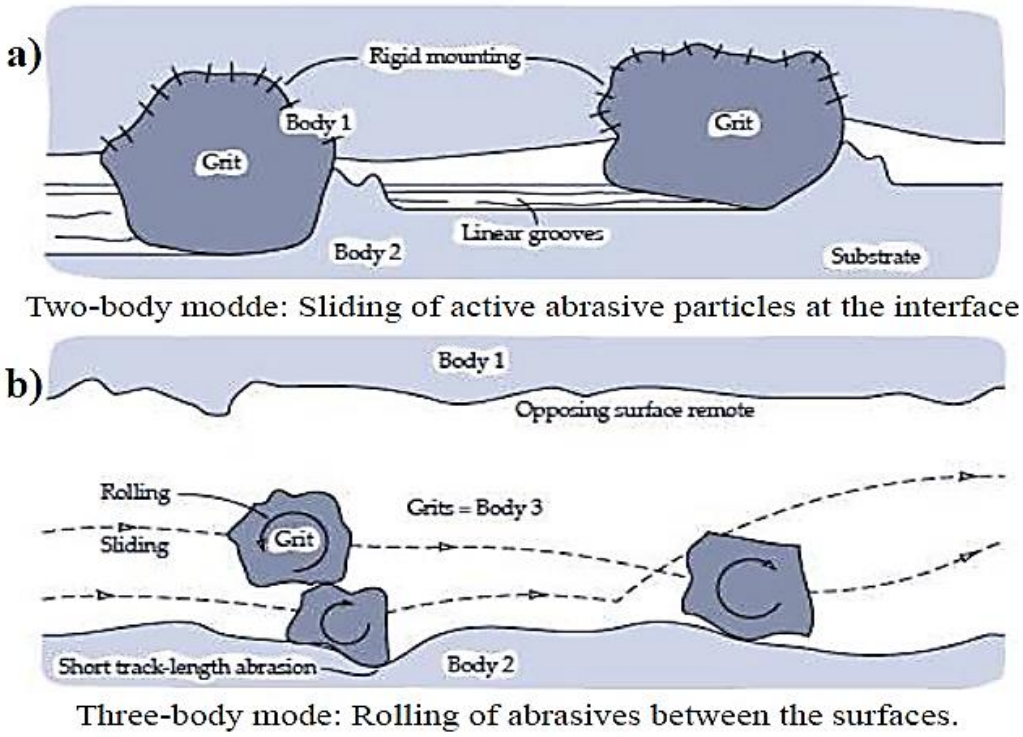

Source: Adapted from (HUTCHINGS; SHIPWAY, 2017; PENAGOS, 2016).

The two and three-bodies classification can be adequate to determine the phenomena of the abrasive process. Rutherford and Hutchings (1996) showed that in three-body abrasive wear, a rotation of acting particles occurs, resulting in scattered indentations on the wear surface.

The interaction between the surface and the abrasive particle promotes the occurrence of micro-mechanisms of abrasion (MULHEARN; SAMUELS, 1962; SEDRIKS; MULHEARN, 1963; ZUM GAHR, 1987). The literature defines the wear mechanisms of sliding the abrasive particle over the surface as micro- ploughing, micro-cutting, micro-cracking, and micro-fatigue (Figure 25).

Figure 25 - Basic wear mechanisms viewed microscopically that operate in a defined system. (F_n normal force on apparent contact surface, F_f friction force between base body and counter body, F_n, as normal force on asperity contact, v relative velocity, HV Vickers hardness).

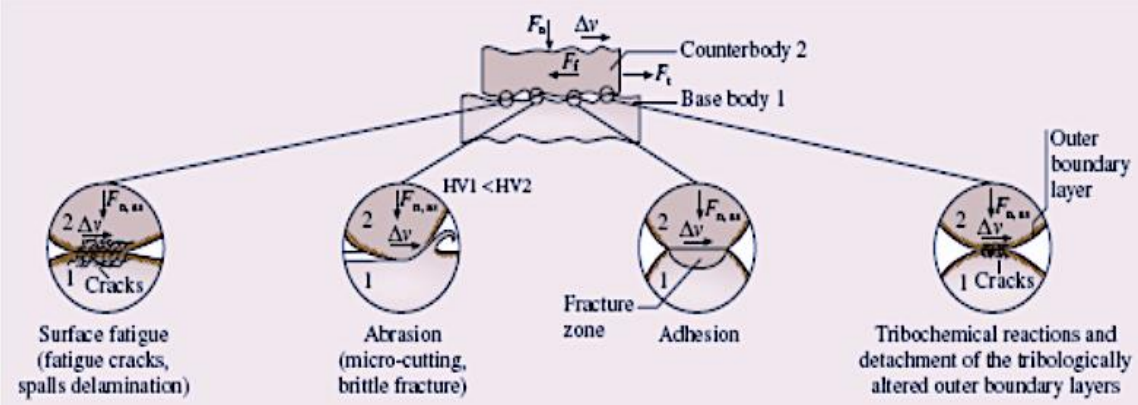

Source: Adapted from (KOVAŘÍKOVÁ et al., 2009).

2.4.1 Micro-mechanisms of abrasion

HUTCHINGS; SHIPWAY, (2017) divides the abrasion mechanisms into plastic deformation and brittle fracture abrasion mechanisms. Among the mechanisms controlled by plastic deformation are micro-ploughing and micro-cutting. The mechanism controlled by brittle fracture is called the micro-cracking mechanism.

ZUM GAHR, (1987), in micro-ploughing, the material is plastically deformed and flows to the sides of the groove. In the ideal case, micro-ploughing due to a single pass of one abrasive particle does not result in any material detachment from a wearing surface (Figure 26a). Micro-cutting refers to removing material as tiny chips and debris due to the shear stress imposed by the abrasive particle, similar to machining processes (Figure 26b). In a pure micro-cutting mechanism, the volume of material lost equals the volume of scratch produced. Micro-fatigue represents micro-ploughing with groove interaction (Figure 26c). Also, during micro-ploughing, material loss may occur due to the simultaneous or successive action of the abrasive particles. As a result, cyclic localized plastic deformation occurs, followed by successive micro-ploughing and damage-denominated micro-fatigue occurrences. Finally, the micro-cracking mechanism occurs due to highly concentrated stresses imposed by the abrasive particles, causing the growth of small cracks and detachment of fragments instead of the growth of one crack (Figure 26d). This micro-mechanism is typical of brittle materials. GAHR (1987) highlighted the four mechanisms shown in Figure 26, ignoring the wedge formation (transition).

Figure 26 - Schematic illustration of the micro-mechanisms of abrasion: (a) micro-ploughing, (b) micro-cutting, (c) micro-fatigue and d) micro-cracking.

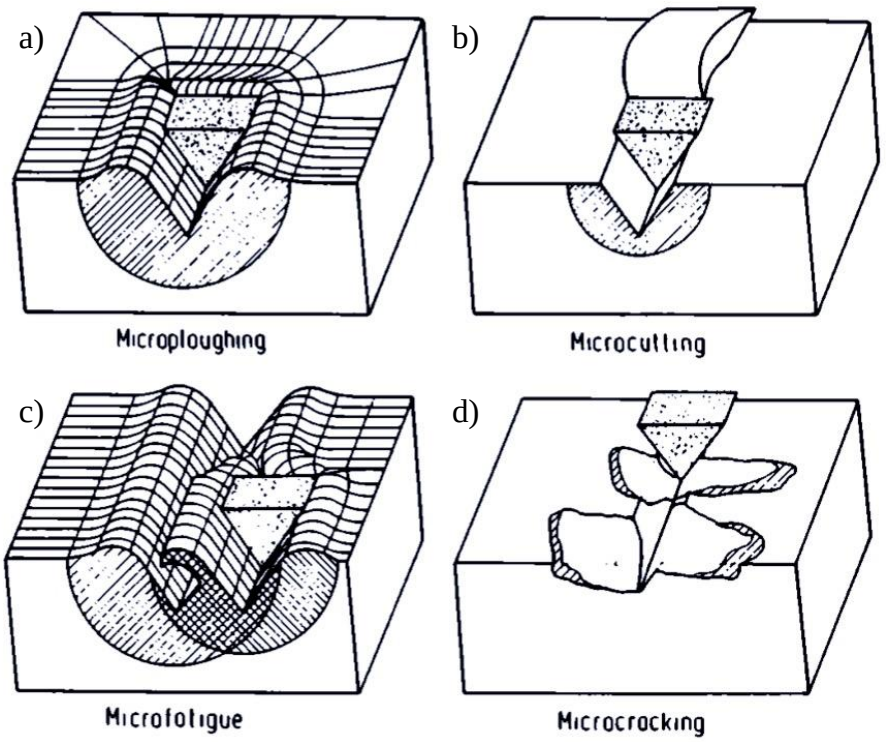

Source: Adapted from (ZUM GAHR, 1987).

2.4.2 Abrasive wear for ductile materials

Rabinowicz, Dunne, and Russell (1961) develop a simple theoretical model for abrasive wear that involves material removal by plastic deformation. Figure 27 shows an abrasive particle, idealized as a cone of half-angle θ, sliding along the surface of a ductile material. It forms a groove in the material, and it is assumed that wear is produced by removing some proportion of the material that is displaced by the particle in the groove. A normal load W is applied to the abrasive particle (SERIACOPI, 2018; FRANCO, 2015; MACHADO, 2017; RABINOWICZ; DUNN; RUSSELL, 1961). The model presented by the authors is complemented by HUTCHINGS; SHIPWAY, (2017), as shown in Figure 26.

Figure 27 - Geometry of contact between an idealized conical abrasive particle and a surface: (a) perspective view; (b) section in elevation; (c) section in plain view.

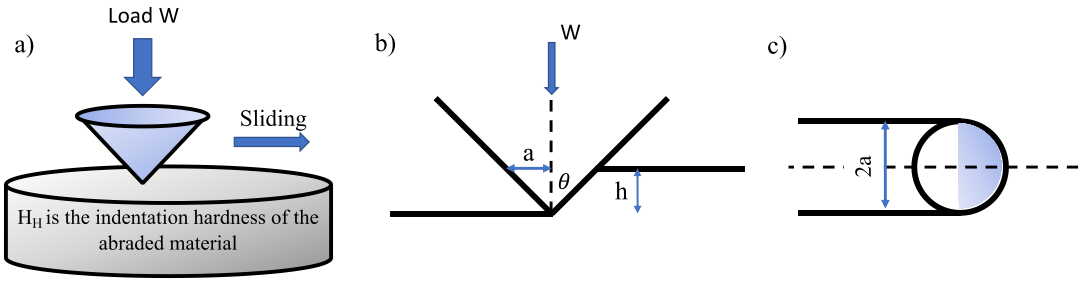

Source: Adapted from (SERIACOPI, 2018; HUTCHINGS; SHIPWAY, 2017).

Where: W is the normal load applied, H_H is the indentation hardness of the abraded material, and a is the indentation radius (Figure 27 c).

$$W = H_H * \underbrace{\frac{1}{2}\pi a^2}_{\text{Contact area}} \tag{3}$$

The volume removal (V) along the sliding distance (L).

$$V = L * a * h = \frac{a^2}{\tan\theta} * L \rightarrow a^2 = \frac{V}{L}\tan\theta \tag{4}$$

In which: h is the depth defined in Figure 27 b, and θ is the semi-angle of the abrasive particle. By replacing **eq. (4)** in **eq. (3)**, **eq. (5)** can be obtained.

$$W = H_H \frac{1}{2}\pi * \frac{V}{L}\tan\theta \rightarrow \underbrace{\frac{V}{L}}_{Q} = \underbrace{\frac{2}{\pi\tan\theta}}_{k} * \frac{W}{H_H}$$
$$\therefore Q = k * \frac{W}{H_H} \; or \; Q = k * W \tag{5}$$

Where k is a dimensionless constant that considers the geometric factor of the abrasive particle (tan θ), and the removed fraction of material displaced during scratch, **eq. (5)** is the Archard equation for sliding wear, which indicates the wear severity.

Abrasive particles tend to deform the softer surface. Therefore, the material is displacement (micro-ploughing) without micro-cutting. CHALLEN; OXLEY; DOYLE, (1983)

explain the different abrasive particle behavior during a scratch on a perfectly plastic material without a flow of material in the normal plane to the sliding surfaces. The authors distinguished three modes of deformation employing a slip-line field analysis which are presented in Figure 28.

Figure 28 - Description of the modes of deformation that generate the abrasive mechanisms in ductile materials, and scheme obtained from the slip-line field analysis presented by and Figures: Study through scanning electron microscopy (SEM) in which the micro-mechanisms of abrasive wear by plastic deformation are illustrated, a) micro-ploughing, b) wedge formation, and c) micro-cutting.

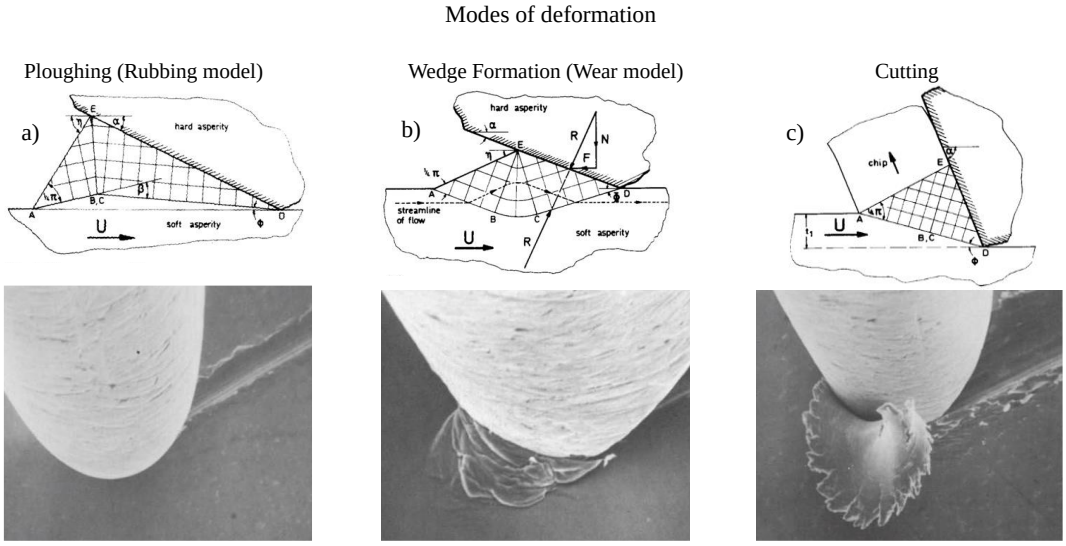

Source: Adapted from (SERIACOPI, 2018; HOKKIRIGAWA; KATO, 1988; CHALLEN; OXLEY, 1979).

In the ploughing no material is removed from the surface; material flows underneath the particle, and pile-ups form on the sides of the scratch track (Figure 28a). The second mode characterizes the wedge formation, which limits the slip or adhesion between the front face of the abrasive particle and the abraded material – transition mechanism (Figure 28b). The buildup of the material may detach, causing a loss of material. The latter mode represents the cutting, in which material is removed by the particle action, forming chips and debris (Figure 28c).

2.4.3 Geometric parameters in abrasive micro-mechanisms

HOKKIRIGAWA and KATO, (1988) performed scratch tests on different materials to study the evolution of the coefficient of friction based on the abrasive micro-mechanisms presented. In Figure 28 (SEM images), the geometric parameters indicated in Figure 27 are:

- Attack angle (θ): The attack angle was initially studied by MULHEAM; SAMUELS, (1962), and it is defined as the angle formed between the particle in the direction of movement and the plane of the surface that suffers the abrasion (Figure 29, **eq. 8**). The attack angle can reach a critical (theoretical) value, and there is an abrupt transition of micro-mechanisms changing from micro-ploughing to micro-cutting (ZUM GAHR, 1987).

-Degree of penetration (D_p), which relates the depth of the spherical tip indenter (h) and the diameter of the indentation produced (Figure 29, **eq. 9**).

Figure 29 - Simplified model of a spherical point (pin) on a flat surface, to represent geometrically and mathematically to obtain the degree of penetration (D_p) and attack angle (θ) as wear severity indices.

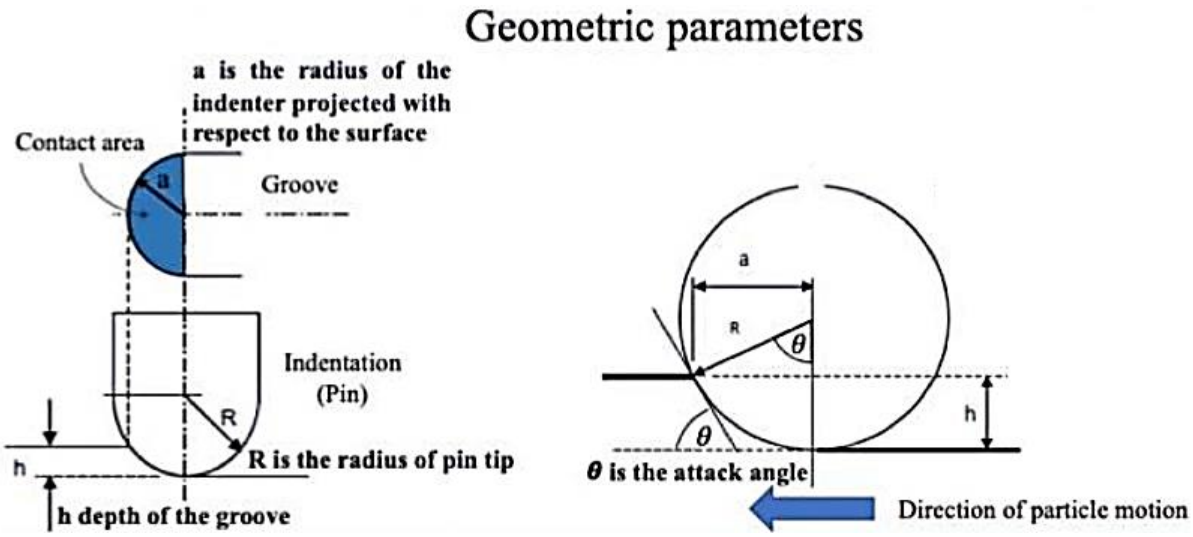

Source: Adapted from (HOKKIRIGAWA; KATO, 1988; HOKKIRIGAWA; KATO; LI, 1988).

From Figure 29, a trigonometric relationship is made, it has the following condition:

$$R^2 = a^2 + (R-h)^2 \rightarrow h = R - \sqrt{R^2 - a^2} \quad \textbf{(6)}$$

The attack angle (θ) is calculated in **eq. (7)** based on the parameters displayed in Figure 29.

$$\sin\theta = \frac{a}{R} \quad \textbf{(7)}$$

The attack angle (θ) is given by the following relationship in Figure 29:

$$\theta = \cos^{-1}\left(\frac{R-h}{R}\right) \quad (8)$$

The degree of penetration (D_p) is calculated in **eq. (9)** based on the parameters displayed in Figure 29.

$$D_p = \frac{h}{a} \quad (9)$$

From **eqs. (6)** and **(9)**, Dp can be expressed as a function of R and a as follows:

$$D_p = \frac{R}{a} - \left(\frac{R^2}{a^2} - 1\right)^{\frac{1}{2}} \quad (10)$$

The degree of penetration D_p was introduced to describe the three-dimensional severity of contact for wear, which was defined by the following **eq. (11).** Also, D_p, can be expressed as a union of the radius of tip (R), the load (W), and the hardness of the flat surface (HV).

$$D_p = \frac{R}{a} = \left(\frac{\pi R^2 H}{2W}\right)^{\frac{1}{2}} - \left(\frac{\pi R^2 H}{2W} - 1\right)^{\frac{1}{2}} \quad (11)$$

There is a direct relationship between D_p and the attack angle, considering the shape factor in **eq. (12)**:

$$D_p = \frac{1-\cos\theta}{\sin\theta} \quad (12)$$

HOKKIRIGAWA; KATO; LI, (1988) obtained a diagram showing wear modes (Figure 30) directly related to the D_p and θ as a function of the hardness of the abraded material (**eq. (10)**).

Figure 30 - Maps of abrasive mechanisms defined for the variation angle attack and degree of penetration as a function of the hardness of the worn material. In this case, the abrasive is spherical with a 25 µm radius.

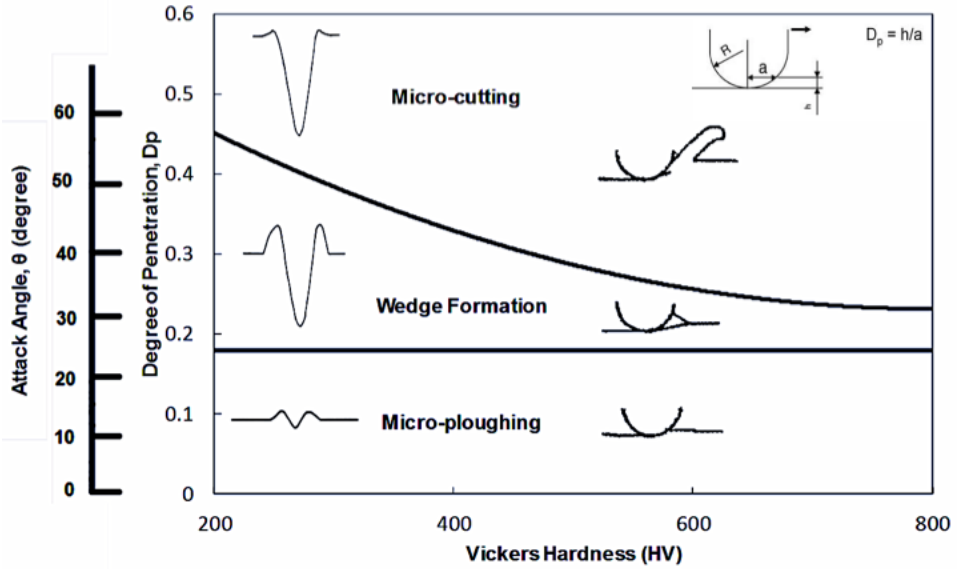

Source: Adapted from (SERIACOPI, 2018; GAHR, 1998; HOKKIRIGAWA; KATO; LI, 1988).

HOKKIRIGAWA and KATO, (1988) showed the increase in hardness of the worn material causes a decrease in the critical attack angle and the degree of penetration associated with the transition of micro-mechanisms. Therefore, the scratch resistance is associated with hardness, forces, and residual groove size. Scratch hardness is defined as the ratio of normal force (F_n) to the projected area on a horizontal section (WANG; SUBHASH; CHANDRA, 2001). It is dominated by attack angle, the microstructure of abraded material, and lubrication. Also, the scratch hardness could be higher or lower than the indentation hardness, depending on the tip features and the hardening of the abraded materials. On the other hand, scratch resistance is defined as the ratio of tangential force (F_t) projected cross-section area, and it is generally associated with scratch speed (WANG; SUBHASH; CHANDRA, 2001).

CHALLEN; OXLEY; DOYLE, (1983) highlighted the decrease in the critical attack angle as a function of the hardening of the metallic material. In addition, the authors evaluated the shear strength at the interface and considered this variable equal to zero for diamond indenters (rigid material).

2.4.4 Relationship between specific energy and abrasive micro-mechanism

According to MAEDA; BISMARCK; BRISCOE, (2005), the scratch test is a convenient method to evaluate the energy dissipated at the interface during scratch contacts and

provides a first-order estimate of the characteristic of the surfaces. Also, this experimental test is used to characterize abrasive processes such as grinding and polishing. It can provide deformation conditions of an abrasive process that contains both micro-cutting and micro-ploughing, so that the energy will depend on the contact geometry (abrasive system) that generates variations in the scratch (depth and width of penetration) along the wear groove. Therefore, the angle of attack also varies during deformation following the response and variations based on the penetration depth.

The overall specific energy (S_e) is generally defined as the ratio between the dissipated energy (E_d) and the volume of material deformed V (groove) under the same contact conditions (velocity, normal load, abrasive geometry, material microstructure) as indicated in **eq. (13)**.

$$S_e = E_d V = \int -LLF_t\,(X)dX \int -LLa_t(X)\,dX = (2L)F_t(2L)A_t = F_t A_t \qquad (13)$$

Where F_t (X) is the instantaneous tangential force, A_t (X) is the instantaneous cross-section of the groove at position X, and L is the length of the scratch. The evaluation of the average tangential force and the average cross-sectional area can be estimated based on the size of the groove measured in micrographs. Therefore, global-specific energy is obtained. It is important to notice that the specific energy mentioned in this thesis is due to only the frictional energy parcel (SERIACOPI, 2018).

On the other hand, the instantaneous specific energy can be defined as the ratio between the instantaneous tangential force F_t(t) and the instantaneous cross-sectional area of the groove a_t (t) as follows:

$$S_e = F_t(t) * a_t(t) \qquad (14)$$

During the abrasive wear, micro-mechanisms mentioned in the previous section are related to material removal and/or displacement of the material. A sequence of scratches in the same region can be used to simulate the sliding of the particles on the surface (ZUM GAHR, 1987)(SEDRIKS; MULHEARN, 1963). To conclude, it is essential to isolate phenomena to model the wear accurately (DA SILVA; COSTA; DE MELLO, 2011).

2.4.5 Scratch test on sintered copper-based materials

Since the indenter can be considered an abrasive particle, the scratch tests evaluate mechanical, friction, and wear behaviors in metals and metal matrix composites. Additionally, the normal force (F_n), tangential force (F_t), depth penetration (h_p), and residual penetration depth (h_r) can also be obtained during the scratch test. Figure 31 shows the essential features of the scratch test (FUTAMI et al., 2009; LIU; SUN; SHEN, 2002).

Figure 31 - Basic diagram of a surface scratch test, b) abrasive wear model by scratch test and c) OM (optical microscopy) images of the scratches of copper-WS_2 15 wt.% (normal load 30 mN and Rockwell conical indenter with a spherical diamond tip of 200 µm of radius).

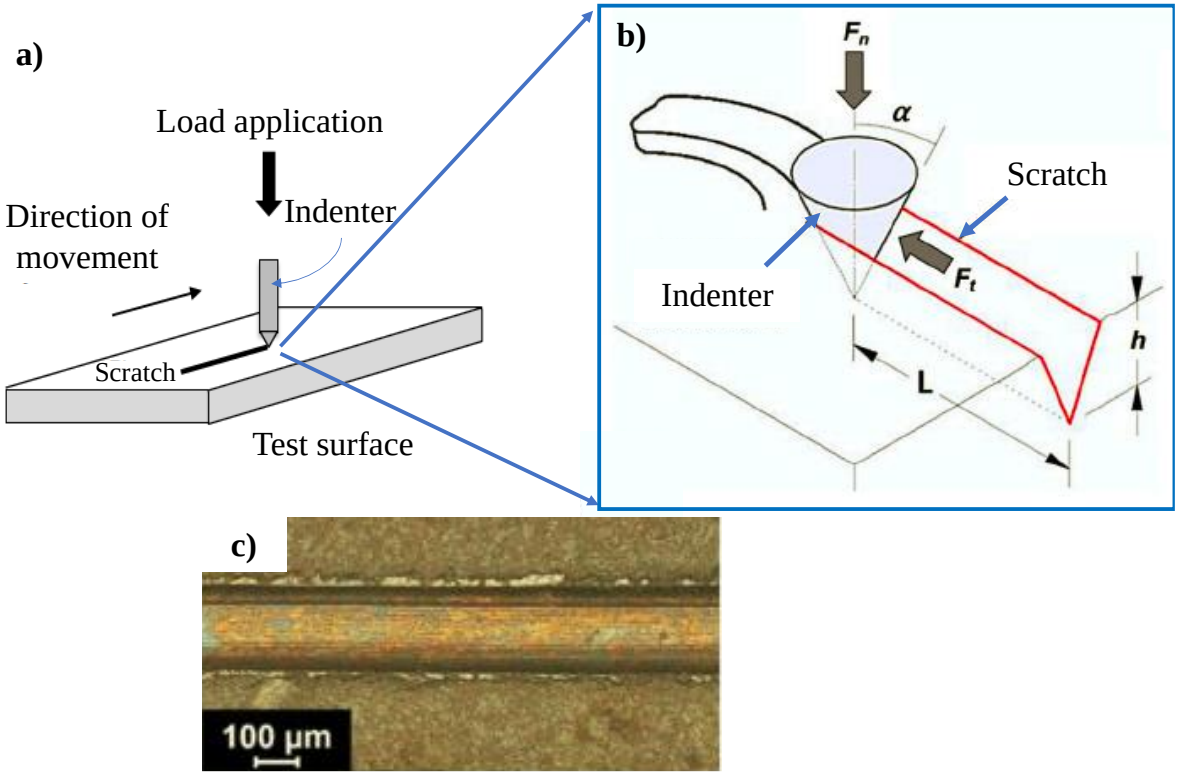

Source: Adapted from (FRANCO, 2015; FRESCHI et al., 2022; MACHADO, 2017).

Including second phases (e.g., particles or fibers or hard particles) into a ductile and soft matrix can decrease the resistance to abrasive wear. The resistance to abrasive wear of composites depends on different microstructural parameters such as hardness, shape, size, volume fraction and phase distribution, matrix properties, the interfacial bond between the second phase and the matrix, and the fraction of pores in the case of sintered materials (SERIACOPI et al., 2020).

GAHR, (1998) presented interactions between abrasive particles and a reinforcement phase. Hard, soft abrasive particles and small and large sizes are distinguished compared to the reinforcement phase. Hard abrasive particles can easily remove small particles and cut or break larger ones. Soft abrasive can remove small particles or produce large cavities. The penetration depth of the soft abrasive particles is substantially reduced with the hard reinforcement phases if the mean free path between them is less than the size of the abrasive particles. Large particles poorly bound to the matrix can be removed. However, the large particles firmly attached to the matrix can dull or fracture the soft abrasive particles (Figure 32).

Figure 32 - Interactions between sliding hard or soft abrasive particles and reinforcing phases.

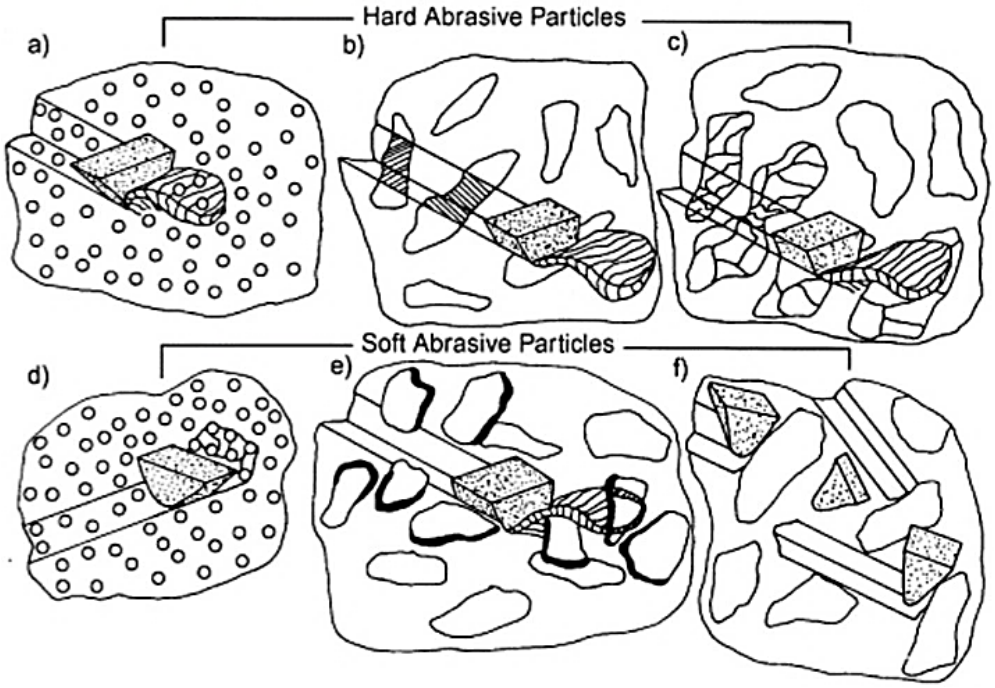

Source: (ZUM GHAR, 1998).

Figure 33 shows the wear grooves caused by a Rockwell C tip (120° diamond indenter with a cone of half-apex angle θ = 60°) on the copper surface at different normal loads (ZHANG et al., 2020). Under small normal loads (90 – 450 mN), the groove is smooth with straight scratch edges, indicating that scratch deformation is driven by material strength. As the normal load (700 – 1500 mN) increases, the scratched edges become wavy. The wavy edges are caused by the shear flow of the copper that piles-up along the contact perimeter. In addition, material pile-up becomes more prominent as the normal load increases. Therefore, the width of the grooves (W_r) becomes increasingly more expansive and irregular with increasing applied normal load. The predominant deformation mode in copper scratch testing is ploughing rather than micro-cutting, as little material is shed from the surface. However, for normal loads of 4500 mN, a micro-mechanism transition from dominant micro-plowing to micro-cutting is observed.

Figure 33 - Optical inspection of scratch morphologies after scratch tests of copper under different applied normal loads. F_n= normal force and W_r= groove width. Different scales of the optical microscopy were used to characterize the scratch width and length.

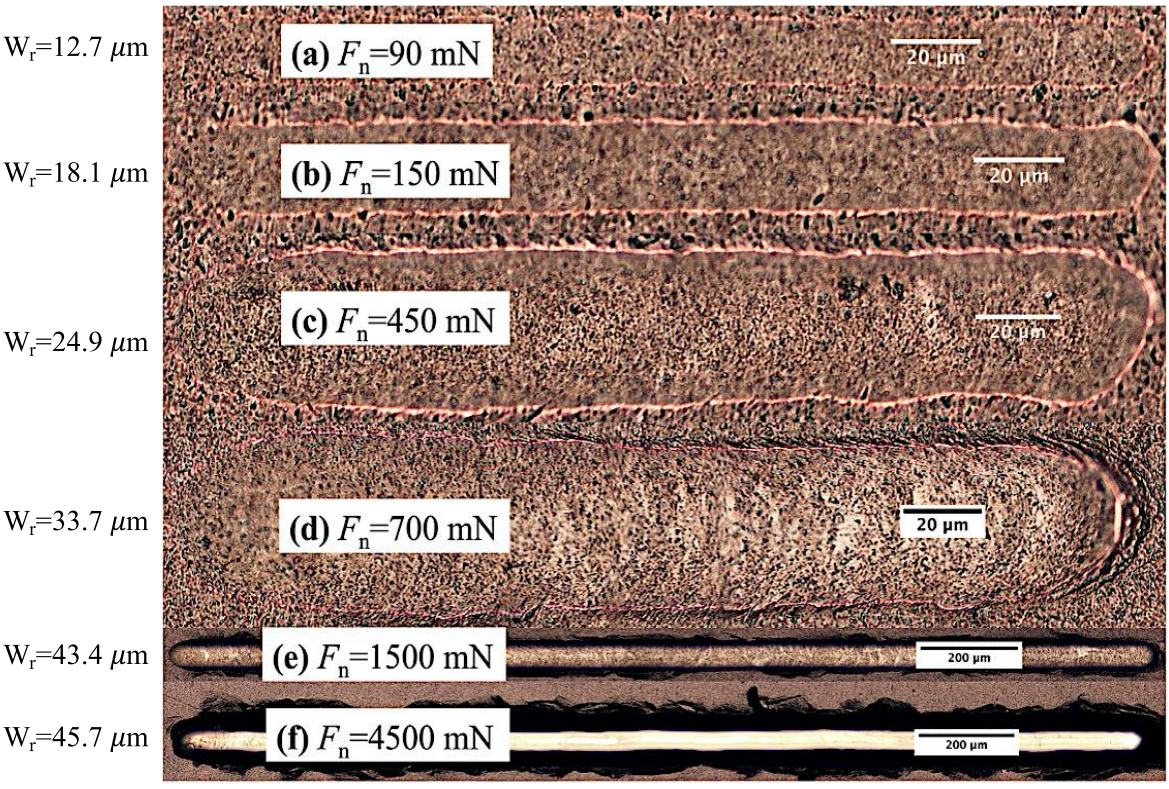

Source: Adapted from (ZHANG et al., 2020).

For the case of copper-based composites, Figure 34 shows the scratch grooves in the Cu-graphite composite surfaces when varying the normal load and the graphite content (XIAO et al., 2013). The scratching was performed with a spherical diamond indenter with a radius of 50 μm—the width and penetration depth of the groove increase with increasing normal load. The material exhibited plastic deformation for a normal load below 1 N, and wear debris was negligible (micro-ploughing dominant). For a normal load more significant than 1.5 N, pile-ups formed by an accumulation of displaced material on the sides of the grooves can be observed, and tears or cracks generated by adherence are revealed inside the grooves. As the normal load increases, a more significant chip formation is observed: a transition from ploughing to cutting mechanisms. As the graphite content increases, the pile-up on both sides of the groove fractures into pieces, and chips are observed on the side and end of the grooves. Compared to composites with little or no graphite addition, tearing or cracking inside the grooves is reduced with composites with the appropriate amount of graphite.

YAN; SUN; DONG, (2007) performed nano-scratch tests on copper to study the effects of the tip on scratch forces, coefficient of friction (COF) and specific energy, as shown in Figure 35. Results show that the scratching depth of about 10–15 nm is a transition depth if a diamond tip was used. Also, COF is different at different tip orientations influenced by the contact area between the tip and attack angle at the scratching depth greater than 10–15 nm.

Figure 34 - SEM micrographs of scratch grooves on Cu–graphite composites with graphite content of (a) 3 vol%, (b) 12 vol%, (c) 20 vol%, and (d) 30 vol%.

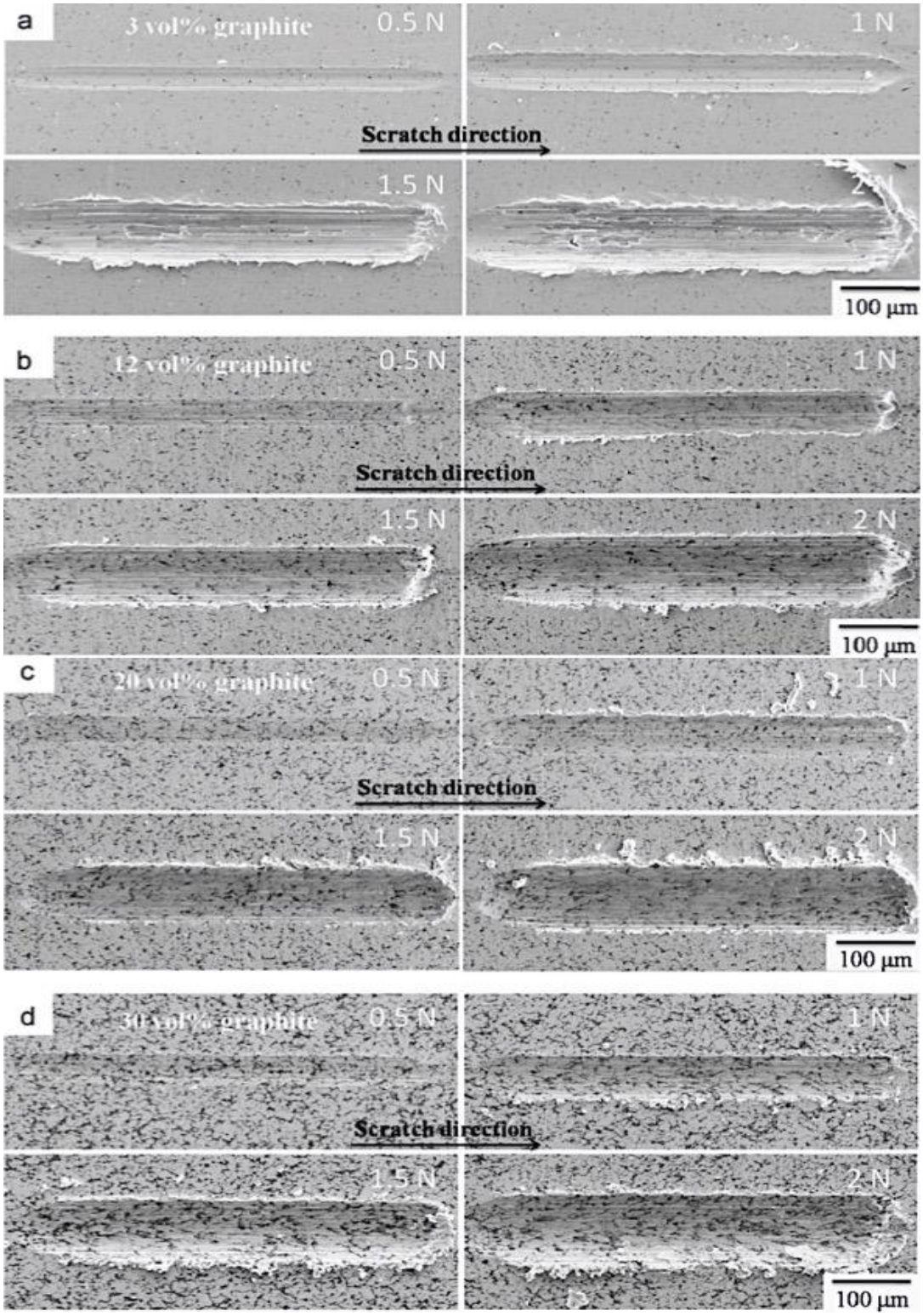

Source: (XIAO et al., 2013).

FUTAMI et al., (2009) used scratch test studies on copper-graphite composites with copper content ranging from 0 to 40 vol% (Figure 36) to understand surface deformation and damage under sliding. They classified scratch deformation into four stages: i) elastoplastic grooving, ii) plastic-ploughing, iii) micro-cracking, and iv) fracture and chipping of graphite particles. Particularly in this work by FUTAMI et al., (2009), there is a micro-mechanism between the ploughing and the cutting, which was a micro-crack.

Figure 35 - Relations between specific energy, scratching forces and scratching depths of copper for different scratching perpendicular directions.

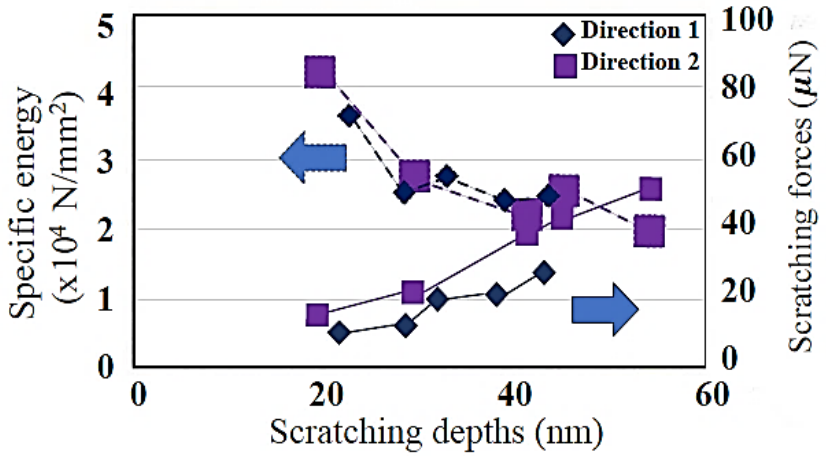

Source: Adapted from (YAN; SUN; DONG, 2007).

Figure 36 - a) The scratch grooves created by a spherical indenter (R = 3.18 mm) under various values of the contact load (F_n: 5 – 80 N), (b) the schematics for the scratch-induced deformation/damage in their sequential stages from I to IV, and (c) the deformation/damage map of the copper–graphite composite materials; the characteristic critical pressures are plotted against the Cu-content at the respective transitions from I to IV.

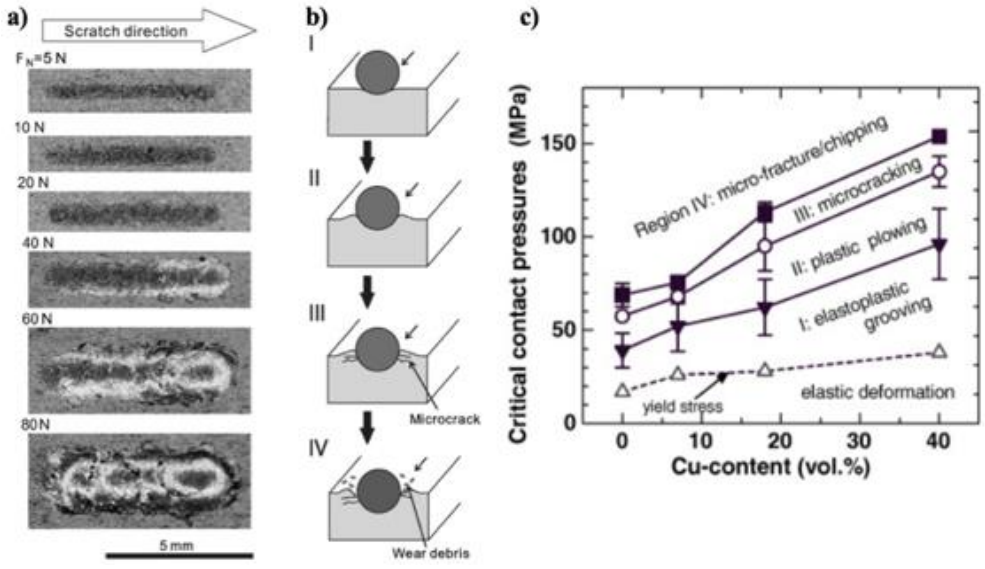

Source: Adapted from (FUTAMI et al., 2009).

2.4.6 Material removal factor F_{ab} as an indicator of micro-mechanisms

The first works on hard particle abrasion mechanisms and wear theories were published more than 50 years ago. BUTTERRY; ARCHARD, (1970) used the denomination "ζ" to quantify the material removed due to a scratch, relating the areas observed in the cross-section of the scratch produced by a particle, as shown in Figure 37 and **eq. (15)**.

Figure 37 - a) typical crag showing the pile-up (A_2) and b) typical cross-section of an idealized scratch (Buttery, 1970).

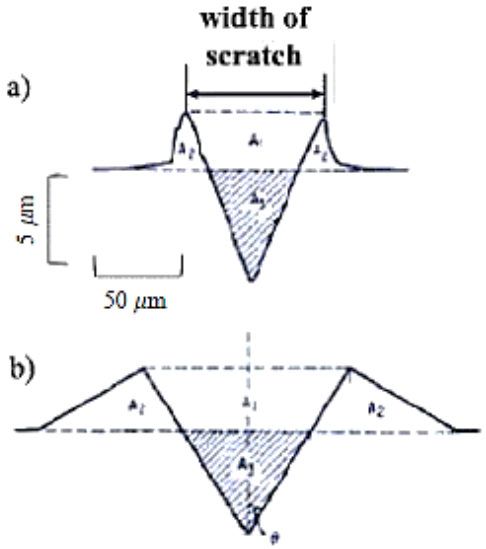

Source: Adapted from (FRANCO, 2015; BUTTERRY; ARCHARD, 1970).

$$\zeta = \frac{A_3 - A_2}{A_3} \quad (15)$$

As early as 1983, GAHR; MEWES, (1983) presented a formal definition of the F_{ab} factor in terms of cross-sectional areas of a line. These authors noted that the Fab factor could indicate the severity of material removal by abrasion and obtained consistent results for a wide range of metals and metal alloys. The authors also cited its similarity to the "ζ" factor defined by BUTTERY; ARCHARD, (1969). ZUM GAHR, (1987) detailed the model he proposed in 1981 and experimentally showed its relationship and dependence on material properties and system parameters, such as hardness, shear strength, Poisson ratio, and indenter tip geometry (shape, dimensions, and angle). Thus, the F_{ab} factor was calculated (**eq. (16)**) based on the

analysis of the areas of material removed/moved from the cross-section of the scratch generated by the particle during the sliding process.

$$F_{ab} = \frac{A_V - (A_1 + A_2)}{A_V} \quad (16)$$

In Figure 38, the area A_V corresponds to the material removed by the action of the indenter (groove), and the areas A_1 and A_2 represent the material deformed for the lateral material accumulated (pile-up). The F_{ab} factor is dimensionless, being calculated using **eq. (16)**, as proposed by GAHR, (1987).

Figure 38 - Schematic of the cross-section of a scratch with a ductile response.

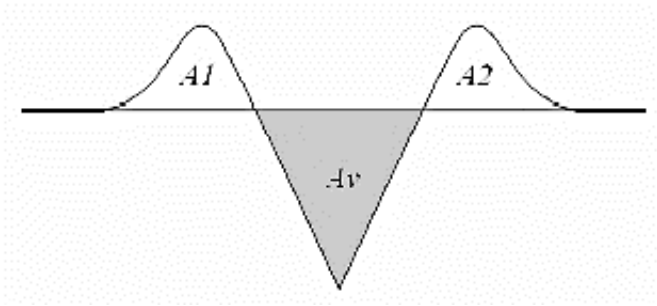

Source: (GAHR, 1987).

GAHR, (1981) also introduced that micro-cutting and micro-ploughing can co-occur during abrasion. Hence, a correction factor better determines the volume of the theoretical (th) material removed (Δ_V) due to abrasion caused by an abrasive particle sliding a distance (L). Wear debris is formed by pure micro-cutting, as shown in **eq. (17)**.

$$\frac{\Delta V}{L} = F_{ab} \cdot \left(\frac{\Delta_V}{L}\right)_{th} \quad (17)$$

F_{ab} is the material removal factor defined by Zum Gahr (1981) and Franco (2017) as "the ratio of the volume of wear debris to the volume of wear groove produced." The F_{ab} factor can relate and quantify the sliding of a particle on a surface with micro-mechanisms, such as ploughing, wedge formation and cutting (FRANCO; SINATORA, 2017; ZUM GAHR, 1987).

F_{ab} equal to zero ($F_{ab} = 0$) means that all the area removed by the indenter has been plastically deformed towards the sides of the groove (pure micro-ploughing) without material removal. F_{ab} equal to one ($F_{ab} = 1$) represents pure micro-cutting. A value between zero and one ($0 \leq F_{ab} \leq 1$) represents a combination of both micro-mechanisms (ZUM GAHR, 1987). In turn, in the brittle behavior, crack propagation, and detachment occur and result in larger areas than those corresponding to the action of the indenter. Therefore, the F_{ab} factor is not used for brittle materials (BARRADAS; COSTA; MELLO, 2001; STACHOWIAK; BATCHELOR, 2001).

In addition, MASEN et al., (2005) observed the formation of chips on the sides of the scratch that was not completely sheared and, consequently, not removed (Figure 39), underestimating the wear. The chip not removed is denominated false pile-up. FRANCO; SINATORA, (2017) detailed in Figure 40 a typical cross-sectional profile of a scratch with the presence of a false pile-up volume as pointed out by MASEN et al., (2005), describing the observations using the scanning electron microscope (SEM).

Figure 39 - Presence of chips along the scratch.

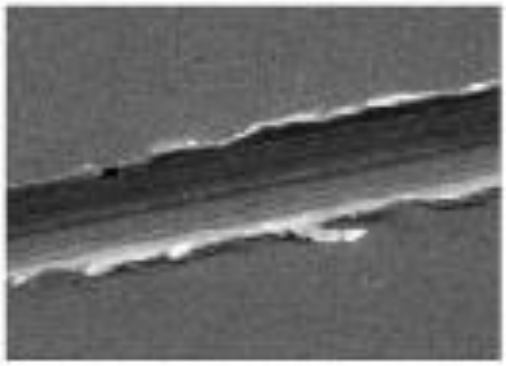

Source: (MASEN et al., 2005).

Figure 40 - Groove profile with chip formation on the left.

Source: (FRANCO; SINATORA, 2017).

Accurately determining the severity and abrasion wear through geometric parameters could be a related degree of penetration (D_p), see Figure 41a. MISHRA; DE ROOIJ; SCHIPPER, (2021) performed a series of scratch tests (diamond indenter) on steel samples of different hardness. A low value of D_p corresponds to ploughing, and a high value corresponds to cutting. Therefore, the transition between low and high values corresponds to the wedge formation. In addition, these results can be related to the attack angle, displayed in Figure 30.

The analysis of micro-mechanisms is related in terms of energy (S_e) loss to generate a scratch in abrasive processes. The F_{ab} factor can be defined as "degree of wear, β," (calculated from the scratch geometry) in Figure 41a. Further, the alteration of the wear regime may be associated with the variation of the active micro-mechanism, according to studies by HOKKIRIGAWA; KATO; LI, (1988), Figure 41b. The authors demonstrated that the wedge formation micro-mechanism was a higher coefficient of friction than micro-ploughing and micro-cutting. FRANCO, (2015) showed a transition from wear micro-mechanism to gray cast iron through the scratch test. The author observed the transition from micro-ploughing to micro-cutting without wedge-forming. To conclude, these parameters and the evaluation of micro-mechanisms depend directly on the microstructure surfaces and mechanical properties (e.g., hardness of Figure 30) of the material surface.

Figure 41 – a) Removal of material and mechanism in function of hardness. F_{ab} vs degree of penetration for dry and lubricated S45C steel in various abrasive wear regimes, and for uncoated and duplex coated nodular cast iron (NCI), shown as solid and dash lines respectively and b) Correlation of coefficient of friction and degree of penetration (D_p) for sclerometry with steel indenter and quenched and tempered steel disc (P: Ploughing mode, W: Wedge formation mode and C: Cutting mode).

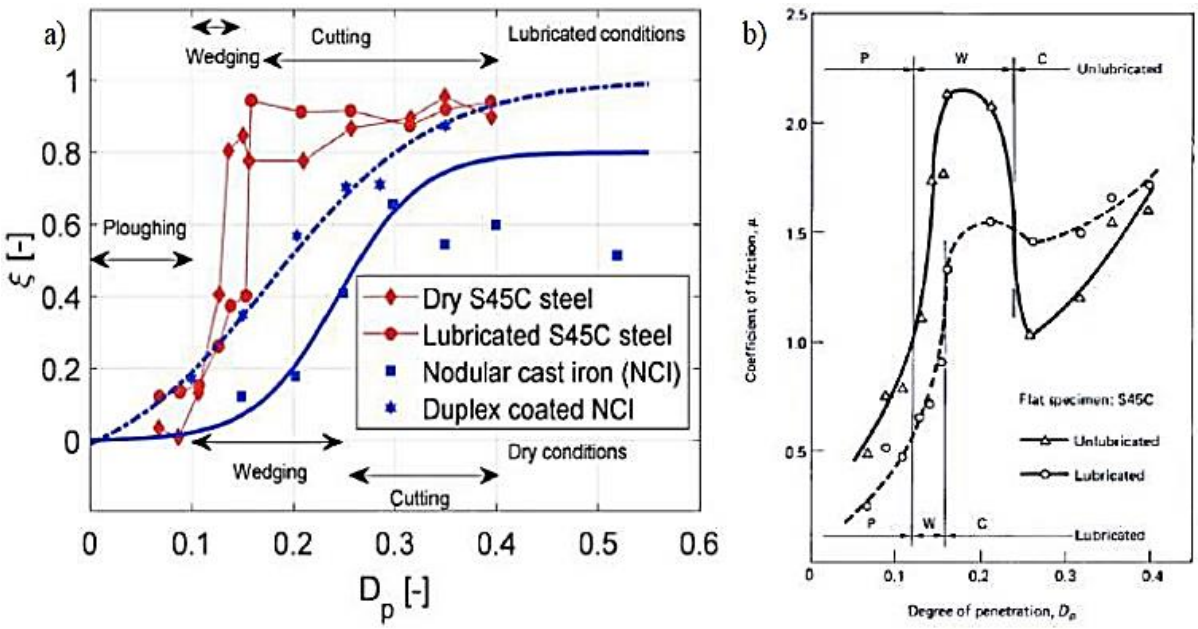

Source: Adapted from (MISHRA; DE ROOIJ; SCHIPPER, 2021) and (HOKKIRIGAWA; KATO, 1988).

3 MATERIALS AND METHODS

The effect of the sintering parameters of copper evaluation started considering the consolidation of the samples. Different sintering routes and pressures were studied, and based on the results of density, grain size, and mechanical properties, a procedure to sinter the composites was established. Therefore, Al_2O_3 was added and mixed to copper as received, and surface alterations were performed to modify interface features and composition using two different techniques. The first deposition method used a pulsed direct current magnetron sputtering system (PDCMS) to deposit thin layers of silver on the surfaces of the Al_2O_3 particles. The second method, the electroless coating technique, was used to coat Al_2O_3 with Ag.

Additionally, the abrasive wear test (scratch test) was carried out on copper and copper composites since the interaction between the matrix and the ceramic particles plays a fundamental role in tribological performance. Figure 42 summarizes the most relevant conditions of the tribological system and the main variables that can influence the tribological performance addressed in this work.

Figure 42- Scheme indicating the main variables involved in the tribological test (scratch test).

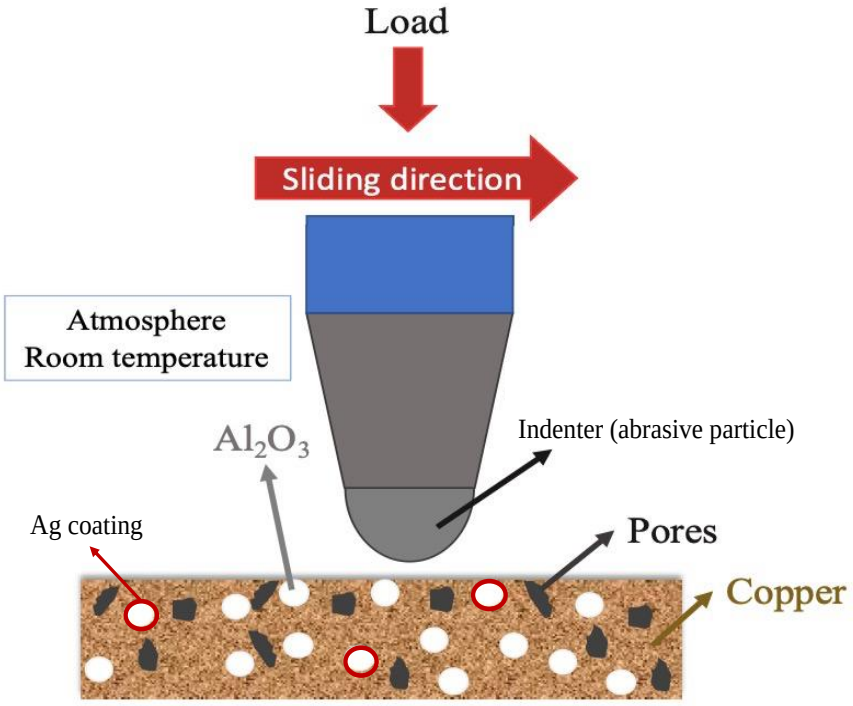

3.1 Materials

3.1.1 Copper (Cu) and Alumina (Al_2O_3)

The materials used for this work consisted of i) atomized copper powder supplied by the Sigma Aldrich company, with a purity of 99.9%, with particle size <75 μm; and (ii) Al_2O_3 powder, manufactured by the company Almatis (trade name Al_2O_3-CT3000LS SG) and supplied by the Ceramic Processes Laboratory (PMT-Poli/USP) with a purity of 99.8%. The nominal chemical compositions of the copper powder and Al_2O_3 as received were obtained by optical spectroscopy and are presented in Table 2. The particle size distribution of the powders was determined by low-angle laser light scattering systems (Malvern Hydro 2000-UM) available at the Technological Characterization Laboratory (LCT/USP). In addition, the microstructural observation of the powders was obtained using a JEOL JSM 6010-LA scanning electron microscope (SEM) coupled to elemental mapping by energy dispersive X-ray spectrometry (EDS) of LFS (Surface Phenomena Laboratory).

Table 2 – Chemical composition analysis of powder copper and Al_2O_3 in wt.%.

	Cu	Fe	Mn	Sn	Ni	Pb	Zn
Copper	-	0.024	0.003	0.204	0.008	0.016	0.059
	Al_2O_3	Na_2O	Fe_2O_3	SiO_2	MgO	CaO	
Alumina	-	0.08	0.015	0.015	0.04	0.015	

3.2 Spark Plasma Sintering (SPS)

3.2.1 Copper sintering parameters

The SPS device, model DR. SINTER® SPS1050 (Fuji Electronic Industrial Co. ld., Japan), was used to sinter the copper powder samples. The copper powders were heated from room temperature to 650 and 750 °C at a heating rate of 93 °C min^{-1}, under a vacuum of about 20 Pa and axial pressure. All sintering conditions were performed in a short holding time of 2 min and cooling within the SPS chamber with a cooling rate of approximately 36 ºC min^{-1}. Copper powders (about 15 g) were placed in high-density graphite die, similar to that used in other works (MACHADO et al., 2021b). The dimensions of the samples produced were 20 mm

in diameter and 5 mm thick (discs). The high-density graphite die had 60 mm in external diameter, 20.1 mm in internal diameter, and 40 mm in height. Two punches were used (cylinders of 20 mm in diameter and 20 mm in height). The powder was placed between the punches. Figure 43 shows a schematic of the die setup.

Figure 43 - a) Schematic representation of the SPS system and b) the die and graphite punches of the SPS during copper sintering at 650 ºC.

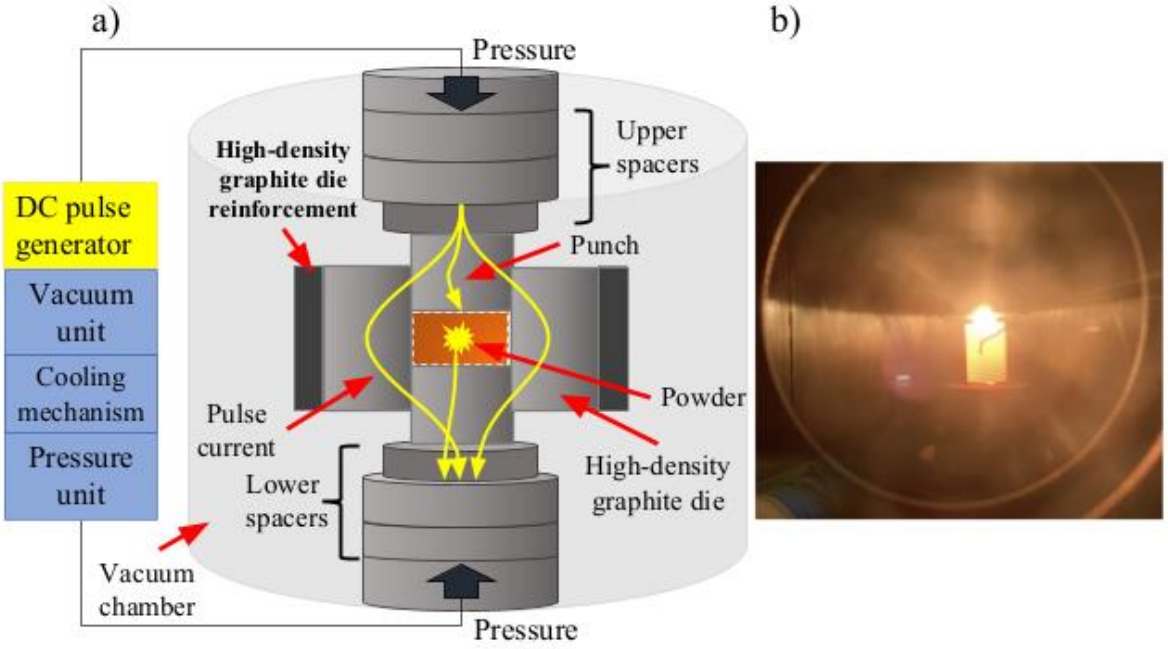

An axial pressure was applied during sintering using two different routes. In the first route, the pressure was maintained at 15 MPa during the heating up to the sintering temperature at 650 or 750 ºC, and it was increased during the holding time. In the second route, the pressure was raised during the heating and kept constant during holding time at 650 or 750 ºC. Three different pressure levels were applied for each route: 110, 65, and 50 MPa. Each route and maximum pressure were applied to lead to different pressure rates. Table 3 and Figure 44 display a graph showing the parameter description and summarize the sintering parameters as well as sample denominations used in this work.

Table 3 - Sintering parameters and identification of copper samples.

Samples	Maximum pressure achieved (MPa)	Pressure rate during the holding time (**HT**) (MPa min^{-1})	Pressure rate during the heating (**H**) (MPa min^{-1})
47.5HT-110 MPa	110	47.5	-
13.6H-110 MPa	110	-	13.6
25HT-65 MPa	65	25	-
7.1H-65 MPa	65	-	7.1
17.5HT-50 MPa	50	17.5	-
5H-50 MPa	50	-	5

Figure 44 - Pressure modes SPS: a) application of pressure rates during holding time and b) application of continuous pressures during holding time. Pressure=constant (P=cte).

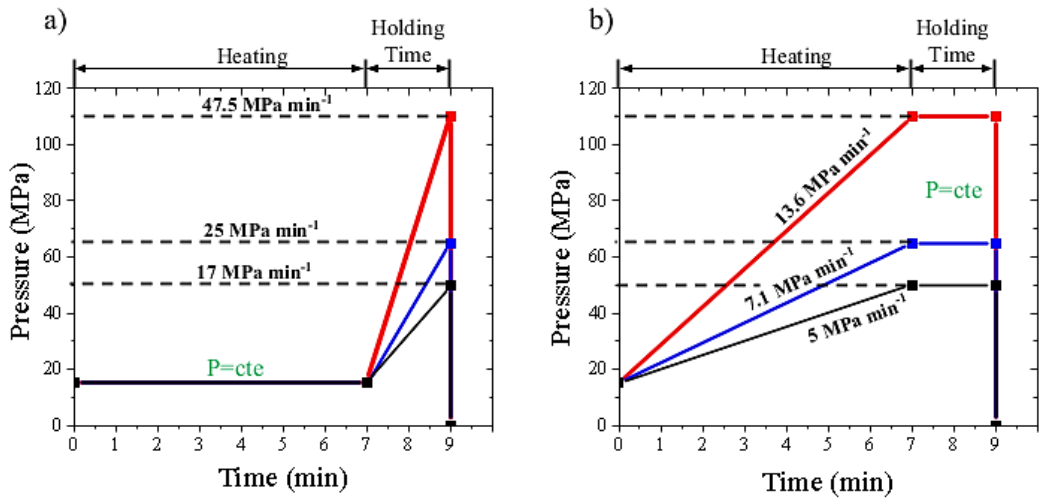

The 650 ºC was the selected temperature based on the results of densification and hardness. Additional information regarding samples sintered at 750 ºC is presented on ANNEX A.

3.3 Characterization techniques

3.3.1 Density measurements

The influence of different pressure routes on the relative density (ρ_r) of the copper samples was determined according to Archimedes' method, ASTM B962 standard. The density was determined considering the value of experimental densities (ρ_e) and the comparison to the

values of the theoretical density of copper (8.96 gcm^{-3}) (ρ_a) (ASM INTERNATIONAL, 2001), using the following **eq** (**18)**:

$$\rho_r = \left[\frac{\rho_e}{\rho_a}\right] x100 \qquad (\mathbf{18})$$

3.3.2 X-ray diffraction analysis (XRD)

X-ray diffraction (XRD) measurements were carried out to identify the crystalline phases in the samples using an Empyrean 3rd generation Malvern Analytical diffractometer. Cu-Kα radiation (λ = 1,542 Å and 2.2 kW) was used. XRD data was recorded in conventional Bragg-Brentano geometry for 2θ scans ranging from 20 to 100° with a step of 0.02° and a step count time of 2 s/step. A current of 20 mA and a voltage of 40 kV were used as settings during this procedure. The phases present in the XRD patterns were determined using MATCH! 3 software version 3.14 equipped with the Crystallography Open Database (COD). The line shape of the diffraction peaks was generated by a pseudo-Voigt function. Crystallite size and microstrain were determined via the traditional Williamson-Hall method. This method considers that peak broadening is produced by variation resulting from both crystallite size and isotropic microstrain (WILLIAMSON; HALL, 1953).

3.3.3 Metallographic preparation

After sintering, samples were withdrawn from the graphite die, and the graphite foil adhered was removed from the sample surface. To perform such removal, a #600 sandpaper was used to grind the surface very carefully not to cause plastic deformation on the surface of the sample. After cleaning, the density of the samples was evaluated. Therefore, microstructural characterization samples were mounted (Bakelite) using Buehler's SimpliMetTM 3000 equipment. The grinding was carried out using sandpaper placed in a Struers equipment model Labopol-1 with a constant water flow. As the surface was smoothed, the grit size of the abrasive was reduced from #800 to #2000 SiC. Subsequently, the automatic polishing was performed with a Struers polisher, model Labopol-60, using different suspensions of diamond (6, 3, and 1 µm). To finish surface, the sample was polished on colloidal silica (0.04 µm). Finally, to eliminate any particles on the surfaces, samples were immersed in alcohol (ultrasonic bath).

After cleaning, samples were dried and observed using an optical microscope (Olympus BX60M) to evaluate their cleanliness.

3.3.4 Microstructural observation

The microstructure of the samples was observed using scanning electron microscopy (SEM) JEOL-JSM 6010LA, secondary (SE), and backscattered electrons (BSE) were used. Furthermore, the semi-quantitative chemical composition of the surfaces was obtained using energy-dispersive X-ray spectroscopy (EDS) coupled with the SEM. Moreover, optical microscopy (OM) and scanning electron microscopy (FEI-Inspect F50 SEM equipped with a field emission gun (FEG)) from the Department of Metallurgical and Materials Engineering (PMT) of the Polytechnic School of the University of São Paulo (EPUSP) were employed.

3.3.5 Image analysis

To evaluate the morphology and distribution of the pores after sintering, the surfaces were observed using OM and SEM at different magnifications without etching to avoid the size and shape of the pores due to etching. Pore features characterization was conducted using grayscale (RGB image conversion to 8 bits), segmentation by threshold, and automatic conversion of images to binary images. The analysis was performed using the "Image J" software. A contrast between pores (black) and copper (light orange or gray) and copper oxides with pores exists; see Figure 45.

Figure 45 - Images of the pores (contrast). a) OM 100x magnification and b) SEM-BSE-image.

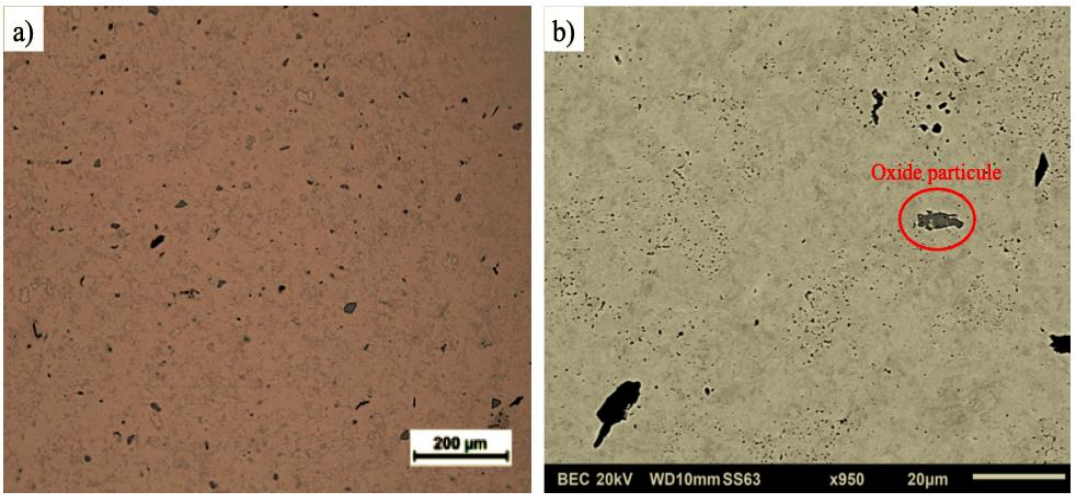

The circularity index (C_i) represents the shape factor that is between 0 and 1. C_i closer to one indicate more circular pores, while values closer to zero indicate more irregular pores, according to **eq (19)**. The size of the pores (S_p) can be calculated using **eq (20)**. The amount of pores was determined by dividing the total detected area of pores by the total area of the image (BAGHERI et al., 2015; BOIDI; FUKUMASU; MACHADO, 2018).

$$C_i = \frac{4\pi A_p}{{P_p}^2} \quad (\mathbf{19})$$

$$S_p = \left(\frac{A_p}{\pi}\right)^{\frac{1}{2}} \quad (\mathbf{20})$$

Where A_p is the area of the pore and P_p is the perimeter of the pore.

3.3.6 Grain Size

The polished (scratch-free) and cleaned copper samples were chemically etched with a solution of ferric chloride III ($FeCl_3$) for 20 s at room temperature, allowing observed grain boundaries.

The method to determine grain size is dependent on the quality of the etching performed to reveal the grain boundaries; thus, the ASTM E 1382-97 standard emphasizes the importance and care that must be taken to reveal the microstructure of the sample, as well as the image treatment through image pre-processing. The grain size copper samples were quantitatively analyzed by micrographs using the “Image J” software. This analysis aimed to characterize and quantify the grain size distribution for each copper sintering parameter selected.

The grain size statistics were also evaluated. Considerations about the representativeness of the sample, statistical analysis, and confidence intervals were carried out (ANOVA One-Way). The manual analysis method allows sufficient grain size to be analyzed (>250 measured grains) by optical microscopy. It also allows the orientation of the results in frequency histograms. However, an important factor is the representativeness of the sample. That is, the number of samples and observation fields must be sufficient for the analysis to be representative, which was eight images per sample, with a total of approximately 300 measured grains.

3.4 Cu-Al_2O_3 mixtures - composites

In this study, to overcome the low hardness and wear resistance of copper, Al_2O_3 was added to copper to improve the mechanical and tribological performance of the composites. The hard particle content limit was defined to obtain a metallic matrix with sufficient mechanical strength to observe the influence of Al_2O_3 particles and their interfaces, Al_2O_3 particle size, porosity, and copper matrix effects in the composites. Therefore, to ensure good dispersion and uniformity of particle distribution of the hard particles after sintering, 20% Al_2O_3 (% volume) was added to each mixture. Two replicas were performed in each mix.

Copper and Al_2O_3 powders were mechanically mixed using a Y-mixer for 3 h and 60 rpm at room temperature. The powder was mixed using 500 mL stainless steel jar to distribute the Al_2O_3 particles in the matrix uniformly. The mechanical mixing medium was three steel balls (10 mm in diameter).

In addition to pristine Al_2O_3, two routes were selected to modify the surfaces of the Al_2O_3 particles to obtain an improved matrix-particle interface. The two selected routes were used considering previous work on metal particle coatings on ceramic particle surfaces, and composites were obtained through SPS sintering (BARSHILIA et al., 2011; SADOUN; MESELHY; ABDALLAH, 2021). The material selected for coating was silver.

Ceramics coated with Ag are part of an extensive collection of protective and functional coatings that modify matrix properties. In these coatings, ceramic phases such as oxides, carbides, nitrides, and nitrides are mixed with metallic silver to improve system functionality (CALDERON VELASCO; CAVALEIRO; CARVALHO, 2016). Silver (Ag) was used in both coating routes to satisfy the above concept because it improves the integrity of the metal-ceramic interface. Furthermore, silver was selected due to its use in copper-based composites, as mentioned.

The pristine surface and the two routes of surface modification of Al_2O_3 particles are presented. The three methods to obtain the Cu-Al_2O_3 composites were summarized in the experimental flowchart displayed in Figure 46, Figure 47, and Figure 48.

Method 1: Consisted of mixing the Al_2O_3 powder, as received, with the copper powder and subsequently sintering via SPS (Figure 46).

Figure 46 - Schematic representation of the procedure for mixing the copper powder with Al_2O_3 particles.

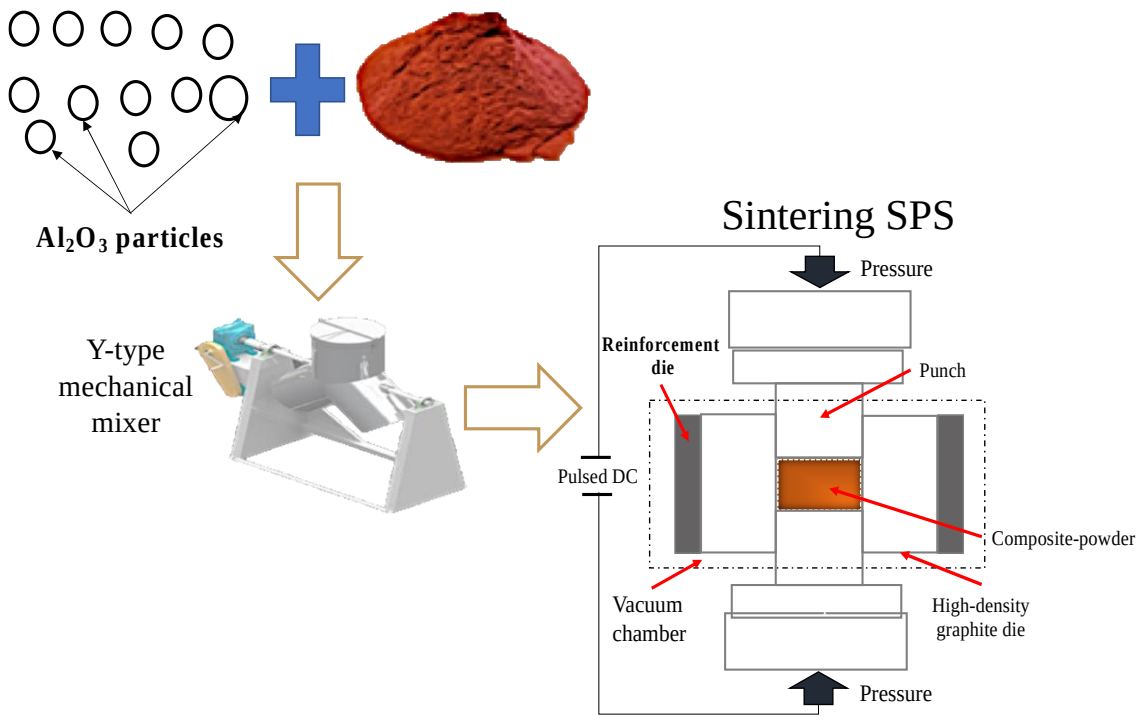

Method 2: A thin layer of silver coating was deposited on the Al_2O_3 particles using a Pulsed Direct Current Magnetron Sputtering (PDCMS). Al_2O_3 particles were ultrasonically cleaned in acetone for 10 minutes and dried at 80 °C before deposition. The deposition process was carried out in a sputtering reactor (PVD - CDV) supplied by the PMT-EPUSP and began with a cleaning step by cathodic sputtering of Ar with high purity to remove residual contamination on the surface of the particles. The process parameters for cleaning with Argon ions considered a gas pressure of 0.02 Torr, a gas flow of 10 sccm, and power applied to the substrate of 150 W using the pulsed DC source with a frequency of 200 kHz, type bipolar, and duty cycle of 2 μs, in a time of 30 min. The distance between the target (Ag) and the particles was around 110 mm and maintained throughout the deposition process. The magnetron heads were powered by a pulsed DC bipolar source with a frequency of 200 kHz and a duty cycle of 2 μs.

The geometry of the reactor was cylindrical, with three magnetron heads arranged parallel to the axial axis of the chamber, oriented orthogonally to the substrate, as described by SANTOS et al., (2022). Mobile support was used to place a plate where the particles were located and positioned under the head during the deposition process. The same Ag magnetron heads were used to deposit on the particles, in argon (Ar) atmosphere at $3x10^{-1}$ Pa. After 30 minutes of the deposition process, the particles were removed and shaken so that new surfaces

of the particles were deposited with silver; this process was repeated ten times (Figure 47). After the deposition, copper, and Al_2O_3+Ag were mixed and sintered by SPS.

Figure 47 - Schematic representation of the magnetron sputtering system and silver coating on the Al_2O_3 particles.

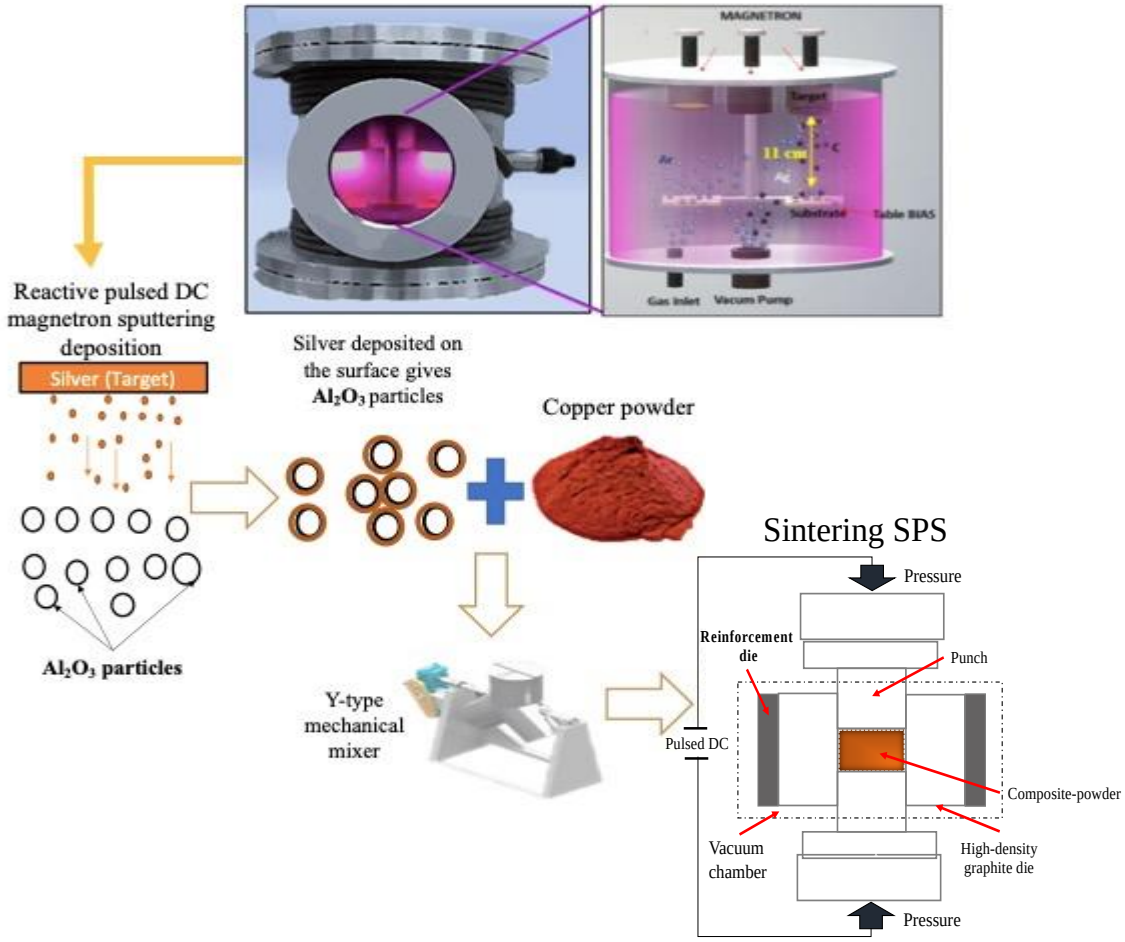

Method 3: Coating of Al_2O_3 particles with Ag particles through the electroless plating technique. The electroless plating process was employed in two steps: cleaning (sensitization) and silver deposition. First, cleaning of Al_2O_3 particles was conducted to remove any contamination on the surfaces by immersing them in acetone through the ultrasonic cleaner for 2 h and was dried in a muffle at 115 ºC for 2 h. Subsequently, the deposition of Ag on the surface of the Al_2O_3 particles was carried out using a chemical bath, which consisted of a solution of 3 g/l of silver nitrate, 300 ml/l of formaldehyde, and ammonia to obtain a pH~12. Immediately after formaldehyde was added, the reaction occurred. The solution was mixed using a magnetic stirrer for 20 min at room temperature to maintain the Al_2O_3 in the solution and not generate agglomerates. The reaction was complete after 50 min. This solution was dried

in an oven at 115 ºC for 2 h. Finally, the alumina powder was added to copper and mixed in a mechanical mixer in Y to achieve greater homogenization and reduce powder agglomerations as described previously (GÜLER et al., 2020; LEON et al., 2014). To conclude, the mixed Cu-Al_2O_3 powders were sintered via SPS (Figure 48).

Figure 48 - Schematic representation of the coating process of Al_2O_3 particles with silver by the electroless process.

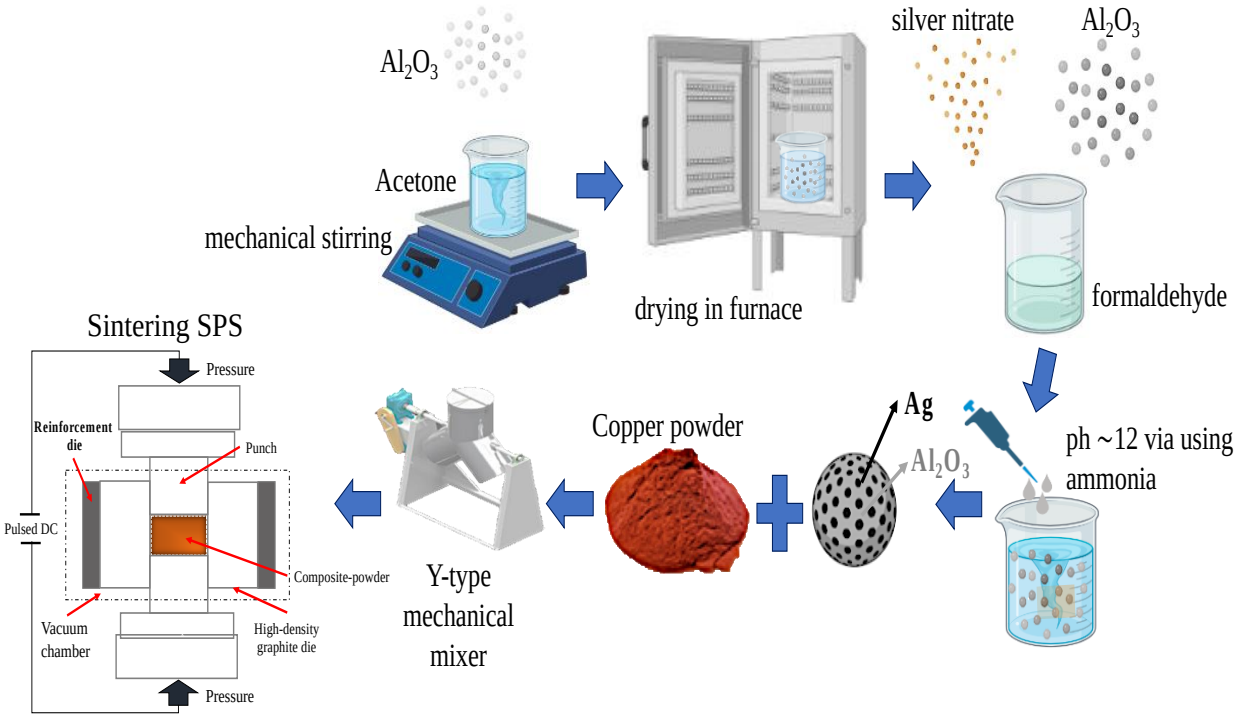

3.5 SPS sintering parameters of Cu–Al_2O_3 composites

The SPS parameters were selected based on the cooper sintering results, in which the microstructural evolution of sintered copper was essential to optimizing the manufacturing processes of Cu-Al_2O_3 composites. The sintering parameters chosen were:

- The heating rate of 93 °C min^{-1};
- Maximum sintering pressure of 110 MPa (P_2): 47.5HT-110 MPa, Table 3;
- The sintering temperature of 650 °C and a holding time of 2 min.

In addition, low vacuum of 20 Pa and the pressure route were employed, applying pressure rates during holding time (1º route (HT); Figure 44a). In conclusion, the pressure rate of about 50 MPa min^{-1} was considered, as depicted in Figure 49.

Figure 49 - Sintering temperature and pressure SPS of the composites.

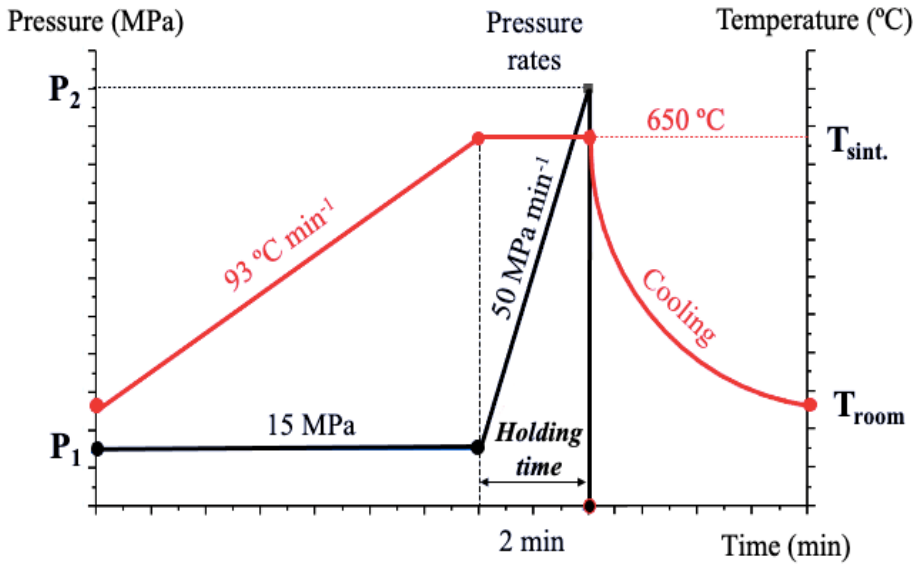

3.5.1 Composite characterization methodology

The metallographic preparation and X-ray diffraction analysis of the composites were the same procedure described in the copper section (3.3.2 X-ray diffraction analysis (XRD) and 3.3.3 Metallographic preparation). The relative density of the composites was determined according to the Archimedes method, ASTM B-962 standard. Also, the theoretical densities of composites were calculated based on the mixtures rule. The relative density was determined by dividing the measured bulk density by theoretical density (8.9 gcm^{-3} for Cu and 2.9 gcm^{-3} for Al_2O_3). The microstructure characterization of the sintered composites was conducted using an Olympus model BX60M optical microscope at the LFS and scanning electron microscopy (FEI-Inspect F50 SEM equipped with a field emission gun (FEGSEM)) (PMT-EPUSP).

3.6 Mechanical Properties

3.6.1 Vickers Microhardness

The hardness measurements were carried out to determine the effect of sintering pressure parameters (copper) and composites. It was assessed using Vickers microhardness tests (MMT-3 micro durometer from Buehler). At least ten indentations were conducted by applying a static load of 10, 50, and 100 gf (copper) and 50 gf (composites), following the

procedure described elsewhere. The static loads were applied for 10 s at room temperature following the ASTM-E92, (1997) standard.

3.6.2 Nanoindentation: Nano hardness (H_H) and elastic modulus (E)

The hardness (H_H) and elastic modulus (E) measurements using instrumented indentation were investigated using a Hysitron TI950, from Bruker, at the LFS. Scanning Probe Microscopy (SPM) with the low load module was used to conduct a profilometry of the surface and to define the area in which the indentation matrices were performed. Subsequently, the results correspond to a map of superimposed values on an image of (20 x 20) μm^2, obtained by SPM from the surface of the sample where the indentations were made.

This nanoindentation equipment uses the Berkovich diamond indenter. The indentations were made on the copper (matrix) and composites (flat and polished surface), applying loads of 500, 800, and 1000 μN. During the nanoindentation test, 64 indentations, with a separation distance between each indentation, were 2.5 μm (8 x 8 matrix) for each load with loading, holding, and unloading times of 5 s to avoid viscoelastic effects. In this last case, the idea consisted of building an indentation map to allow analyzing phases of the copper composites. The 500 μN showed the best results to observe the influence of the Al_2O_3 to relate the depth of penetration with the scratch tests based on plasticity index (E/H_H). In addition, the relationship between elastic recovery energy and total indentation work (W_E/W_T) was also calculated.

The mechanical properties obtained from the nanoindentation test are the reduced elastic modulus (E) and the hardness (H_H), which were evaluated from the load-displacement (Figure 50a) data according to the method of Oliver and Pharr (OLIVER; PHARR, 1992). The reduced elastic modulus (E_r) was calculated from the unloading part of the load-displacement curve, while the hardness (H_H) was calculated by **eq (21)**, which shows that the hardness is the ratio between the maximum indenter load (P_{max}) to the projected contact area (A_c) at the maximum indenter load.

$$H_H = \frac{P_{max}}{A_c} \qquad (21)$$

In **eq (22)**, S is the contact stiffness, which corresponds to the slope of the discharge curve (Figure 50). The area, which corresponds to the projected area of the indenter, depends on the contact depth h_c being $A(h_c) = 24.5h_c^2$ for a Berkovich tip with ideal geometry.

$$S = \left[\frac{dP}{dh}\right]_{h=h_{max}} \quad (22)$$

Also, the reduced elastic modulus (E_r) can be expressed as a relationship of the Poisson ratio of the samples (υ_s) and the indenter (υ_i) and the elastic modulus of the sample (E_s) and the indenter (E_i) respectively (ROOP KUMAR; WANG, 2002), which is shown in **eq (23)**. The elastic modulus and the Poisson's ratio of the Berkovich diamond indenter are usually expressed as E_i= 1141 GPa and υ_i = 0.07.

$$\frac{1}{E_r} = \frac{1-\upsilon_s^2}{E_s} + \frac{1-\upsilon_i^2}{E_i} \quad (23)$$

Figure 50 - Nanoindentation: a) a typical load vs displacement curve and b) a schematic representation of indentation showing various quantitates used in the analysis.

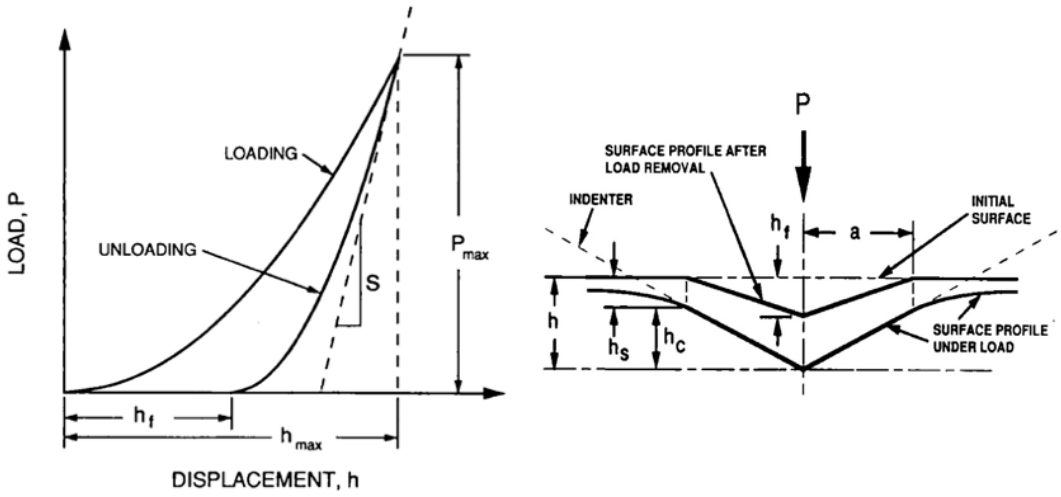

Source: (ROOP KUMAR; WANG, 2002).

3.7 Scratch Test

In this work, the study of the abrasive wear behavior of copper and composites was based on scratch tests at two different scales, meso and micro-scale. The definition (classification) of the scale appears consistent with the abrasive particle size and microstructural features of the materials studied. It has been shown that the predominant wear mechanism is connected to the tip geometry used at the wear interface (GAHR, 1981; RICHARDSON, 1967). Therefore, two tribometers with different geometry of the tips were used and described in the next section.

The apparent friction coefficient is defined as the ratio between the tangential force and the normal load applied to a moving point. At the meso-scale, the apparent friction coefficient (COF) and the wear were measured after the test, when the sample was unloaded, considering the elastic recovery of all the tested samples. At micro-scale tests, the apparent friction coefficient (COF) was in-situ, and elastic recovery was not considered.

3.8 Meso-scale scratch test

Scratch tests were carried out using a Bruker UMT-2 Tribometer available at the LFS (Figure 51, a-b). The scratches were performed using a Rockwell-C spherical cone diamond indenter with a radius of 200 µm and 120º of spherical radius (Figure 51c). The data acquisition rate configured for the test was 124 points per second, totaling 86,808 points, from which the first 620 points were removed to calculate the average friction coefficient. These points were removed to eliminate the running-in period in the first 5 s.

Figure 51 - Tribometer and tip for scratch tests. a) general view of the Bruker Tribometer, b) sample and indenter configuration and c) Rockwell-C tip for scratch tests.

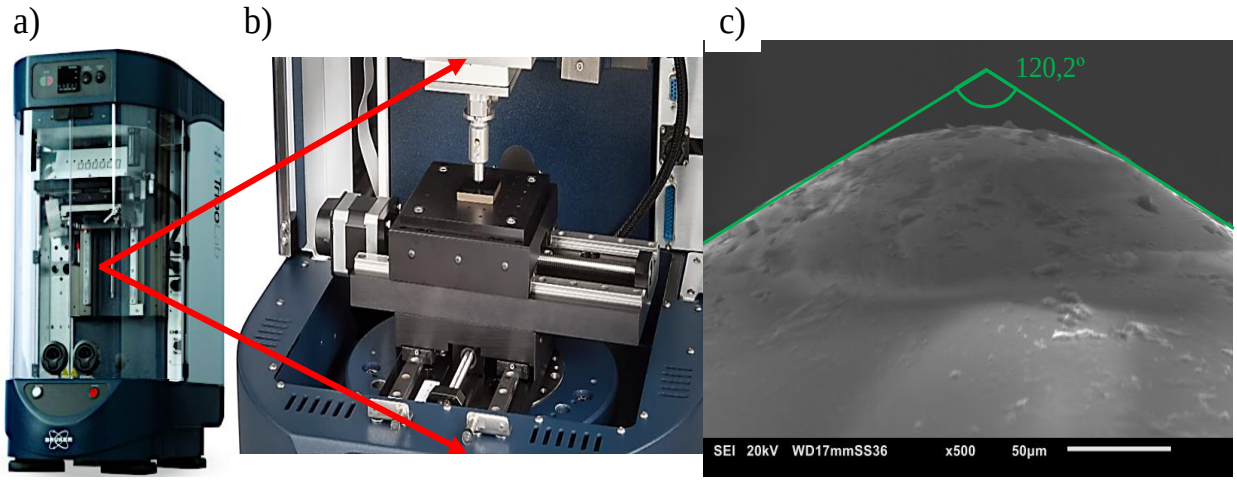

The UMT-2 tribometer has a load cell with a force sensor (1.5 mN resolution), which is two-dimensional (2D), and used to measure the sliding friction force (tangential force) between the indenter and the surface of the sample to control the loading force applied on the sample. The coefficient of friction (COF) is measured from normal (F_n) and tangential (F_t) force results.

The samples of copper were a cylinder with a diameter of 40 mm and a thickness of ~8 mm (samples mounted in Bakelite). The samples were subjected to polishing (fine finish). This procedure was described in the metallographic sample preparation section of this chapter.

The average initial surface average roughness (S_a) of samples was (0.02 ± 0.01) μm, as suggested by ASTM G171 (2009).

The single pass scratch test was carried out at a constant speed and the distance from the scratch was kept constants for all samples. Scratch tests were performed at ambient temperature and humidity. Each scratch test consists of three consecutive steps: (1) a preload, penetration of the indenter into the surface of the sample until reaching the normal test load, (2) start of scratching, performed by the indenter, with the selected normal load, generating a scratch, and (3) The normal load applied to the surface was released after the scratch test was completed. Each scratch was repeated three times under the same conditions for repeatability. The parameters of the test are summarized in Table 4.

Table 4 - Detailed test conditions for single pass scratch test.

Parameter	Specifications	Unit
Samples	Copper	
Number pass	1	
Load	5, 10, 15 and 25	N
Distance	5	mm
Sliding speed	0.25	mm/s
Temperature	Room temperature	º C
Repeatability	3	
Indenter	Rockwell-C	
Tip radius	200	μm
Cone angle	120.2	º
Attack angle	Varies with depth	

3.9 Micro-scale scratch test

Micro scratch experiments were performed using a Hysitron TI950 Triboindenter, from Bruker, at the LFS (Figure 52a). The test experiments were performed on copper and composite samples with the same dimensions and surface roughness mentioned above. Scratches were made using a spherical cone diamond tip with ~5 μm tip radius and ~60° apex angle (Figure 52b). The high load module was used, which reaches a maximum normal load of 2 N, allowing the acquisition of the signal of the forces and displacements in the 3D Cartesian system.

Figure 52 - a) Nanoindentation Hysitron and b) Conical indenter.

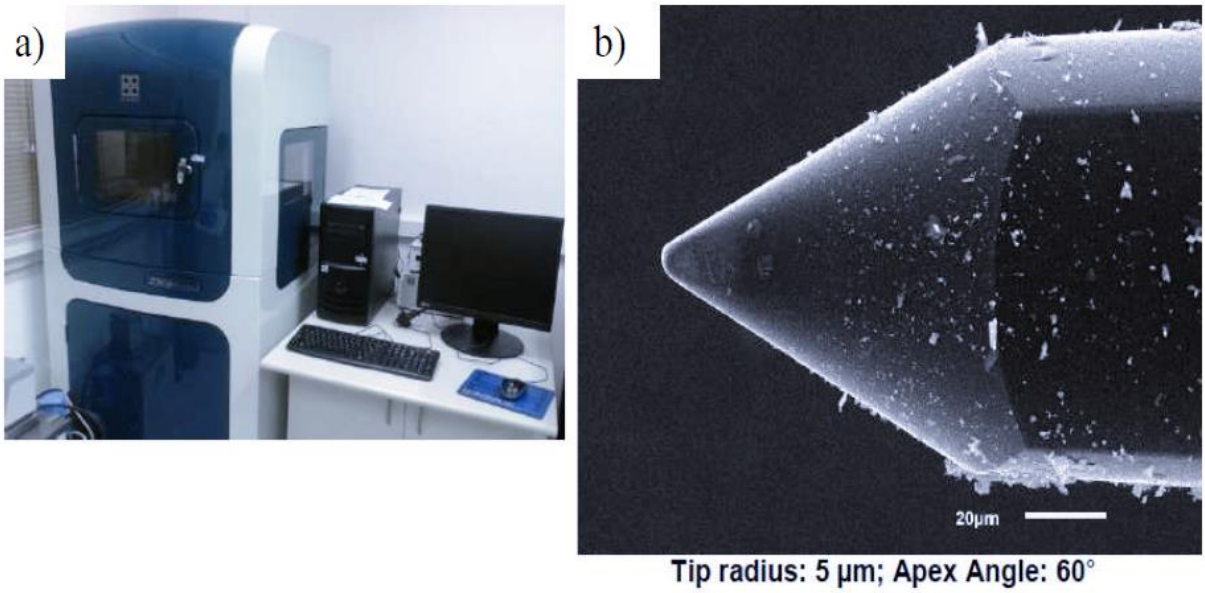

Source: (SERIACOPI, 2018).

Micro scratch tests were performed at constant load and speed. The test procedure for each scratch can be divided into five steps:

- Calibration of the tip (indenter);
- Mapping of the test area;
- Positioning of the tip on the surface;
- Profilometry of the location where the scratch was made;
- Scratching.

The data acquisition rate configured for the test was 198 points per second, totaling 12,501 points for each line, of which the first 121 points were not considered to calculate the coefficient of friction and the average depth. The points assessed for calculating the COF average are contained in the range of 247 to 0.1 µm of the line length. Three random areas were selected to scratch at different normal loads, and scratches were made in two perpendicular directions (identified as 0 and 90°) for each normal load, with ~150 µm spacing between scratches to avoid overlapping abrasion effects. The results of the scratch tests are obtained from the tangential load, which allows the COF to be determined using its relationship with the constant normal load and the penetration depth values taking into account the initial profilometry of the sample. A summary of the micro-scratch conditions for each material is presented in Table 5.

Table 5 - Detailed test conditions for single pass scratch test.

Parameter	Specifications	Unit
Samples	Copper and Composites	
Number pass	1	
Load Samples	5, 20 and 50	mN
Distance	250	µm
Sliding speed	0.25	µm /s
Temperature	Room temperature	º C
Repeatability	3	
Indenter	-	
Tip radius	~5	µm
apex angle	~60	º
Attack angle	Varies with depth	

3.10 Scratch evaluation

3.10.1 Meso-scale scratch test

The profiles of the wear groove were analyzed using the 3D interferometry technique with the Taylor-Hobson model CCI MP equipment. The data obtained were analyzed through the software Talymap Gold v6.2.661 of LFS. The beginning and the end of the scratches were excluded, according to the ASTM G171 (2008) standard; since there is a transition region of the scratch test, the profiles were superimposed to form an average scratch profile, according to Figure 53. In the profiles delivered by the software, it is not possible to directly obtain the averages or the dispersion measures of the profiles. However, the cross-sections of the lines made on a meso-scale were measured at every 16 µm, corresponding to a mean value of 15 profiles. Thus, the characterization of the profiles obtained was compared with the average profile delivered by the software to get consistent results.

Figure 53 - Superposed profiles to form the average profile.

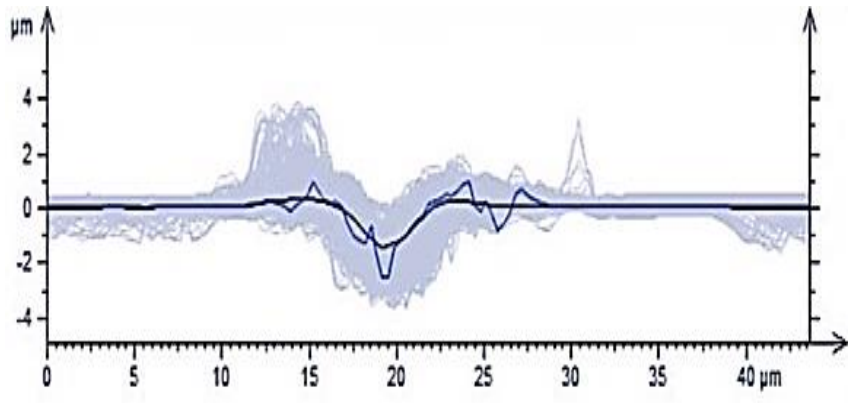

Source: Adapted from (FRANCO; SINATORA, 2017).

From the profiles, geometric parameters indicated the abrasive micro-mechanisms of the sintered materials. The parameters were the area of the groove (A_v), the area of the shoulders (Pile-up A_1 and A_2), the residual penetration depth of the groove (h_r), the width of the groove without considering the pile-ups (W_r), and the width between the peaks of the pile-ups (W_p) are presented in the cross-sectional profile in Figure 54. These parameters give the area of the depth of the groove and the area of the pile-up of two edges (Talymap Gold v6.2.661 software). The procedure for obtaining these parameters was applied according to the methodology described by (FRANCO, 2015).

Figure 54 - Mean profile/geometric parameters.

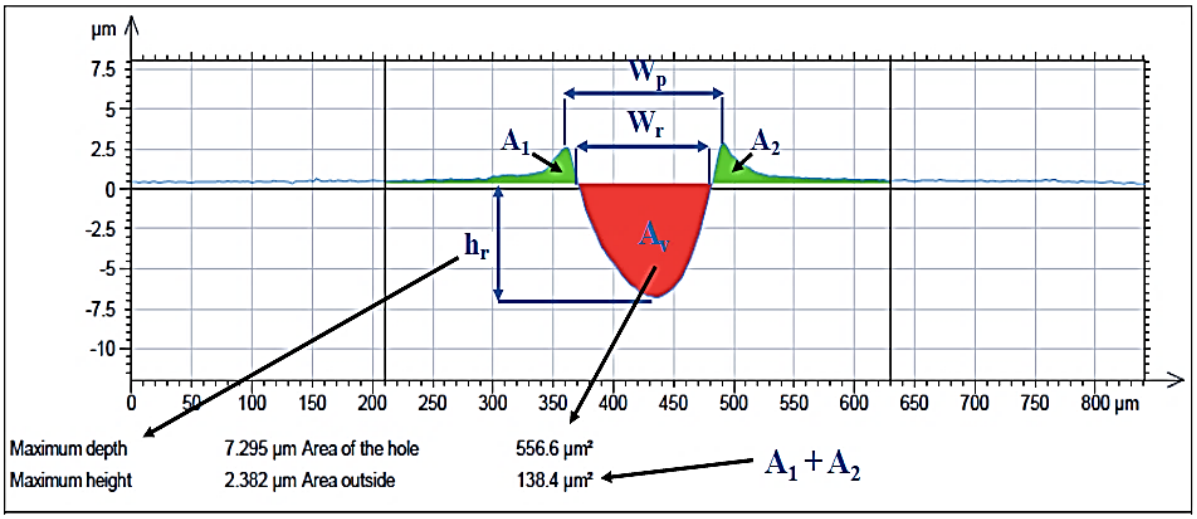

To evaluate the abrasive mechanisms in the materials subjected to normal loads on a meso-scale (Bruker). First, the F_{ab} values calculated from the previously described methodology were analyzed to obtain the values of the pile-up areas (A_1+A_2) and the area of the grooves (A_v) (Figure 55). Also, the analysis of the abrasion mechanisms from the F_{ab} factor was supported by the microstructure and the profile of the scratches characterized via SEM and FEGSEM.

Figure 55 - Scratch test - copper sintered at 110 MPa, 5 N - mean profile/geometric parameters, to obtain the F_{ab} value.

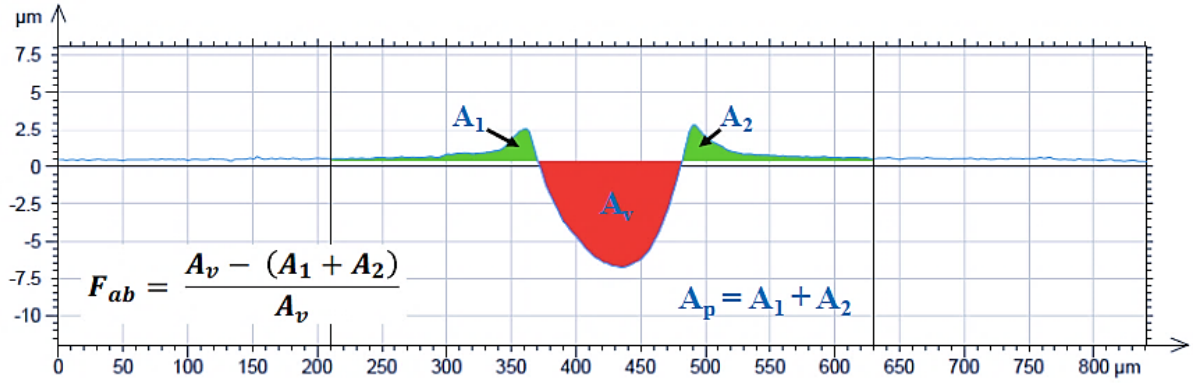

3D interferometry technique (CCI) was also used to characterize the scratch profile. The software has enabled the wear groove observation and displacement of material at the edges in fifteen different sections of the wear groove for each normal load. The volume of the groove was considered as the material that originally was the groove, without considering the formation of the pile-up. The average material displacement due to wear or displaced volume W_v has been calculated through:

$$W_v = \left(A_V - (A_1 + A_2)\right) * L \qquad \textbf{(24)}$$

3.10.2 Micro-scale scratch test

Figure 56 illustrates the geometric relationship between the penetration depth (h_p) it was measured during normal sliding abrasive wear and the geometry of the tip (abrasive). Tip was considered a sphere to make the schematic representation easier (microscale), where A is the projected contact area between the tip and the sample surface, θ is defined as the angle formed between the particle in the direction of movement and the plane of the surface that suffers the abrasion, and s is arch length (see Figure 29, **eq. (8)**).

Figure 56 - Schematic of a spherical tip scratching over the surface of sintered sample.

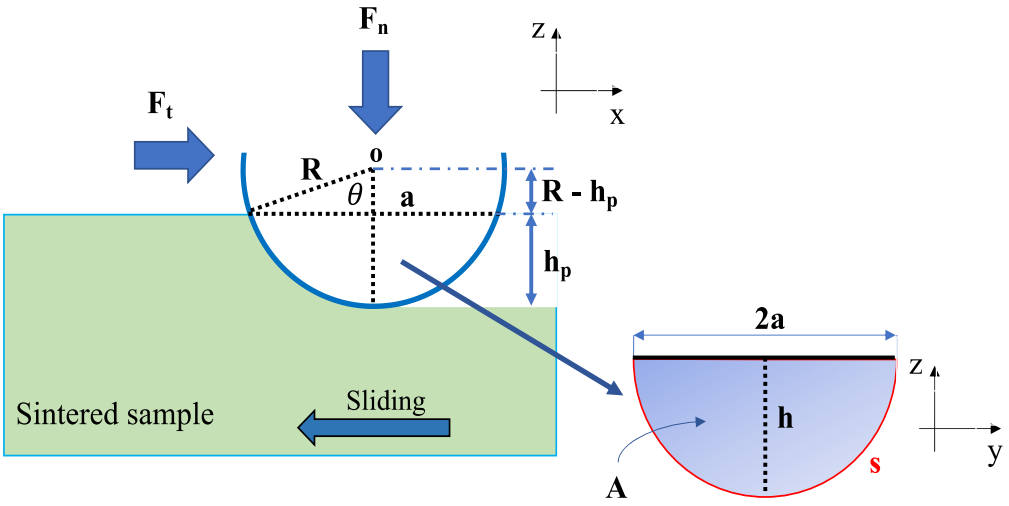

The groove area can be defined with **eqs. (25-26)**.

$$s = 2R\cos^{-1}\frac{R - h_p}{R} \qquad \textbf{(25)}$$

$$A = \frac{1}{2}Rs - \left(R - h_p\right)\sqrt{R^2 - (R - h_p)^2} \qquad \textbf{(26)}$$

Which are consistent with the results in ZHANG et al., (2020) and XIAO et al., (2013).

Based on the projected area (A), is used to determine the material removal, given in terms of the total volume (V_T).

$$V_T = \int A\, dL \qquad \textbf{(27)}$$

In which: L is the scratch length or sliding distance.

In the case of micro-scale tests, the calculate the pile-up volume (V_{pu}) is predicted from the methodology presented by the work done by (SERIACOPI, 2018; NIKAS, 2016;

SERIACOPI et al., 2020) (**eq. (28)**) it is based on an analytical expanding cavity model (ECM) and electrohydrodynamic rolling contacts, which can be applied to evaluate the spherical tip of an elastic-plastic surface with work hardening considerations, which is applicable for copper-based materials.

$$V_{pu} = \pi \left(dR_h^2 - \frac{\sigma_y}{E} r_p^3 \right) \quad (\mathbf{28})$$

Where: R_h is the radius of the ECM hydrostatic core; elastic modulus (E), strain-hardening coefficient (n), yield stress σ_y of the indented material and outer radius of the ECM plastic zone (r_p).

The volume removed is estimated following the most predominant abrasive mechanism depending on the normal load applied during the scratch test in micro-scale.

When the micro-plowing mechanism prevails, the volume removed (V) corresponds to the difference between the total volume removed (V_T) and the pile-up volume (V_{pu}) (SERIACOPI, 2018; NIKAS, 2016; SERIACOPI et al., 2020).

$$V = V_T - V_{pu} \quad (\mathbf{29})$$

When the micro-cutting mechanism prevails, the volume removed (V) is equal to the total volume removed (V_T).

$$V = V_T \quad (\mathbf{30})$$

A scheme is proposed with the inputs and outputs of the scratch test on two scales, for the characterization of the abrasive mechanisms from micro-ploughing to micro-cutting, in Figure 57.

Figure 57 - General scheme that contains the steps related to the study of the abrasive effect on copper samples and composites in two scales.

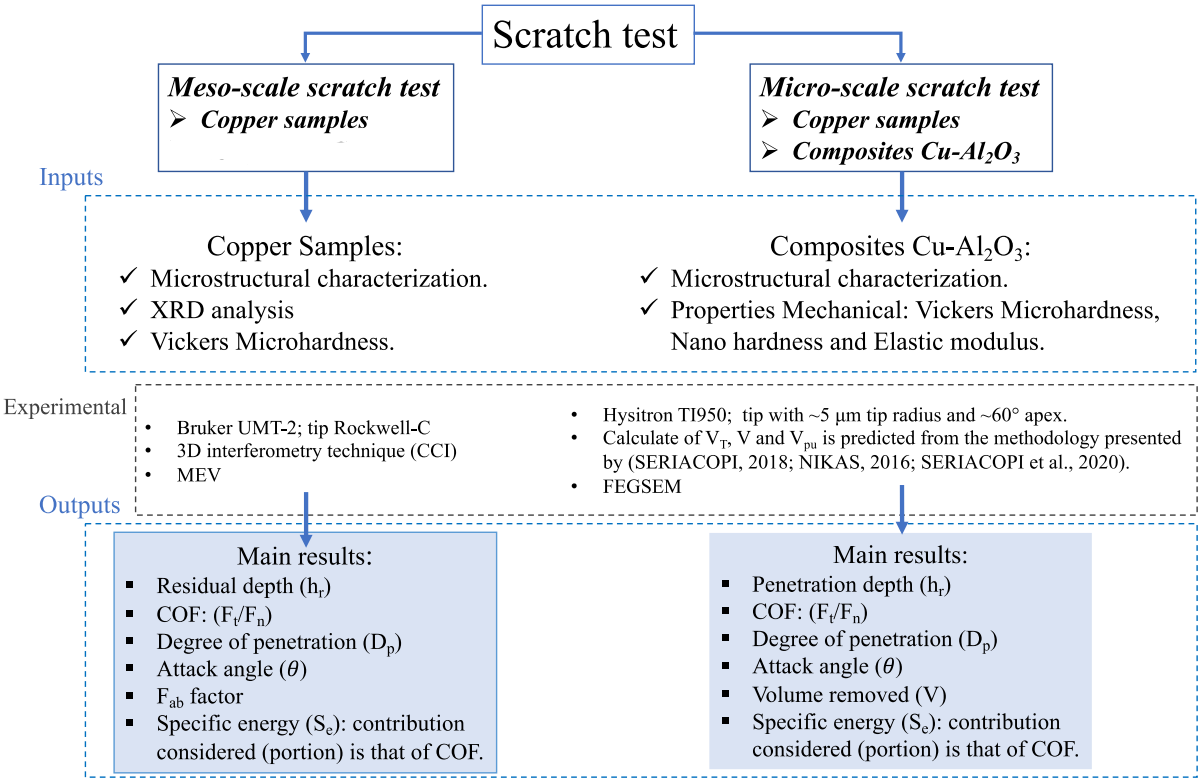

4 RESULTS AND DISCUSSIONS

4.1 Microstructural evolution and mechanical properties of sintered copper via SPS

The evaluation of copper densification was fundamental to the development of composites. The copper powder was consolidated by SPS using different sintering pressure routes during holding or heating time. The characteristics microstructural of copper powders are presented in the first part of the chapter. The results of porosity, density, grain size, and mechanical properties of the different routes of sintering pressure of sintered copper are presented and discussed. Finally, the hardness and pore fraction are related to the mean free path between pores. The results obtained allowed to select the sintering conditions used in the preparation of the composites, adding Al_2O_3 particles to copper to be SPS.

4.1.1 Displacement curves of the copper during the SPS process

The versatility of the SPS pressure-assisted system allows for applying 50-110 MPa during consolidation, which was crucial to the development of this present work. The displacement curves of punches during sintering for each condition are shown in Figure 58. The punches are part of high-density graphite die, displayed in Figure 43. Under the conditions of pressure application, the displacement of the punches can provide information about the shrinkage of the samples during sintering. The shrinkage of the samples is the combination of the formation of other phases (constituents), but it is mainly a result of the densification due to the sintering process. The copper shrinkage is only associated with the densification process (elimination of pores and coarsening grain). In addition, the real-time displacement (shrinkage) data obtained in the SPS should be considered, which does not reflect only the volumetric change of the sample, but also includes other minor sources of volume change, including the other components (die, punches, and graphite spacers) due to applied pressure and thermal expansion.

In the displacement curve during holding time, it is observed that all the samples (H and HT) experience a considerable shrinkage at the same sintering temperature, that is, maintaining the thermal effect as a constant variable. Therefore, sintering occurred even in the samples at

low compaction pressures (50 MPa). It is observed that the end of the sintering process occurs when the punches release the compaction pressure, thus causing a decrease in the displacement curve (circle green).

Furthermore, a significant displacement of the punches is observed as the pressure increases. In addition, a greater displacement is observed for the cases of pressure was applied during holding time (HT) compared to pressures applied during heating (H). The pressure applied during the holding time shows a dependence with temperature (650 ºC), causing more remarkable deformation of the material, increase in the contact points between particles and accommodation of the powders (ZHAOHUI et al., 2008).

Figure 58 - Displacement curves of all samples sintered at 650 ºC.

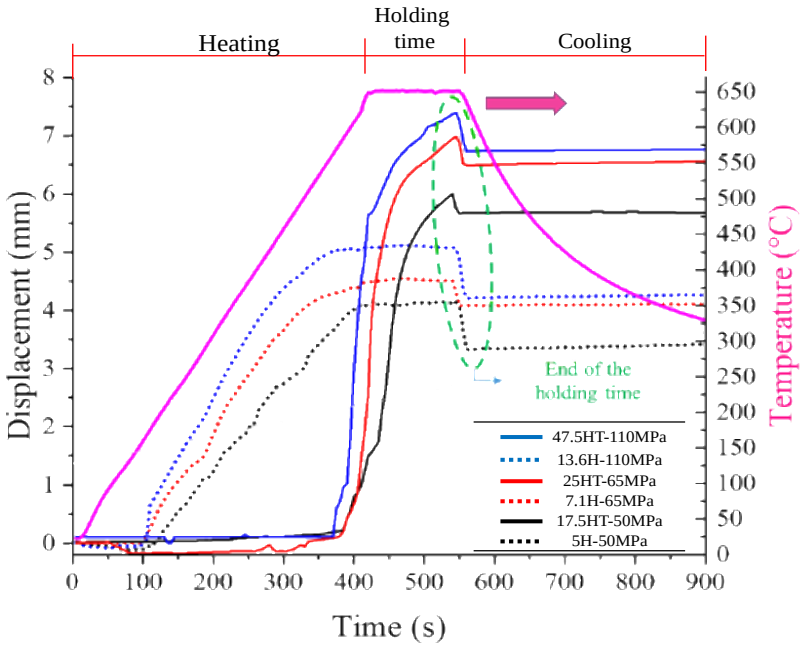

4.1.2 Copper powder

Figure 59a-b, shows the copper powder (Sigma Aldrich, 99.9% purity), from which it is possible to observe an irregular morphology of the particles and rounded edges. Agglomerates of particles were also observed. The particle size distribution is shown in Figure 59c, and a monomodal size distribution can be observed. The particle diameters´ equivalents were: d_{90} = 33.05 µm, d_{50} = 17.88 µm, and d_{20} = 8.91 µm.

Figure 59d shows the results of the X-ray diffraction analysis. The copper particles are indexed as α-Cu single phase, and no secondary phases are identified in the X-ray diffraction pattern.

Figure 59 - (a-b) Images SEM of size and shape of copper powder, c) Copper particle size distribution and d) copper powder XRD patterns.

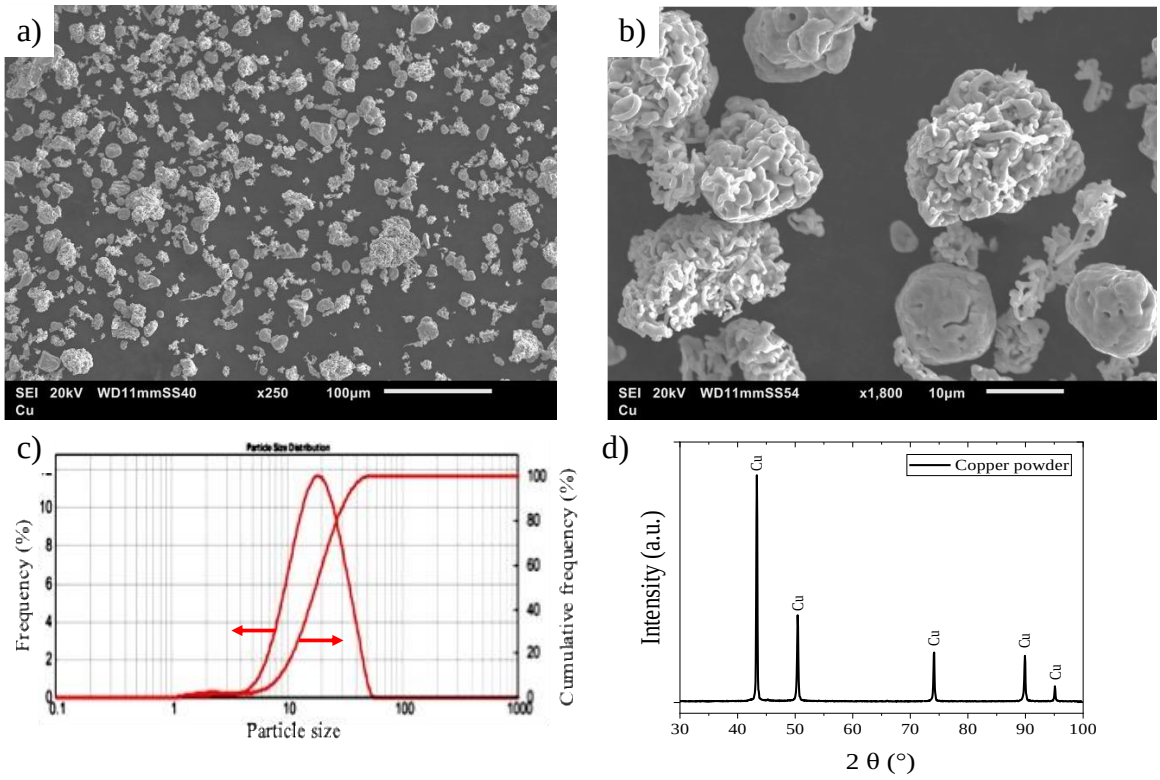

4.1.3 Phases identification

The SPS samples were sintered in the conditions displayed in Table 3 and Figure 44. To evaluate the sintered samples, different and complementary techniques were used. Figure 60 shows the X-ray diffraction patterns of the sintered samples in other sintering conditions. Copper diffraction peaks from the XRD analysis indicate the minimal presence of copper oxides (Cu_2O and CuO) in the sintered copper samples showing the effectiveness of the SPS sintering process. The presence of these oxides could be attributed to the oxidation of copper powder exposed to the environment. However, no copper oxide was detected from powder XRD, indicating the effectiveness of the SPS sintering process.

According to ROMARIC et al. (2017) the presence of oxide on the surface of the particles can delay the sintering mechanisms in cases of a high presence of oxides and low sintering pressures (4 MPa). However, in this study, pressures above 50 MPa and the presence of these oxides in small quantities do not influence the densification, according to reports in the literature (WANG et al., 2000).

Figure 60 - Copper XRD diffraction pattern.

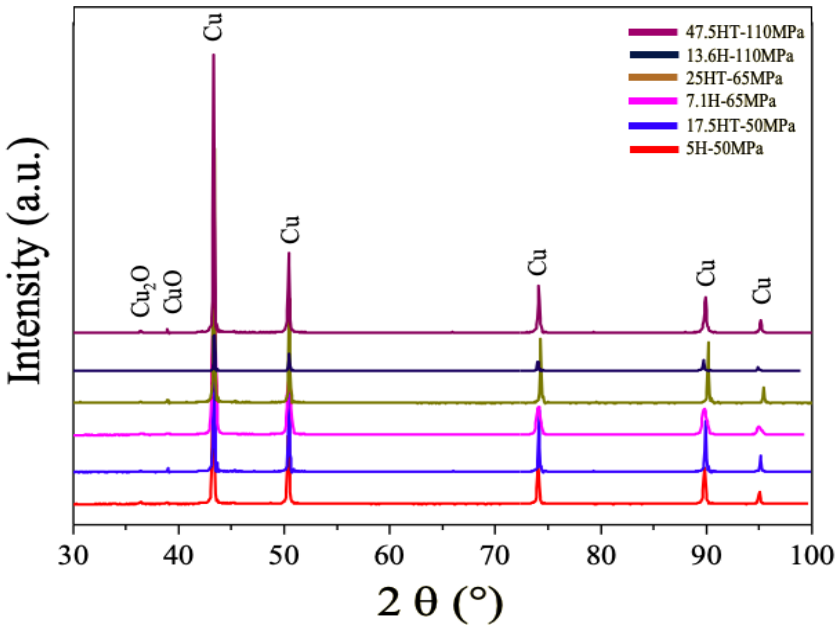

Table 6 presents the microstructural parameters obtained from the X-ray diffraction patterns using the Williamson-Hall method. The crystallite size is influenced by the pressures applied during sintering. From the results analyzed, it can be extracted that the higher the pressure applied (110 MPa) during the SPS process, the crystallite size decreases. Conversely, no significant variations are observed at pressures less than 65 MPa, regardless of the pressure application route used. Regarding the microstrain ($<\varepsilon^2>^{1/2}$), the higher the applied pressure, the higher the results are.

Table 6 - Characterization of microstructural parameters obtained from the Williamson-Hall method for the sintered samples.

Samples	Crystallite Size (nm)	$<\varepsilon^2>^{1/2}*10^{-3}$
47.5HT-110 MPa	34.165±0.008	1.528±0.008
13.6H-110 MPa	50.967±0.014	0.896±0.014
25HT-65 MPa	65.232±0.010	0.766±0.010
7.1H-65 MPa	71.875±0.004	0.522±0.004
17.5HT-50 MPa	73.700±0.007	0.539±0.007
5H-50 MPa	75.533±0.008	0.478±0.008

4.1.4 Densification

The relative density obtained by the Archimedes method and the porosity measurement using image analysis of sintered samples are shown in Table 7. The results allow observing the

contribution of the different routes of pressure application, which resulted in a higher density for 47.5HT-110 MPa sample (8.78 g/cm^3) than 17.5HT-50 MPa (7.71 g/cm^3) as well as 13.6H-110 MPa sample (8.60 g/cm^3) compared to 5H-50 MPa one (7.17 g/cm^3).

Therefore, samples in which pressure was applied during holding time presented an improved relative density, as displayed in Table 7. Additionally, there was a significant reduction in the number of large pores. The porosity results (Table 7) obtained from the Archimedes method (indirect methodology) and porosity image analysis (direct methodology) show the same trend. The differences were expected since the Archimedes method is a volume evaluation (3D), in contrast to the image analysis which is based on the area measurements (2D). Furthermore, the porosity determined by image analysis is influenced by the preparation of the samples and the parameters used for the analysis, such as binarization and segmentation thresholds (SHAHEDI ASL et al., 2017).

Table 7 - Density of samples sintered.

	Density			
Samples	Density (g/cm^3)	Relative density (%)	Porosity - Archimedes method (%)	Porosity-image analysis (%)
47.5HT-110 MPa	8.78	98.0	2.0±0.5	1.4±0.4
13.6H-110 MPa	8.60	96.5	3.5±0.9	2.5±0.6
25HT-65 MPa	8.15	91.0	9.0±0.8	4.1±1.2
7.1H-65 MPa	7.88	88.0	12.0±1.7	6.8±1.9
17.5HT-50 MPa	7.71	86.0	14.0±1.1	9.0±1.8
5H-50 MPa	7.17	80.0	20.0±0.7	13.0 ±1.3

4.1.5 Microstructural characterization of sintered samples

Figure 61 shows microstructures of sintered samples obtained by SEM. The sintered samples revealed different sizes, and irregular and interconnected pores distributed throughout the microstructure. The microstructures of the 47.5HT-110 MPa and 13.6H-110 MPa samples show lower porosity than the other samples. These results were expected based on relative density analysis. In turn, the 25HT-65 MPa and 7.1H-65 MPa samples presented higher pores. When comparing samples sintered at 17.5HT-50 MPa and 5H-50 MPa, an increase in pore size and morphologies of the pores ranging from irregular to spherical can be observed. Therefore, the increased applied pressure and rate pressure improved the densification, morphology, and connectivity of the pores.

Figure 61 - SEM images of the morphology and pore sizes for each synthesized copper sample.

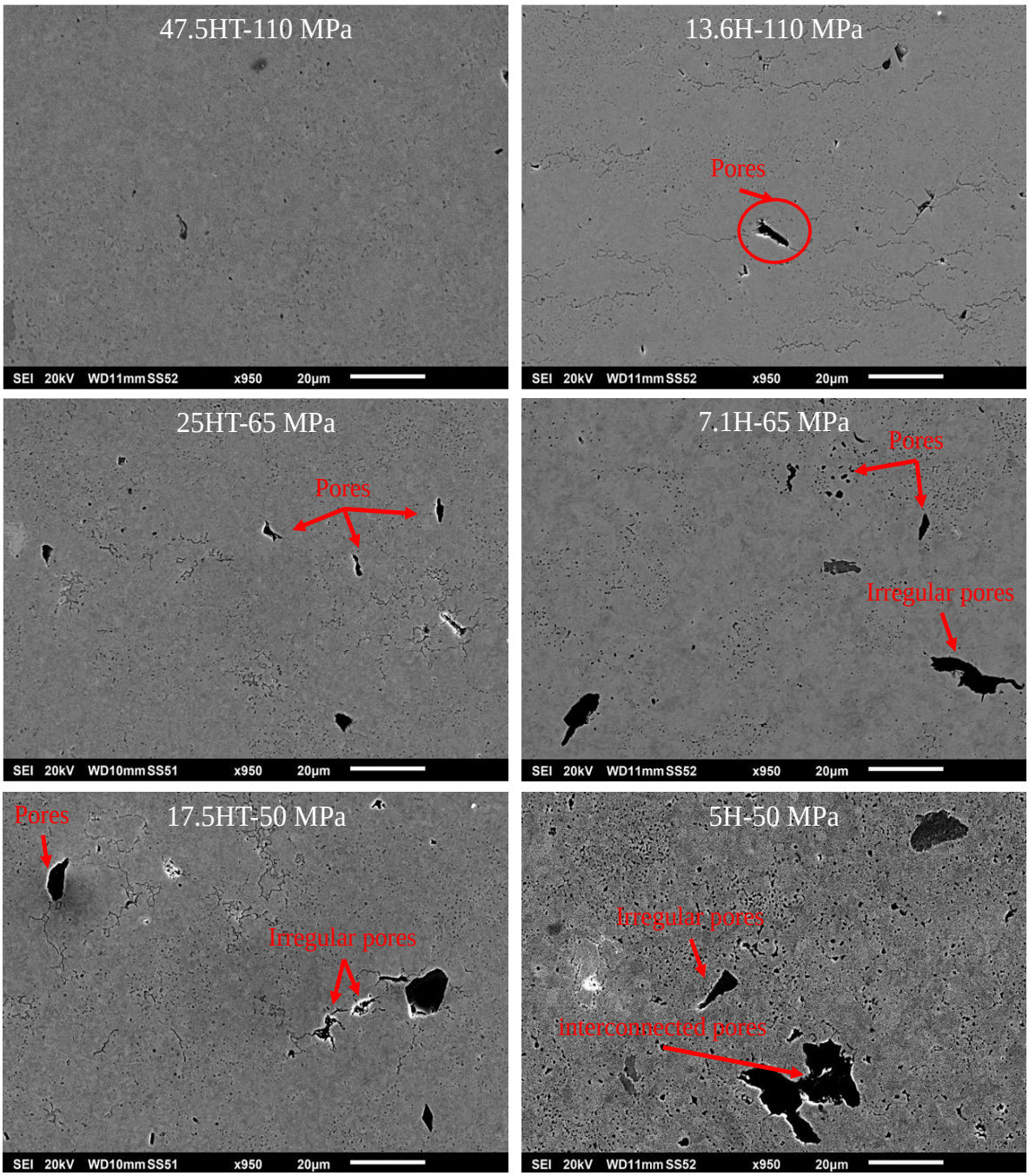

Figure 62 and Figure 63 provides a better understanding of the effect of pressure on the number (volume fraction), size (S_p), and circularity of pores (C_i) on sintered samples. As expected, pressure reduced the number of large pores, as discussed above. Regarding the analysis of the pore sizes distribution, a trend of a higher percentage of pores smaller than 10 µm was observed for the case of the samples sintered at 110 MPa, mainly for the 47.5HT-110MPa sample. Samples sintered at 50 MPa present a larger size and volume fraction of the pores, as well as a higher number of isolated pores were observed. The shift towards smaller pore sizes occurred mainly in the range of 3-15 µm (Figure 62) as found in other works (LI et al., 2012; MAKENA et al., 2017; WEGNER et al., 2013).

Figure 62 - Histogram of the pore size for the sintered materials.

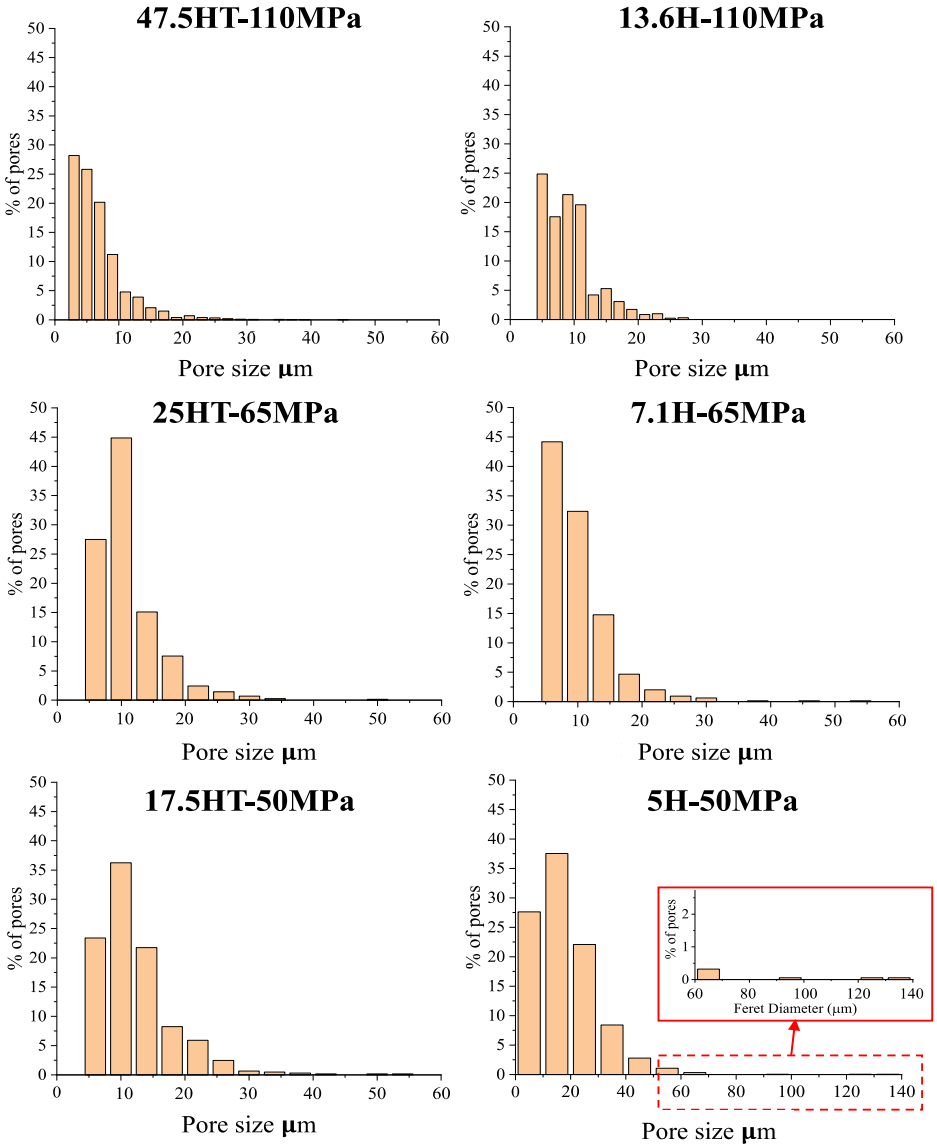

Figure 63 - Histogram of the circularity index pores for the sintered materials.

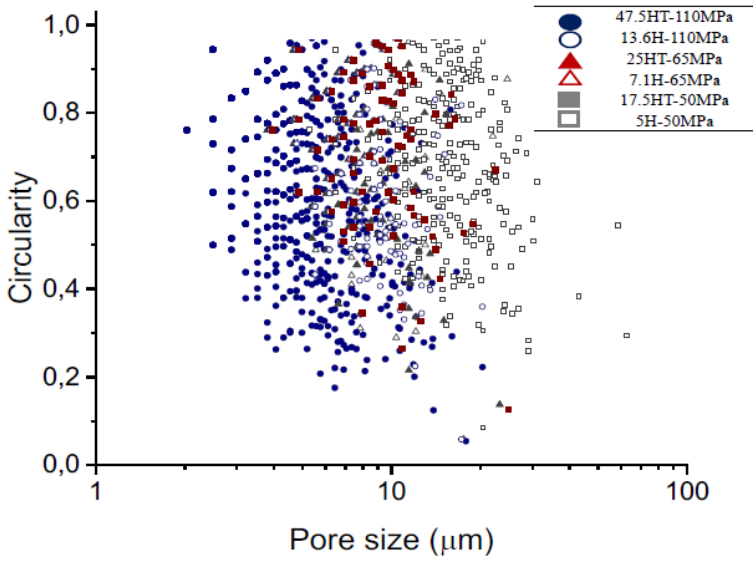

The relationship between the circularity index and pore size is another critical aspect. See Figure 63. Circularity did not tend towards more regular pores with pressure increase. Thus, 52% of the measured pores present a circularity index greater than 0.67. Furthermore, it was confirmed that the increased applied pressure reduces the size and number of pores.

Concluding, the different routes of pressures applied during the holding or and heating were selected based on previous studies (i.e., Table 1) to induce a variation and comparison between the morphology and pore sizes, thanks to the versatility of the SPS and high pressures could significantly decrease pore volume fraction.

4.1.6 Grain size

Figure 64 shows the microstructures of copper after sintering. The average grain size and their standard deviation are displayed in Table 8. The increase in pressure reduces the average grain size as expected. The analysis of the crystallite size corroborates this result described previously in Table 6. It is worth mentioning that the pressure rate is the most striking factor in controlling grain growth during sintering. Studies have addressed the variation of sintered copper grain sizes using spark plasma sintering following the second route (H), in which the pressure is kept constant during holding time (ZHANG et al., 2009; ZHAOHUI et al., 2008). However, the increase in pressure during holding time helps to reduce particle agglomeration, which often contributes to grain coarsening (QUACH et al., 2010). When comparing the 47.5HT-110 MPa sample with the 5H-50 MPa sample, abnormal grain growth

can be observed (red circle) in the sample 5H-50 MPa, and complementary analysis of results was carried out based on analysis of variance (ANOVA).

Figure 64 - SEM micrographs, microstructure of the effect of the applied pressure of the sintered samples.

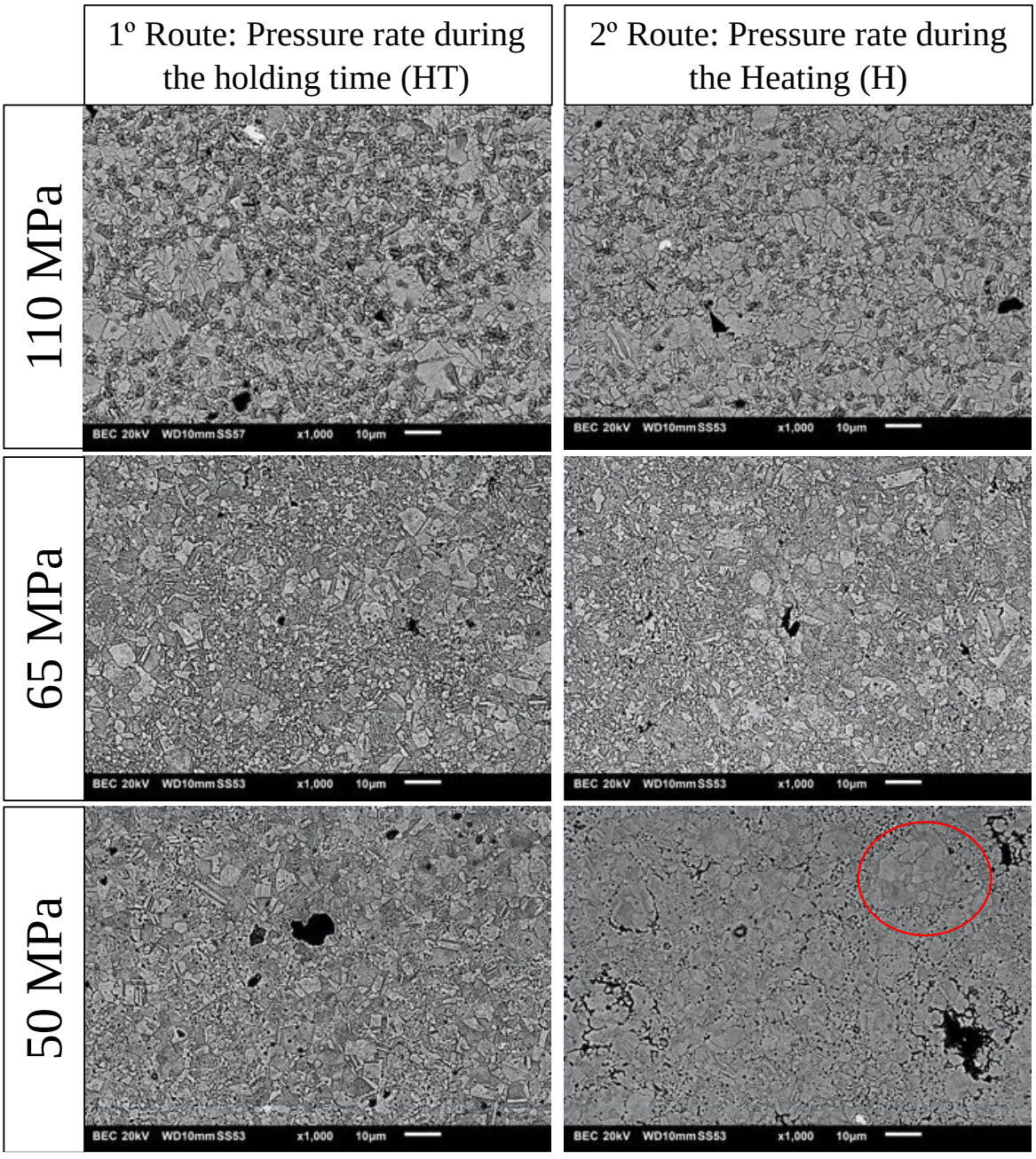

Table 8 - Average grain size of each sintered sample.

Samples	Average Grain Size (μm)
47.5HT-110 MPa	3.10±0.80
13.6H-110 MPa	3.33±1.01
25HT-65 MPa	4.16±1.03
7.1H-65 MPa	4.84±1.17
17.5HT-50 MPa	4.50±1.20
5H-50 MPa	5.31±1.04

4.1.6.1 Statistical analysis

Table 9 shows the ANOVA results to assess the statistical significance of the grain size distribution under different applied pressures and different sintering routes.

In addition, Tukey (T) test comparisons were carried out to confirm where the differences occurred. This method was selected because the data was not normally distributed. Analyzes were performed to investigate whether the differences between the average between the two data sets were significantly different. This analysis helps to determine if there is a relationship between Factor A - the maximum pressure reached during holding time, and Factor B - the rate pressure on HT and H route, considering a level of significance of 5%, as used in previous studies (CHÁVEZ-VÁSCONEZ et al., 2022; RIBEIRO et al., 2022).

Table 9 - ANOVA tests (p<5% significance level) of the grain sizes of the samples sintered.

Factor A	Factor B
50	Pressure rate during holding time (HT) Pressure rate during heating (H)
65	Pressure rate during holding time (HT) Pressure rate during heating (H)
110	Pressure rate during holding time (HT) Pressure rate during heating (H)

ANOVA Grain Size

Source of variation	Sum of Squares (S_q)	Degree of Freedom (DF)	Mean Square (MS)	F_o	P_value
Factor A	397.9	2	198.9	47.1	0.0
Factor B	211.0	1	211.0	50.0	$2.2e^{-12}$
Interaction	317.3	2	158.8	37.6	$1.1e^{-16}$
Error	7342.6	1740	4.2		
Total	8268.8	1745			

The statistical results indicated that the sintering pressure (Factor A) and the route pressure (Factor B) had influenced the average grain sizes of the samples since ANOVA showed statistically significant effects of factors A and B, as well as the interaction ($p<0.05$).

According to Tuckey's test, shown in Table 10, the average grain size of the sintered samples was not statistically different between the pressure routes, considering the pressure of 110 MPa (Factor A). Although, there was a statistical difference between the pressures of 65 and 50 MPa because the $T_{0.05}$ obtained for this pairwise test was 0.33, which is less than the difference between the mean values. Additionally, Tukey tests were performed in pairs between continuous pressures and pressure rates (Factor B). The average grain sizes of the sintered samples at continuous pressures (65 and 50 MPa) were not different, as well as the average grain sizes of the different routes (i.e., 25 and 17.5 MPa min^{-1} pressure rates).

Considering that the sintering pressure and pressure routes cause changes in the average grain size of the copper samples, the following considerations are proposed:

- For the two samples sintered at high pressures (110 MPa), no significant changes in the average grain sizes. However, the different routes caused changes in pore sizes (see Figure 61). When the first route (HT) and the second route (H) are compared for 65 and 50 MPa of maximum pressure, a significant decrease in porosity is observed (see porosity Figure 64 and Figure 63). In addition, the difference between the average grain sizes is close to the critical value of 0.33 ($T_{0.05}$).
- The increase in pressure causes a decrease in the average grain size. Nevertheless, the 47.5HT-110 MPa sample performs better between lower porosity and grain size. Consequently, an optimization of the sintering parameters of the sintered copper via SPS has been obtained.

Table 10 - Pairwise comparisons of grain sizes (Factor A and Factor B) based on Tukey's honest significant difference (HSD) test after ANOVA analysis.

Tukey		*Subtraction between average grain sizes*	*Statistically significant?*
Factor B	$T_{0.05}$ (3.32)		
H			
13.6H-110 MPa v/s 7.1H-65MPa	0.399	1.51	Yes
13.6H-110 MPa v/s 5H-50 MPa	0.399	2.00	Yes
7.1H-65MPa v/s 5H-50 MPa	0.399	0.37	No
HT			
47.5HT-110 MPa v/s 25HT-65 MPa	0.399	1.06	Yes
47.5HT-110 MPa v/s 17.5HT-50 MPa	0.399	1.45	Yes
25HT-65MPa v/s 17.5HT-50 MPa	0.399	0.39	No
Factor A	$T_{0.05}$ (2.77)		
110 MPa			
47.5HT-110 MPa v/s 13.6H-110 MPa	0.333	0.23	No
65 MPa			
25HT-65MPa v/s 7.1H-65 MPa	0.333	0.68	Yes
50 MPa			
17.5HT-50MPa v/s 5H-50 MPa	0.333	*0.78*	Yes

4.1.7 Hardness

Table 11 presents the mean values and standard deviation of Vickers hardness. Generally, an increase in hardness is expected with decreasing porosity (JANA et al., 2022). However, if the standard deviation is analyzed, it can be seen that the results are almost the same at 65 and 50 MPa pressures. Significant differences are observed when sintering pressures of 110 MPa and a pressure of 65 MPa during the holding time.

The 47.5HT-110 MPa sample presented the highest hardness, similar to that found in nanometric copper powder and the manufacture of sintered copper composites by SPS (SUREKHA; ELS-BOTES, 2011; ZHANG et al., 2009; ZHU et al., 2017). The microhardness was analyzed at different loads (10, 50 e 100 gf). An increase in Vickers hardness at lower loads is expected (Meyers law), but the values showed the same trend.

Table 11 - Mean values and their dispersions for the Vickers Micro-hardness of samples sintered.

	Vickers Micro-Hardness		
Samples	$HV_{0.100}$	$HV_{0.050}$	$HV_{0.010}$
47.5HT-110 MPa	88.5±2.6	91.8±3.3	108.0±5.7
13.6H-110 MPa	86.4±5.5	84.7±4.7	95.4±12.2
25HT-65 MPa	72.7±2.5	81.3±3.9	84.9±5.3
7.1H-65 MPa	61.1±4.4	67.3±5.7	88.9±13.1
17.5HT-50 MPa	52.0±6.7	76.1±5.5	78.2±32.6
5H-50 MPa	63.7±2.5	69.8±3.4	75.9±8.3

4.1.7.1 Mean free path

The mean free path between pores (λ) is a measure of the spatial distribution of the pores, defined as the mean distance between the limits of the pores, **eq. (30)** (DE MELLO et al., 2001).

$$\lambda = d\left(\frac{1 - \mathrm{Vvp}}{\mathrm{Vvp}}\right) \qquad (\mathbf{30})$$

Where d is the mean pore diameter and V_{vp} is the total volume fraction of porosity.

The mean free path can be used to explain the effects of the microstructure and hardness of sintered samples. Figure 65 shows the relationship between the different sintering pressure routes and the mean free path between the pores. As the pressure increases, the mean free path increases due to the increased distance between pores and a decrease in pore size, as observed in Figure 61 and Figure 64. The sintered samples, with pressures of 50 MPa, had a mean free path lower due to a higher fraction of pores, as a trend exhibited in Table 7 and Figure 62. Therefore, there is a directly proportional relationship between hardness and the mean free path between the pore volume fraction, where a decrease in the mean free path leads to an increase in hardness. The sample sintered at 47.5HT-110 MPa is expected to have optimal mechanical properties.

Figure 65 - Variation of the average microhardness, density and mean free path between pores (λ) of samples sintered.

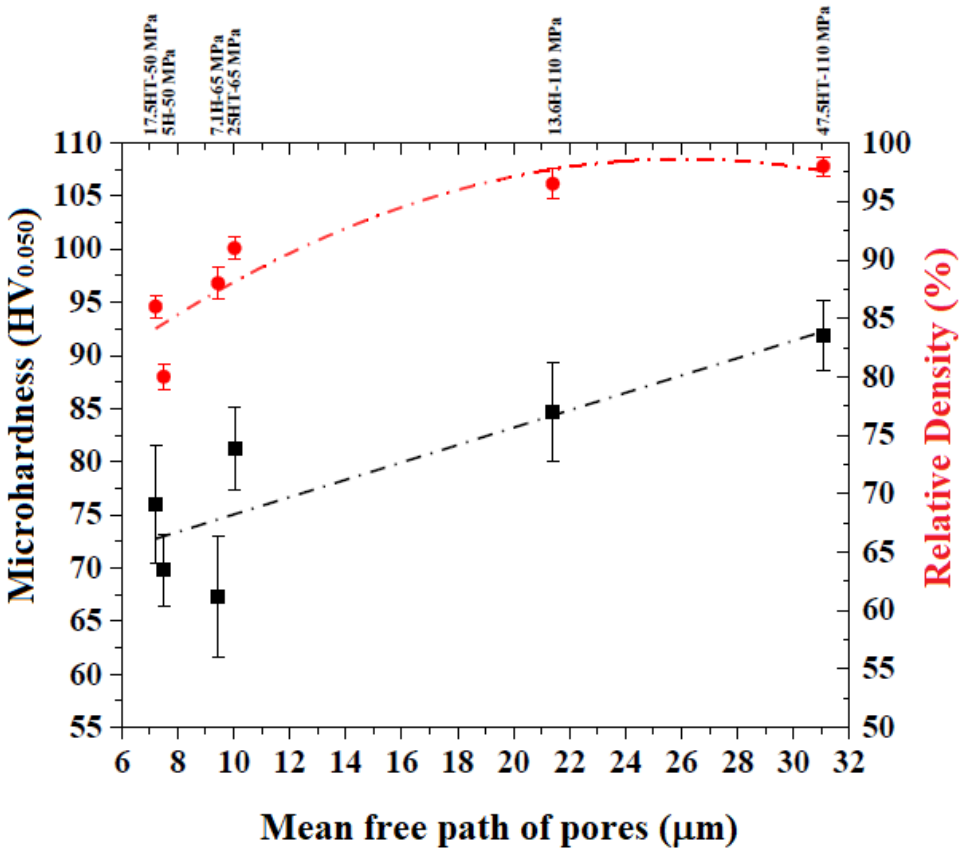

4.2 Microstructural characterization and mechanical properties of composites Cu-Al_2O_3

After the microstructure and mechanical characterizations of the copper samples, the sintering parameters selected to sintering the composites were the sample 47.5HT-110 MPa (maximum pressure applied 110 MPa, sintered at 650 ºC, 2 min of holding time, and pressure was applied during holding time).

The microstructures and chemical compositions of the Al_2O_3 particles were characterized by SEM with EDS and XRD. Then, the effect of the addition of particles on the dispersion in the copper powder was evaluated. In the final part of this chapter, the microstructure and the positive effect of adding Al_2O_3 particles on the densification and increase of the mechanical properties of the composites are shown and evaluated.

4.2.1 Morphology and composition of Al_2O_3 particles

Figure 66 shows the SEM images of alumina particles: Al_2O_3 (pristine), Al_2O_3+Ag: PDCMS and Al_2O_3+Ag: electroless coated. Al_2O_3 particles (Figure 66a) present the characteristic equivalent particle diameters: d_{50} = 7.88 and d_{90} = 13.05 μm. In addition, a round morphology and size of less than 5 μm is observed, which forms the network of particles in the copper matrix, causing an increase in the hardness in those rich regions of alumina particles.

Figure 66b shows the surface morphology of Al_2O_3 particles after the deposit of a thin Ag coating film. The silver coating did not cause visible effects on the surfaces of the coated particles. Figure 66c presents the Al_2O_3 particles after the electroless coating of Ag; the Al_2O_3 particles became smoother with smooth edges. A lower agglomeration and a higher dispersion were observed after the Ag coating, which helps a better dispersion of the Al_2O_3 particles in the copper matrix. In addition, many Ag porous fragments can be seen to gather on the surface of the Al_2O_3 powder.

Figure 66 - Effects of different methods of modifying the surfaces of Al_2O_3 particles: a) Al_2O_3 without surface modification, b) Al_2O_3+Ag: PDCMS and c) Al_2O_3+Ag: electroless coated.

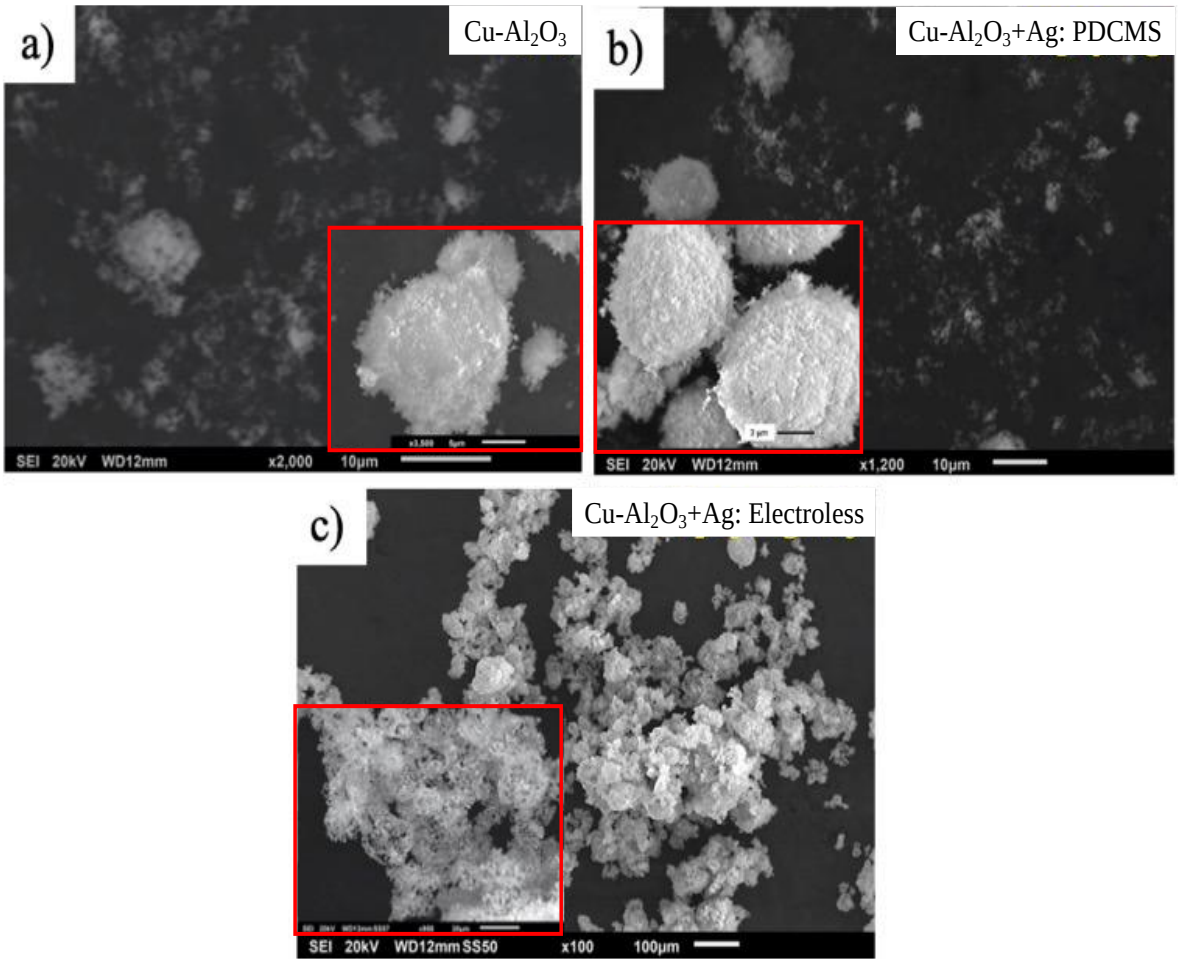

Figure 67 presents the SEM images and element mappings (EDS) corresponding to Al_2O_3+Ag: PDCMS. According to the element mappings, it is observed that the element Ag exhibits uniform dispersion presence on the surface of the particle. Thus, it indicates that the Al_2O_3 particle surfaces were effectively modified with Ag particles, providing changes at the interface between copper and Al_2O_3 during sintering.

Figure 67 – SEM and elementary EDS analysis of Al_2O_3+Ag particles (Al_2O_3+Ag: PDCMS).

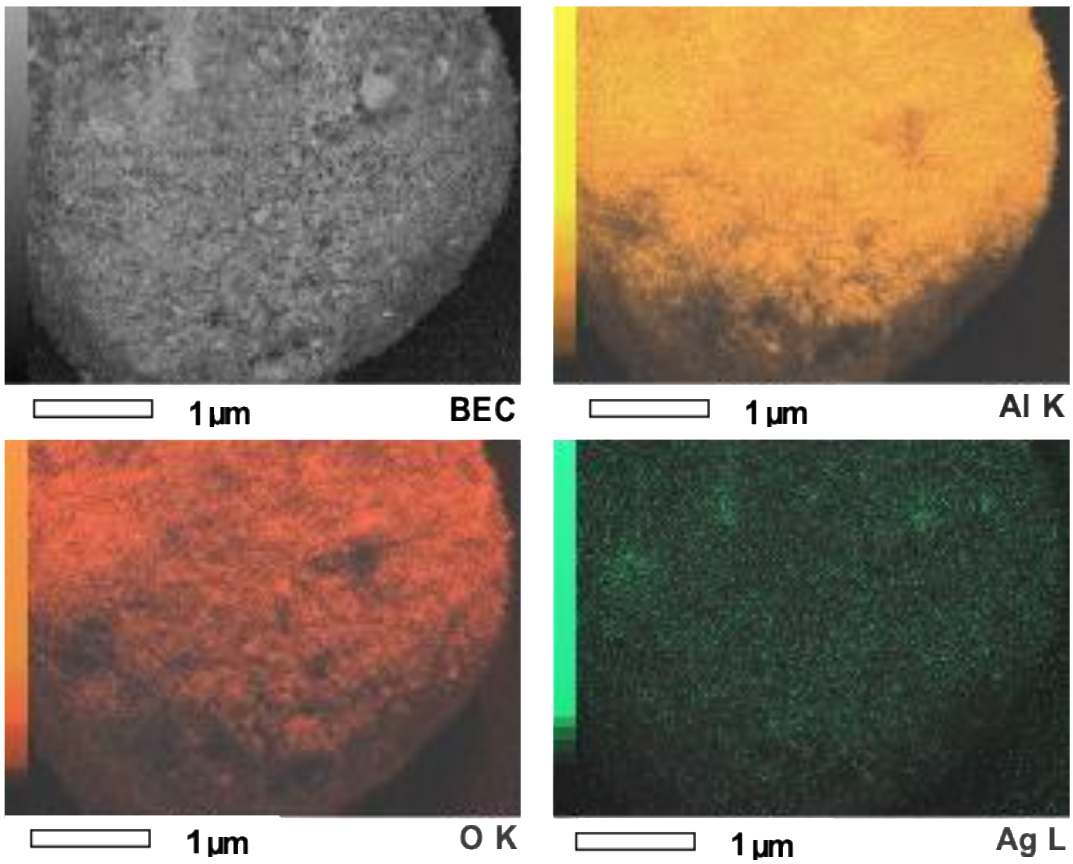

Another exploratory method to modify the interface properties between copper and Al_2O_3 during sintering was used. Figure 68 presents the Al_2O_3 particles coated with Ag using the electroless plating technique (Al_2O_3+Ag: electroless). The microstructure of the powder is different from the received powder and silver deposition (PDCMS) methods. The fine silver particles appear uniformly dispersed between the powders, which did not affect the dispersion in the copper matrix but generated new pores.

Figure 68 - SEM, EDS images of Al_2O_3 particles after the electroless plating process (Al_2O_3+Ag: electroless).

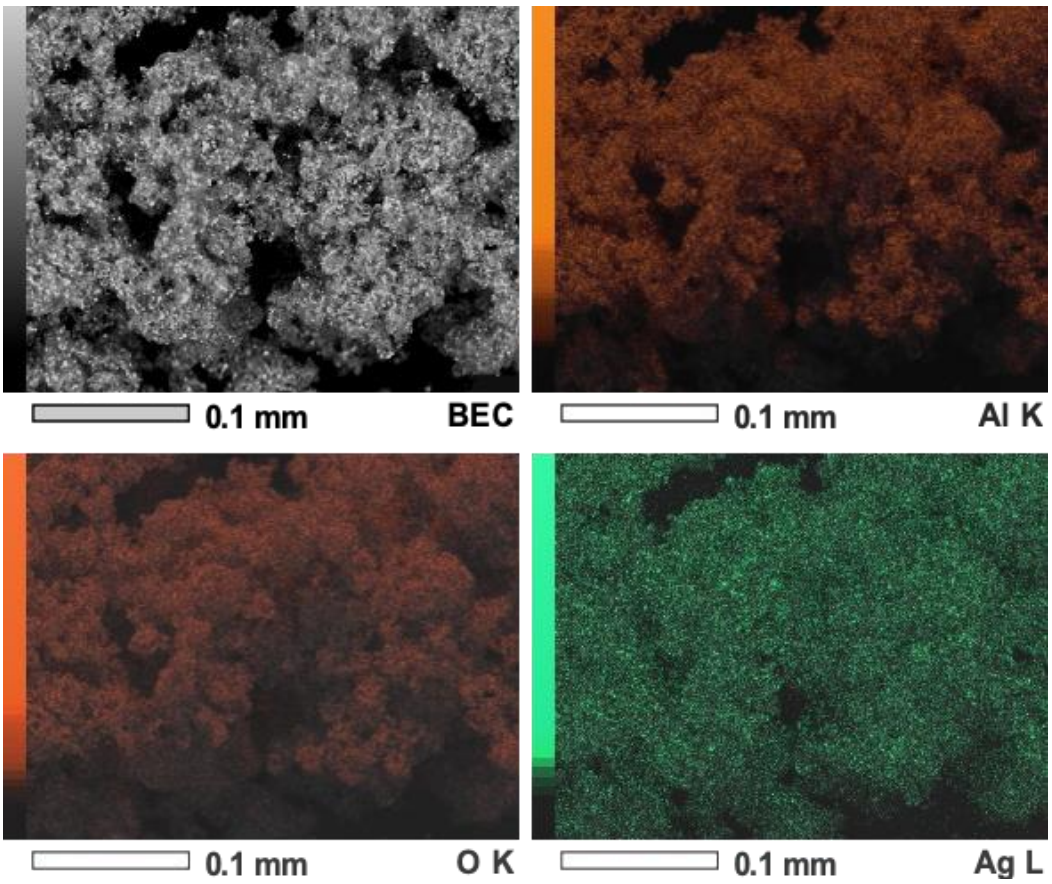

4.2.2 Densification

The results of the densities of the composites are listed in Table 12. The copper sintered at almost complete density (98.6±1.5%) is presented again to observe the changes in densities with the different composites. The increase in density after sintering is due to the shrinkage effect of copper and the pressure applied during SPS sintering, which was discussed. However, the presence of Al_2O_3 particles, which is metallurgically incompatible with copper, can prevent copper diffusion and grain growth; as a result, its densification process will be delayed (NGAI; ZHENG; LI, 2013). Therefore, the incorporation of Al_2O_3 particles in the copper matrix decreased the relative density (83.0±2.1%), indicating that the Al_2O_3 particles, in general, contributed to an increase in the porosity of the composite.

In the traditional process of powder metallurgy of Cu-Al_2O_3 composites, the primary sintering mode is Al_2O_3 to Al_2O_3, Al_2O_3 to Cu, and Cu to Cu. Consequently, this study's particular structure of the composite powders can significantly change the sintering mode; the primary mode becomes sintering between Ag to Cu and Cu to Cu. This occurs because the melting point of Ag is lower than that of Cu; Cu and Ag can form a solid solution with each

other, even at relatively low temperatures (SAYYAD et al., 2020). Therefore, the Cu and Ag area has good mobility and sinterability that promote the elimination of the pores between the Al_2O_3 particles of the composite. In addition, the relative density of the Cu-Al_2O_3+Ag: PDCMS composite was 90.0 ± 1.5%, increasing by 8% compared to the Cu-Al_2O_3 composite. This density increase is due to silver in the composite and by method PDCMS.

From the densities presented, the effect of the electroless plating process of Ag coated with Al_2O_3 showed the most remarkable changes in the relative density of the composites (81.0±2.3%). In addition, the sintering parameters used are a factor to consider in the density results. Compared to other works, the sintering temperature was higher than 1000 ºC and times longer than 1 h, which improved densities by only 7% compared to the Cu-Al_2O_3+Ag: Electroless composite (CHEN et al., 2016; SADOUN; MESELHY; ABDALLAH, 2021).

Table 12 - Relative and theoretical density of the composites.

Samples	Density (g/cm^3)	Relative density (%)
Cu: copper	8.78	98.0±0.5
Cu-Al_2O_3	6.39	83.0±2.1
Cu-Al_2O_3+Ag: PDCMS	6.86	90.0±1.5
Cu-Al_2O_3+Ag: Electroless	6.18	81.0±2.3

4.2.3 Microstructural characterization of sintered composites

Figure 69 shows SEM images of copper (matrix) and composites obtained by different methods to modify the surfaces of the Al_2O_3 particle. The first micrograph shows the microstructure of sintered copper with a pressure rate of 47.5HT-110 MPa. These sintering parameters were chosen to sinter the composites based on the study discussed in the copper (Chapter 2, Item 2.3 SPSed copper and copper composites), which focused on copper sintering as a basis for the metal matrix composites. According to the presented microstructure of the three composites, a homogeneous distribution of the Al_2O_3 particle network (with and without surface modification) is observed. In general, in metallic matrix composites, the presence of ceramic particles hinders the densification process, which has been previously discussed in the literature (ACIKBAS et al., 2022; JAYASHREE et al., 2022). However, for the Cu-Al_2O_3+Ag: PDCMS composite, several regions with low inter-particle porosity are seen compared to the

Cu-Al_2O_3 composite. Therefore, the presence of Ag plays an essential role in the SPS process, improving the sintering process (densification) between the particles and the copper.

On the other hand, the Cu- Al_2O_3+Ag: Electroless composite shows a different feature on the surface of Al_2O_3 particles coated with Ag, which was also observed in the powders of the composite. Literature also reports that the Al_2O_3 particle network is found within the limits of copper grain boundaries and hinders the grain from improving growth improve mechanical resistance in comparison to copper (ACIKBAS et al., 2022; JAYASHREE et al., 2022; SADOUN et al., 2020a, 2020b; SADOUN; MESELHY; ABDALLAH, 2021). However, for this composite, the particular Al_2O_3 network is found around a set of copper grains (matrix), also generating improvements in the mechanical properties.

Figure 69 - SEM micrographs of the microstructure of copper and the composites, etched with $FeCl_3$ reagent for 7 s.

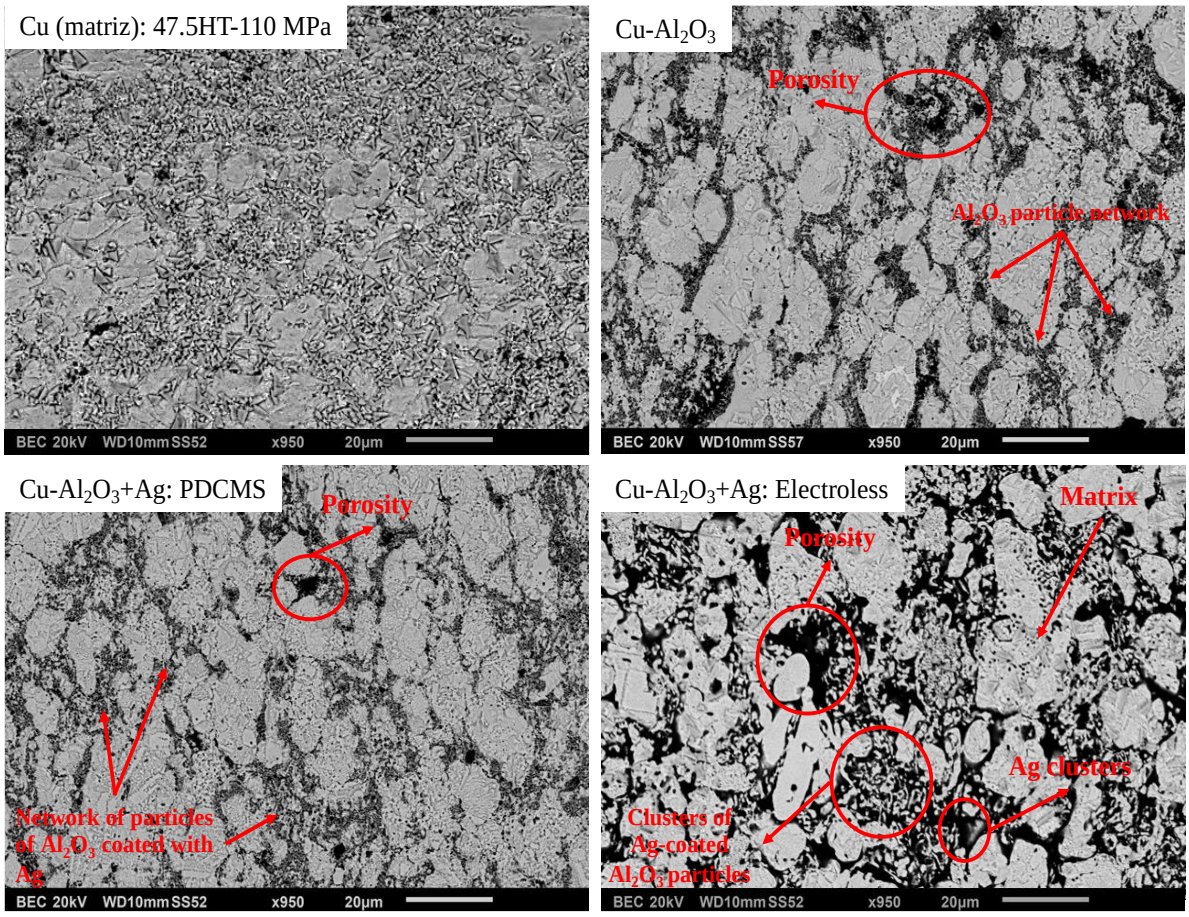

Surface analysis of the sample was performed using SEM and composition maps (EDS) to determine the distribution of elements in the composites. The SEM observations and EDS elemental map of the Cu-Al_2O_3 composite are presented in Figure 70. These observations

indicate a homogeneous distribution of Al and O (Al_2O_3) elements in the copper matrix, generally surrounding a set of copper grains, as shown in Figure 69. They obtained a homogeneous distribution of reinforcement in the matrix for composite materials, which is pointed out in literature as necessary for improving mechanical, electrical, and thermal properties (CELEBI EFE et al., 2011).

Figure 70 - SEM micrograph and EDS elemental mapping of the microstructure of Cu-Al_2O_3 composite.

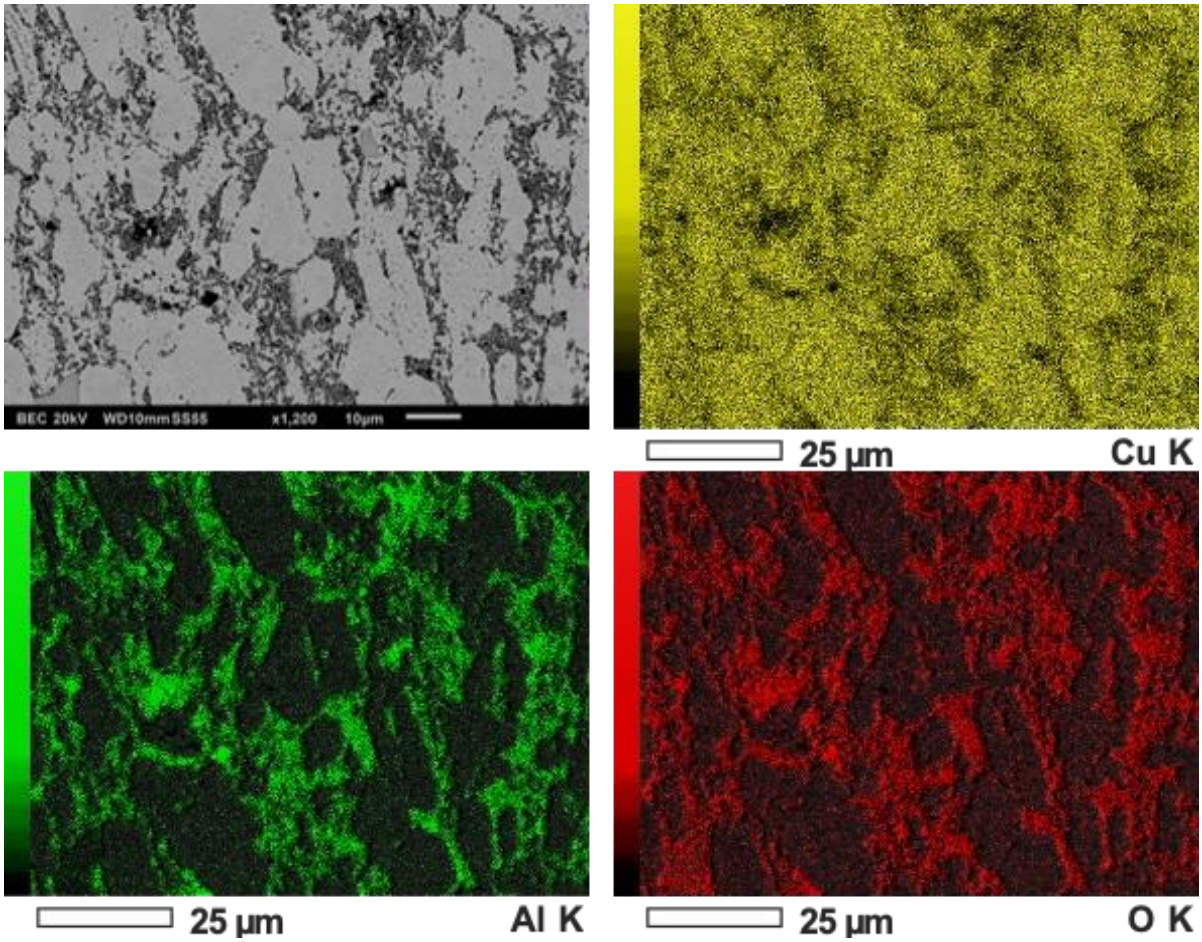

Figure 71 shows the EDS elemental mapping of a Cu-Al_2O_3: PDCMS composite region. The analysis also revealed the presence of silver, despite the thin layer of silver on the Al_2O_3 particles after the sintering process.

Figure 71 - SEM micrograph and EDS elemental mapping of the microstructure of Cu-Al_2O_3: PDCMS composite.

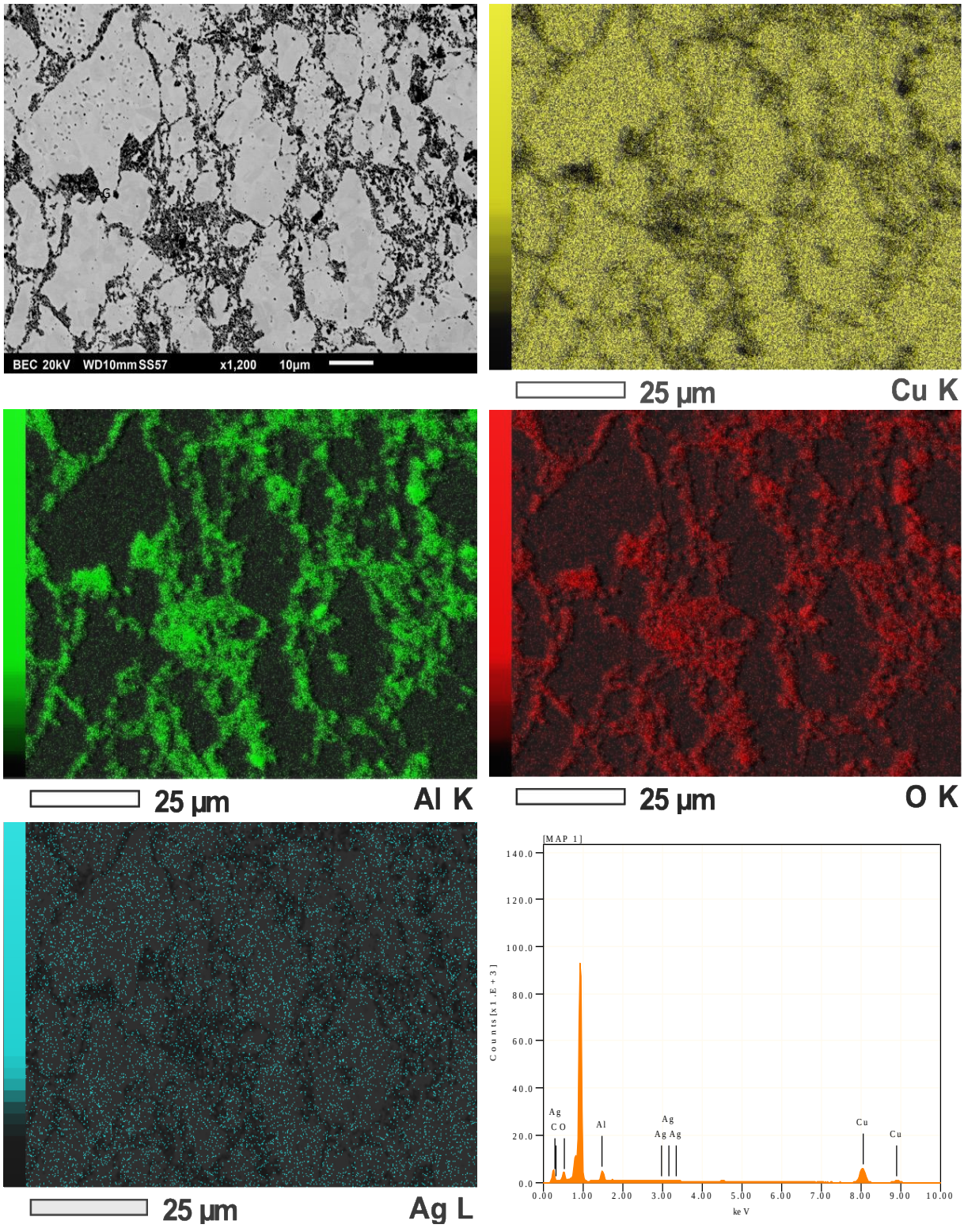

Figure 72 - SEM micrograph and EDS elemental mapping of the microstructure of Cu-Al_2O_3: Electroless composite.

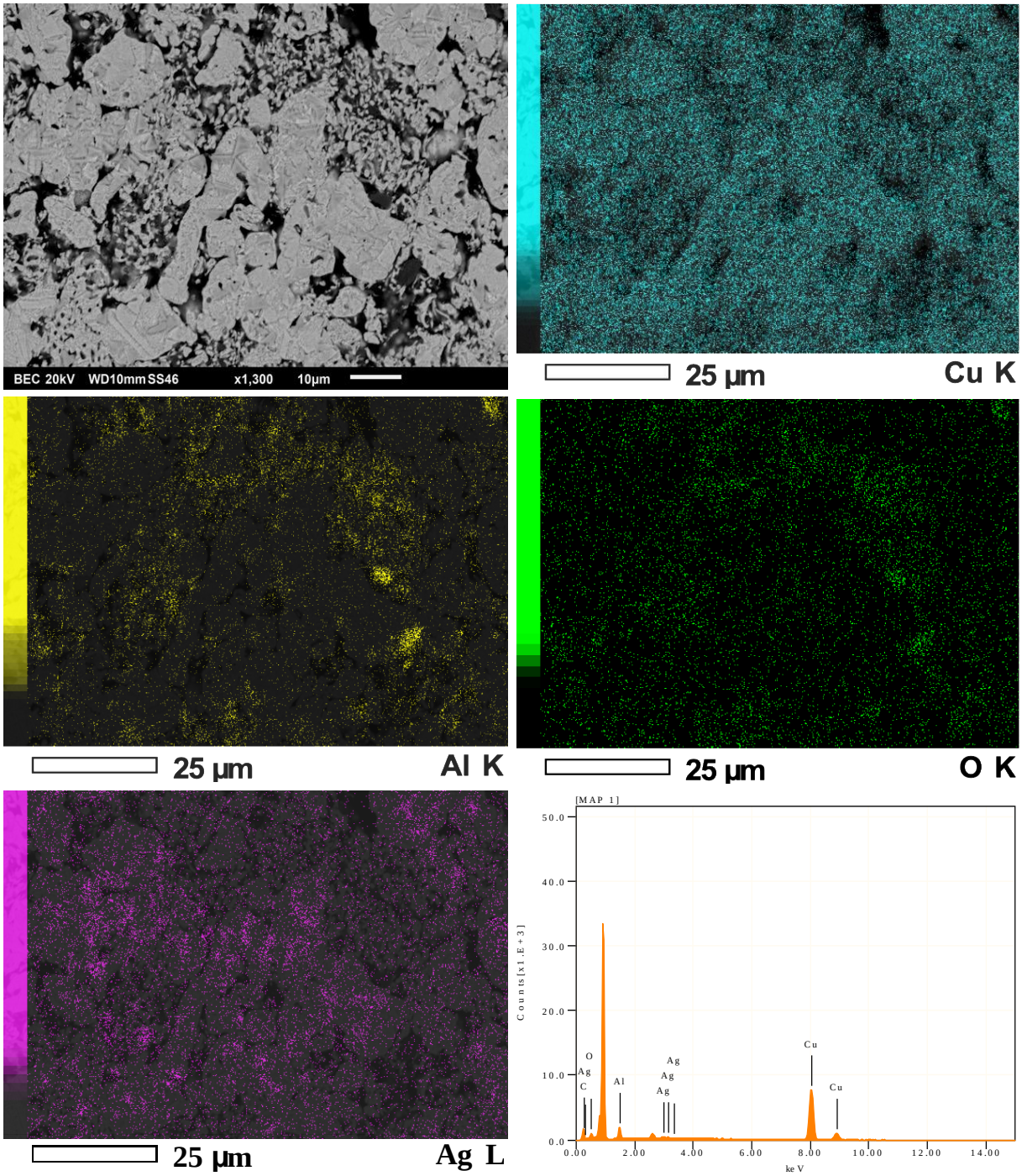

The EDS maps of the Ag-coated Al_2O_3 composite exhibit the quality of the silver layers on the Al_2O_3 powders after the sintering process (Figure 72). The magenta and cyan regions are copper and silver, respectively. The silver exhibits the same distribution and agglomeration of the elements Al and O (Al_2O_3). This can be attributed to the fact that the silver particles do not detach from the surface of the Al_2O_3 particles. In turn, when the silver coating process was applied to the Al_2O_3 particles, a homogeneous silver layer formation was observed around the particles, as observed in Figure 68.

4.2.4 Mechanical properties of composites

The effect of Al_2O_3 particles on Vickers hardness is shown in Figure 73; hardness can be significantly improved by adding Al_2O_3 reinforcements to the copper matrix (91.8±3.3 $HV_{0,050}$). In addition, the metal-ceramic interface modification method and the homogeneous distribution of Al_2O_3 particles also have a significant effect on the hardness of the composites. The hardness increases to 165±17 $HV_{0,050}$ only due to Al_2O_3 particles in the matrix (Table 13). However, the standard deviation is analyzed, and dispersion is observed in the microhardness measurements, which is caused by the increase in the dispersions of the Al_2O_3 particles and porosity.

Moreover, when the Ag-coated Al_2O_3 particles (PDCMS) were added, the hardness was 190 ±13.7 $HV_{0,050}$. This improvement in hardness is attributed to the decrease in porosity, homogenization and presence of the particles observed in the previous Figures. The microhardness results obtained for Cu-Al_2O_3+Ag: Electroless composite (110±31.3 $HV_{0,050}$) result from a relatively uniform distribution of Al_2O_3 and silver nitrate particles in the copper matrix. The high standard deviation is a function of the presence of particles, matrix, and the decrease in porosity. However, the relative density was not affected when comparing the composite without coating (Cu-Al_2O_3). GÜLER et al. (2020) studied the effect of Al_2O_3 content and milling time in copper matrix composites manufactured by electroless coating and hot pressing (HP). As a result, the researchers obtained the maximum hardness values (105-125 HV) in composites sintered with copper powders milling for 2-4 h and with 3 %wt. Al_2O_3. Furthermore, similar microhardness values were observed in the report of SADOUN et al., (2020b), where the Cu-Al_2O_3 nanocomposites, in which the Al_2O_3 particles were coated with Ag, using the electroless plating technique, obtained microhardness results between 90-130 HV with a percentage of Ag coated with 3-12 % wt. Al_2O_3.

Figure 73 - Microhardness Vickers of composites: load 50 gf.

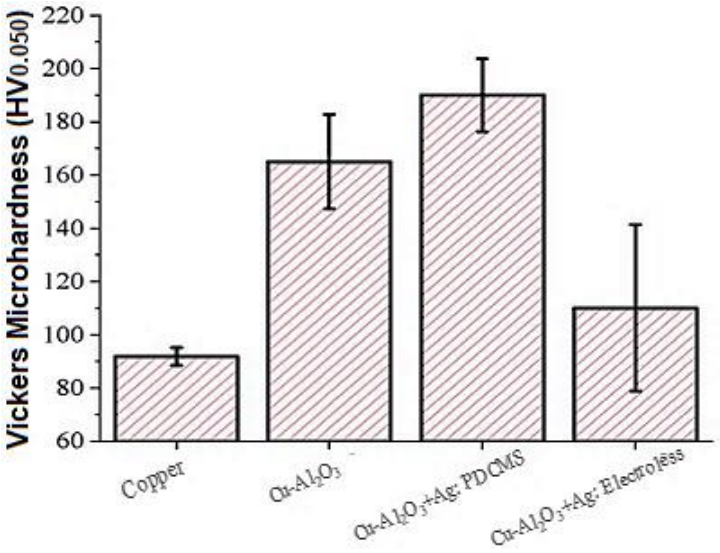

The load-displacement curves (P-h) of the composites obtained from the instrumented indentation (load of 500 μN) of each constituent phase of the composite are shown in Figure 74. Compared with the indentation response of the phases, the nanoindentations were applied in the copper grains, the Al_2O_3 particles, and the Copper/Al_2O_3 interface.

Figure 74 - Load-displacement curves resulting from the instrumented indentation. a) Copper, b) Cu-Al_2O_3, c) Cu- Al_2O_3+Ag: PDCMS and d) Cu- Al_2O_3+Ag: Electroless.

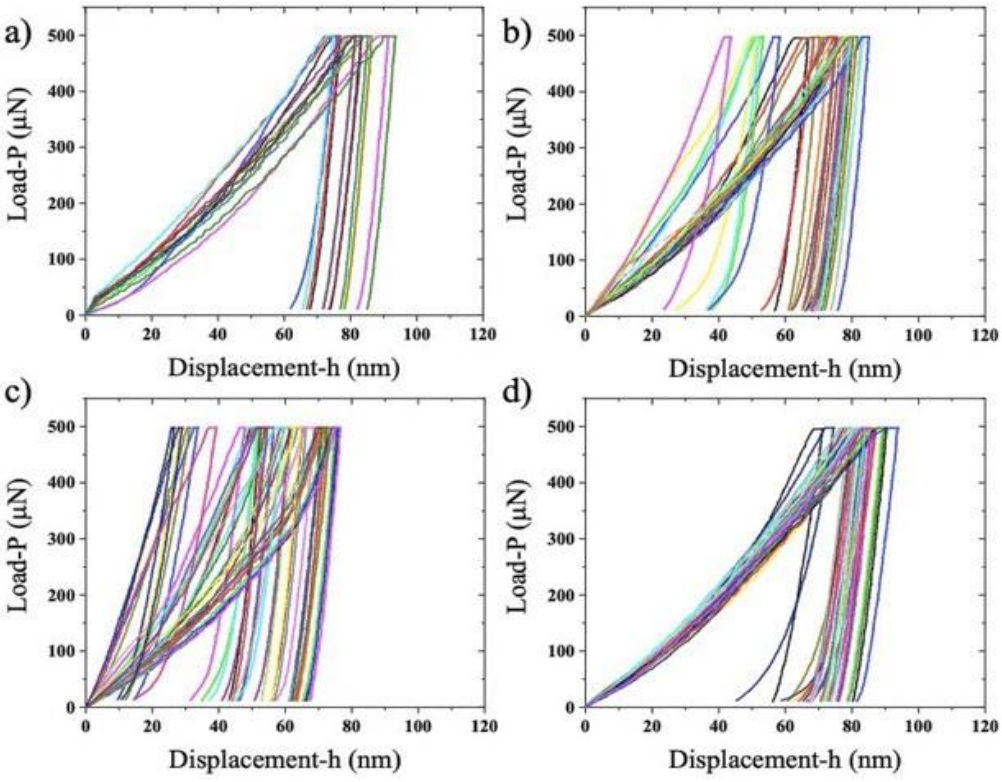

Figure 75 - Images obtained in situ using SPM, which exemplify the indentations made. a) copper before the indentations, b) copper with the indentations matrix using a load of 500 μN, c) Cu-Al_2O_3+Ag: PDCMS before the indentations, displaying an Al_2O_3+Ag particle (lower left corner) and d) Cu- Al_2O_3+Ag: PDCMS showing the indentation matrix using a load of 500 μN.

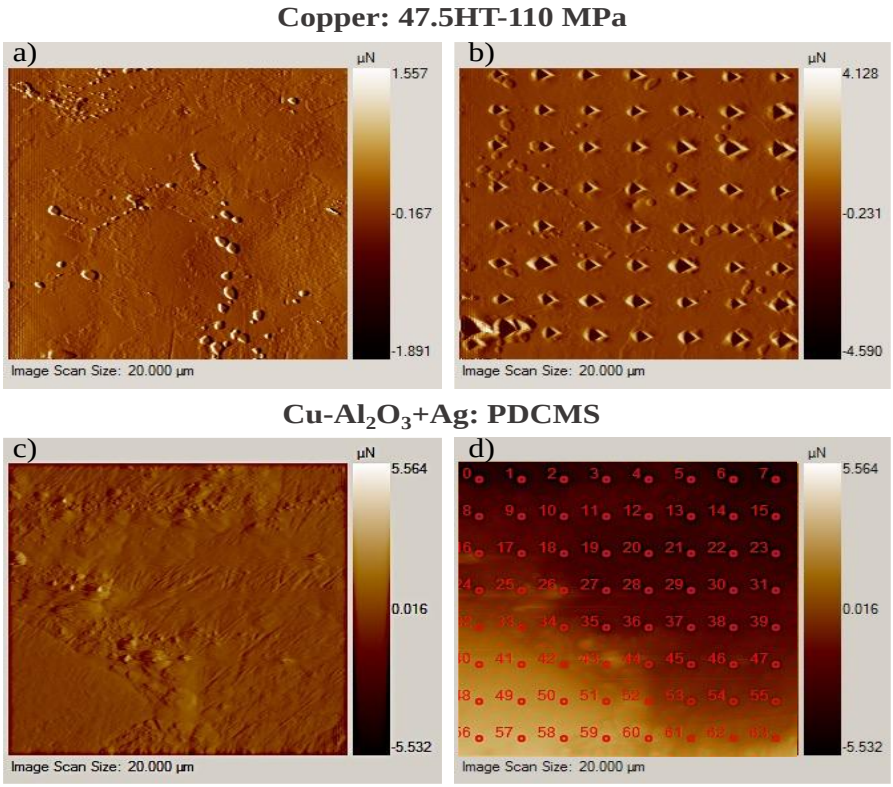

Table 13 - Hardness (H_H), reduced Young's modulus (E_r), index used to indicate the wear resistance (H_H/E_r) and index that indicates the plastic deformation resistance (H_H^3/E_r^2) of copper, Al_2O_3 with no interface modification and composite.

Samples	H_H (GPa)	E_r (GPa)	H_H/E_r (-)	H_H^3/E_r^2 (GPa)
Cu: 47.5HT-110 MPa	2.29 ± 0.27	125.78 ± 8.98	1.7×10^{-2}	5.9×10^{-4}
Cu-Al_2O_3	2.88 ± 1.00	130.88 ± 21.14	2.2×10^{-2}	1.4×10^{-3}
Al_2O_3	5.10 ± 0.99	155.61 ± 24.56	3.3×10^{-2}	5.5×10^{-3}
Cu-Al_2O_3+Ag: PDCMS	2.82 ± 4.44	161.68 ± 24.33	1.7×10^{-2}	8.5×10^{-4}
Al_2O_3+Ag	12.45 ±2.05	191.00± 18.26	6.5×10^{-2}	5.3×10^{-2}
Cu-Al_2O_3+Ag: Electroless	2.31 ± 0.62	90.13 ± 26.59	2.6×10^{-2}	4.2×10^{-2}
Al_2O_3+Ag	3.61 ± 0.71	85.56 ± 35.58	4.2×10^{-2}	1.5×10^{-4}

The observed shape of the curves implies that indented materials give an elastic-plastic response to the indentation force. It can be seen that the Cu-Al_2O_3+Ag: PDCMS composite has the highest elastic recovery, while the ductile copper matrix has the highest plastic work (lower elastic recovery). Cu-Al_2O_3+Ag: Electroless composite presents an elastic work similar to copper in the interface, which can be induced by defects such as micropores.

A reduction in indentation depth was also observed in composite Cu-Al_2O_3+Ag: PDCMS and Cu-Al_2O_3 under the applied indentation load. In particular, a lower depth and increased hardness are observed in PDCMS composite, reaching average hardness values of 12.45 GPa at the interface (Al_2O_3+Ag). This shows that the deposition method efficiently increases the resistance to plastic deformation. Consequently, an improvement in hardness and stiffness is expected in the sintered composite compared to copper due to the effective load transfer from the matrix to the reinforcement. These results confirm that the Al_2O_3 ceramic particles have a marked influence on the total mechanical properties of the sintered composites since these values of hardness and Young's modulus of the Al_2O_3 ceramic particles are notably higher than those of the metal matrix and change depending on the method of modifying the surfaces of these particles. It is expected that the higher hardness and modulus values are related to more excellent load support and resistance to plastic deformation phenomena, such as those associated with abrasive wear. Note that Al_2O_3+Ag has higher values of H_H/E and H^3/E_r^2 compared to Al_2O_3 and Al_2O_3+Ag: Electroless, suggesting that the method used to modify the surface of Al_2O_3 particles by deposition may reduce the mechanisms of plastic deformation and increase resistance to abrasive wear.

4.3 Tribological characterizations of copper at meso-scale

This chapter shows the COF response, material removal mechanisms, abrasive wear mechanisms, and specific frictional energy of copper abraded by diamond indenter.

4.3.1 Coefficient of friction (COF) - copper samples

Figure 76 shows the evolution of the friction coefficient (F_t/F_n) as a distance function for each sintered sample at normal loads ranging from 5 to 25 N. The sintered samples gave rise to a higher coefficient of friction as the normal load increased. The COF results presented variations in a range from 0.21 to 0.44. During the scratch test, the COF fluctuations are more significant as the normal load decreases. COF fluctuations along the scratch path can be attributed to surface roughness, dynamic slip test characteristics, adhesive strength and microstructure change (KUMAR; STAEDLER; JIANG, 2013). However, among the different scratch tests, fluctuations were observed related to the porosity along the scratch path due to the presence of a soft zone and increased friction force (purple arrows). On the contrary, when the indenter meets a grouping of pores, a tangential force drops (orange arrows).

Similar COF values for sintered copper have been reported in different investigations, where the copper contains graphite and is reinforced with WC particles (XIAO et al., 2013; ZHOU et al., 2015). Consequently, the effect of the pores is subject to normal and shear stresses, which results in a higher strain energy consumption and a higher variation in COF. Furthermore, during scratch tests, the material is pushed in front of the indenter and moves to the edges of the grooves. Therefore, the greater the load, the residual depth of the scratch increases, as well as the volume of material that moves laterally, which produces a greater tangential force, and therefore, an increase in the coefficient of friction.

Figure 76 – Overall COF during scratching with constant applied normal loads for each copper sample.

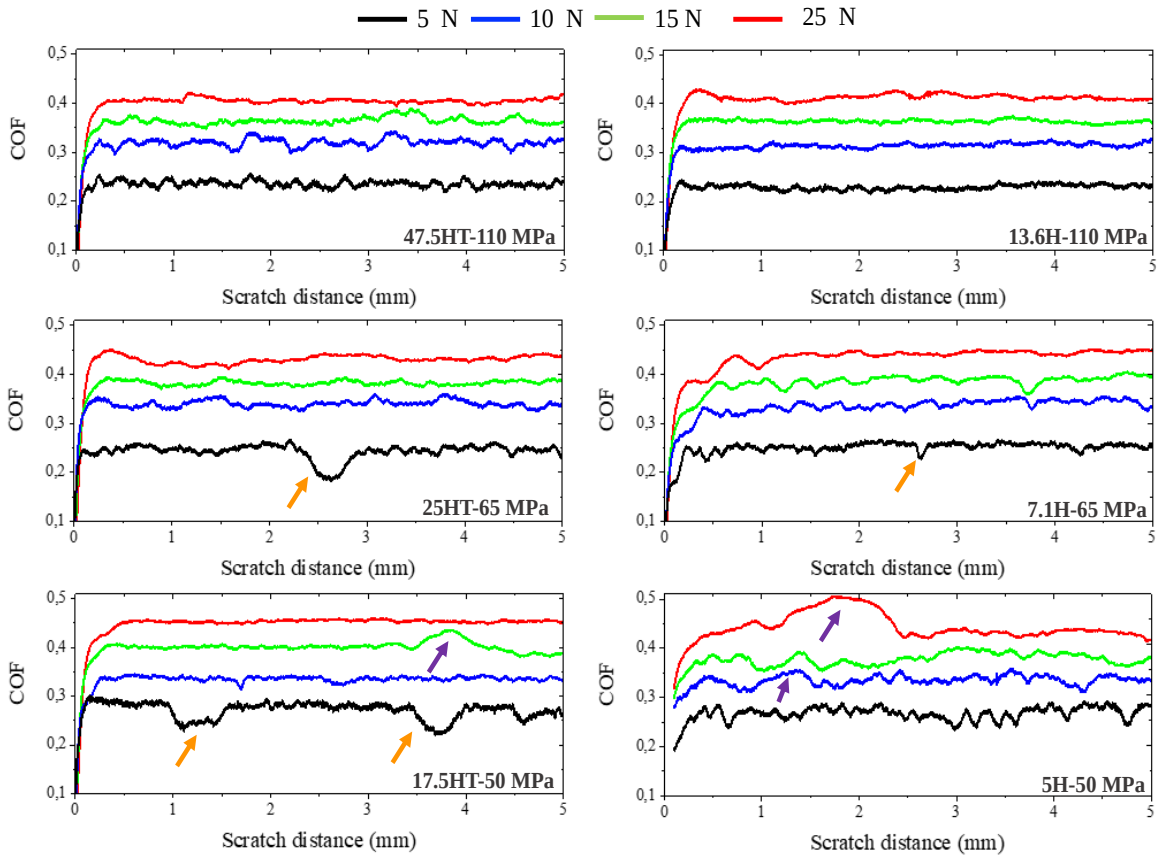

As summarized in Figure 77, the samples exhibit a general increase in average COF with increasing normal load. The decrease in the size and volume fraction of the pores and the decrease in the grain size are related to the slight reduction in the average COF exhibited by the samples sintered at pressures of 110 MPa. This decreasing COF trend exhibits data scatter due to material heterogeneity which affects the COF results at the scale. This result suggests that particular advantages are obtained in terms of the effect of different pressure routes, as observed in Figure 78, the differences in microstructures of the 47.5HT-110 MPa and 5H-50 MPa samples at the same constant normal load.

Figure 77 - COF as a function of normal load. a) 1º Route: Pressure rate during the holding time (HT) and b) 2º Route: Pressure rate during the heating (H).

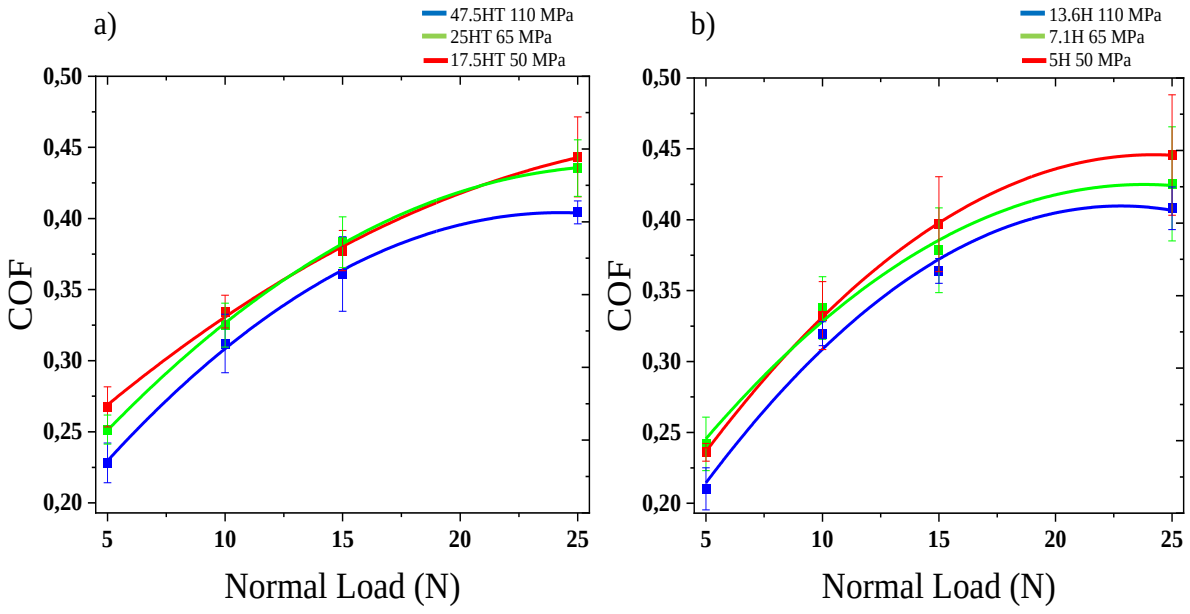

Figure 78 - SEM image of the differences in the microstructure (pores and grain size); a and c) for samples 47.5HT-110 MPa and 5H-50 MPa and b and d). Before and after scratching (10 N).

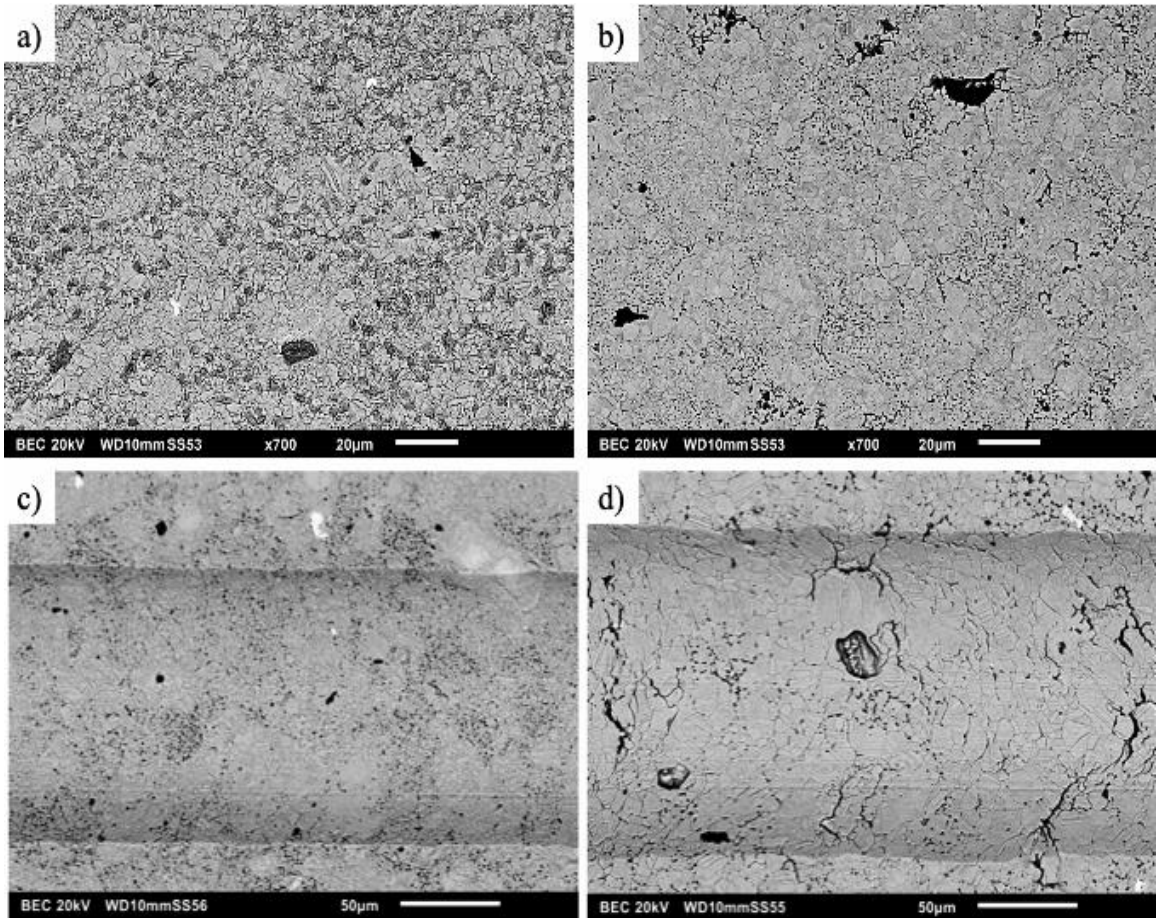

4.3.2 Residual penetration depth (h_r) and geometrical parameters of the scratch of copper samples

Figure 79 shows the topographies and 3D cross-sectional profiles of the wear surfaces obtained after scratch tests using a normal load of 5 N. The worn surface of the copper samples exhibited variations in the section profile cross-section of the worn surfaces due to the microstructural variations of the samples, in which the direction of plastic deformation and volume material displacement caused a difference in residual penetration depth (h_r), accumulation of material on the side of the wear track (A_1+A_2) and the groove width (W_r) for each sintered sample. The profiles of the wear surfaces are displaced material called pile-up, which is expected behavior because copper is a ductile material with low hardness (ZUM GAHR, 1987).

Figure 79 - 3D and 2D profiles of wear tracks obtained by laser interferometry. For copper samples scratched at a normal load of 5 N.

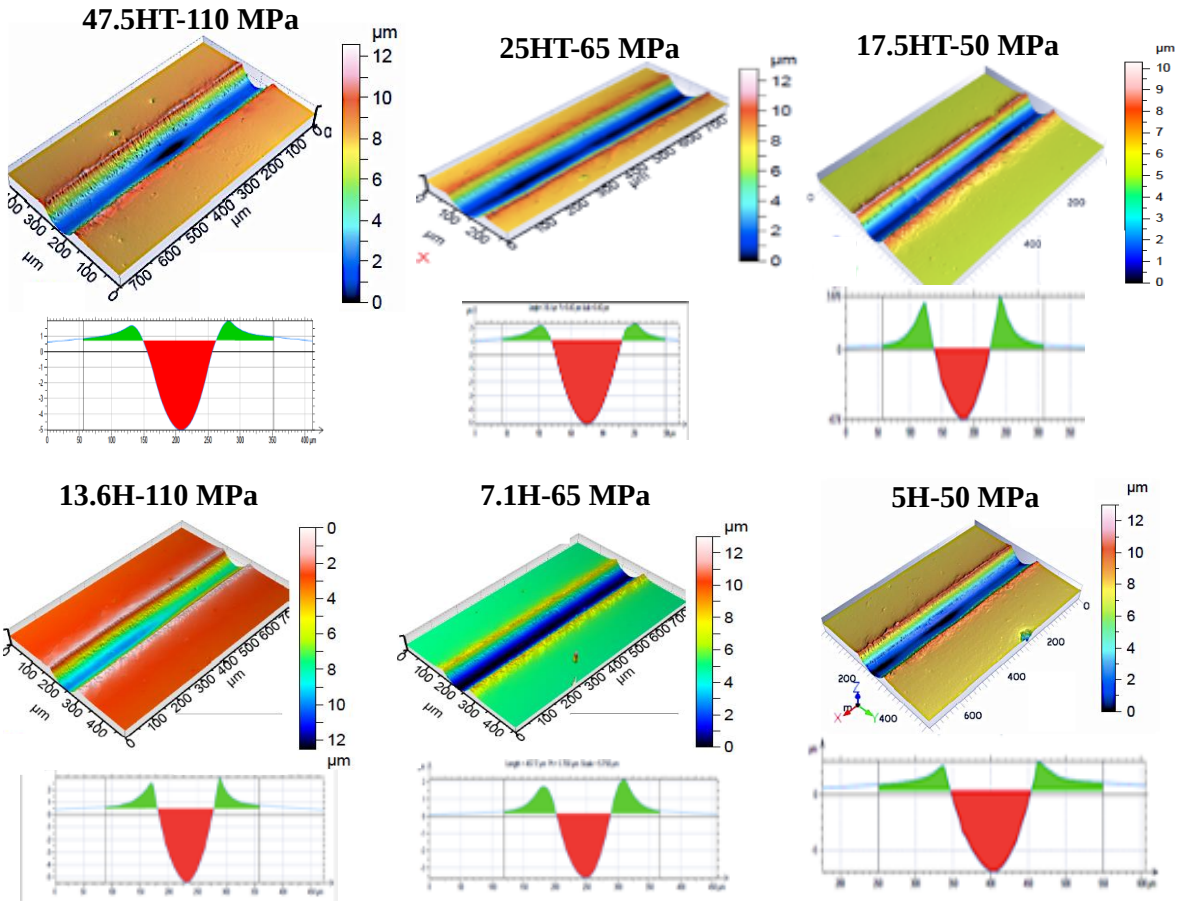

The result of the parameters measured through 3D profilometry of the samples scratched at 5N is presented in Table 14. From the action of the spherical tip (Rockwell-C), flatter pile-ups are expected compared to the angular indenter (Vickers) (FRANCO, 2015). However, if the 17.5HT-50 MPa sample is observed, narrower shoulders and greater height of the pile-up peaks are observed. In addition, sample 5H-50 MPa was a larger groove area, consequently increasing the COF and surface wear. These increases in the pile-up and groove area are related to high porosity, causing a decrease in mechanical resistance and hardness of these two samples sintered with pressures of 50 MPa. As the size and number of pores increase, they act as a damage factor that reduces the mechanical properties of sintered components. This property reduction is directly related to the decrease in wear resistance, that is, the tribological performance influenced by the morphology and volume fraction pores. In addition, the wear depends on other factors, such as the distribution of the pores in the sample and their connectivity, which were discussed and analyzed in the previous chapters on sintered copper.

Note that, for the sample sintered at 65 MPa, the area of material removed (A_v - (A_1+$A_{2)}$) is less than for the samples sintered at 50 MPa, and the h_r did not change concerning those two-sintering pressure. In other words, those that are more porous can favor the displacement of deformed material along the sides of the scratch more than the depth.

Table 14 - Parameters measured in the cross-section profiles of the scratch tested at 5 N.

Samples	Groove area A_v (μm^2)	Pile-up area A_1+A_2 (μm^2)	Area of material removed A_v-(A_1+A_2) (μm^2)	Width of scratch W_r (μm)	Residual penetration depth h_r (μm)
47.5HT-110 MPa	277.15	153.26	123.89	108	4.69
25HT-65 MPa	505.52	153.26	352.26	121	6.90
17.5HT-50 MPa	569.73	108.78	460.95	132	6.74
13.6H-110 MPa	269.15	162.47	106.68	121	5.97
7.1H-65 MPa	558.05	103.12	454.93	110.5	7.50
5H-50 MPa	597.67	198.33	399.34	155	8.06

The different routes of applying the pressure led to different tribological responses represented in the cross-section of the samples. In addition to studying these differences by 3D profilometry, the wear marks were analyzed by SEM, as shown in Figure 80. The material accumulation area on the sides of the scratch (pile-up) of the 13.6HT-110 MPa and 5H-50 MPa samples at normal loads of 5 and 25 N. In Figure 80a-b (5 N), it was possible to find differences in the formats of the pile-ups and a notable increase in deformed material for sample 5H-50 MPa, as confirmed by profilometry. Figure 80c-d (25 N) the severe plastic deformation and layers of deformed material with a more significant accumulation of material in Figure 80d (red circled), which are factors considered in the measured parameters (Table 14), which affect wear micro-mechanisms.

Figure 80 - SEM images of secondary electrons corresponding to the pile-up of samples (a and c) 13.6H-110 MPa and (b and d) 5H-50 MPa, with loads of 5 and 25 N.

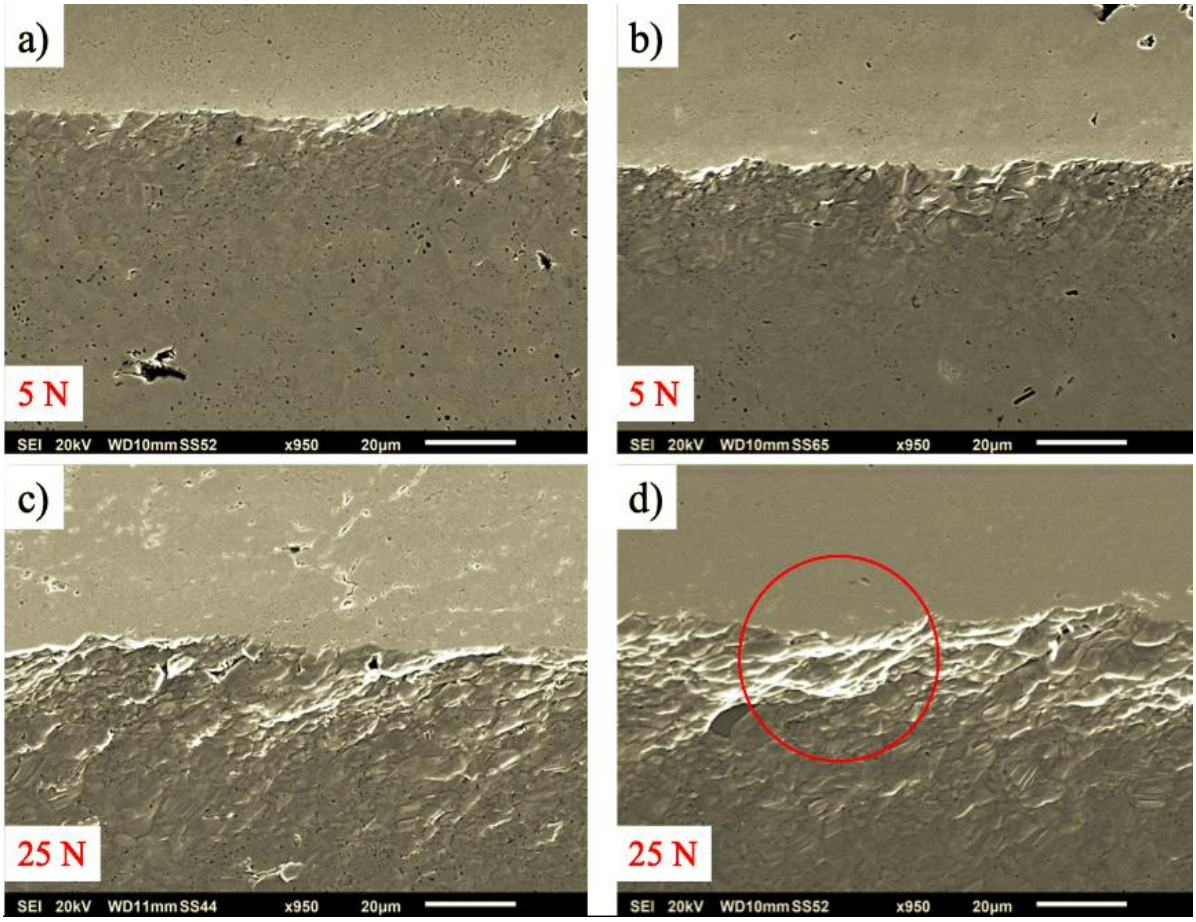

Figure 81 shows the residual penetration depth as a function of the scratch distance for the four normal loads. Residual penetration depth represents the depth reached in the center of the groove after scratch. As the load increases, minor fluctuations in residual penetration depths

are observed. However, for the same normal load, differences in residual penetration depths are observed, indicating that the surfaces (microstructure) of the samples are different at this scale level, which is consistent with the COF results. The residual penetration depth results show a first run-in period and a second steady-state period. During the running-in period, as soon as the tip penetrates the sample, the scratch transition is irregular and reaches a particular deviation in depth due to the change in the tip of movement (static to dynamic), in which a higher drop for more porous samples. Specifically, the 5H-50 MPa sample, at a normal load of 25 N, presented a more significant transition that reached almost 1/5 of the total distance of the scratch. According to XU et al., (2017), in the first stage of running, once the applied normal force becomes more significant, the COF increases while, at the same time, the rate of elastic recovery decreases continuously with increasing normal force. In addition, further accumulation of materials begins to occur at this stage. Therefore, the authors indicate that the tip requires more force to set it in motion in the horizontal direction due to the need to deform and displace the materials surrounding the tip.

After a while, the depth normalizes, and the surface reaches the steady state period. Among the four normal loads tested, in the normal load of 5 and 10 N, a significant difference is observed in the residual penetration depth, which is related to porosity along the scratch. The average values of the residual penetration depth with loads of 10 N were: 47.5HT-110 MPa (8.55±0.29 μm), 25HT-65 MPa (14.12±0.48 μm), 17.5HT-50 MPa (12.77±0.4 μm), 13.6H-110 MPa (11.49±0.5 μm), 7.1H-65 MPa (13.61±0.84 μm) and 5H-50 MPa (13.11±0.75 μm). The 47.5HT-110 MPa sample presented the lowest average penetration depth due to its microstructure characteristics of the surface, increased hardness, and less presence of pores. In addition, it influences lower ductility, as evidenced by the decreased deformation within the scratch (A_v).

Figure 81 - Residual penetration depth after scratching with under 4 normal loads: a) 5 N, b)10 N, c) 15 N and d) 25 N.

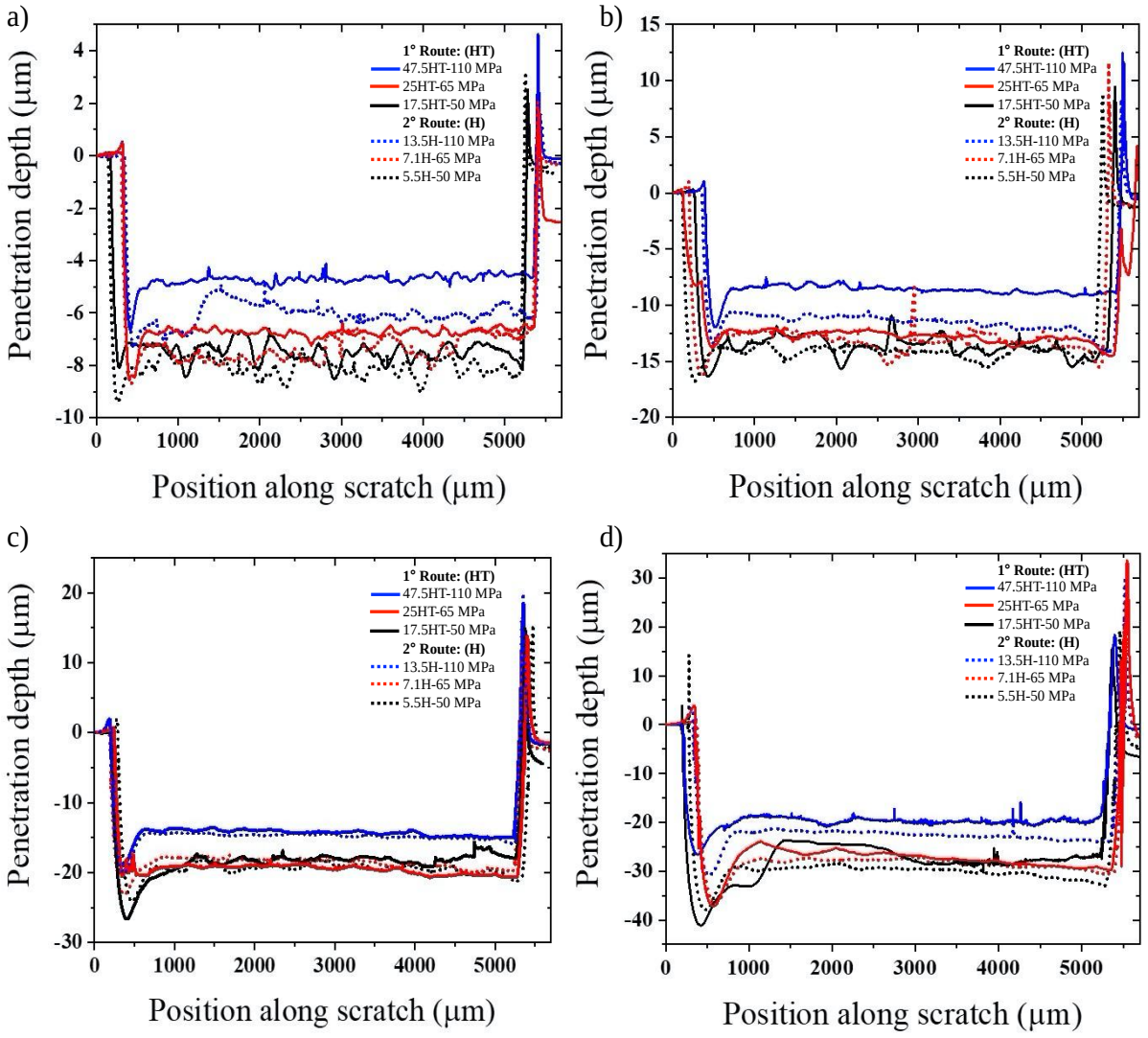

The analysis of Figure 82a-b represents the global friction coefficient against the attack angle, according to the route of applying the pressure (HT and H). The overall coefficient of friction increases with the attack angle. This result is comparable to those obtained for other alloys of steel and metals and developed in other works such as (GAHR, 1981; KHELLOUKI; RECH; ZAHOUANI, 2013; PENFORNIS; JOURANI; MAZERAN, 2021). According to these works, a slight attack angle favors ductile mechanisms and lower COFs that corroborate the ductile behavior found. However, it is essential to point out that the Rockwell-C indenter is a spherical contact shape. Thus, the attack angle increases progressively with normal load, which causes a transition between the deformation regimes and the active micro-mechanisms dependent on the penetration depth and gives rise to more severe mechanisms at higher loads. In addition, plastic deformation and displaced material flow are additional mechanisms of

attack angle increase, which may explain the increase in the COF in more severe wear mechanisms in porous samples since the deformation is higher.

Figure 82 - Coefficient of friction as a function of the attack angle (θ). a) 1° Route: (HT) and b) 2° Route: (H).

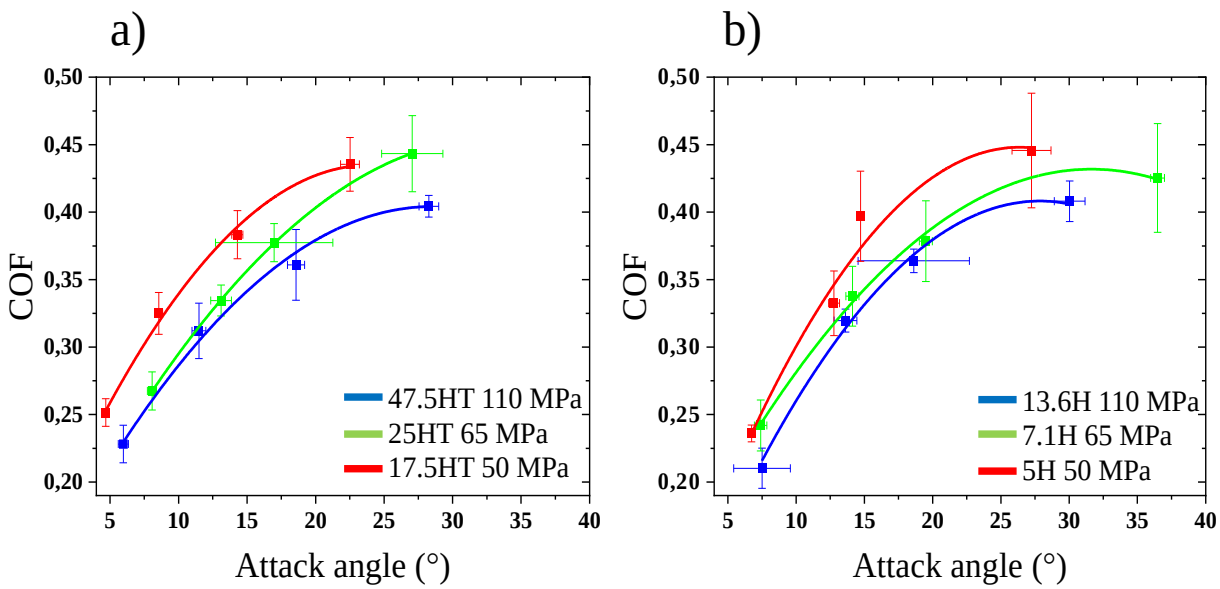

Based on the slip line theory of CHALLEN; OXLEY; DOYLE, (1983) and the analysis method presented by HOKKIRIGAWA; KATO, (1988). The authors allow evaluating the relationship between the coefficient of friction and the micro-mechanism of wear associated with the degree of penetration (D_p); see Figure 41b. As well as the attack angle, the degree of penetration is observed as the normal load increases, as shown in Figure 83. Figure 83a-b are compared under the same sintering pressure (for example, the sample 25HT-65 MPa and 7.1H - 65 MPa) and increases in the degree of penetration are observed in the sintered samples with the route of applying pressure during heating (H). This increase is attributed to the decrease in the hardness of these samples. For example, sample 25HT-65 MPa was a hardness of 81.25 ± 3.9 $HV_{0.050}$, and sample 7.1H-65 MPa was a hardness of 67.31 ± 5.72 $HV_{0.050}$. In the case of the attack angle, no variations were observed due to the effect of hardness. Similar behaviors were observed by MACHADO et al., (2017).

Figure 83 - Coefficient of friction (COF) as a function of the degree of penetration (D_p). a) 1° Route: (HT) and b) 2° Route: (H).

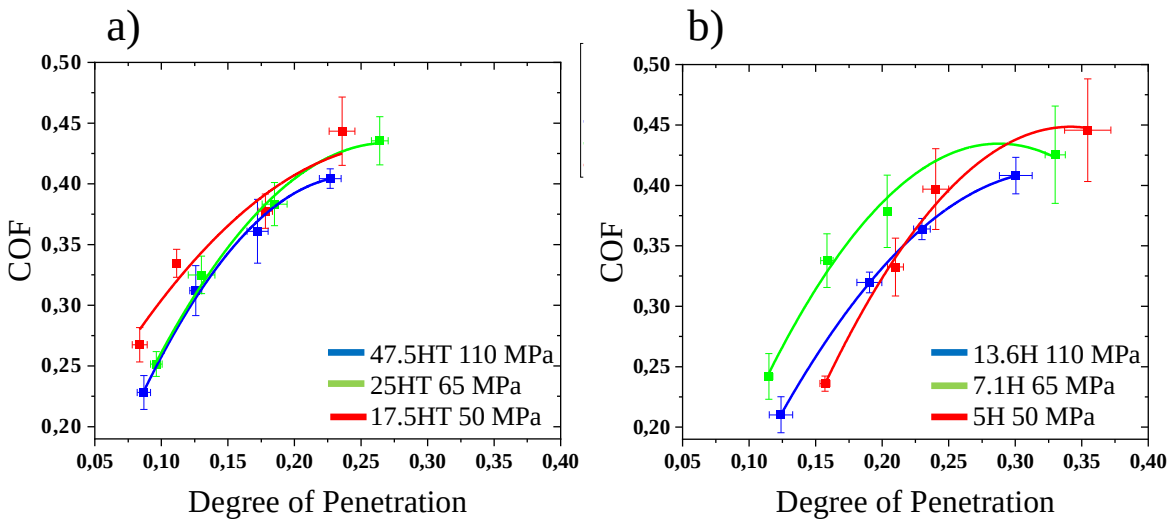

Based on the classical literature and actual (HOKKIRIGAWA; KATO, 1988; HOKKIRIGAWA; KATO; LI, 1988; MISHRA; DE ROOIJ; SCHIPPER, 2021), it can make possible to define the wear micro-mechanisms present in copper samples. The attack angle and degree of penetration results indicate several different wear mechanisms involved in scratching processes, and the dominant wear mechanism varies with scratch conditions. As seen in Figure 84, the first micro-mechanism under a 5 N load corresponds to the micro-ploughing as the dominant micro-mechanism. As normal loading increases, micro-cutting becomes more prevalent. However, normal loads of 10 and 15 N cause a transition micro-mechanism from plow to wedge formation. In the case of a normal load of 25 N, the sample surfaces exhibited a high plastic deformation with chip formation in which the dominant mechanism would be cutting.

Figure 84 - Overlapping results of wear modes. Wear mode diagram that relates between hardness and degree of penetration of copper samples (5 and 25 N). D_p*, corresponds to the transition from the ploughing mode to the wedge-forming mode; D_p**, corresponds to the transition from the wedge-forming mode to the cutting mode. Hardness is shown in HV units in this graph.

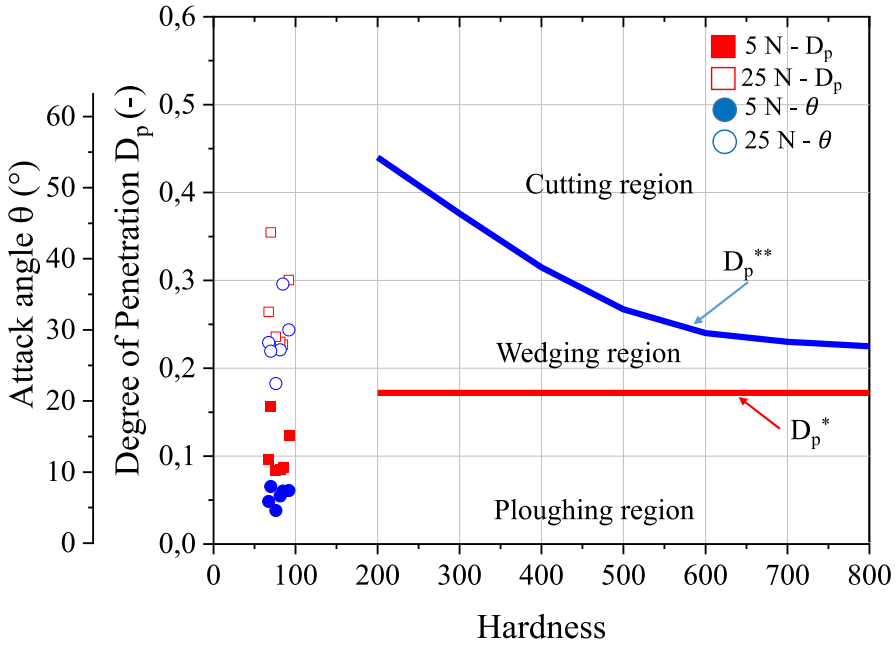

Source: Adapted from (HOKKIRIGAWA; KATO; LI, 1988).

4.3.3 Material removal and specific energies of copper samples

Cross-sectional profiles (groove and pile-up) determination are essential for calculating the F_{ab} - material removal factor. Figure 85 shows the 13.1H-110 MPa sample cross-section profile of the scratch obtained at different normal loads to observe the material displacement.

Figure 85 - SEM images and cross-sectional profiles of the worn surfaces of the 13.1H-110 MPa sample after scratch testing using an applied load of a) 5 N, b) 10 N, c) 15 N, and d) 25 N.

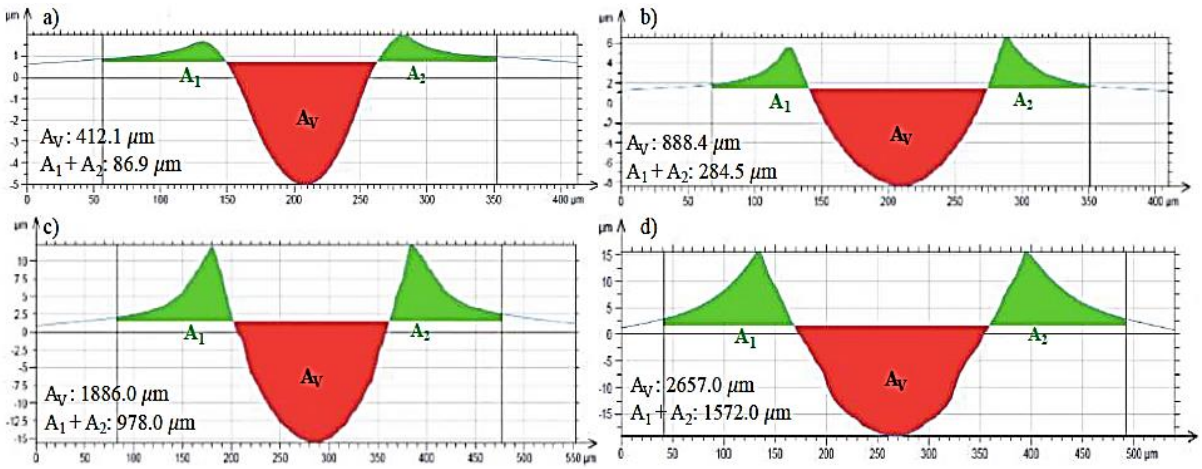

The plastic deformation of each sintered sample is presented by the F_{ab} factor in Figure 86. The F_{ab} tends to decrease as the normal load increases for samples. Significant differences in F_{ab} values are observed for each sample and loads of 5 and 10 N. The results of F_{ab} at 15 and 25 N tend to be the same, even considering the fluctuations in the values resulting from the heterogeneity of the sample surfaces. An increase in the F_{ab} factor would be expected as load increases, as presented in the literature (PÖHL; HARDES; THEISEN, 2019)(RAJARAMAN et al., 2021). However, these unusual decreasing results found herein are influenced by the presence of pores and grain size variation in contact with the indenter during scratching, causing consequences due to work hardening according to the microstructure of each sample with a clear preference for the formation and accumulation of material on the sides of the scratch.

To define the transitions of the abrasive micro-mechanism, based on the factor F_{ab}, the procedures for measuring the areas must be carefully considered due to the uncertainties in evaluating this value, which was analyzed and discussed by (FRANCO; SINATORA, 2017).

Figure 86 - Factor F_{ab} as a function of the load of the sintered samples. a) 1° Route: (HT) and b) 2° Route: (H).

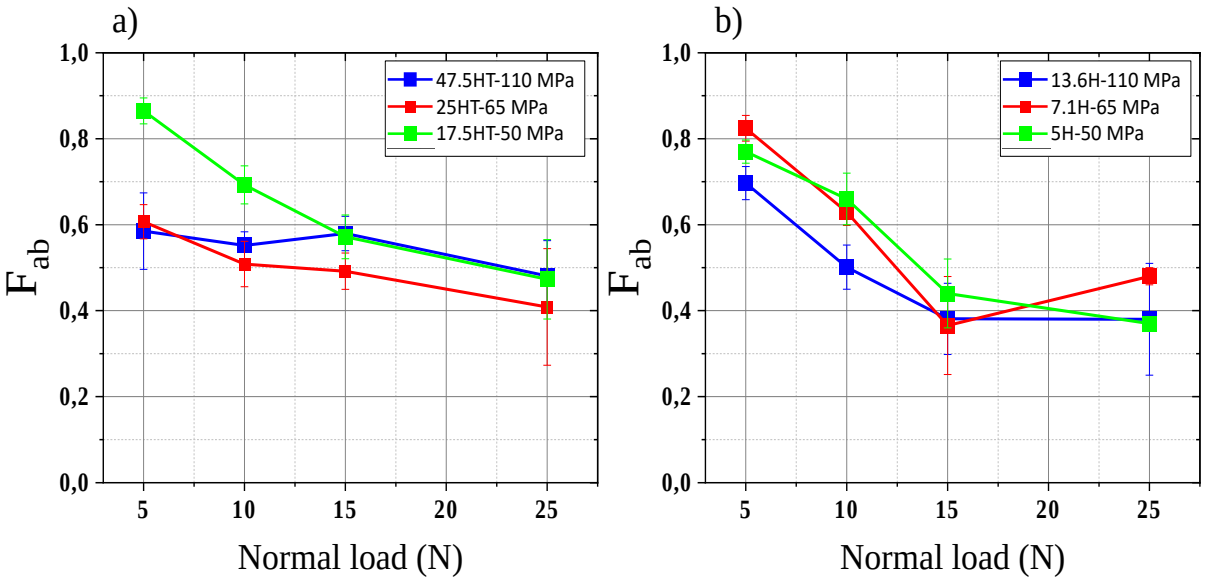

The specific energy is an important parameter to explain the effect of the abrasion on the microstructure of the sintered samples at the scales studied. The specific energy is the one dissipated (E) per displaced volume (W_v). The dissipated frictional energy depends on the tangential force and the slip distance, as explained in the literature review chapter (item 2.4.4 (relationship between specific energy and abrasive micro-mechanism). In the case of copper, a ductile material, the specific frictional energy is associated with the energy required for elastic recovery and plastic deformation due to shearing and yield. Figure 87 shows the global specific

energy of the sintered samples with the different normal loads. Specific energy is inversely proportional to material removal. The low difference observed between the results obtained in the dissipated energy can be explained by the influence of the high ductility and plastic deformation of the samples. However, the difference is found mainly at loads of 5 and 10 N. The heterogeneities and work hardening of the porous copper samples resulted in reduced material removal, occasioning the overall specific energy increases with the load, which was not expected. Nonetheless, the more porous samples exhibited a lower resistance to plastic deformation and pile-up formation (BARGE et al., 2008).

Figure 87 - Specific energy in scratch - Joule per volume, loads of 5, 10, 15 and 25 N: sintered samples. a) 1° Route: (HT) and b) 2° Route: (H).

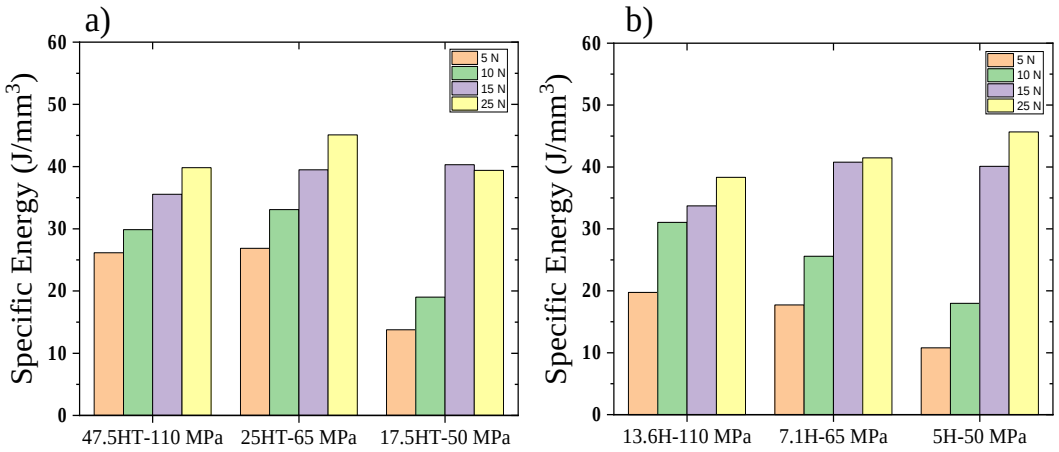

The variation of the global specific energy at loads of 15 and 25 N varies between 35-40 and 39-45 (J/mm^3), respectively, which do not exhibit a significant difference between the two loads (WANG; SUBHASH; CHANDRA, 2001).

4.3.4 Discussion of the effect of microstructure on wear micro-mechanisms in copper samples

Figure 88 shows the SEM images of the wear tracks of the copper samples (normal load of 5 N). In the grooves, the presence of pores is observed as the sintering pressure decreases (greater densification at pressures of 110 MPa). In the images, pores within the lines without pore closure are noted for the samples sintered at 110 and 65 MPa (yellow arrows). However, in the samples sintered at 50 MPa, it is possible to observe pore closure in the scratch direction (red circle) and the formation of microchips on the sides of the scratches (blue circle). This

phenomenon is related to greater plastic deformation and pile-up formation, which influences greater ductility represented in a greater residual penetration depth and a greater area of the groove (Figure 79 and Table 14).

Figure 88 - SEM image of the scratches of the sintered samples and tested with the normal load of 5 N.

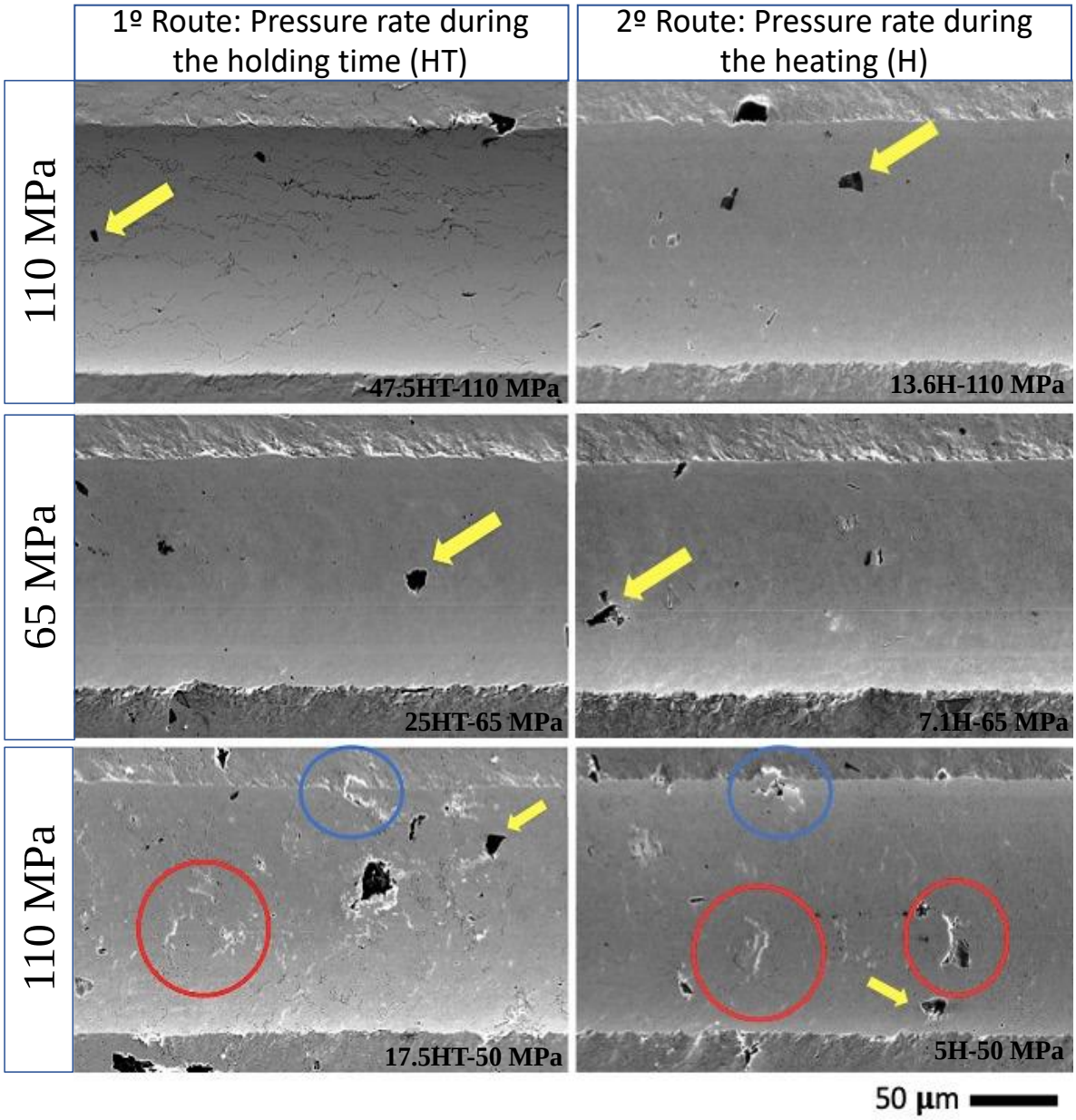

Figure 89 shows higher magnification SEM images of samples 17.5HT-50 MPa and 5H-50 MPa scratched with a normal load of 5 N. The predominant micro-mechanism wear is micro-ploughing (as discussed). However, in the samples sintered with pressures of 50 MPa, they exhibit pore closure within the wear track. Figure 89a shows that the pore closure tends to close perpendicular to the direction of tip sliding. On the contrary, Figure 89b shows that the

absence of pores generates only plastic deformation (dominant micro-ploughing). However, the pores that are located on the sides of the wear track cause the formation of chips, generating a local micro-mechanism transition from micro-ploughing to micro-cutting (Figure 89c-d). Therefore, the transition of the micro-mechanisms is not only due to the increase in the residual penetration depth, which results in increases in the attack angle (θ) until reaching the critical attack angle (θ_c) of the abrasive, but also the porosity of the sintered samples. Therefore, the pores located around and close to the scratch cause the three micro-mechanisms (micro-ploughing; wedge formation and micro-cutting) to be active during the scratch test.

Figure 89 - SEM images of the effect of the location of the pores in the wear track on the activation of the micro-mechanism. a-b) 17.5HT-50 MPa and c-d) 5H-50 MPa, with a normal load of 5 N.

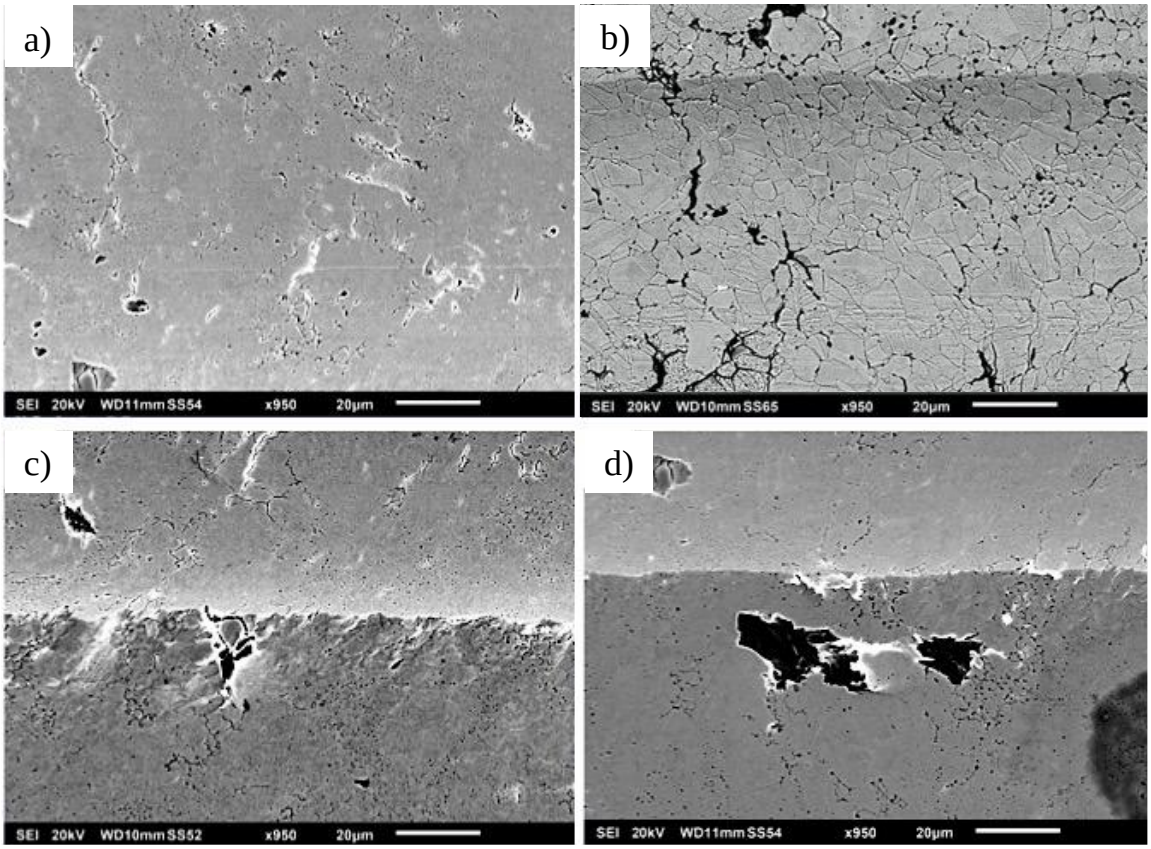

SEM images of the final section of the scratch of the 13.1H-110 MPa sample presented a more significant accumulation of material observed in front of the tip, with loads between 10-15 N. A transition of the abrasion micro-mechanisms is observed, the change from dominant micro-ploughing to wedge formation (HOKKIRIGAWA; KATO, 1988). SEM images of the final scratch section of the 13.1H-110 MPa sample are presented in Figure 90. The further material buildup is to be expected as the normal load increases. The transition micro-mechanisms of abrasion are observed, and the change of the micro-plow as the dominant micro-

mechanism (Figure 90a-b) to wedge-formation (Figure 90c-d) was between loads of 5 and 15 N. For at a 25 N load (Figure 90e-f), plastic deformation is increased by plowing, and material buildup at the end of the specimen wear track is increased, as is often reported as an essential wear mechanism for metallic materials (HONG et al., 2011).

Figure 90 - SEM images end of scratch at loads of a-b) 5 N, c-d) 15 N and e-f) 25 N.

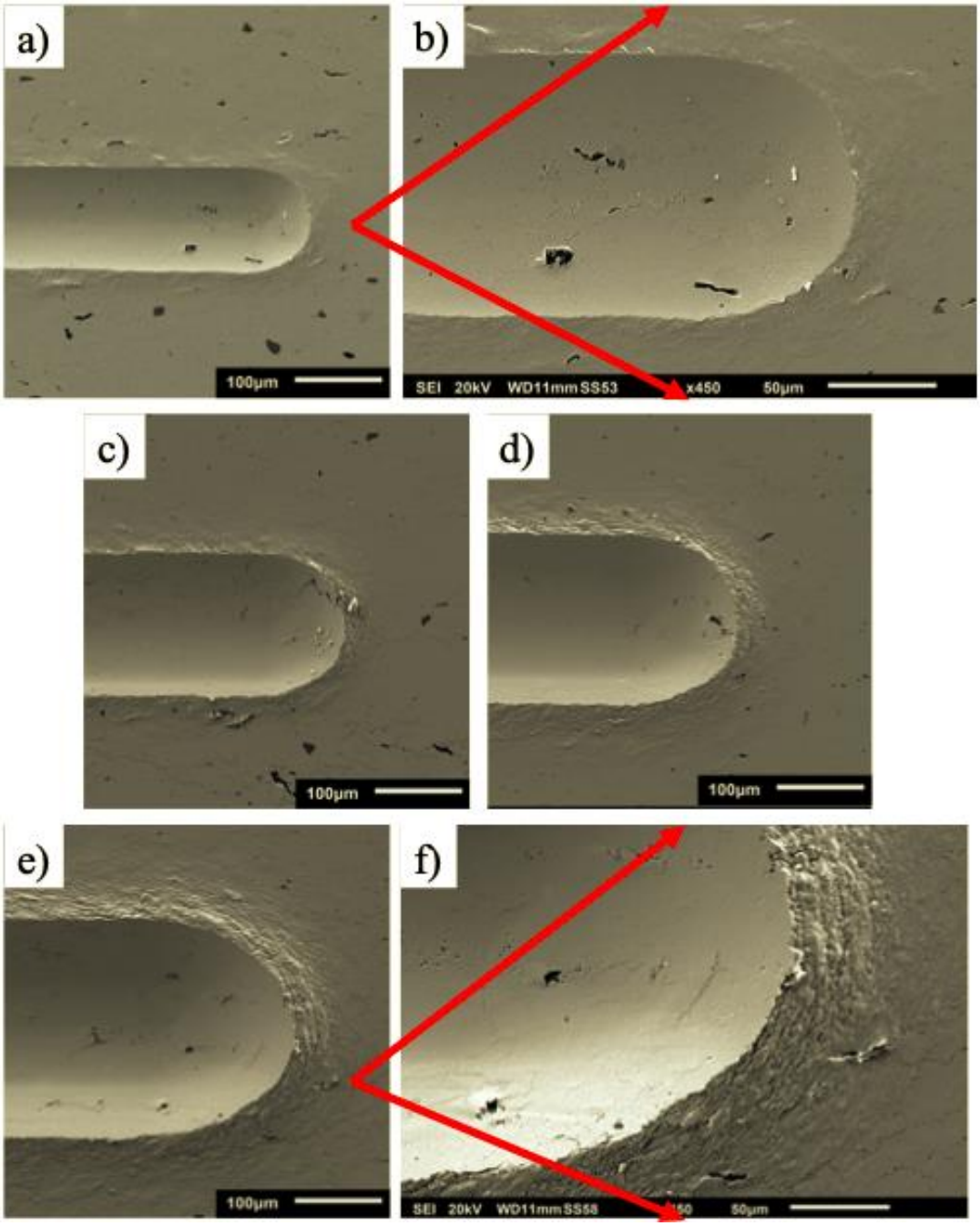

4.4 Tribological characterizations of copper at micro-scale

This chapter shows the COF response, abrasive wear mechanisms, material removal mechanisms, and specific frictional energy of copper and composites with different Cu-Al_2O_3 coating methods abraded with diamond in micro-scale.

4.4.1 Coefficient of friction (COF)

Figure 91 shows the mean values of the COF (F_n/F_t) as a function of the applied normal load for each sintered copper sample. The spherical cone tip (abrasive), which scratches the surface of copper samples, causes elastic-plastic deformation, which produces a considerable increase in deformation as the applied normal load increases. The increase in sintering pressure from 50 to 110 MPa caused changes in the copper microstructure that can be recognized by the reduction in the global friction coefficient of the 47.4HT-110 MPa sample compared to the 5H-50 MPa sample. This difference (mean values) was 56%, 33%, and 16% for loads of 5, 20, and 50 mN, respectively. However, at normal loads of 50 mN no difference is observed considering the error bars.

Figure 91 - Overall coefficient of friction (COF) as a function of the normal load applied in the sintered samples.

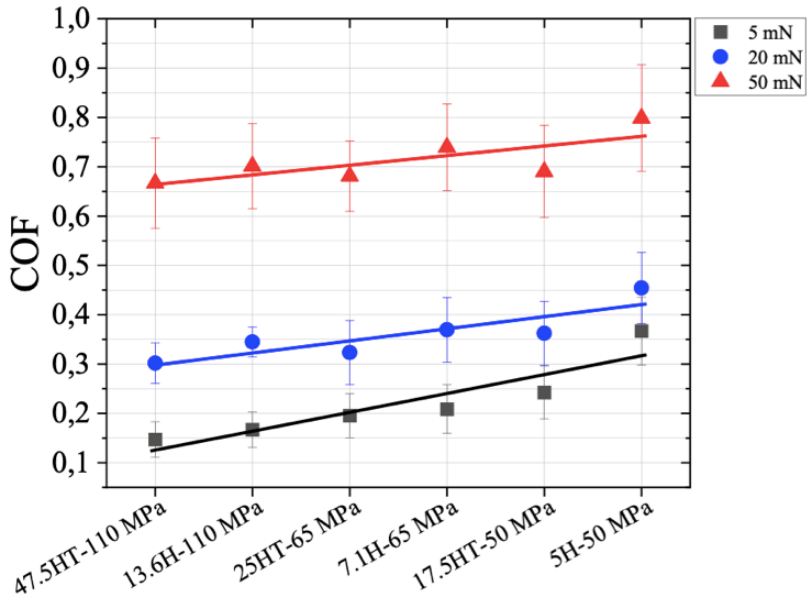

A slightly increasing trend of the overall COF with decreasing sintering pressure is observed for the different loads, although for 50 mN, the data scatter becomes high. These deviations are probably due to the microstructural heterogeneity (pores and grain boundaries)

of the copper samples at this test level (micro-scale) verified by the micro-scratch test (Figure 92a). Another possible and complementary explanation could be the transition of the dominant abrasive micro-mechanisms (Figure 92b), which will be discussed later, considering the influence of the normal load.

Figure 92 - COF as a function of scratch length for the case: a) 5H-50 MPa - 5 mN and b) 7.1H-65 MPa – 20 mN.

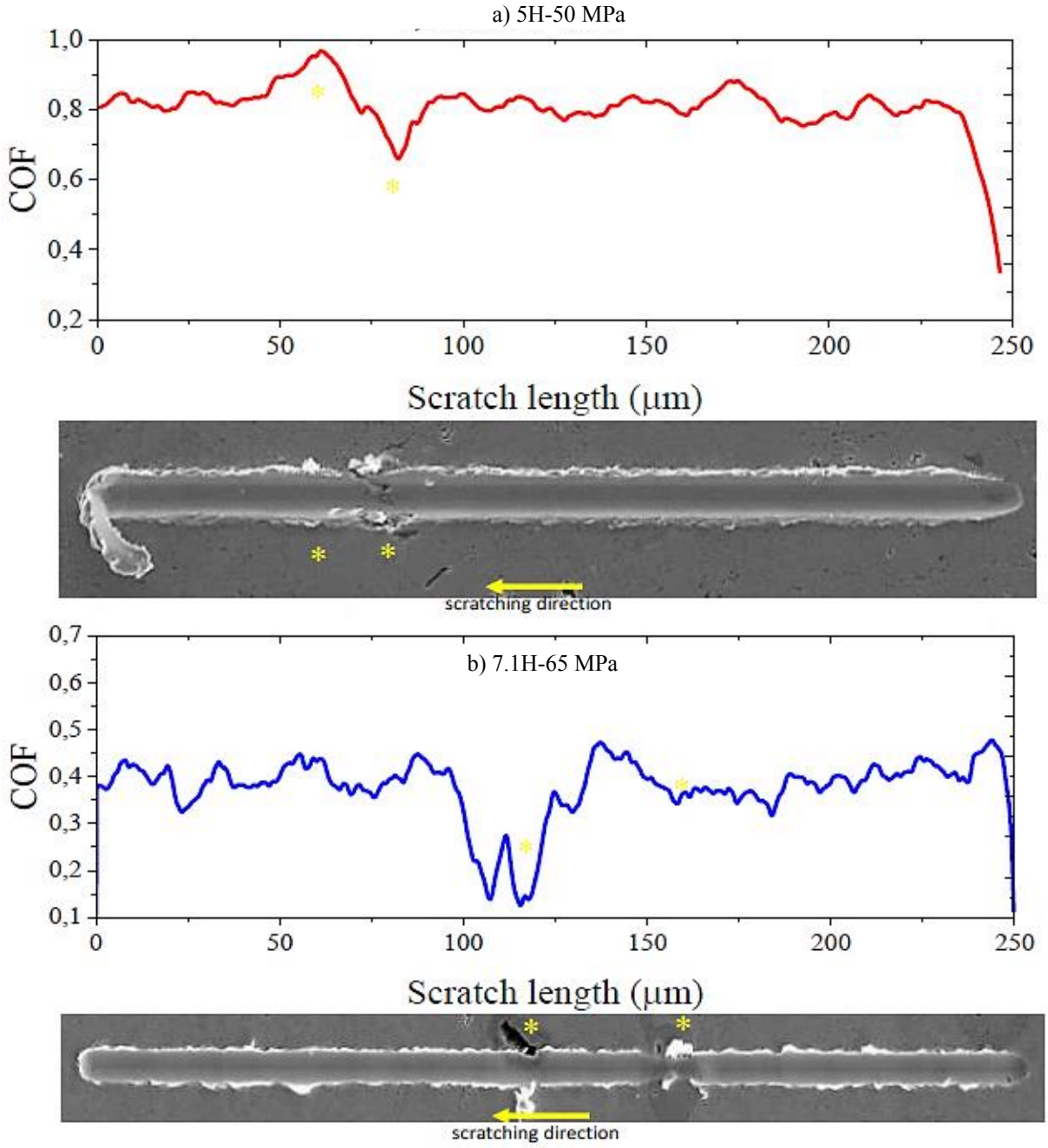

ZHANG et al., (2020) analyzed evaluated scratch variables such as normal load, lateral load, coefficient of friction, and penetration depth in copper, using a hemispherical tip

(Rockwell-C). The authors confirmed that the increased coefficient of friction is caused by increased ploughing and adhesion effects. The coefficient of friction is obtained from two components can be written as:

$$\mu = \mu_a + \mu_p \quad (31)$$

Where μ_a is the friction coefficient of the adhesion component, and μ_p is the friction coefficient of the ploughing component.

The adhesion component increases with increasing penetration depth. It approaches a constant value under large penetration depths, indicating that the role of the adhesion part in friction is more significant than that of the plow part, especially with little penetration depth. The effects of adhesion-plowing and micro-mechanisms will be more pronounced when using a spherical cone tip with a tip radius of 5 μm and apex angle of 60° (a sharper tip).

COF fluctuations at a constant normal load applied during the sliding are likely a result of pores and grain boundaries. Moreover, Figure 93 shows the results of the COF that was monitored during all scratch tests (in-situ). The different routes of pressure application caused changes in the local friction coefficient. Therefore, the COF fluctuation varies depending on each sintered sample. For example, for normal loads of 5 and 20 mN, samples sintered at 50MPa (17.5HT-50 MPa and 5H-50 MPa) exhibit more local COF fluctuations. In addition, depending on the position and morphology of the pore, during scratching, higher amplitudes are produced (orange inset) when the tip (abrasive) is positioned to enter and subsequently exit the pore (orange arrow).

Figure 93 - Evolution of the local COF versus the sliding distance for different normal loads at the micro-scale.

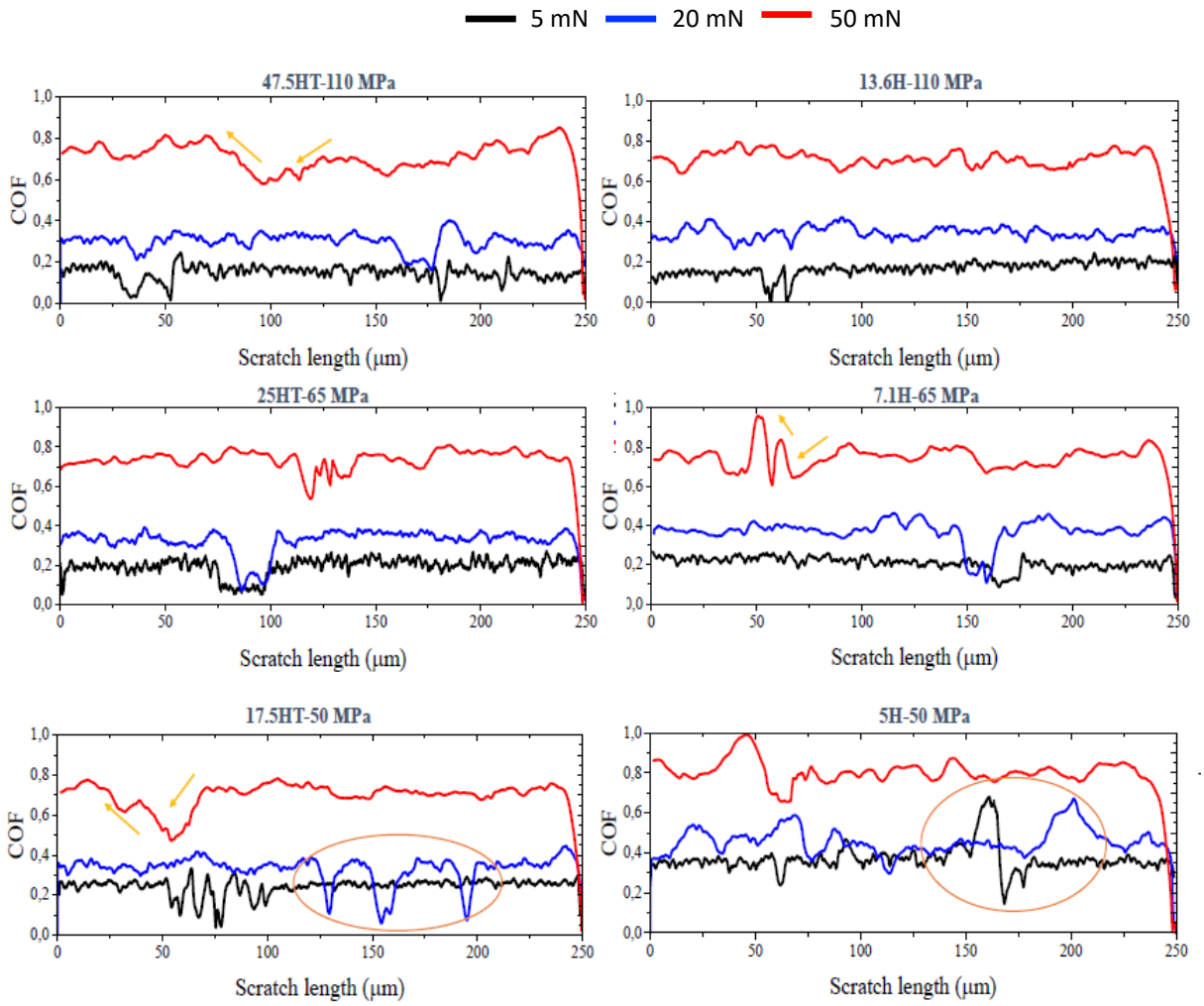

4.4.2 Penetration depth (h_p)

Figure 94 shows the average penetration depth of the sintered samples. Penetration depth (h_p) increases with increasing normal load (F_n) for all samples. In general, the difference in average (global) penetration depth between the samples was insignificant for the three normal loads when analyzing the standard deviation and trend lines across. Furthermore, the depth of penetration (h_p), which represents the amount of total deformation during scratching, as well as the residual penetration depth (h_r), which represents the amount of plastic deformation minus the depth of elastic recovery (h_e), is proportional to the normal applied load. Therefore, the relationship between the residual penetration depth and the penetration depth can be considered constant, varying between h_r/h_p ~0.65, independent of F_n (XIAO et al., 2013; ZHANG et al., 2020).

Figure 94 - Average penetration depth values of as a function of normal load for sintered samples.

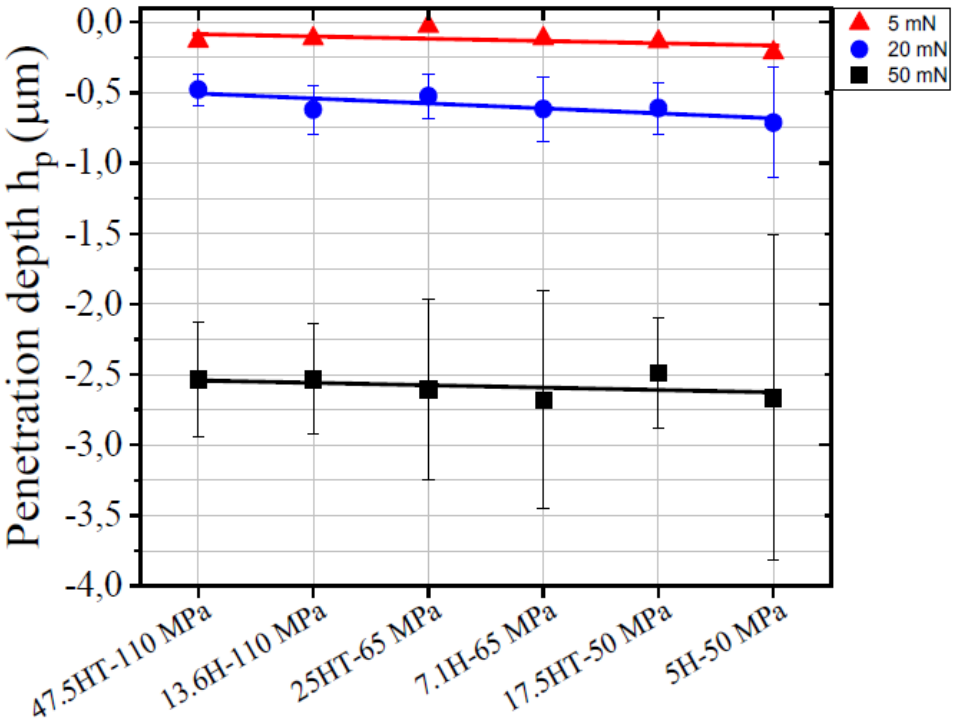

However, suppose the penetration depth curves are analyzed locally, as shown in Figure 94. In that case, local changes in the penetration depth are observed, which are attributed to the surface heterogeneity of the samples, which are related to the depth of penetration tip slip (abrasive).

Figure 95 - COF fluctuations depending on the length of the scratch for the case: 17.5HT-65 MPa - 5 mN.

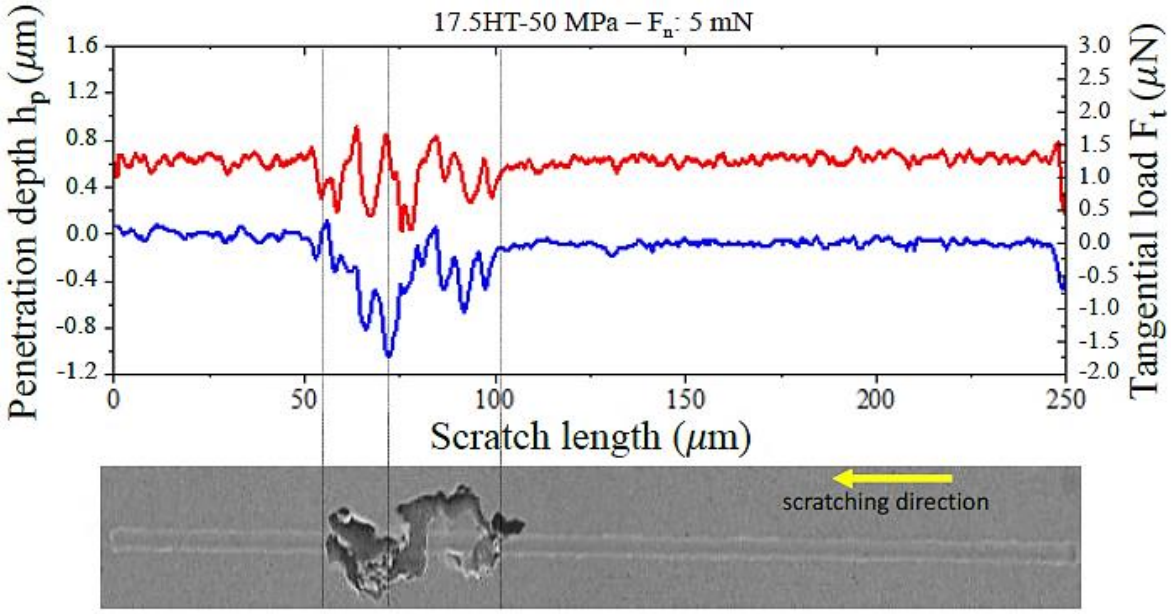

Figure 96 presents the penetration depth along the scratch length for all samples and normal loads. Analogous to the COF results, the average penetration depth for a given normal load increases with decreasing sintering pressure. The penetration depth for 5 and 20 mN are relatively in the same range; on the other hand, at higher penetration depths (50 mN), there is non-direct increase in the depth. Another important aspect is the active micro-mechanisms, which are sensitive to the normal applied load and influenced by the microstructure. Moreover, hardness is primarily related to grain size rather than pore size. Based on the hardness results of the samples, it is expected that the higher the hardness, the shallower the penetration depth. This relationship could have a local effect on fluctuations in penetration depth and wear. For comparison, Figure 97 shows different FEGSEM images of the regions that were indicated in Figure 96 (green arrows); this observation suggests that from the presence of pores or oxide, the sample sintered at 110 MPa (47.5HT-110 MPa) exhibited less chip formation (Figure 96) compared to samples sintered at 65 and 50 MPa (7.1H-65 MPa and 5H-50 MPa), for the same normal load (50 mN).

Figure 96 - Evolution of the penetration depth versus the sliding distance of samples, with the 4 normal loads.

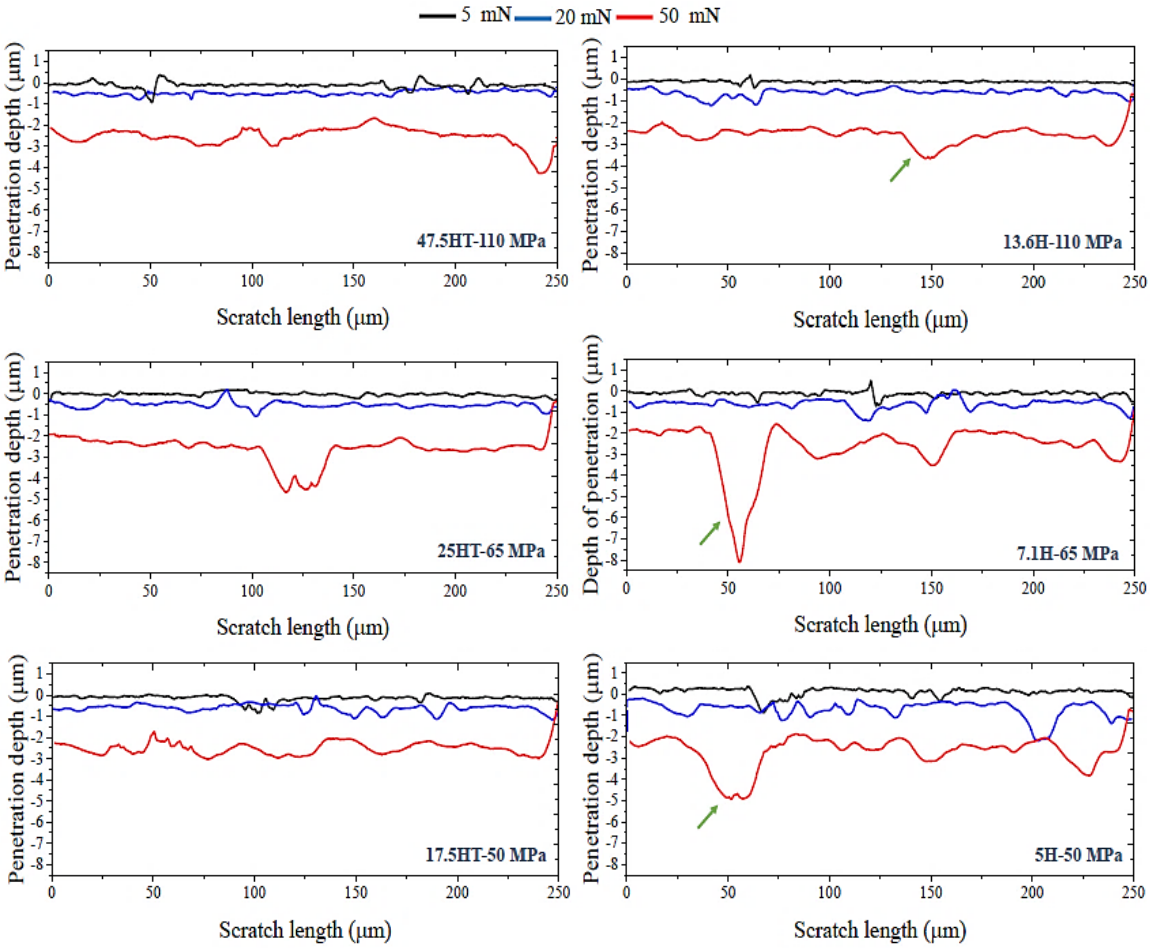

Figure 97 - FEGSEM images of the scratch highlighting the wear micro-mechanisms after testing at 50 mN normal load.

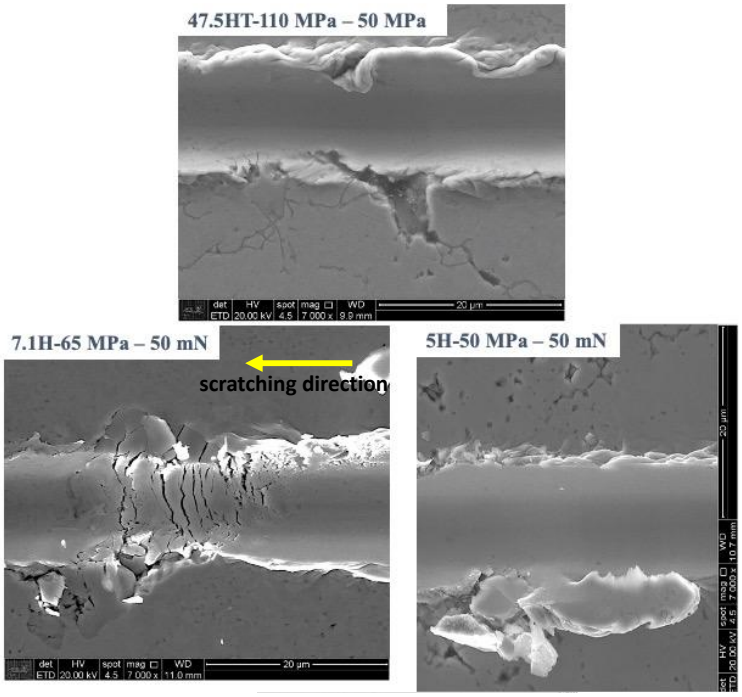

4.4.3 Geometric parameters (D_p and θ) and comparison with the literature

The work on sliding scratching was conducted by MULHEARN; SAMUELS, (1962) on the scratching of pure metals with pyramidal tips. It was established that the attack angle is important to determine if the material is plowed or cut. In a subsequent study, HOKKIRIGAWA; KATO, (1988) adapted the expressions for the coefficient of friction and the critical angle of attack (θ_c) for the transition in wear mechanisms. In addition, the authors mapped the abrasive wear modes into "ploughing mode, wedge-forming mode, and cutting mode" on a wear-mode diagram as a function of the degree of asperity penetration (D_p) and the coefficient of friction (COF). Regarding the abrasive micro-mechanisms in the copper samples, the results of the COF, θ, and D_p are presented in Table 15.

Figure 98 shows the results of the COF based on the D_p in graphics adapted from (HOKKIRIGAWA; KATO, 1988) (Figure 98a and c) and COF as a function of attack angle (Figure 98b and d); with these results, allows grouping into 3 categories according to the characterizations geometric parameters, which are:

- 5 mN: micro-ploughing as the dominant micro-mechanism (plastic deformation) and wedge formation for the 5H-50 MPa sample. The attack angle is less than a critical value ($\theta < \theta_c$), the tip (abrasive) plows through the material, and no chips are formed.
- 20 mN: less severe micro-cut. However, the 47.5HT-110 MPa sample is in a micro-mechanism transition. ($\theta \sim \theta_c$).
- 50 mN: more severe micro-cut, a slight difference is observed between the samples. The attack angle is greater than the critical value ($\theta > \theta_c$), chip formation and growth and wear become significant.

Table 15 - Average results of the a θ, D_p and COF as a function of the normal load applied to the different samples evaluated.

Samples	Normal Load (mN)	Attack Angle (°)	D_p	COF
1° Route: Pressure rate during holding time				
47.5HT-110 MPa	5	10±2	0.11±0.02	0.15±0.02
	20	25±3	0.22±0.03	0.30±0.03
	50	56±4	0.58±0.07	0.67±0.09
25HT-65 MPa	5	9±4	0.07±0.03	0.20±0.04
	20	26±4	0.23±0.04	0.32±0.07
	50	56±4	0.59±0.09	0.68±0.07
17.5HT-50 MPa	5	12±5	0.10±0.05	0.24±0.05
	20	28±3	0.25±0.04	0.36±0.07
	50	58±2	0.57±0.06	0.69±0.09
2° Route: Pressure rate during heating				
13.5H-110 MPa	5	11±2	0.10±0.01	0.17±0.04
	20	28±3	0.25±0.03	0.34±0.03
	50	56±4	0.58±0,06	0.70±0.09
7.1H-65 MPa	5	11±4	0.10±0.04	0.21±0.05
	20	28±5	0.25±0.05	0.37±0.07
	50	57±3	0.61±0.11	0.74±0.09
5.5H-50 MPa	5	15±4	0.12±0.02	0.37±0.07
	20	30±7	0.26±0.08	0.45±0.07
	50	59±1	0.60±0.16	0.80±0.11

Figure 98 - a and c) Results overlaid on HOKKIRIGAWA; KATO, (1988) abrasive wear modes map: COF as a function of the D_p for the samples studied (P: Ploughing mode, W: Wedge forming mode and C: Cutting mode) and b and d) COF as a function of θ for studied samples.

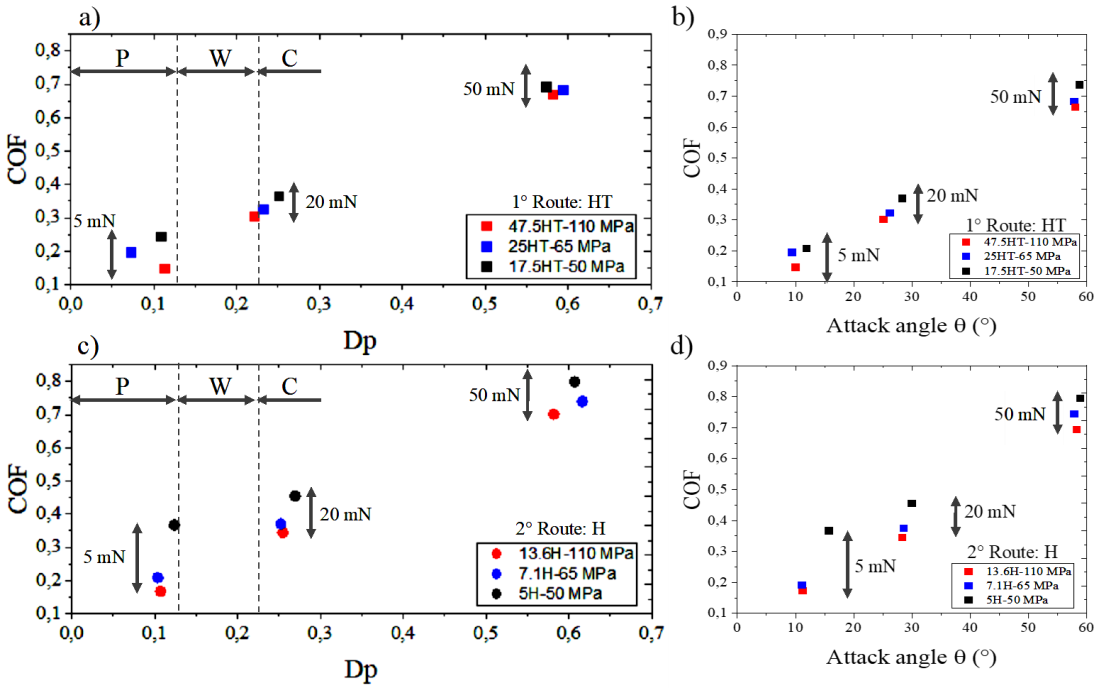

The considerations mentioned above should be evaluated and validated through post-scratching microstructural characterization. In addition, the results presented agree with (SERIACOPI, 2018; MACHADO et al., 2017; FRANCO, 2015), indicating that the critical attack angle of is around 30°. Below this angle, dominant micro-ploughing occurs; above this angle, it can increase up to 60° (the angle of the cone vertex). However, the local results indicate changes in the angle of attack while sliding the tip. As an example, Figure 99 presents the variations of the attack angle along the scratch due to the presence of pores (blue arrows).

Figure 99 - Results of the local attack angle during scratching, applying a normal load of 5 mN.

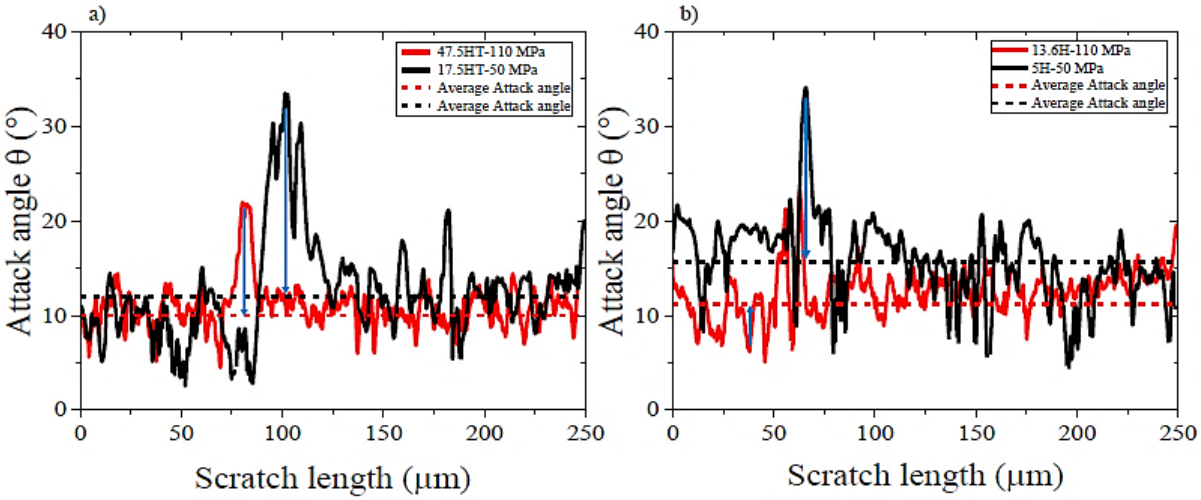

4.4.4 Material removal and specific energy

The material removal process in the scratch test can be considered as the result of the interaction effects between the conical indenter and the sintered materials. The abrasive micro-mechanisms estimated based on the literature described above and comparing them with the results of the angle of attack and depth of penetration of the sintered samples, the following approaches were used: i) pile-up volume subtracted from the total volume removed to the dominant micro-ploughing (5 mN); ploughing occurs with both elastic and plastic deformation, the material tends to accumulate in front of the conical penetrator and on the sides (pile-up), without loss of material and ii) the total volume removed for the transition and the dominant micro-cutting (20 and 50 mN); chip formation occurs and material is removed. The results of the pile-up volume and the intermediate parameters for its calculation are shown in Table 16.

Table 16 - Pile-up calculated using penetration depth data of 5 mN and using an analytical model from the literature SERIACOPI, (2018); NIKAS, (2006).

Samples	Penetration Depth (μm)	Pile-up height (μm)	Volume of spherical cap (μm^3)	Radius of the ECM hydrostatic core (μm)	Outer radius of the ECM plastic zone (μm)	Pile-up Volume (μm^3)
47.5HT-110 MPa	0.12±0.16	0.008±0.01	2.45±1.92	3.14±0.02	12.68±0,10	14.19±0.32
25HT-65 MPa	0.12±0.05	0.006±0.002	1.83±0.71	3.15±0.01	12.87±0.03	14.28±0.11
17.5HT-50 MPa	0.20±0.18	0.003±0.003	0.92±0.84	3.56±0.01	13.14±0.03	14.25±0.11
13.5H-110 MPa	0.11±0.12	0.006±0.005	1.91±1.63	3.15±0.01	13.84±0.08	14.10±0.25
7.1H-65 MPa	0.14±0.14	0.008±0,008	2.32±2.34	3.14±0.02	13.82±0.13	14.01±0.39
5.5H-50 MPa	0.22±0.19	0.010±0.006	3.12±1.74	3.14±0.02	13.36±0.10	18.55±0.65

4.4.5 Dominant micro-ploughing

For the micro-ploughing (5 mN), the results of the volume removed and the specific energy for each sample are shown in Figure 100. The results showed a significant influence on the fluctuations due to the presence of pores and the microstructural features of samples. The presence of grain boundaries (differences in grain size) acted as an effective barrier, changing the response materials as the tip (abrasive) slid. An inflection in the curve was identified in the grain boundary region. This result partially agrees with the finding reported by SASAKI et al. (2006). This author showed the effect of microstructural characteristics (for heterogeneous materials) on wear resistance for low severity conditions, that is, a small abrasive size (5 μm radius) and low loads (5 and 20 mN). Specific energy (S_e) in pore regions causes specific energy drops.

Since lower lateral forces (F_t) are required, and theoretically, more material is removed due to the local increase in penetration depth. The energy then increases sharply or gradually after the abrasive has passed through the pore due to the material resistance against the abrasive particle or the resistance of the pore walls, respectively. Really, nor does the specific energy decrease because there is no matter in the pore. There was no removal of material. That is, the sample's surface and the walls of the pore (depending on the morphology) function as a barrier. Therefore, the specific energy necessary for the abrasive to overcome a pore can be obtained indirectly. On the other hand, the variations for both the specific energy and the volume removed from the samples exhibit changes that seem to be substantially influenced by the grain boundaries (variation of grain sizes).

To conclude, the COF for the samples sintered at 110 MPa are showed in Figure 100 with less variations because of higher densities and, thus, lower presence of the heterogeneities in these cases.

Figure 100 - Tribological responses of the scratch tests (volume removed and specific energy) for the copper samples. In this condition, the test was performed with a constant normal load of 5 mN. As a result, the dominant abrasive micro-mechanism was micro-ploughing. Also, the length of the scratch shown in the micrograph is consistent with the scales on the graph.

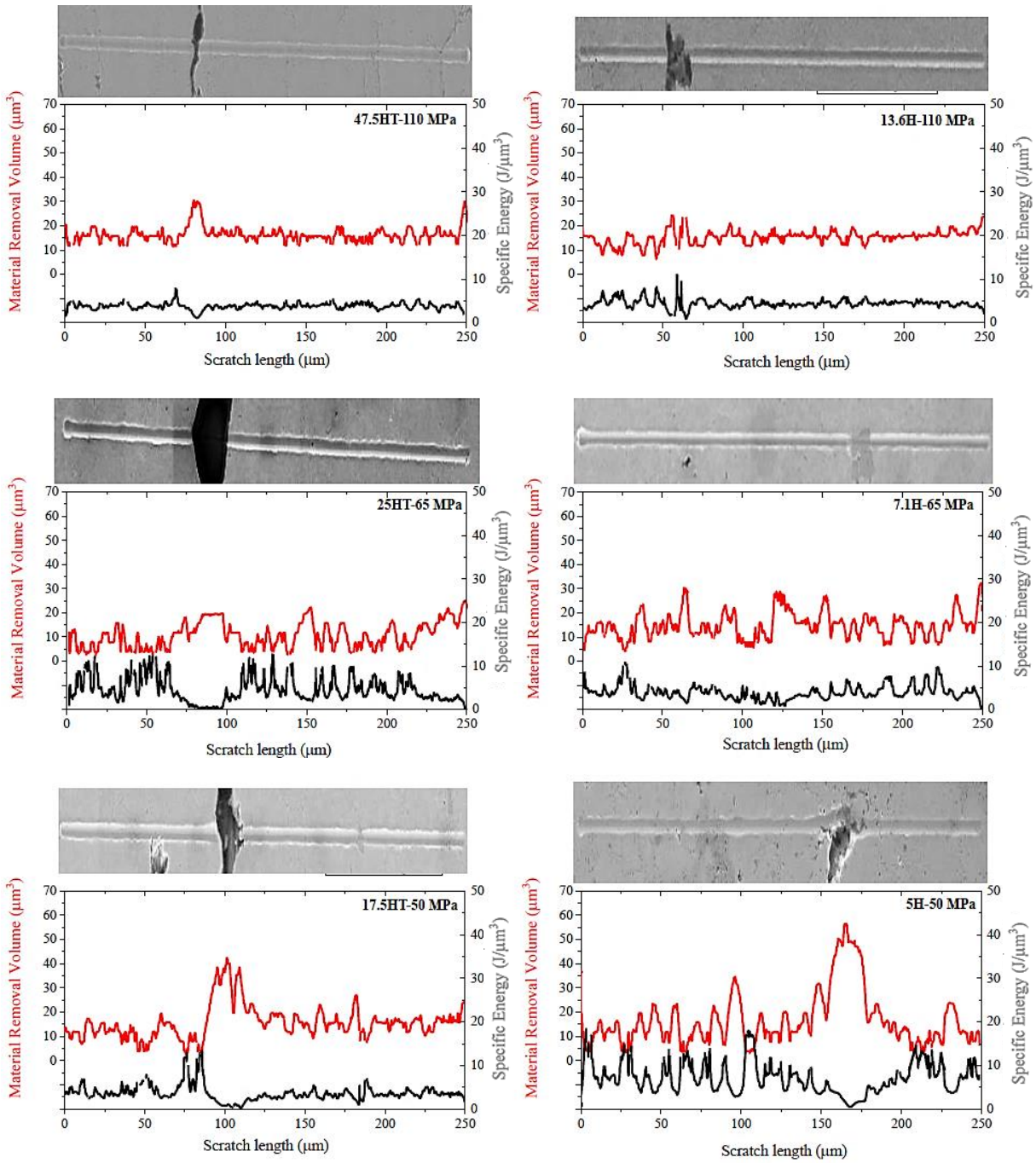

4.4.6 Transition from micro-ploughing to micro-cutting

Applying a normal load of 20 mN, the local effects of volume removed, and specific energy is more significant than those observed in the dominant micro-ploughing case. However, fluctuations in specific energy and volume removed are reduced, especially in the pore regions (Figure 101). This indicates a possible transition from micro-ploughing to micro-cutting. Generally, a greater accumulation of material is obtained on the sides of the samples, and the chip formation is partially generated but discontinuous. This shows that the primary wear mechanism is the transition stage of abrasive wear. However, high fluctuations are observed in the 5H-50 MPa sample. Mainly, a peak of material removed and a drop in specific energy are observed, which can be the result of the scratching process, in which the abrasive inside the pore does not have a frictional resistance (low tangential force) and a high depth of abrasion penetration.

On the other hand, in this transition stage, the effect of morphology, size, and position of the pore affects the volume removed and the specific energy. The results observed in Figure 101 corroborate this local aspect of the pores, particularly for the samples sintered at 110MPa, the presence of the pore on the wear surface does not exhibit significant peaks in the curves of the material removed and the specific energy. However, for the 7.1H-65 MPa sample, the presence of the pore (located at the upper end of the wear track) and oxide caused peaks in the curves and significant chip formation. The effect of the morphology and depth of the pores modifies the micro-mechanisms activation concerning the total specific energy since the energy consumed with the chip formation tends to exceed the other energies as a plow and slip (MEZGHANI; EL MANSORI; SURA, 2009).

Figure 101 - Tribological responses of the scratch tests (volume removed and specific energy) for the copper samples. In this condition, the test was performed with a constant normal load of 20 mN. The abrasive micro-mechanism was transition. Also, the length of the scratch shown in the micrograph is consistent with the scales on the graph.

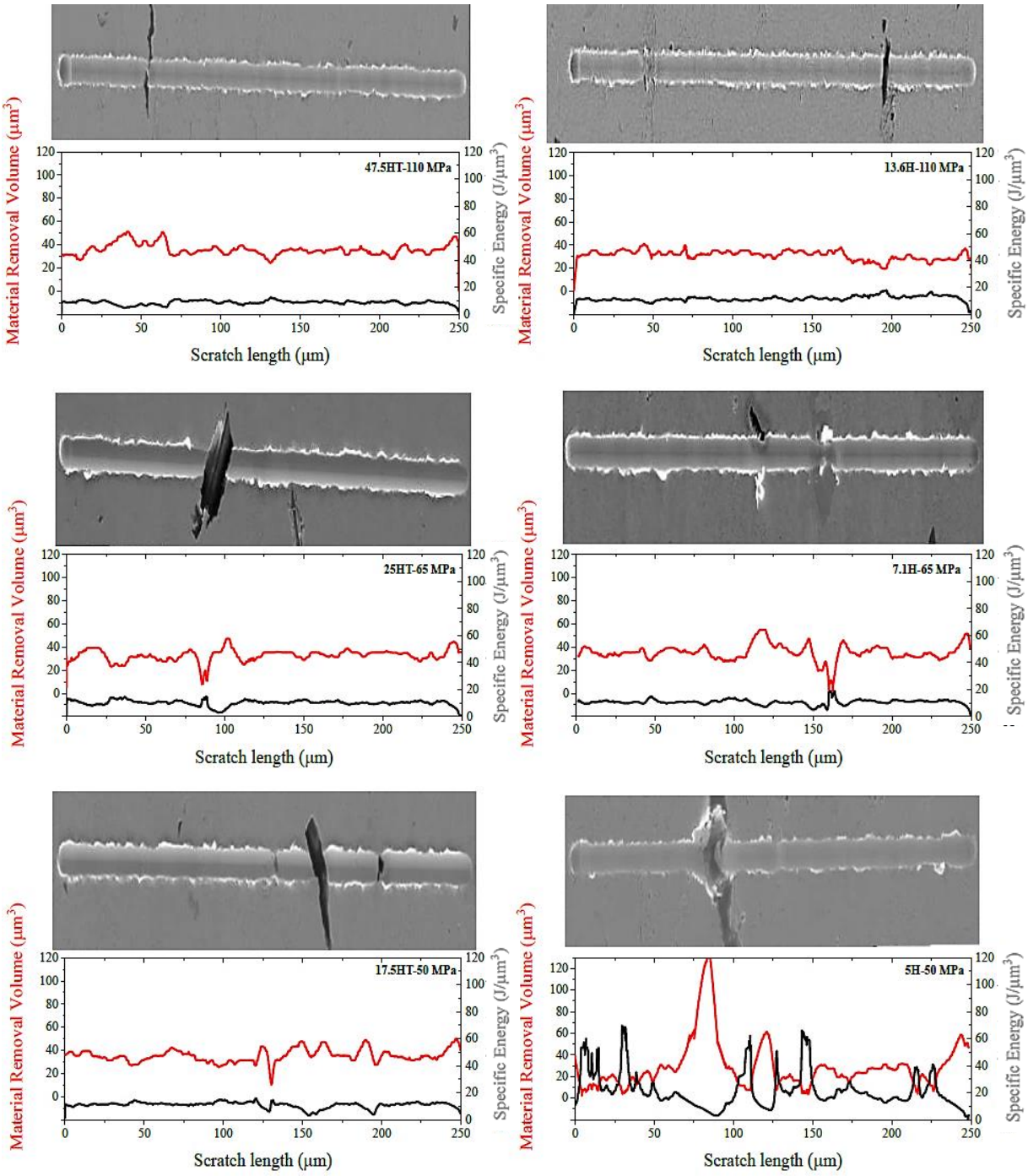

4.4.7 Dominant micro-cutting

For the micro-cutting (50 mN), the results indicated a more significant material removal in the copper samples (Figure 102). At this level of wear, the presence of pores generated falls in the specific energy; these peaks are more significant as the sintering pressure decreases. Observations on the FEGSEM images of the scratch in Figure 102 corroborate this local aspect of the pores. The pores behaved as stress-concentrating regions, intensifying the localized removal volume for micro-shear loading. Furthermore, the energy expended with chip formation tends to outweigh the ploughing and sliding components of the total specific energy (MEZGHANI; EL MANSORI; SURA, 2009).

Figure 102 - Tribological responses of the scratch tests (volume removed and specific energy) for the copper samples. In this condition, the test was performed with a constant normal load of 50 mN. The abrasive micro-mechanism was dominated micro-cutting. Also, the length of the scratch shown in the micrograph is consistent with the scales on the graph.

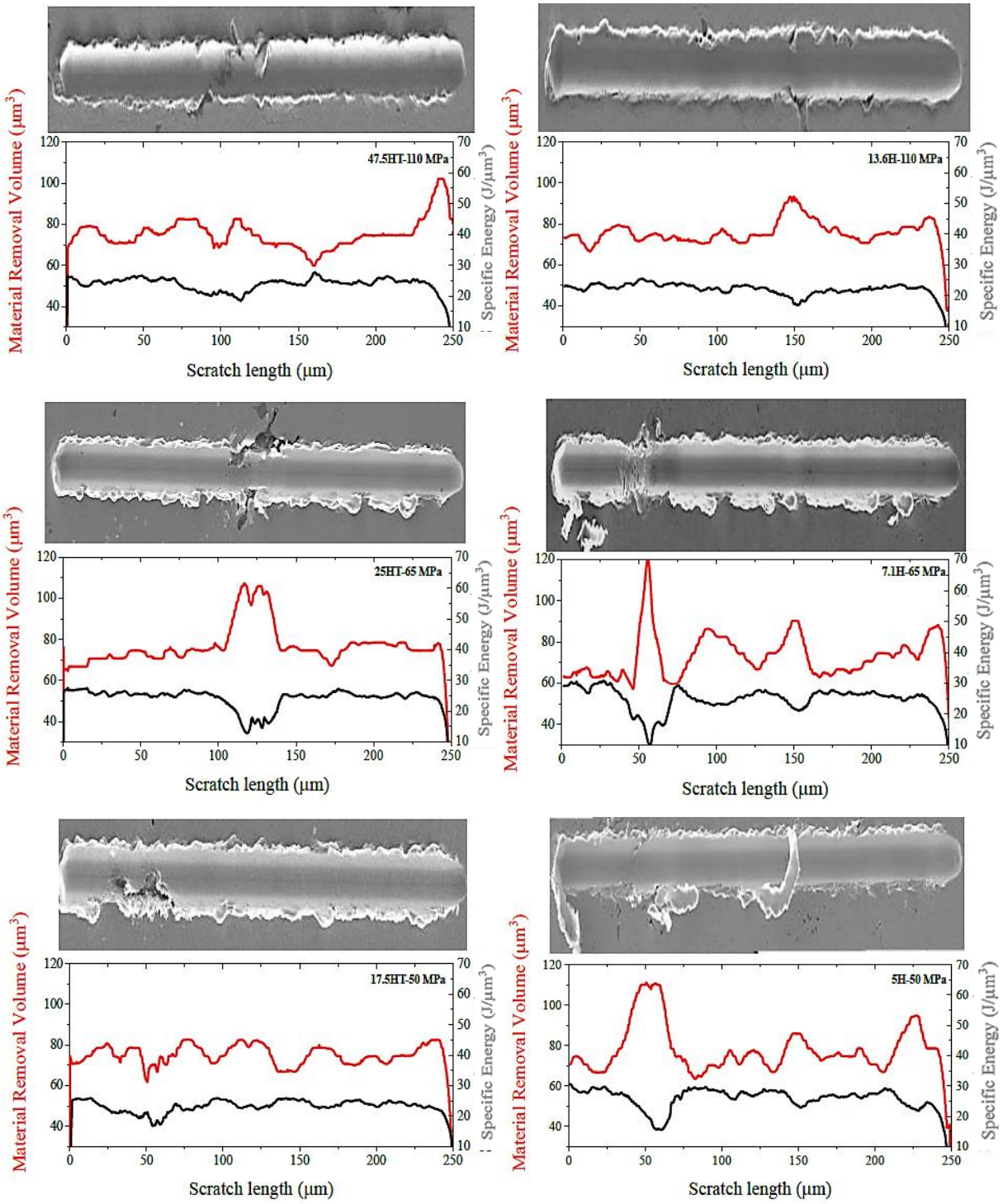

4.5 Tribological characterization in composites Cu-Al_2O_3 at micro-scale

4.5.1 Coefficient of friction (COF)

The average (overall) coefficient of friction (COF) results with normal loads of 5, 20, and 50 mN are shown in Figure 103. COF values were in the range between 0.15 and 0.63. Adding Al_2O_3 particles (uncoated, PVD coating, and chemical coating) modified the coefficient of friction compared to the copper sample (47.5HT-110 MPa). However, minor differences are observed among the samples at loads of 50 mN. The average values of COF in the two scratch directions (0 and 90°) at each load showed minor differences, which were related to the random presence of the alumina (Al_2O_3).

Figure 103 - Average COF as a function of the normal load applied.

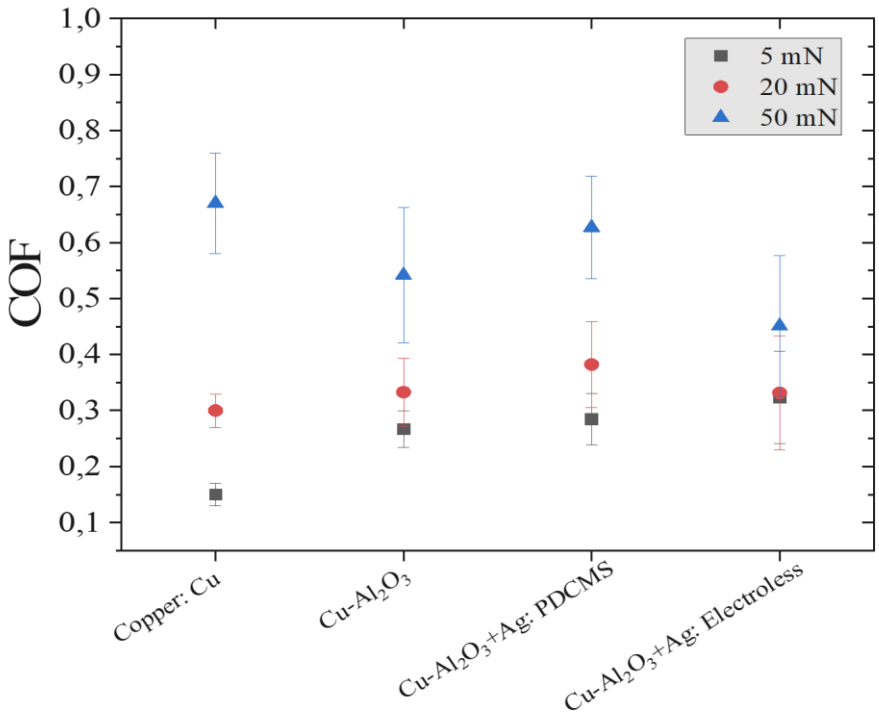

Figure 104 shows the FEFSEM micrographs of the worn grooves after scratching on the composites. The grooves become more apparent as the normal load applied increases. The copper sample (matrix) is considered to observe the microstructural differences between the composites. To further characterize the worn grooves of the composites, the COF and local penetration depths of the worn grooves.

Figure 104 - FEGSEM image of the scratches of the composites with normal loads of 5, 20, and 50 mN.

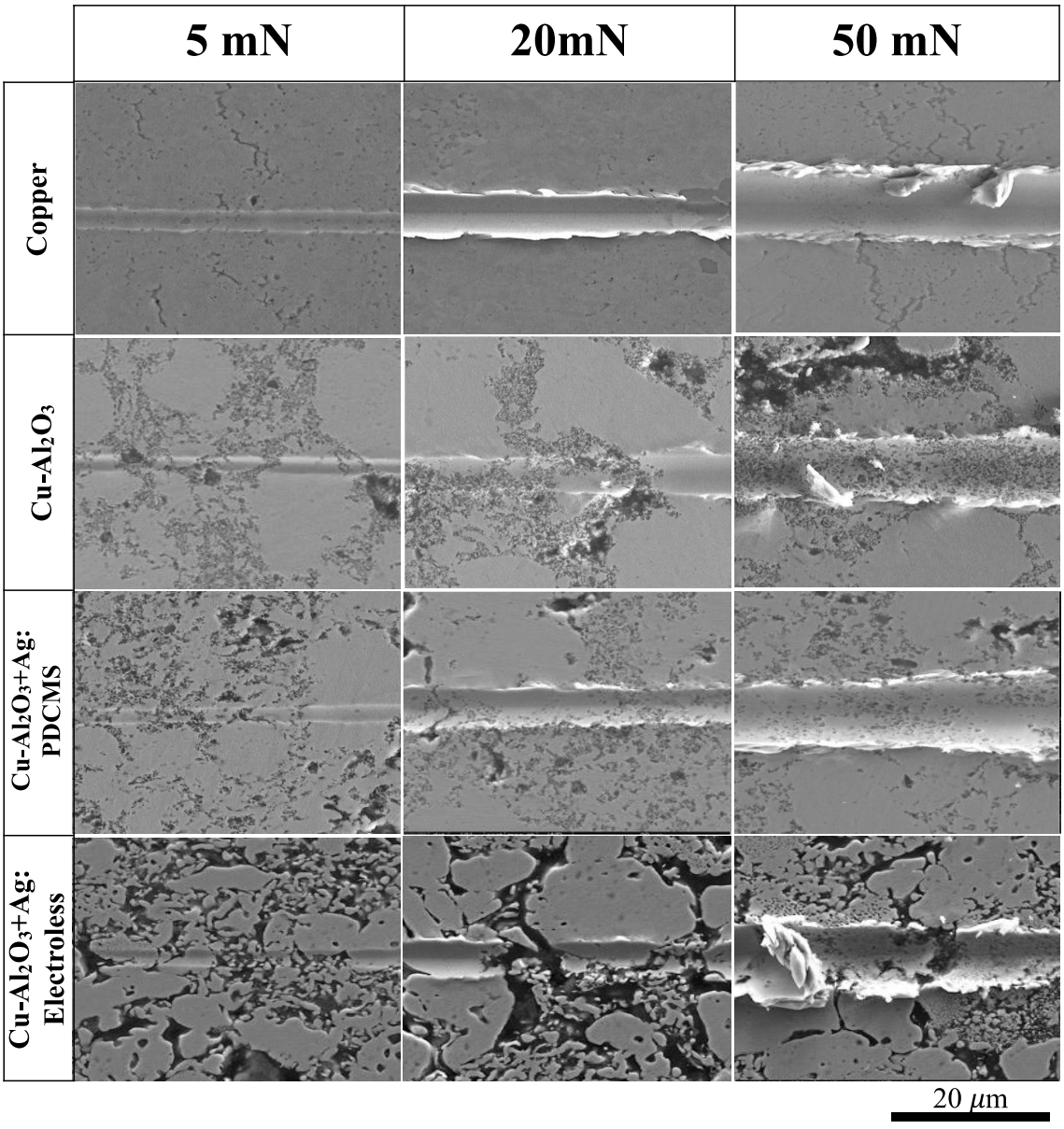

Figure 105 shows the local COF of the three composites obtained using different normal loads. COF results corresponded to the position of the indenter (length of scratch track). The effects of different Al_2O_3 addition modify the local COF during scratching. At loads of 5 mN, minor COF variations are observed for the Cu-Al_2O_3 and Cu-Al_2O_3+Ag: PDCMS samples compared to the Cu-Al_2O_3+Ag: Electroless composite. The differences were also attributed to the densification. Another point to consider is the similarity of the behavior of the COF for loads of 5 and 20 mN in the three composites, which was not observed in the copper sample.

When the load increases to 50 mN, the effect of the microstructure of each composite is more pronounced, causing differences in the profile and magnitude of the COF (Figure 104).

Figure 105 - Tribological responses COF (local) of the composites. a) Cu-Al_2O_3, b) Cu-Al_2O_3+Ag: PDCMS and c) Cu-Al_2O_3+Ag: Electroless.

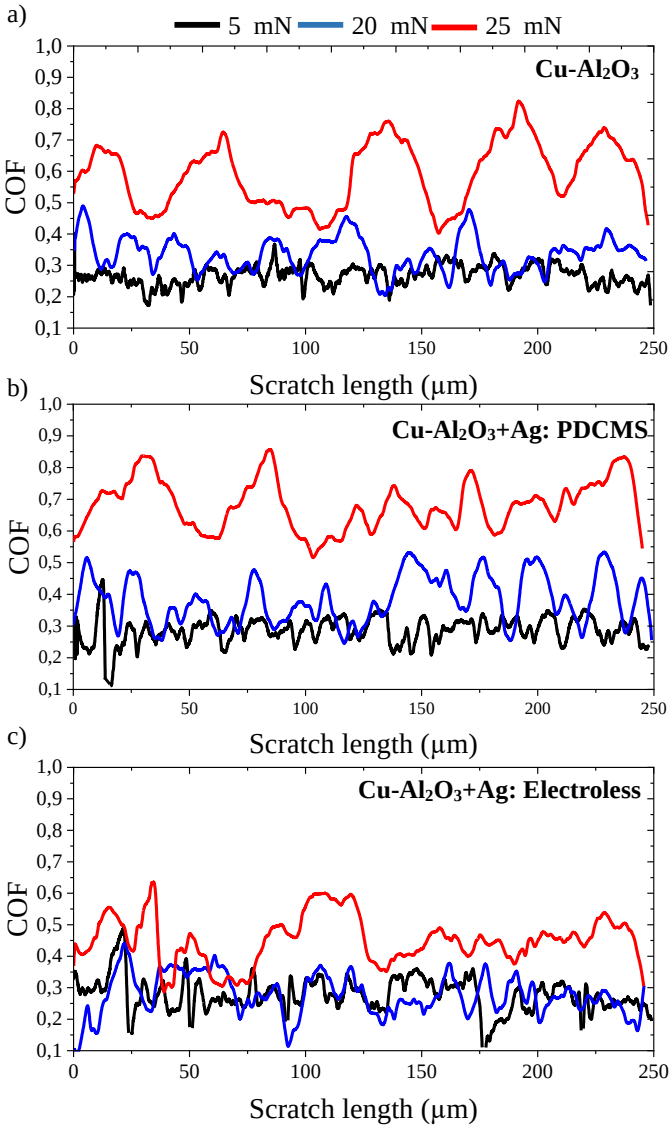

4.5.2 Penetration depth (h_p)

The penetration depth h_p is presented in Figure 106. These results show that the penetration depth can be related to the normal load. Locally, the hard particles help sustain the normal external load applied on the heterogeneous material, acting as barriers (ZUM GAHR, 1987) and becoming more perceptible for low loads. However, for high loads, more significant variations are observed in the curves at (50 mN), where the Cu-Al_2O_3 composite was an average

variation (amplitude) of 0.72; in the case of the Cu-Al_2O_3+Ag: PDCMS composite, there was a decrease of 0.46 and the Cu-Al_2O_3+Ag: Electroless composite obtained an average variation of 0.25. In addition, the hard particles tend to be removed or deformed with the copper matrix, considering the consequences of the penetration depth compared to the second phase sizes (Figure 104).

Figure 106 - Penetration depth (h_p) during scratching. a) Cu-Al_2O_3, b) Cu-Al_2O_3+Ag: PDCMS and c) Cu-Al_2O_3+Ag: Electroless.

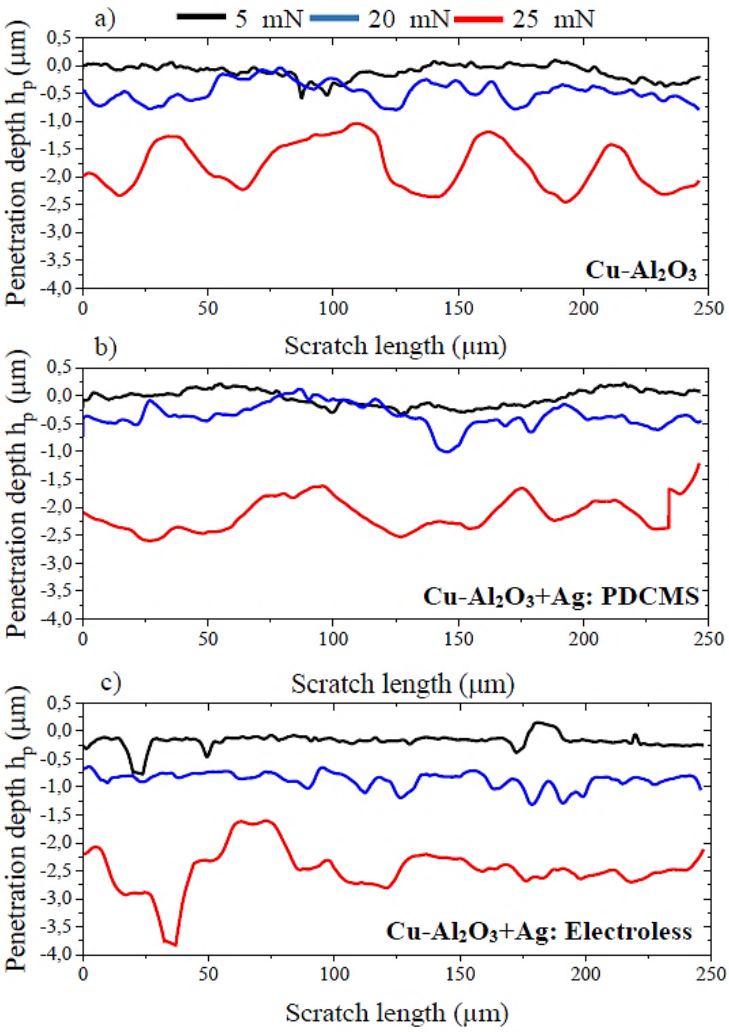

Figure 107 shows the average and standard deviation of the penetration depth of the composites at each applied load; it is possible to consider that the values are statistically equal. However, for Cu-Al_2O_3+Ag: Electroless, an increase in penetration depth is observed, due to scratch areas with high porosity, following the density results described. Another justification is associated with the combination of Al_2O_3 particles, Ag, and pores in the case of the Cu-Al_2O_3+Ag: Electroless composite. This microstructural characteristic generates variations, amplitudes, and pronounced peaks in the penetration depth (Figure 106c). Moreover, the local hardness correlates with the penetration depths. The nano hardness results for the Al_2O_3 particles were 5.1 GPa, and the Al_2O_3+Ag particles were 12.45 GPa (Cu-Al_2O_3+Ag: PDCMS). The higher the hardness, the smaller the amplitude in the local penetration depth for each composite.

Figure 107 - Average penetration depth as a function of loads normal to copper and sintered composites.

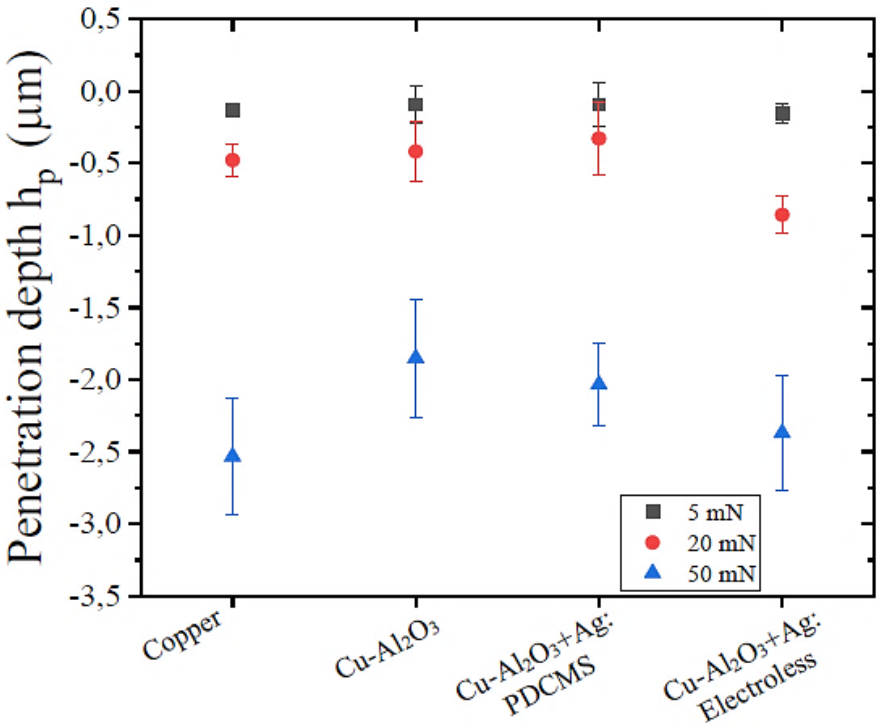

Some justifications are suggested to explain these results. The first justification is related to the local effect of matrix areas during sliding, which causes less load support associated with higher contact areas for the tip, which leads to a decrease in the contact pressure and the ability to penetrate the surface more (Figure 108, circles 1), compared to local areas with the presence of Al_2O_3 particles (Figure 108, circle 2). Despite the variations in the results, the penetration depth decreased by the presence of Al_2O_3 particles.

Figure 108 - Local variations of penetration depth (h_p) and COF of Cu-Al_2O_3+Ag: Electroless composite (20 mN).

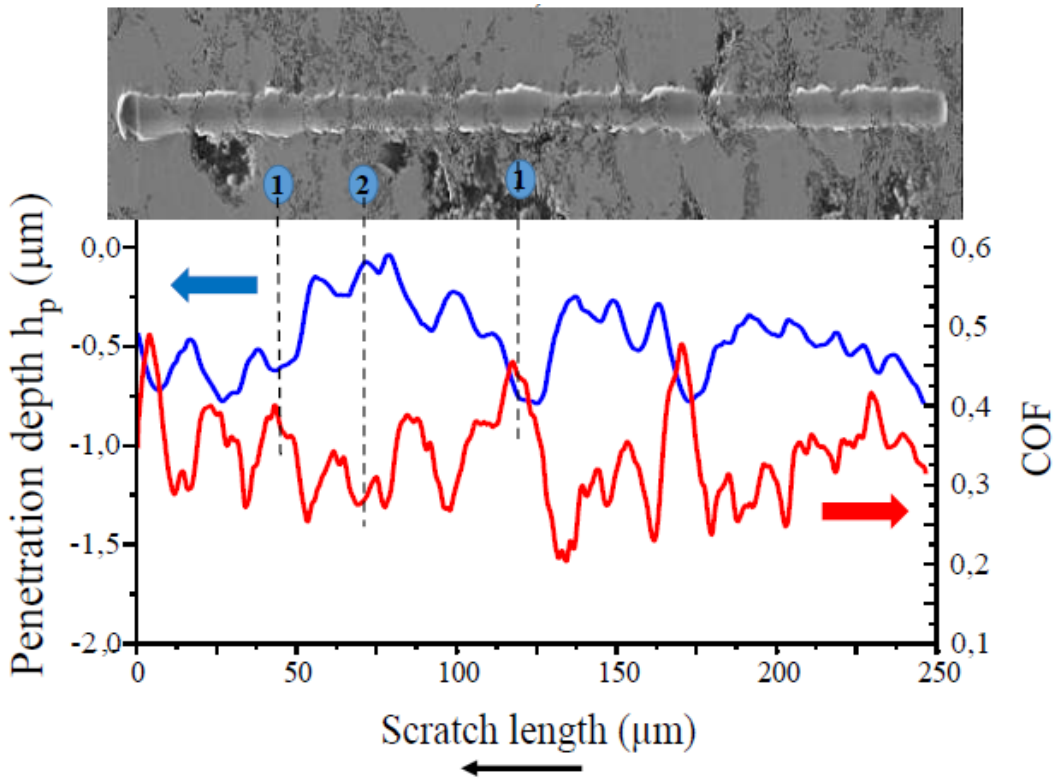

Figure 109 shows the tangential force as a function of the lateral displacement of the tip. The average distance between amplitudes and the tangential load peak amplitude was measured from each tangential force of the composite curves, considering the arithmetic mean as the reference line (average line). In the case of the **Cu-Al_2O_3 composite**, there is a specific repetitive variation in the tangential force as a function of the displacement, which is also related to the penetration depth (h_p) (Figure 106a) curve whose amplitude is similar among themselves. Therefore, the average distance between peaks of 22.9±10.2 µm and an average load amplitude of 8.7±0.6 mN.

With the addition of silver in the Al_2O_3 particles by the coating method (**Cu- Al_2O_3+Ag: PDCMS composite**), the results of the tangential force were lower than the Cu- Al_2O_3 composite. More specifically, the Cu- Al_2O_3+Ag: PDCMS composite was an average distance between peaks of 37.9±8.2 µm and an average load amplitude of 4.8±0.6 mN, generating a 44% decrease in load amplitude. These results indicate that silver-coated particles lead to a higher normal load strength due to a lower plastic strain rate and decreased porosity in silver-coated Al_2O_3-rich regions. Also, the reduction in local values of the tangential force decrease since it is proportional to the contact area at a constant normal load.

The characteristic microstructure of the **Cu-Al_2O_3+Ag: Electroless composite** presents average distance between peaks of 40.2±10.4 µm and an average load amplitude of 6.8±1.4 mN. The low average amplitude of the Cu-Al_2O_3+Ag: Electroless can be attributed to the low hardness of the composite for the applied normal load, generating localized plastic deformation in the front part of the tip, generating closure of the pores. Therefore, passing the tip through these closed pores does not modify the average tangential force. This behavior of low tangential force variations is observed between 250-130 µm. Also, a load peak amplitude of 13.7 mN (point 1) is generated due to an area that combines particles of Al_2O_3, Ag, and a more significant number and size of the pores, which eventually produces a threshold tangential force that is low enough to overcome the resistance regret by the tip to continue sliding.

Figure 109 - Tangential force (F_t) during scratching; with a normal load of 50 mN on the composites.

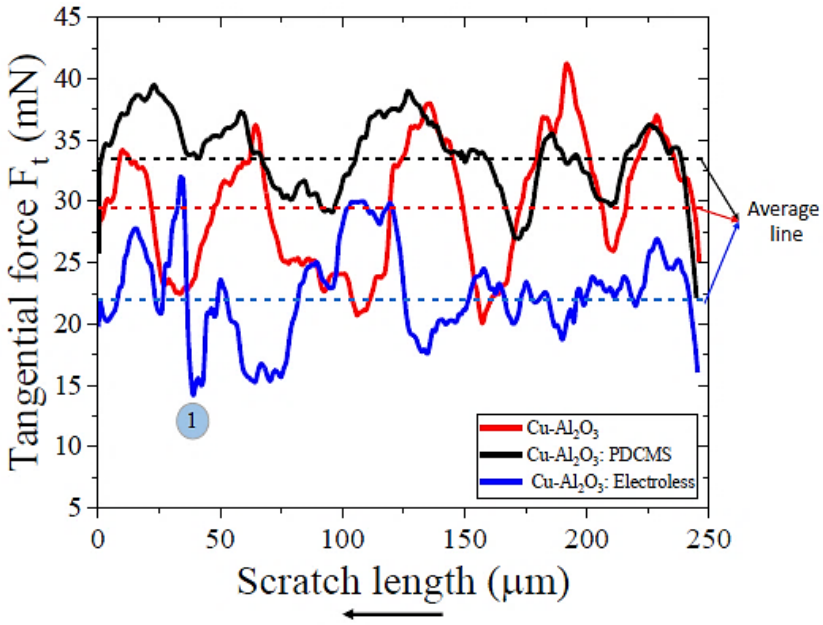

4.5.3 Geometric parameters (D_p and θ) and comparison with the literature

The attack angle (θ) and the degree of penetration (D_p) were calculated to associate and predict the effect of the normal load on the abrasive wear, and to study the abrasive micro-mechanisms involved during scratching of the matrix copper and composites. It should be noted that these scratch test results depend on the geometry of the tip (abrasive radius of 5 µm), normal loads and the mechanical properties (local elastic modulus and yield stress) of the tested composites in comparison to modes of wear observed by HOKKIRIGAWA; KATO; LI, (1988).

Table 17 presents the attack angle, degree of penetration and COF of the composites. The average coefficient of friction increases significantly with the attack angle. This result is comparable to those obtained for steel and metal alloys developed by many authors such as (HOKKIRIGAWA; KATO, 1988; KHELLOUKI; RECH; ZAHOUANI, 2013; YAN; SUN; DONG, 2007). They observed the relationship between the attack angle and the COF with the normal load increase for a spherical tip. When the attack angle reaches a critical value (θ_c), a transition occurs between the wear micro-mechanisms, increasing COF and surface wear by changing the wear regime from mild to severe. So far, the analysis of Table 17 indicates that the transition from dominant micro-ploughing to micro-cutting; occurred with a normal load of 20 mN for all composites. This analysis indicates that the critical attack angle was between 25 - 28º. Below this angle, the COF was low and micro-ploughing was accentuated; above this angle, the COF increased until the angle reached ~60° (reached at 50mN). The apex angle of the indenter cone was 60°, representing the maximum systems attack angle. For this loading regime, the increase in the COF is due, in particular, to the increase in plastic deformation and flow of each composite.

Table 17 - Average results of the angle of attack, degree of penetration and COF as a function of the normal load applied to the different composites evaluated.

Composites	Normal Load (mN)	Attack Angle **θ** **(°)**	Degree of penetration $\mathbf{D_p}$	COF
Copper	5	12±7	0.11±0.02	0.15±0.02
	20	25±6	0.22±0.03	0.30±0.03
	50	60	0.58±0.07	0.67±0.09
Cu-Al_2O_3	5	9±1	0.09±0.05	0.27±0.03
	20	23±11	0.22±0.05	0.33±0.06
	50	53±6	0.44±0.05	0.58±0.11
Cu-Al_2O_3+Ag: PDCMS	5	11±8	0.11±0.04	0.24±0.02
	20	24±12	0.23±0.06	0.35±0.05
	50	57±2	0.49±0.03	0.68±0.06
Cu-Al_2O_3+Ag: Electroless	5	15±8	0,13±0.04	0.28±0.06
	20	28±6	0.26±0.03	0.28±0.07
	50	54±5	0.51±0.07	0.45±0.08

The results obtained from the COF as a function of the angle of attack (Table 18), obtained with the radius of abrasive particles of 5 μm, were compared with the data recently published in the literature (FRANCO, 2015; MACHADO et al., 2017; SERIACOPI, 2018) presented in Table 18, in order to confirm the dominant micro-mechanism transition. Also, in the classic

literature (CHALLEN; OXLEY, 1979; HOKKIRIGAWA; KATO, 1988), the micro-mechanisms present in the samples can be validated. These works indicate that the transition from dominant micro-ploughing to micro-cutting occurs around 30º using normal loads close to those in this work. Below this angle, the COF was low and micro-ploughing was accentuated; above this angle, the COF increased until the angle reached 60° (apex angle of the cone). It should be considered that the ranges in the angle of attack are sensitive to different microstructures of the materials.

Table 18 - Comparison with the literature: normal load as a function of COF and attack angle for the samples studied.

Material	Normal Load (mN)	COF	Angle attack (°)	Reference
AISI 304	40	0.132 ± 0.004	25.2	(SERIACOPI, 2018)
	50	0.646 ± 0.001	32.0	
	60	0.933 ± 0.003	38.2	
	70	0.958 ± 0.002	44.5	
Gray cast iron	20	0.18	27	(FRANCO, 2015)
	50	0.6	48	
	75	0.76	56	
	100	0.9	60	
Hadfield steel	20	0.22±0.01	18	(MACHADO et al., 2017)
	50	0.23±0.01	22	
	100	0.58±0.10	37	

Figure 110a shows the degree of penetration (D_p) as a function of the normal load and the hardness of the samples studied. The analysis method presented follows the HOKKIRIGAWA; KATO, (1988) work, which allows evaluating the relationship between the COF and the micro-mechanism of wear associated with the D_p due to the applied load Figure 110b. An increase in D_p resulting from the normal load is accompanied by an increase in COF. Under the highest load conditions (50 mN), the composites tended to have values further apart from D_p. A more pronounced increase was observed in the copper sample reaching a Dp of 0.58. According to the authors, the wear map with clear limits between the abrasion mechanism is defined by Dp * and Dp ** values. Therefore, to predict the micro-mechanisms from the Dp data, results are presented in Figure 8. Micro-ploughing is the dominant micro-mechanism for loads of 5 mN. In the case of the wedging region, all the scratched samples presented a transition from dominant micro-ploughing to micro-cutting that occurred at 20 mN. Finally, for loads of 50 mN, the increase in Dp favors micro-cutting as the dominant wear micro-mechanism.

Figure 110 - Overlapping results of wear modes from the (HOKKIRIGAWA; KATO, 1988; HOKKIRIGAWA; KATO; LI, 1988). a) Wear mode diagram: D_p*, critical D_p which corresponds to the transition from the ploughing mode to the wedge-forming mode; D_p**, critical degree of penetration which corresponds to the transition from the wedge-forming mode to the cutting mode and b) Wear mode diagram that relates between coefficient of friction and degree of penetration; P: plowing mode, W: wedge forming mode, C: cutting mode.

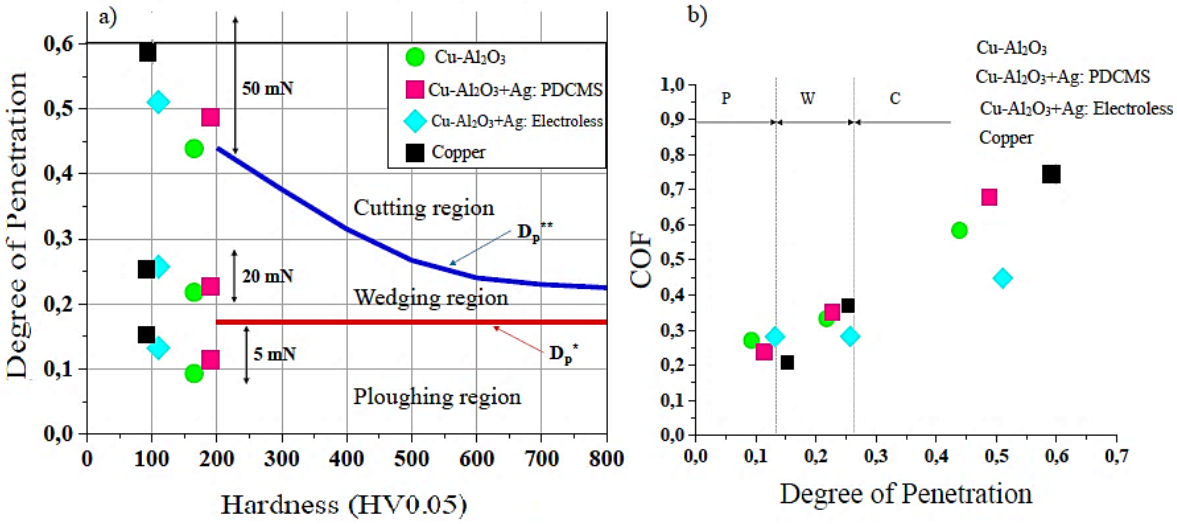

Source: Adapted from (HOKKIRIGAWA; KATO, 1988) and (HOKKIRIGAWA; KATO; LI, 1988).

Figure 111 presents the FEGSEM images of the scratches at 5 mN normal load of the and Cu-Al_2O_3 and Cu-Al_2O_3+Ag: PDCMS composites, in which micro-ploughing is the dominant micro-mechanism. The scratch width changes when the composites are analyzed locally, comparing silver coating on the Al_2O_3 particles and without coating. This variation is reflected in the local result of the D_P related to the width of the scratch and depth. In addition, for the sample which Al_2O_3, no displaced material is observed in the area where the Al_2O_3+Ag particle is seen. Therefore, a clear separation of the effect of modifying the surface of the particles and relating them to the variations of the h_p and the COF is possible (SERIACOPI et al., 2020).

Figure 111 - FEGSEM image of two scratches at 5 mN normal load: comparison between particles without modification of the surfaces of the Al_2O_3 particles and with Ag coating.

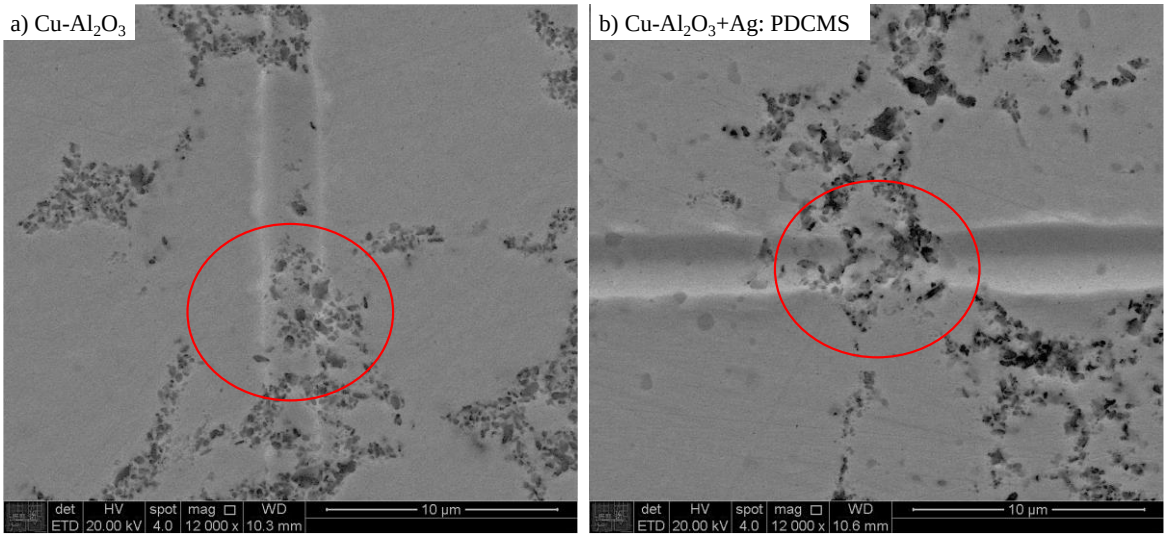

For Cu-Al_2O_3+Ag: Electroless composite, the FEG-SEM images of the scratch track (normal load of 5 mN) are presented. It is evident from the images that the scratch deformation is greatly influenced of Al_2O_3 and micropores (Figure 112a). On the other hand, the penetration depth increases even more, when areas with the presence of larger pores are observed (Figure 112b), which lead to larger amplitudes and pronounced variations.

Figure 112 - FEGSEM images of the scratch of Cu-Al_2O_3+Ag: Electroless composite at 5 mN normal load.

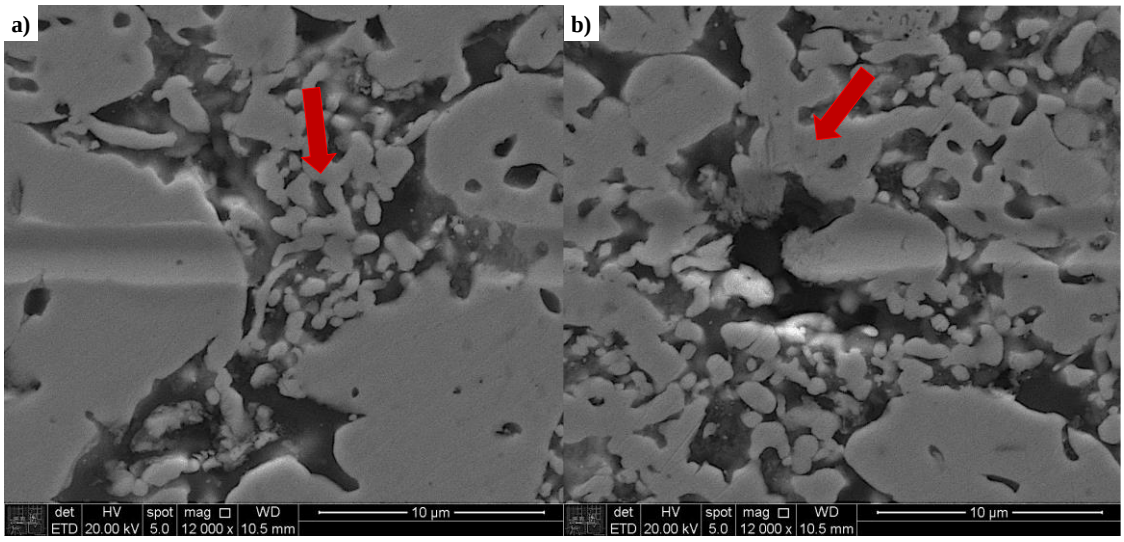

4.5.4 Material removal and specific energy

As described in Chapter 3, material removal and specific frictional energy were calculated based on the circular segment and penetration depth during the test. Taking into account the abrasive micro-mechanisms using penetration depth, attack angle, literature, and SEM images. The material removal and specific frictional energy were grouped into 3 categories:

- 5 mN - Micro-ploughing, as the dominant micro-mechanism (plastic deformation).
- 20 mN - Transition from micro-ploughing to micro-cutting, material displacement (wedge formation).
- 50 mN - Micro-cutting, accentuated material removal, and chip formation.

The results of the pile-up volume, total material removed, and the parameters for calculation are shown in Table 19. They were estimated by applying the results of the penetration depth and analytical models from the literature (SERIACOPI, 2018; NIKAS, 2016).

Table 19. Pile-up calculated using penetration depth (h_p) data and using an analytical model.

Composites	Depth of Penetration (μm)	Pile-up Height (μm)	Volume of spherical (μm^3)	Radius of the ECM hydrostatic core R_h (μm)	Outer radius of the ECM plastic zone r_p (μm)	Total removed volume (μm^3)
Cu-Al_2O_3	0.13±0.12	0.015±0.01	0.25±0.03	1.19±0.90	3.36±0.260	13.38±6.47
Cu-Al_2O_3+Ag: PSCMS	0.12±0.08	0.021±0.01	0.34±0.04	1.05±0.39	3.10±0.468	14.5±5.10
Cu-Al_2O_3+Ag: Electroless	0.19±0.12	0.04±0.1	0.78±1.72	1.32±0.33	4.27±1.50	17.75±2.99

4.5.5 Dominant micro-ploughing

The removed volume tends to decrease of Al_2O_3 particles are found and micro-ploughing predominates, for the case of 5 mN (Figure 113). Al_2O_3 particles help sustain the applied normal load and minimize the abrasive effect on the heterogeneous material, acting as barriers. However, the presence of pores increases the volume removed (voids that affect not only the penetration depth, but also plastic deformation mechanisms).

It should be noted that the calculation of the specific energy of the composites is obtained from the tangential force (frictional energy). A decrease in energy loss due to friction is predicted due to the presence of the particles and the decrease in the removed volume. The effect of the second hard phase decreasing material removal is in agreement with several authors (HU; LI; LLEWELLYN, 2007; PÖHL; HARDES; THEISEN, 2019).

Figure 113 - Volume removed and specific energy for the composites determine after scratch tests. In this condition, the test was performed with a constant normal load of 5 mN. The dominant abrasive micro-mechanism was micro-ploughing (low wear). Also, the length of the scratch shown in the micrograph is consistent with the scales on the graph.

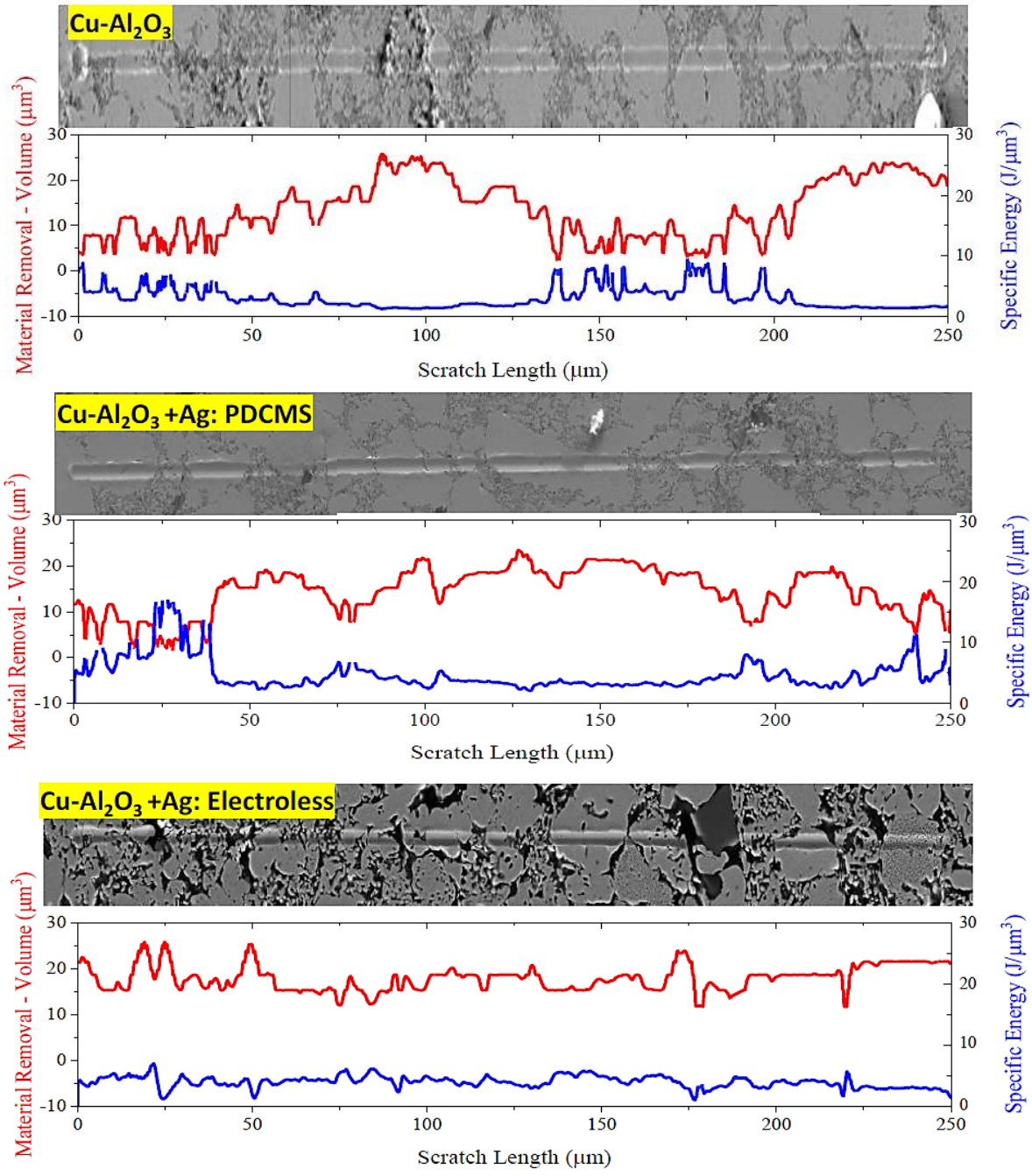

4.5.6 Transition from micro-ploughing to micro-cutting

Applying the local effects of porosity on volume removed and specific energy is important at normal load of 20 mN. The specific energy presents low oscillations in regions with an ensemble of particles and matrix continuity (Figure 114). FUTAMI et al., (2009) divided the specific energy components into a ploughing, related to the frictional part; and chip formation, including the contribution of cutting. However, in this thesis, only the frictional part was considered.

Figure 114 – FEGSEM images of the top views (yellow rectangle, following Figure 115) of the deformed microstructure of each composite with the presence of pores, matrix, and pore grouping.

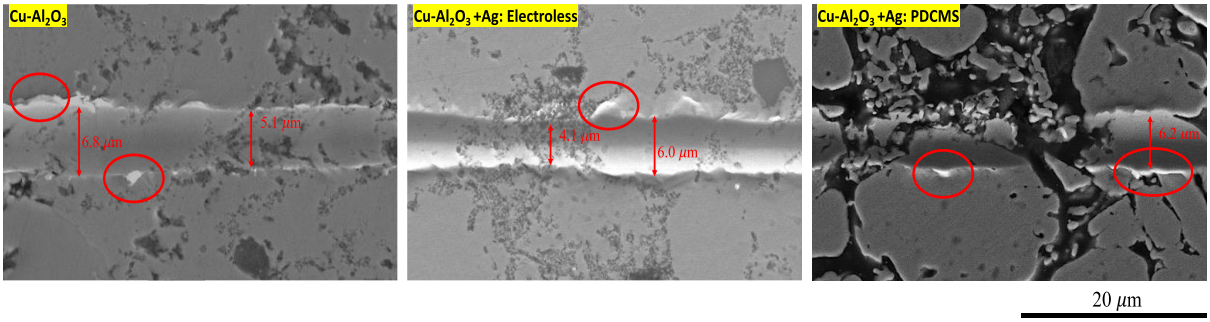

As for the case of the normal load of 20 mN, chip formation and greater width of the scratch are observed in positions where the tip slides through the copper matrix and only a minor plastic deformation in particle positions. Likewise, in the Figure 115 of 20 mN specific energy peaks are observed, which designates the presence of pores and grouping of pores, for each composite.

Figure 115 - Tribological responses of the scratch tests (volume removed and specific energy) for the composites. In this condition, the test was performed with a constant normal load of 20 mN. The abrasive micro-mechanism was transition (moderate wear). Also, the length of the scratch shown in the micrograph is consistent with the scales on the graph.

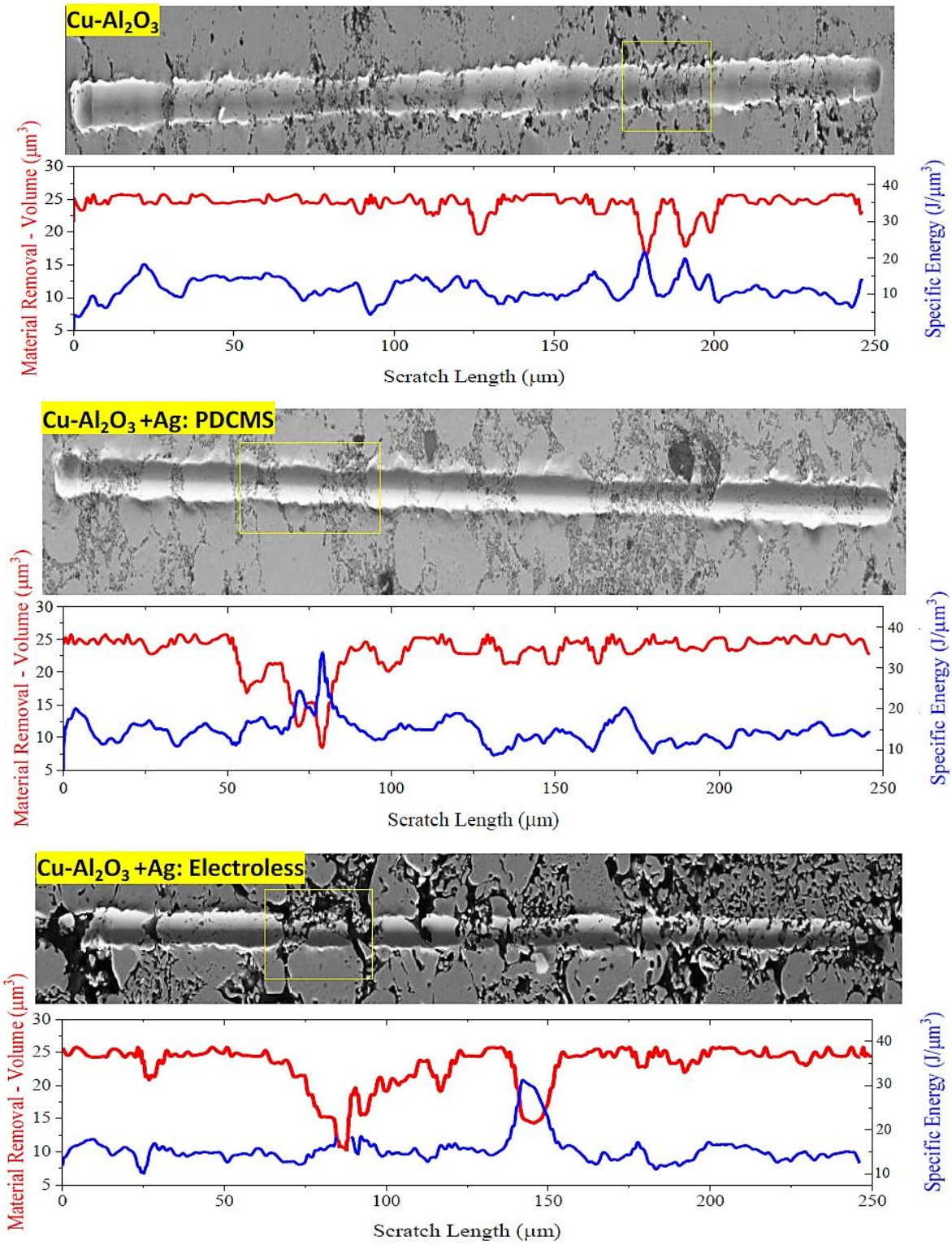

4.5.7 Dominant micro-cutting

The characterization by micro-cutting of the composites was carried out at a load of 50 mN. According to Figure 116, where there is a greater tendency to micro-cut. FEGSEM images (Figure 117) of the scratches allow for verifying the formation of chips, mainly in the areas of the matrix and the presence of pores. In addition, Al_2O_3 particles remain on the wear track and can hold back chip formation. Evidence for micro-cutting can be supported by evaluating the COF and penetration depth along the length of the scratch when a normal 50mN load was applied. In this case, the COF peaks occurred due to localized plastic deformation of the copper matrix and pores, which increases deformation along the micro scratch to provide micro-cutting (GAHR, 1987). As a consequence of abrasion on the composite, the following aspects can be verified:

- The specific frictional energy for the case of the Cu-Al_2O_3 composite: the maximum points occur in the positions of the most significant grouping of Al_2O_3 particles (less material removal).

- The specific frictional energy for the Cu-Al_2O_3+Ag: PDCMS composite, unlike the others, in this case, the specific energy presents slight variations and smaller chip size, with an optimal relationship of high resistance to particle wear and spacing, generating a decrease in the local eliminated volume, which significantly increased the local specific energy.

-The specific frictional energy for the Cu-Al_2O_3+Ag: electroless composite shows a greater volume removed in the areas of greater porosity. During the dominant micro-cutting, a notable amount of chips is formed: probably due to the set of pores and Al_2O_3 particles generating a decrease in specific energy.

Figure 116 - Tribological responses of the scratch tests (volume removed and specific energy) for the composites. In this condition, the test was performed with a constant normal load of 50 mN. The abrasive micro-mechanism was dominated micro-cutting (severe wear). Also, the length of the scratch shown in the micrograph is consistent with the scales on the graph.

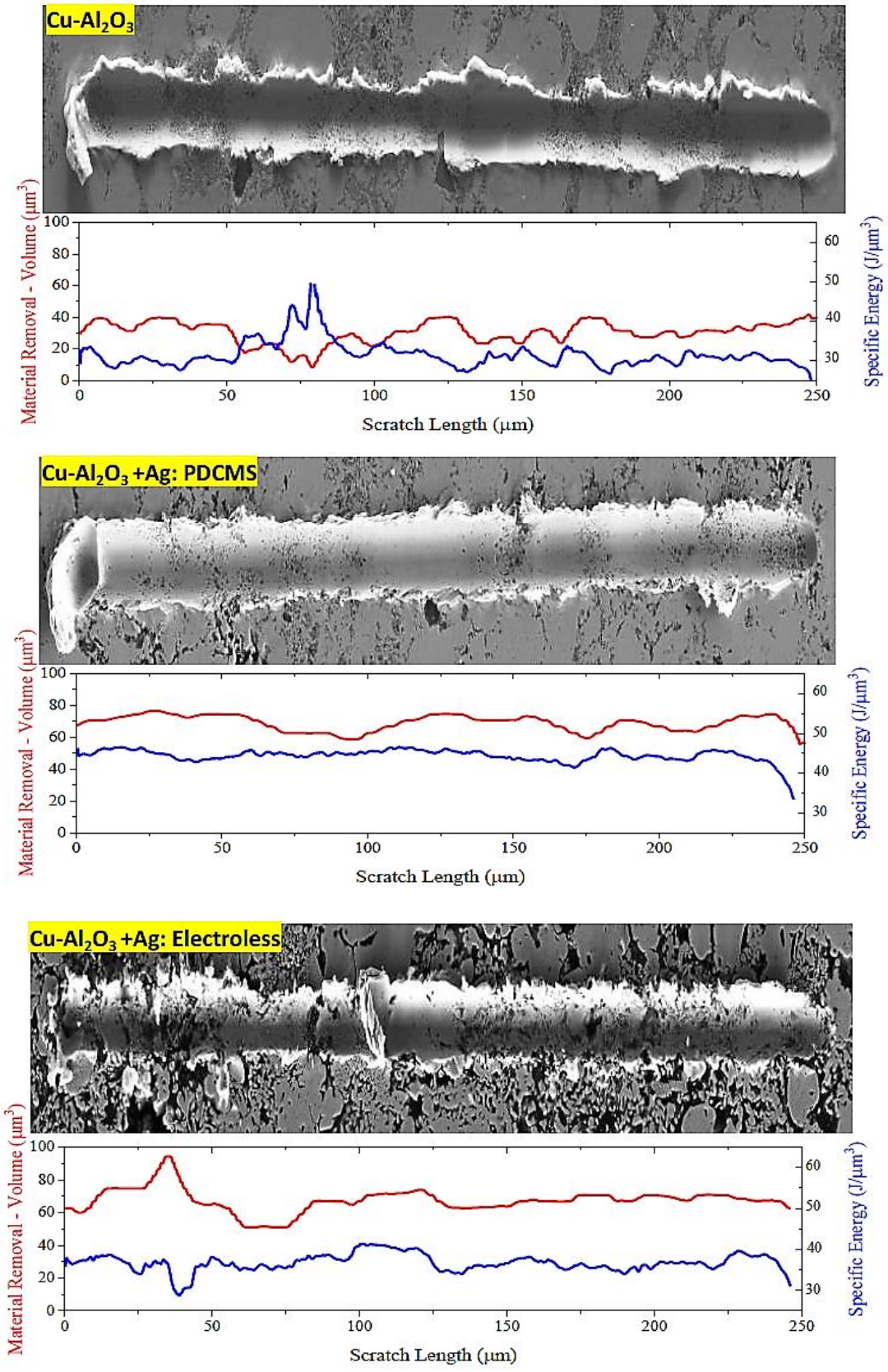

Figure 117 - FEGEM images (higher magnification) of the wear groove of the composites.

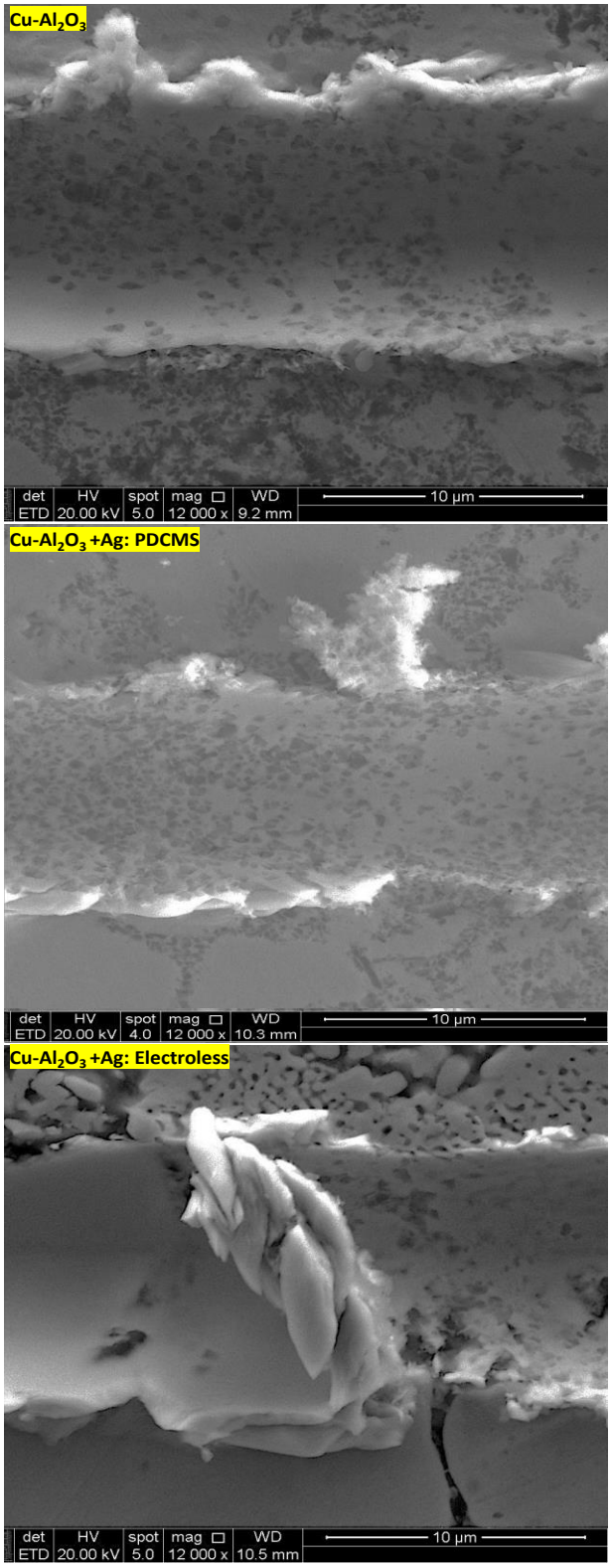

5 CONCLUSIONS AND FINAL REMARKS

The effect of sintering parameters on copper and the different methods of adding Al_2O_3 to copper on the microstructural features, density, hardness, and tribological performance of copper samples and composites sintered using the SPS technique was studied. From the results obtained, the following conclusions were obtained:

The effect of pressure applied during the SPS process of copper samples.

The copper samples sintered under the two sintering routes (HT and H) showed variation in the microstructure of the samples, either in the size and number of pores or the inhibition of grain growth. At a pressure of 110 MPa and route HT, there was a significant decrease in the pore fraction and a reduction in the number of large pores (high densification). The sintered sample in which pressure was applied during the holding time presented a pore fraction of 2.0 ± 0.5% with regular morphology and a lower pore area fraction. However, with a pressure of 50 MPa applied during heating, the pore fraction found was 20.0 ± 0.7%, with larger pores in area fraction and irregular morphology (interconnected pores). In addition, the microhardness of these two samples presents average values of 92 HV (110-HT) and 67 HV (50-H) due to the modification of the two pressure routes used. This result suggests that the effect of porosity and average grain size directly influences the hardness results, increasing by 27% when the pressure is increased from 50 to 110 MPa.

Tribological characterization of sintered copper samples.

Meso-scale:

The COF for the abrasive contact pair-heterogeneous samples: the variations of COF were more pronounced at lower normal loads (5-10 N), and the differences between the samples were intensified due to the influences of anisotropy, grain boundary, and the presence of pores. The coefficient of friction between the samples fluctuated approximately between 0.21 and 0.44 for different conditions (5-25 N). The geometric parameters θ and D_p of the samples were correlated with the sintering route and pressure. The scratch features measurements performed by optical profilometer and SEM images, the material removal parameter, F_{ab}, did not prove to be reliable in characterizing the modes of abrasion and plastic deformation for each sintered sample leading to material displacement with a clear preference for the formation and accumulation of material on the sides of the scratch (pile-up).

Abrasive micro-mechanisms were predicted based on the classical literature; The relationship between θ-D_p x COF and the normal load is increasing, and the depth tends to increase linearly with the load, providing high values. There is a noticeable micro-mechanism transition between micro-ploughing and wedge formation as a function of normal load increase, but no abrupt transitions were observed. However, the presence and location of the pores generate local micro-cutting activation in the scratches.

Micro-scale

The relationship between COF, penetration depth, and normal load is linear in that depth tends to increase linearly with load, giving high COFs. The results of the scratch tests on this scale allowed us to identify the differences in micro-mechanisms in the different samples. The 47.5HT-110 MPa sample showed slight decreases in the results of θ, D_p, and COF, generating a delay in the transitions of the micro-mechanisms.

The presence of pores: they increased the local penetration depth and, consequently, caused an increase in the local removed volume and a decrease in the local specific energy. When the penetration depth reaches its critical size (often for the most severe micro-cutting), the pores generate chip growth and a local increase in wear severity.

Microstructural characterization and mechanical properties of copper-based composites.

The microstructure of Al_2O_3-reinforced composites consists of a network of Al_2O_3 particles around the copper grains, which contributes to higher load resistance and reduced abrasive wear. The method of altering the surface of the Al_2O_3 particles allowed the identification of different microstructures of the composites. The composite without surface modification (Cu-Al_2O_3) exhibited a higher porosity between the particle networks, generating a relative density of 83%. After silver coating on the Al_2O_3 particles via PDCMS (Cu-Al_2O_3+Ag: PDCMS), they exhibited a homogeneous distribution of the coated particles around the matrix, increasing relative density 90 % and nanohardness matrix at the particle-particle interface of 12.45 GPa. Al_2O_3 particles were successfully coated with Ag particles using an electroless coating technique (Cu- Al_2O_3+Ag: Electroless), which modified their surface characteristics with improved dispersion of Al_2O_3 particles. However, the relative density (81 %) and hardness (110 HV) did not increase significantly compared to copper due to the characteristic microstructure formed by matrix pores and Al_2O_3+Ag particles.

Tribological characterization of copper-based composites.

Micro-scale

Al_2O_3 hard particles: they decreased the local penetration depth and, consequently, caused the reduction of the local removed volume and an increase of the local specific energy. When the penetration depth reached its critical size (often for the most severe micro-cutting), the particles carried the loads. They were not pulled or fragmented from the matrix, decreasing the volume removed and modifying the amplitude of the specific energy compared with the copper matrix; The observation of the scratch tests allowed us to identify the effect of the method of modifying the surface of the particles on the friction response and the active micro-mechanisms—the microstructural modification of Cu-Al_2O_3+Ag: PDCMS composite minimize chip formation at loads of 50 mN. The observation of the scratch and the results of the tangential force along the scratch confirmed an increase in the specific frictional energy.

Abrasive micro-mechanisms were predicted based on the results of classical literature. Abrasion resistance map of hardness, attack angle, COF, and degree of penetration: this map provided two main types of information: the first is the division between the dominant ductile or less ductile effect in the microstructure considering abrasion; the second refers to delimiting the borders of abrasive micro-mechanisms (from micro-ploughing to micro-cutting).

Finally, the contribution of this work is presented in three different areas.

i) a significant contribution was the realization of a new methodology for sintering copper via SPS. Mainly applying pressure during holding time with pressures greater than 100 MPa, it was observed an increase in the density, hardness, and resistance to abrasive wear of the sample. Furthermore, this sintering methodology was not found in the literature.

ii) Surface coating methods, specifically hybrid coating deposition methods, such as pulsed DC magnetron sputtering (PDCMS), is a novel route to improve the interfaces between ceramic particles and metals (Cu-Al_2O_3) for the sintering of MMC composites. They improve the density, hardness, and tribological performance of sintered composites.

iii) The tribological characterization of abrasive wear of copper samples and Cu-Al_2O_3 composites contributes to understanding the wear mechanisms present in abrasive wear and relating them to the volume removed and the specific friction energy.

6 FUTURE WORKS

Based on the conclusions reached in this work, questions were made to focus on new research related to the tribological characterization of sintered copper-composites.

1. Sinter copper samples using nanometric particles combine the best hardness ratio and a low coefficient of friction and wear.
2. Perform sliding wear tests under conditions of equal or greater loads on the copper samples and composites with Al_2O_3 particles. The objective would be to study the resistance to wear under conditions of more significant deformation of the matrix and the differences in the composition of the tribofilms formed at higher normal loads, allowing a link between the microstructural influence on the macro and microscopic analysis.
3. Include microstructural characterization of the interface between Al_2O_3 - Cu and Al_2O_3-Ag particles in order to understand the effect of the coating on the tribological behavior of the composite.
4. Include the other parcels to complement and understand the specific energy and material removal response.
5. Stress-strain tests can be considered in this evaluation and incorporate damage or fracture mechanics models.

REFERENCES

A. WIJAYA, B. EICHINGER, F.F. CHAMASEMANI, B. SARTORY, R. HAMMER, V. MAIER-KIENER, D. KIENER, M. MISCHITZ, R. Brunner. Multi-method characterization approach to facilitate a strategy to design mechanical and electrical properties of sintered copper. **Materials and Design**, *[S. l.]*, v. 197, p. 109188, 2021. DOI: 10.1016/j.matdes.2020.109188. Disponível em: https://doi.org/10.1016/j.matdes.2020.109188.

ABD-ELWAHED, M. S.; WAGIH, A.; NAJJAR, I. M. R. Correlation between micro/nano-structure, mechanical and tribological properties of copper-zirconia nanocomposites. **Ceramics International**, *[S. l.]*, v. 46, n. 1, p. 56–65, 2020. DOI: 10.1016/j.ceramint.2019.08.230. Disponível em: https://doi.org/10.1016/j.ceramint.2019.08.230.

ACIKBAS, Gokhan; CALIS ACIKBAS, Nurcan; ISLAK, Bilge Yaman; AYAS, Erhan; BAYRAK, Kübra Gürcan; ATAMAN, Alican. Copper reinforced SiAlON matrix composites produced by spark plasma sintering. **Ceramics International**, *[S. l.]*, v. 48, n. 9, p. 13260–13270, 2022. DOI: 10.1016/j.ceramint.2022.01.204. Disponível em: https://doi.org/10.1016/j.ceramint.2022.01.204.

AKBARPOUR, M. R.; ALIPOUR, S. Wear and friction properties of spark plasma sintered SiC/Cu nanocomposites. **Ceramics International**, *[S. l.]*, 2017. DOI: 10.1016/j.ceramint.2017.07.037.

AL-ASADI, Maitham Mohammed; AL-TAMEEMI, Hamza A. A review of tribological properties and deposition methods for selected hard protective coatings. **Tribology International**, *[S. l.]*, v. 176, n. August, p. 107919, 2022. DOI: 10.1016/j.triboint.2022.107919. Disponível em: https://doi.org/10.1016/j.triboint.2022.107919.

ASM INTERNATIONAL. **ASM Speciality Handbook, Copper and Copper Alloys**. [s.l: s.n.].

ASM INTERNATIONAL HANDBOOK COMMITEE. **Powder Metal Technologies and Applications**. 1. ed. Ohio: ASM International, 1998.

ASTM-E92. Standard Test Method for Vickers Hardness of Metallic Materials. **ASTM International**, *[S. l.]*, 1997.

ASTM G40. **Standard Test Method for G40-15: Standard Terminology Relating to Wear and Erosion**. West Conshohocken, PA. v. 1 DOI: 0.1520/G0040-17.

BAGHERI, G. H.; BONADONNA, C.; MANZELLA, I.; VONLANTHEN, P. On the characterization of size and shape of irregular particles. **Powder Technology**, *[S. l.]*, v. 270, n. Part A, p. 141–153, 2015. DOI: 10.1016/j.powtec.2014.10.015. Disponível em:

http://dx.doi.org/10.1016/j.powtec.2014.10.015.

BARGE, Matthieu; RECH, Joël; HAMDI, Hédi; BERGHEAU, Jean Michel. Experimental study of abrasive process. **Wear**, *[S. l.]*, v. 264, n. 5–6, p. 382–388, 2008. DOI: 10.1016/j.wear.2006.08.046.

BARSHILIA, Harish C.; KUMAR, Prashant; RAJAM, K. S.; BISWAS, A. Structure and optical properties of AgAl2O3 nanocermet solar selective coatings prepared using unbalanced magnetron sputtering. **Solar Energy Materials and Solar Cells**, *[S. l.]*, v. 95, n. 7, p. 1707–1715, 2011. DOI: 10.1016/j.solmat.2011.01.034. Disponível em: http://dx.doi.org/10.1016/j.solmat.2011.01.034.

BARSOUM, Michel W. **Fundamentals of ceramics**. [s.l: s.n.]. DOI: 10.1887/0750309024.

BOIDI, G.; FUKUMASU, N. K.; MACHADO, I. F. Wear and friction performance under lubricated reciprocating tests of steel powder mixtures sintered by Spark Plasma Sintering. **Tribology International**, *[S. l.]*, 2018. DOI: 10.1016/j.triboint.2018.01.032.

BOIDI, G.; PROFITO, F. J.; KADIRIC, A.; MACHADO, I. F.; DINI, D. The use of Powder Metallurgy for promoting friction reduction under sliding-rolling lubricated conditions. **Tribology International**, *[S. l.]*, v. 157, n. November 2020, p. 106892, 2021. DOI: 10.1016/j.triboint.2021.106892. Disponível em: https://doi.org/10.1016/j.triboint.2021.106892.

BORDIA, Rajendra K.; KANG, Suk Joong L.; OLEVSKY, Eugene A. Current understanding and future research directions at the onset of the next century of sintering science and technology. **Journal of the American Ceramic Society**, *[S. l.]*, v. 100, n. 6, p. 2314–2352, 2017. DOI: 10.1111/jace.14919.

BORKAR, Tushar; BANERJEE, Rajarshi. Influence of spark plasma sintering (SPS) processing parameters on microstructure and mechanical properties of nickel. **Materials Science and Engineering A**, *[S. l.]*, v. 618, p. 176–181, 2014. DOI: 10.1016/j.msea.2014.08.070. Disponível em: http://dx.doi.org/10.1016/j.msea.2014.08.070.

CALDERON VELASCO, S.; CAVALEIRO, A.; CARVALHO, S. Functional properties of ceramic-Ag nanocomposite coatings produced by magnetron sputtering. **Progress in Materials Science**, *[S. l.]*, v. 84, p. 158–191, 2016. DOI: 10.1016/j.pmatsci.2016.09.005. Disponível em: http://dx.doi.org/10.1016/j.pmatsci.2016.09.005.

CAPUS, Joseph M. PM2Tec 2005: Pressure increases on North American industry. **Powder Metallurgy**, *[S. l.]*, 2005. DOI: 10.1179/pom.2005.48.3.222.

CAVALIERE, Pasquale. **Spark plasma sintering of materials: Advances in processing and applications**. [s.l: s.n.]. DOI: 10.1007/978-3-030-05327-7.

CELEBI EFE, G.; YENER, T.; ALTINSOY, I.; IPEK, M.; ZEYTIN, S.; BINDAL, C. The effect of sintering temperature on some properties of Cu-SiC composite. **Journal of Alloys and Compounds**, *[S. l.]*, v. 509, n. 20, p. 6036–6042, 2011. DOI: 10.1016/j.jallcom.2011.02.170. Disponível em: http://dx.doi.org/10.1016/j.jallcom.2011.02.170.

CHALLEN, J. M.; OXLEY, P. L. B. An explanation of the different regimes of friction and wear using asperity deformation models. **Wear**, *[S. l.]*, v. 53, n. 2, p. 229–243, 1979. DOI: 10.1016/0043-1648(79)90080-2.

CHALLEN, J. M.; OXLEY, P. L. B.; DOYLE, E. D. The effect of strain hardening on the critical angle for abrasive (chip formation) wear. **Wear**, *[S. l.]*, v. 88, n. 1, p. 1–12, 1983. DOI: 10.1016/0043-1648(83)90307-1. Disponível em: https://linkinghub.elsevier.com/retrieve/pii/0043164883903071.

CHÁVEZ-VÁSCONEZ, Ricardo; LASCANO, Sheila; SAUCEDA, Sergio; REYES-VALENZUELA, Mauricio; SALVO, Christopher; MANGALARAJA, Ramalinga Viswanathan; GOTOR, Francisco José; ARÉVALO, Cristina; TORRES, Yadir. Effect of the processing parameters on the porosity and mechanical behavior of titanium samples with bimodal microstructure produced via hot pressing. **Materials**, *[S. l.]*, v. 15, n. 1, 2022. DOI: 10.3390/ma15010136.

CHAWLA, N.; DENG, X. Microstructure and mechanical behavior of porous sintered steels. **Materials Science and Engineering A**, *[S. l.]*, v. 390, n. 1–2, p. 98–112, 2005. DOI: 10.1016/j.msea.2004.08.046.

CHE, Q. L. et al. Spark plasma sintering of titanium-coated diamond and copper-titanium powder to enhance thermal conductivity of diamond/copper composites. **Materials Science in Semiconductor Processing**, *[S. l.]*, v. 33, p. 67–75, 2015. DOI: 10.1016/j.mssp.2015.01.041.

CHEN, Pingan; SHEN, Qiang; LUO, Guoqiang; WANG, Chuanbing; LI, Meijuan; ZHANG, Lianmeng; LI, Xiangchen; ZHU, Boquan. Effect of interface modification by Cu-coated W powders on the microstructure evolution and properties improvement for Cu-composites. **Surface and Coatings Technology**, *[S. l.]*, v. 288, p. 8–14, 2016. DOI: 10.1016/j.surfcoat.2016.01.014. Disponível em: http://dx.doi.org/10.1016/j.surfcoat.2016.01.014.

COBLE, Robert L. Diffusion models for hot pressing with surface energy and pressure effects as driving forces. **Journal of Applied Physics**, *[S. l.]*, v. 41, n. 12, p. 4798–4807, 1970. DOI: 10.1063/1.1658543.

DA SILVA, W. M.; COSTA, H. L.; DE MELLO, J. D. B. Transitions in abrasive wear mechanisms: Effect of the superimposition of interactions. **Wear**, *[S. l.]*, v. 271, n. 5–6, p. 977–

986, 2011. DOI: 10.1016/j.wear.2011.04.010. Disponível em: http://dx.doi.org/10.1016/j.wear.2011.04.010.

DASH, K.; RAY, B. C.; CHAIRA, D. Synthesis and characterization of copper-alumina metal matrix composite by conventional and spark plasma sintering. **Journal of Alloys and Compounds**, *[S. l.]*, v. 516, p. 78–84, 2012. DOI: 10.1016/j.jallcom.2011.11.136. Disponível em: http://dx.doi.org/10.1016/j.jallcom.2011.11.136.

DE MELLO, J. D. B.; BINDER, R.; KLEIN, A. N.; HUTCHINGS, I. M. Effect of compaction pressure and powder grade on microstructure and hardness of steam oxidised sintered iron. **Powder Metallurgy**, *[S. l.]*, v. 44, n. 1, p. 53–61, 2001. DOI: 10.1179/003258901666176.

DENG, Shenghua; LI, Jianan; LI, Ruidi; ZHAO, Hongjin; YUAN, Tiechui; LI, Lanbo; ZHANG, Yingjie. The effect of particle size on the densification kinetics of tungsten powder during spark plasma sintering. **International Journal of Refractory Metals and Hard Materials**, *[S. l.]*, v. 93, n. April, p. 105358, 2020. DOI: 10.1016/j.ijrmhm.2020.105358. Disponível em: https://doi.org/10.1016/j.ijrmhm.2020.105358.

DIOUF, S.; MOLINARI, A. Densification mechanisms in spark plasma sintering: Effect of particle size and pressure. **Powder Technology**, *[S. l.]*, v. 221, p. 220–227, 2012. DOI: 10.1016/j.powtec.2012.01.005. Disponível em: http://dx.doi.org/10.1016/j.powtec.2012.01.005.

DIXIT, Manish; SRIVASTAVA, R. K. Effect of compaction pressure on microstructure, density and hardness of Copper prepared by Powder Metallurgy route. *In*: IOP CONFERENCE SERIES: MATERIALS SCIENCE AND ENGINEERING 2018, **Anais** [...]. [s.l: s.n.] DOI: 10.1088/1757-899X/377/1/012209.

DOBRZAŃSKI, L. A.; BRYTAN, Z.; GRANDE, M. Actis; ROSSO, M. Influence of sintering parameters on the properties of duplex stainless steel. **Journal of Achievements in Materials and Manufacturing Engineering**, *[S. l.]*, v. 20, n. 2, p. 231–234, 2007.

FOGAGNOLO, Joao B.; RUIZ-NAVAS, Elisa M.; ROBERT, Maria H.; TORRALBA, José M. The effects of mechanical alloying on the compressibility of aluminium matrix composite powder. **Materials Science and Engineering A**, *[S. l.]*, v. 355, n. 1–2, p. 50–55, 2003. DOI: 10.1016/S0921-5093(03)00057-1.

FRANCO, L. A. Abrasion of gray cast iron: Application to automotive engines. Thesis. *[S. l.]*, p. 1–239, 2015.

FRANCO, Luiz Alberto; SINATORA, Amilton. Material removal factor (fab): A critical assessment of its role in theoretical and practical approaches to abrasive wear of ductile materials. **Wear**, *[S. l.]*, v. 382–383, n. April, p. 51–61, 2017. DOI:

10.1016/j.wear.2017.04.006. Disponível em: http://dx.doi.org/10.1016/j.wear.2017.04.006.

FRESCHI, Marco; DI VIRGILIO, Matteo; HAIKO, Oskari; MARIANI, Marco; ANDENA, Luca; LECIS, Nora; KÖMI, Jukka; DOTELLI, Giovanni. Investigation of second phase concentration effects on tribological and electrical properties of Cu–WS2 composites. **Tribology International**, *[S. l.]*, v. 166, n. November 2021, 2022. DOI: 10.1016/j.triboint.2021.107357.

FU, Yabo; PAN, Qinfa; CAO, Zhiqiang; LI, Shufeng; HUO, Yanqiu. Strength and electrical conductivity behavior of nanoparticles reaction on new alumina dispersion-strengthened copper alloy. **Journal of Alloys and Compounds**, *[S. l.]*, 2019. DOI: 10.1016/j.jallcom.2019.05.271.

FUTAMI, T.; OHIRA, M.; MUTO, H.; SAKAI, M. Contact/scratch-induced surface deformation and damage of copper-graphite particulate composites. **Carbon**, *[S. l.]*, 2009. DOI: 10.1016/j.carbon.2009.05.034.

GAHR, K. H. Zu. Formation of wear debris by the abrasion of ductile metals. **Wear**, *[S. l.]*, v. 74, n. 2, p. 353–373, 1981. DOI: 10.1016/0043-1648(81)90173-3.

GAHR, K. H. Zu. Wear by hard particles. **Tribology International**, *[S. l.]*, 1998. DOI: 10.1016/S0301-679X(98)00079-6.

GERMAN, R. M. Powder metallurgy & Particulate Materials Processing,. **Metal Powder Industry**, *[S. l.]*, 2005.

GÜLER, Onur; VAROL, Temel; ALVER, Ümit; CANAKCI, Aykut. Effect of Al2O3 content and milling time on the properties of silver coated Cu matrix composites fabricated by electroless plating and hot pressing. **Materials Today Communications**, *[S. l.]*, v. 24, n. March, p. 101153, 2020. DOI: 10.1016/j.mtcomm.2020.101153. Disponível em: https://doi.org/10.1016/j.mtcomm.2020.101153.

H. R. CASTRO, Klaus van Benthem. Sintering-Mechanisms of Convention Nanodensification and Field Assisted Processes. *In*: **Engineering Materials**. [s.l: s.n.]. v. 35p. 2–3. Disponível em: http://link.springer.com/10.1007/978-3-642-31009-6.

HAN, Quanquan; GENG, Yanquan; SETCHI, Rossitza; LACAN, Franck; GU, Dongdong; EVANS, Sam L. Macro and nanoscale wear behaviour of Al-Al2O3 nanocomposites fabricated by selective laser melting. **Composites Part B: Engineering**, *[S. l.]*, v. 127, p. 26–35, 2017. DOI: 10.1016/j.compositesb.2017.06.026. Disponível em: http://dx.doi.org/10.1016/j.compositesb.2017.06.026.

HAN, Sang Jo; SEO, Jeonghyuk; CHOE, Kyeong Hwan; KIM, Myung Ho. Fabrication of Al2O3 dispersion strengthened copper alloy by spray in-situ synthesis casting process. **Metals and Materials International**, *[S. l.]*, v. 21, n. 2, p. 270–275, 2015. DOI: 10.1007/s12540-015-

3469-z.

HOKKIRIGAWA, K.; KATO, K. An experimental and theoretical investigation of ploughing, cutting and wedge formation during abrasive wear. **Tribology International**, *[S. l.]*, v. 21, n. 1, p. 51–57, 1988. DOI: 10.1016/0301-679X(88)90128-4.

HOKKIRIGAWA, K.; KATO, K.; LI, Z. Z. The effect of hardness on the transition of the abrasive wear mechanism of steels. **Wear**, *[S. l.]*, v. 123, n. 2, p. 241–251, 1988. DOI: 10.1016/0043-1648(88)90102-0.

HONG, Eunji; KAPLIN, Bradley; YOU, Taehoon; SUH, Min soo; KIM, Yong Suk; CHOE, Heeman. Tribological properties of copper alloy-based composites reinforced with tungsten carbide particles. **Wear**, *[S. l.]*, v. 270, n. 9–10, p. 591–597, 2011. DOI: 10.1016/j.wear.2011.01.015. Disponível em: http://dx.doi.org/10.1016/j.wear.2011.01.015.

HU, J.; LI, D. Y.; LLEWELLYN, R. Synergistic effects of microstructure and abrasion condition on abrasive wear of composites-A modeling study. **Wear**, *[S. l.]*, v. 263, n. 1- 6 SPEC. ISS., p. 218–227, 2007. DOI: 10.1016/j.wear.2007.01.069.

HUTCHINGS, Ian; SHIPWAY, Philip. **Tribology: Friction and wear of engineering materials: Second Edition**. [s.l: s.n.].

J.E. CARSLEY, A. FISHER, W.W. MILLIGAN, And E. C. AIFANTIS. Mechanical behavior of a bulk nanostructured iron alloy. **Metallurgical and Materials Transactions A**, *[S. l.]*, v. 29, n. September, p. 2261–2271, 1998.

JANA, Prasanta; RAY, Sumit; GOLDAR, Diya; KOTA, Navya; KAR, Sujoy Kumar; ROY, Siddhartha. Study of the elastic properties of porous copper fabricated via the lost carbonate sintering process. **Materials Science and Engineering A**, *[S. l.]*, v. 836, n. November 2021, p. 142713, 2022. DOI: 10.1016/j.msea.2022.142713. Disponível em: https://doi.org/10.1016/j.msea.2022.142713.

JAYALAKSHMI, S.; GUPTA, M. **Metallic Amorphous Alloy Reinforcements in Light Metal Matrices**. Cham: Springer International Publishing, 2015. DOI: 10.1007/978-3-319-15016-1. Disponível em: http://link.springer.com/10.1007/978-3-319-15016-1.

JAYASHREE, Priyadarshini; MENAPACE, Cinzia; TURANI, Simone; STRAFFELINI, Giovanni. Dry sliding behavior of copper based composite materials prepared using conventional compaction and sintering technique and spark plasma sintering. **Wear**, *[S. l.]*, v. 490–491, n. November 2021, p. 204209, 2022. DOI: 10.1016/j.wear.2021.204209. Disponível em: https://doi.org/10.1016/j.wear.2021.204209.

JENA, P. K.; BROCCHI, E. A.; SOLÓRZANO, I. G.; MOTTA, M. S. Identification of a third phase in Cu-Al2O3 nanocomposites prepared by chemical routes. **Materials Science and**

Engineering A, *[S. l.]*, v. 371, n. 1–2, p. 72–78, 2004. DOI: 10.1016/S0921-5093(03)00642-7.

KHELLOUKI, A.; RECH, J.; ZAHOUANI, H. Micro-scale investigation on belt finishing cutting mechanisms by scratch tests. **Wear**, *[S. l.]*, v. 308, n. 1–2, p. 17–28, 2013. DOI: 10.1016/j.wear.2013.09.016. Disponível em: http://dx.doi.org/10.1016/j.wear.2013.09.016.

KOVALCHENKO, A. M.; FUSHCHICH, O. I.; DANYLUK, S. The tribological properties and mechanism of wear of Cu-based sintered powder materials containing molybdenum disulfide and molybdenum diselenite under unlubricated sliding against copper. **Wear**, *[S. l.]*, 2012. DOI: 10.1016/j.wear.2012.05.001.

KOVAŘÍKOVÁ, Ingrid; SZEWCZYKOVÁ, Beáta; BLAŠKOVITŠ, Pavel; HODÚLOVÁ, Erika; LECHOVIČ, Emil. Study and Characteristic of Abrasive Wear Mechanisms. *[S. l.]*, p. 1–9, 2009.

KUMAR, Aditya; STAEDLER, Thorsten; JIANG, Xin. Effect of normal load and roughness on the nanoscale friction coefficient in the elastic and plastic contact regime. **Beilstein Journal of Nanotechnology**, *[S. l.]*, v. 4, n. 1, p. 66–71, 2013. DOI: 10.3762/bjnano.4.7.

KUMAR, Ashwini; VICHARE, Omkar; DEBNATH, Kishore; PASWAN, Manikant. Fabrication methods of metal matrix composites (MMCs). **Materials Today: Proceedings**, *[S. l.]*, v. 46, p. 6840–6846, 2020. DOI: 10.1016/j.matpr.2021.04.432. Disponível em: https://doi.org/10.1016/j.matpr.2021.04.432.

LEON, Carlos A.; RODRIGUEZ-ORTIZ, Gabriel; NANKO, Makoto; AGUILAR, Ena A. Pulsed electric current sintering of Cu matrix composites reinforced with plain and coated alumina powders. **Powder Technology**, *[S. l.]*, v. 252, p. 1–7, 2014. DOI: 10.1016/j.powtec.2013.10.025. Disponível em: http://dx.doi.org/10.1016/j.powtec.2013.10.025.

LI, Wei; OLEVSKY, Eugene A.; MCKITTRICK, Joanna; MAXIMENKO, Andrey L.; GERMAN, Randall M. Densification mechanisms of spark plasma sintering: Multi-step pressure dilatometry. **Journal of Materials Science**, *[S. l.]*, v. 47, n. 20, p. 7036–7046, 2012. DOI: 10.1007/s10853-012-6515-y.

LI, Xingsheng; WANG, Yumeng; YIN, Chengri; YIN, Zhenxing. Copper nanowires in recent electronic applications: Progress and perspectives. **Journal of Materials Chemistry C**, *[S. l.]*, v. 8, n. 3, p. 849–872, 2020. DOI: 10.1039/c9tc04744a.

LI, Yuan; LIU, Ruxia; ZHANG, Jian; LUO, Guoqiang; SHEN, Qiang; ZHANG, Lianmeng. Fabrication and microstructure of W-Cu composites prepared from Ag-coated Cu powders by electroless plating. **Surface and Coatings Technology**, *[S. l.]*, v. 361, n. August 2018, p. 302–307, 2019. DOI: 10.1016/j.surfcoat.2019.01.030. Disponível em:

https://doi.org/10.1016/j.surfcoat.2019.01.030.

LIU, Z.; SUN, J.; SHEN, W. Study of plowing and friction at the surfaces of plastic deformed metals. **Tribology International**, *[S. l.]*, v. 35, n. 8, p. 511–522, 2002. DOI: 10.1016/S0301-679X(02)00046-4.

LORNA J. GIBSON AND MICHAEL F. ASHBY. **Cellular solids**. **Journal of Biomechanics**, 1999. DOI: 10.1016/0021-9290(89)90056-0.

MACHADO, I. F.; BOIDI, G.; FUKUMASU, N. K.; TERTULIANO, A. J. O.; SERIACOPI, V.; SOUZA, R. M. Effect of sintering densification on micro-scale mechanical and tribological behaviour of niobium carbide. **Wear**, *[S. l.]*, v. 482–483, n. December 2020, p. 203958, 2021. a. DOI: 10.1016/j.wear.2021.203958. Disponível em: https://doi.org/10.1016/j.wear.2021.203958.

MACHADO, I. F.; BOIDI, G.; FUKUMASU, N. K.; TERTULIANO, A. J. O.; SERIACOPI, V.; SOUZA, R. M. Effect of sintering densification on micro-scale mechanical and tribological behaviour of niobium carbide. **Wear**, *[S. l.]*, v. 482–483, n. June, p. 203958, 2021. b. DOI: 10.1016/j.wear.2021.203958. Disponível em: https://doi.org/10.1016/j.wear.2021.203958.

MACHADO, P. C.; PEREIRA, J. I.; PENAGOS, J. J.; YONAMINE, T.; SINATORA, A. The effect of in-service work hardening and crystallographic orientation on the micro-scratch wear of Hadfield steel. **Wear**, *[S. l.]*, v. 376–377, p. 1064–1073, 2017. DOI: 10.1016/j.wear.2016.12.057. Disponível em: http://dx.doi.org/10.1016/j.wear.2016.12.057.

MACHADO, Paulo Cordeiro. Ao Manganês Aplicados Em Britadores De Minério. *[S. l.]*, p. 309, 2017.

MAEDA, K.; BISMARCK, A.; BRISCOE, B. J. Mechanisms of scratching frictions and damage maps for rubber compounds. **Wear**, *[S. l.]*, v. 259, n. 1–6, p. 651–660, 2005. DOI: 10.1016/j.wear.2005.02.046.

MAKENA, Moraka Isaac; SHONGWE, Mxolisi Brendon; RAMAKOKOVHU, Munyadziwa Mercy; OLUBAMBI, Peter Apata. Effect of sintering parameters on densification, corrosion and wear behaviour of Ni-50Fe alloy prepared by spark plasma sintering. **Journal of Alloys and Compounds**, *[S. l.]*, v. 699, p. 1166–1179, 2017. DOI: 10.1016/j.jallcom.2016.12.368. Disponível em: http://dx.doi.org/10.1016/j.jallcom.2016.12.368.

MARTÍNEZ, Carola; BRIONES, Francisco; AGUILAR, Claudio; ARAYA, Nicolás; ITURRIZA, Iñigo; MACHADO, Izabel; ROJAS, Paula. Effect of hot pressing and hot isostatic pressing on the microstructure, hardness, and wear behavior of nickel. **Materials Letters**, *[S. l.]*, 2020. a. DOI: 10.1016/j.matlet.2020.127944.

MARTÍNEZ, Carola; BRIONES, Francisco; ARAYA, Nicolas; AGUILAR, Claudio;

MACHADO, Izabel; GUERRA, Carolina; MEDINA, Ariosto; SANCY, Mamie. Influence of the synthesis technique on tribological behavior of a Ti-6Al-4V alloy. **Materials Letters**, *[S. l.]*, 2020. b. DOI: 10.1016/j.matlet.2020.128627.

MAZUMDAR, Sanjay K. **Composites Composites**. [s.l: s.n.].

MEZGHANI, S.; EL MANSORI, M.; SURA, E. Wear mechanism maps for the belt finishing of steel and cast iron. **Wear**, *[S. l.]*, v. 267, n. 1–4, p. 86–91, 2009. DOI: 10.1016/j.wear.2008.12.113.

MISHRA, Tanmaya; DE ROOIJ, Matthijn; SCHIPPER, Dirk J. The effect of asperity geometry on the wear behaviour in sliding of an elliptical asperity. **Wear**, *[S. l.]*, v. 470–471, n. December 2020, p. 203615, 2021. DOI: 10.1016/j.wear.2021.203615. Disponível em: https://doi.org/10.1016/j.wear.2021.203615.

MONNIER, Judith; CHAMPION, Yannick; PERRIÈRE, Loïc; VILLEROY, Benjamin; GODART, Claude. Spark plasma sintering and hydrogen pre-annealing of copper nanopowder. **Materials Science and Engineering A**, *[S. l.]*, v. 621, p. 61–67, 2015. DOI: 10.1016/j.msea.2014.10.040. Disponível em: http://dx.doi.org/10.1016/j.msea.2014.10.040.

MULHEARN, T. O.; SAMUELS, L. E. The abrasion of metals: A model of the process. **Wear**, *[S. l.]*, v. 5, n. 6, p. 478–498, 1962. DOI: 10.1016/0043-1648(62)90064-9. Disponível em: https://linkinghub.elsevier.com/retrieve/pii/0043164862900649.

MUNIR, Z. A.; ANSELMI-TAMBURINI, U.; OHYANAGI, M. The effect of electric field and pressure on the synthesis and consolidation of materials: A review of the spark plasma sintering method. **Journal of Materials Science**, *[S. l.]*, v. 41, n. 3, p. 763–777, 2006. DOI: 10.1007/s10853-006-6555-2.

NEFEDOVA, E.; ALEKSANDROVA, E.; GRIGORYEV, E.; OLEVSKY, E. Research high-temperature consolidation of nanostructured bimodal materials. **Physics Procedia**, *[S. l.]*, v. 72, p. 390–393, 2015. DOI: 10.1016/j.phpro.2015.09.079.

NGAI, Tungwai L.; ZHENG, Wei; LI, Yuanyuan. Effect of sintering temperature on the preparation of Cu–Ti3SiC2 metal matrix composite. **Progress in Natural Science: Materials International**, *[S. l.]*, v. 23, n. 1, p. 70–76, 2013. DOI: 10.1016/j.pnsc.2013.01.011. Disponível em: http://dx.doi.org/10.1016/j.pnsc.2013.01.011.

NIELSEN, Lauge Fuglsang. Elasticity and Damping of Porous Materials and Impregnated Materials. **Journal of the American Ceramic Society**, *[S. l.]*, p. 1–6, 1983.

NIKAS, George K. Algebraic equations for the pile-up geometry in debris particle indentation of rolling elastohydrodynamic contacts. **Journal of Tribology**, *[S. l.]*, v. 138, n. 2, p. 1–14, 2016. DOI: 10.1115/1.4031516.

NOWACKI, J.; KLIMEK, L. The mechanism of reaction sintering of iron-iron boride cermets. **Journal of Materials Science**, *[S. l.]*, 1993. DOI: 10.1007/BF00353202.

OLIVER, W. C.; PHARR, G. M. An improved technique for determining hardness and elastic modulus using load and displacement sensing indentation experiments. *[S. l.]*, n. 1, 1992.

PAN, Yu et al. Fabrication, mechanical properties and electrical conductivity of Al2O3 reinforced Cu/CNTs composites. **Journal of Alloys and Compounds**, *[S. l.]*, v. 782, p. 1015–1023, 2019. DOI: 10.1016/j.jallcom.2018.12.222. Disponível em: https://doi.org/10.1016/j.jallcom.2018.12.222.

PELLIZZARI, Massimo; CIPOLLONI, Giulia. Tribological behaviour of Cu based materials produced by mechanical milling/alloying and spark plasma sintering. **Wear**, *[S. l.]*, v. 376–377, p. 958–967, 2017. DOI: 10.1016/j.wear.2016.11.050. Disponível em: http://dx.doi.org/10.1016/j.wear.2016.11.050.

PENAGOS, Jose Jimmy. Efeito do refinamento da microestrutura e da adição de nióbio na resistência ao desgaste abrasivo de ferros fundidos de alto cromo. *[S. l.]*, p. 140, 2016. Disponível em: http://www.teses.usp.br/teses/disponiveis/3/3151/tde-25082016-082141/en.php%5Cnhttps://drive.google.com/open?id=0B0fTxDBXtHZMS19HNHZ2UkZiVUU.

PENFORNIS, C.; JOURANI, A.; MAZERAN, P. E. Experimental and modelling study of the effect of martensite volume fraction on friction and wear of dual-phase steel at microscopic scale. **Wear**, *[S. l.]*, v. 484–485, n. March, p. 203878, 2021. DOI: 10.1016/j.wear.2021.203878. Disponível em: https://doi.org/10.1016/j.wear.2021.203878.

PÖHL, F.; HARDES, C.; THEISEN, W. Deformation behavior and dominant abrasion micro mechanisms of tempering steel with varying carbon content under controlled scratch testing. **Wear**, *[S. l.]*, v. 422–423, n. January, p. 212–222, 2019. DOI: 10.1016/j.wear.2019.01.073. Disponível em: https://doi.org/10.1016/j.wear.2019.01.073.

PÖHL, F.; MOHR, A.; THEISEN, W. Effect of matrix and hard phase properties on the scratch and compound behavior of wear resistant metallic materials containing coarse hard phases. **Wear**, *[S. l.]*, v. 376–377, p. 947–957, 2017. DOI: 10.1016/j.wear.2016.10.028. Disponível em: http://dx.doi.org/10.1016/j.wear.2016.10.028.

PORTER, David A.; EASTERLING, Kenneth E.; SHERIF, Mohamed Y. **Phase transformations in metals and alloys, third edition**. [s.l: s.n.].

QUACH, Dat V.; AVILA-PAREDES, Hugo; KIM, Sangtae; MARTIN, Manfred; MUNIR, Zuhair A. Pressure effects and grain growth kinetics in the consolidation of nanostructured fully stabilized zirconia by pulsed electric current sintering. **Acta Materialia**, *[S. l.]*, v. 58, n. 15, p.

5022–5030, 2010. DOI: 10.1016/j.actamat.2010.05.038. Disponível em: http://dx.doi.org/10.1016/j.actamat.2010.05.038.

RABINOWICZ, E.; DUNN, L. A.; RUSSELL, P. G. A study of abrasive wear under three-body conditions. **Wear**, *[S. l.]*, v. 4, n. 5, p. 345–355, 1961.

RAJARAMAN, Dhanraj; KEIM, Vincent; PONDICHERRY, Kannaki; NONN, Aida; HERTELÉ, Stijn; FAUCONNIER, Dieter. Stress state characterization of ductile materials during scratch abrasion. **Wear**, *[S. l.]*, v. 476, n. January, 2021. DOI: 10.1016/j.wear.2021.203712.

RAJKOVIC, Viseslava; BOZIC, Dusan; DEVECERSKI, Aleksandar; JOVANOVIC, Milan T. Characteristic of copper matrix simultaneously reinforced with nano- and micro-sized Al 2O 3 particles. **Materials Characterization**, *[S. l.]*, v. 67, p. 129–137, 2012. DOI: 10.1016/j.matchar.2012.02.022. Disponível em: http://dx.doi.org/10.1016/j.matchar.2012.02.022.

RAJKOVIC, Viseslava; BOZIC, Dusan; JOVANOVIC, Milan T. Properties of copper matrix reinforced with nano- and micro-sized Al2O3 particles. **Journal of Alloys and Compounds**, *[S. l.]*, v. 459, n. 1–2, p. 177–184, 2008. DOI: 10.1016/j.jallcom.2007.04.307.

RAZAVI-TOUSI, S. S.; YAZDANI-RAD, R.; MANAFI, S. A. Effect of volume fraction and particle size of alumina reinforcement on compaction and densification behavior of Al-Al2O3 nanocomposites. **Materials Science and Engineering A**, *[S. l.]*, v. 528, n. 3, p. 1105–1110, 2011. DOI: 10.1016/j.msea.2010.09.085. Disponível em: http://dx.doi.org/10.1016/j.msea.2010.09.085.

RIBEIRO, Yara Daniel; SOARES, Alexandre Candido; OLIVEIRA, Michel Picanço; DE OLIVEIRA, Bárbara Ferreira; PEREIRA, Artur Camposo; MONTEIRO, Sergio Neves. Development and characterization of spark plasma sintered novel Ni, Cu, WC containing Nb-Based alloys for high-temperature applications. **Journal of Materials Research and Technology**, *[S. l.]*, v. 17, p. 789–801, 2022. DOI: 10.1016/j.jmrt.2022.01.030.

RICHARDSON, R. C. D. THE WEAR OF METALS BY RELATIVELY SOFT ABRASIVES. **Wear**, *[S. l.]*, v. 10, n. 4, p. 291–309, 1967. DOI: 10.1016/0043-1648(67)90093-2.

RITASALO, R.; CURA, M. E.; LIU, X. W.; SÖDERBERG, O.; RITVONEN, T.; HANNULA, S. P. Spark plasma sintering of submicron-sized Cu-powder-Influence of processing parameters and powder oxidization on microstructure and mechanical properties. **Materials Science and Engineering A**, *[S. l.]*, v. 527, n. 10–11, p. 2733–2737, 2010. DOI: 10.1016/j.msea.2010.01.008.

RITASALO, R.; LIU, X. W.; SÖDERBERG, O.; KESKI-HONKOLA, A.; PITKÄNEN, V.;

HANNULA, S. P. The microstructural effects on the mechanical and thermal properties of pulsed electric current sintered Cu-Al2O3 composites. **Procedia Engineering**, *[S. l.]*, v. 10, p. 124–129, 2011. DOI: 10.1016/j.proeng.2011.04.023.

ROBERTSON, I. M.; SCHAFFER, G. B. Some effects of particle size on the sintering of titanium and a master sintering curve model. **Metallurgical and Materials Transactions A: Physical Metallurgy and Materials Science**, *[S. l.]*, v. 40, n. 8, p. 1968–1979, 2009. DOI: 10.1007/s11661-009-9894-1.

ROMARIC, Collet; SOPHIE, Le Gallet; FOAD, Naimi; FRÉDÉRIC, Charlot; GUILLAUME, Bonnefont; GILBERT, Fantozzi; JEAN-MARC, Chaix; FRÉDÉRIC, Bernard. Effect of current on the sintering of pre-oxidized copper powders by SPS. **Journal of Alloys and Compounds**, *[S. l.]*, v. 692, p. 478–484, 2017. DOI: 10.1016/j.jallcom.2016.08.191. Disponível em: https://doi.org/10.1016/j.jallcom.2016.08.191.

ROOP KUMAR, R.; WANG, M. Modulus and hardness evaluations of sintered bioceramic powders and functionally graded bioactive composites by nano-indentation technique. **Materials Science and Engineering A**, *[S. l.]*, v. 338, n. 1–2, p. 230–236, 2002. DOI: 10.1016/S0921-5093(02)00080-1.

SADOUN, A. M.; MESELHY, A. F.; ABDALLAH, A. W. Microstructural, mechanical and wear behavior of electroless assisted silver coated Al2O3–Cu nanocomposites. **Materials Chemistry and Physics**, *[S. l.]*, v. 266, n. January, p. 124562, 2021. DOI: 10.1016/j.matchemphys.2021.124562. Disponível em: https://doi.org/10.1016/j.matchemphys.2021.124562.

SADOUN, A. M.; MOHAMMED, M. M.; ELSAYED, E. M.; MESELHY, A. F.; EL-KADY, Omyma A. Effect of nano Al2O3 coated Ag addition on the corrosion resistance and electrochemical behavior of Cu-Al2O3 nanocomposites. **Journal of Materials Research and Technology**, *[S. l.]*, v. 9, n. 3, p. 4485–4493, 2020. a. DOI: 10.1016/j.jmrt.2020.02.076. Disponível em: https://doi.org/10.1016/j.jmrt.2020.02.076.

SADOUN, A. M.; MOHAMMED, M. M.; FATHY, A.; EL-KADY, Omyma A. Effect of Al2O3 addition on hardness and wear behavior of Cu-Al2O3 electro-less coated Ag nanocomposite. **Journal of Materials Research and Technology**, *[S. l.]*, v. 9, n. 3, p. 5024–5033, 2020. b. DOI: 10.1016/j.jmrt.2020.03.020. Disponível em: https://doi.org/10.1016/j.jmrt.2020.03.020.

SAMAL, C. P.; PARIHAR, J. S.; CHAIRA, D. The effect of milling and sintering techniques on mechanical properties of Cu-graphite metal matrix composite prepared by powder metallurgy route. **Journal of Alloys and Compounds**, *[S. l.]*, v. 569, p. 95–101, 2013. DOI:

10.1016/j.jallcom.2013.03.122. Disponível em: http://dx.doi.org/10.1016/j.jallcom.2013.03.122.

SANTOS, M. D.; FUKUMASU, N. K.; TSCHIPTSCHIN, A. P.; LIMA, N. B.; FIGUEROA, C. A.; WEBER, J. S.; SOUZA, R. M.; MACHADO, I. F. Effect of Ti/Si and Ti/TiN/Si interlayers on the structure, properties, and tribological behavior of an a-C film deposited onto a C17200 copper-beryllium alloy. **Surface and Coatings Technology**, *[S. l.]*, v. 441, n. May, p. 128561, 2022. DOI: 10.1016/j.surfcoat.2022.128561. Disponível em: https://doi.org/10.1016/j.surfcoat.2022.128561.

SASAKI, T.; YAKOU, T.; UMEMOTO, M.; TODAKA, Y. Two-body abrasive wear property of cementite. **Wear**, *[S. l.]*, v. 260, n. 9–10, p. 1090–1095, 2006. DOI: 10.1016/j.wear.2005.07.010.

SAYYAD, Reza; GHAMBARI, Mohammad; EBADZADEH, Touradj; PAKSERESHT, Amir Hossein; GHASALI, Ehsan. Preparation of Ag/reduced graphene oxide reinforced copper matrix composites through spark plasma sintering: An investigation of microstructure and mechanical properties. **Ceramics International**, *[S. l.]*, v. 46, n. 9, p. 13569–13579, 2020. DOI: 10.1016/j.ceramint.2020.02.142. Disponível em: https://doi.org/10.1016/j.ceramint.2020.02.142.

SCHULTZ, B. F.; FERGUSON, J. B.; ROHATGI, P. K. Microstructure and hardness of Al2O3 nanoparticle reinforced Al-Mg composites fabricated by reactive wetting and stir mixing. **Materials Science and Engineering A**, *[S. l.]*, v. 530, n. 1, p. 87–97, 2011. DOI: 10.1016/j.msea.2011.09.042. Disponível em: http://dx.doi.org/10.1016/j.msea.2011.09.042.

SEDRIKS, A. J.; MULHEARN, T. O. Mechanics of cutting and rubbing in simulated abrasive processes. **Wear**, *[S. l.]*, v. 6, n. 6, p. 457–466, 1963. DOI: 10.1016/0043-1648(63)90281-3.

SERIACOPI, Vanessa; PRADOS, Erika F.; FUKUMASU, Newton K.; SOUZA, Roberto M.; MACHADO, Izabel F. Mechanical behavior and abrasive mechanism mapping applied to micro-scratch tests on homogeneous and heterogeneous materials: FEM and experimental analyses. **Wear**, *[S. l.]*, 2020. DOI: 10.1016/j.wear.2020.203240.

SHAHEDI ASL, Mehdi; AHMADI, Zohre; PARVIZI, Soroush; BALAK, Zohre; FARAHBAKHSH, Iman. Contribution of SiC particle size and spark plasma sintering conditions on grain growth and hardness of TiB2 composites. **Ceramics International**, *[S. l.]*, v. 43, n. 16, p. 13924–13931, 2017. DOI: 10.1016/j.ceramint.2017.07.121. Disponível em: http://dx.doi.org/10.1016/j.ceramint.2017.07.121.

SHAO, Guosen; LIU, Ping; ZHANG, Ke; LI, Wei; CHEN, Xiaohong; MA, Fengcang. Mechanical properties of graphene nanoplates reinforced copper matrix composites prepared

by electrostatic self-assembly and spark plasma sintering. **Materials Science and Engineering A**, *[S. l.]*, 2019. DOI: 10.1016/j.msea.2018.10.067.

SHEHATA, F.; FATHY, Adel; ABDELHAMEED, M.; MOUSTAFA, S. F. Fabrication of copper-alumina nanocomposites by mechano-chemical routes. **Journal of Alloys and Compounds**, *[S. l.]*, 2009. DOI: 10.1016/j.jallcom.2008.08.065.

SHI, Yingge; CHEN, Wenge; DONG, Longlong; LI, Hanyan; FU, Yongqing. Enhancing copper infiltration into alumina using spark plasma sintering to achieve high performance Al2O3/Cu composites. **Ceramics International**, *[S. l.]*, 2018. DOI: 10.1016/j.ceramint.2017.09.062.

STROJNY-NĘDZA, Agata; PIETRZAK, Katarzyna; WĘGLEWSKI, Witold. The Influence of Al2O3 Powder Morphology on the Properties of Cu-Al2O3 Composites Designed for Functionally Graded Materials (FGM). **Journal of Materials Engineering and Performance**, *[S. l.]*, 2016. DOI: 10.1007/s11665-016-2204-3.

SUREKHA, K.; ELS-BOTES, A. Development of high strength, high conductivity copper by friction stir processing. **Materials and Design**, *[S. l.]*, v. 32, n. 2, p. 911–916, 2011. DOI: 10.1016/j.matdes.2010.08.028. Disponível em: http://dx.doi.org/10.1016/j.matdes.2010.08.028.

TABOR D. The hardness of solids. **Rev Phys Technol**, *[S. l.]*, 1970. DOI: 10.1088/0034-6683/1/3/i01.

TAN, Wenyue; JIANG, Xiaosong; SHAO, Zhenyi; SUN, Hongliang; SONG, Tingfeng; LUO, Zhiping. Fabrication and mechanical properties of α-Al2O3 whisker reinforced cu-graphite matrix composites. **Powder Technology**, *[S. l.]*, 2020. DOI: 10.1016/j.powtec.2020.07.105.

TRAPP, Johannes; SEMENOV, Artem; NÖTHE, Michael; WALLMERSPERGER, Thomas; KIEBACK, Bernd. Fundamental principles of spark plasma sintering of metals: part III–densification by plasticity and creep deformation. **Powder Metallurgy**, *[S. l.]*, v. 63, n. 5, p. 329–337, 2020. DOI: 10.1080/00325899.2020.1834748. Disponível em: https://doi.org/10.1080/00325899.2020.1834748.

WANG, Hong; SUBHASH, Ghatu; CHANDRA, Abhijit. Characteristics of single-grit rotating scratch with a conical tool on pure titanium. **Wear**, *[S. l.]*, v. 249, n. 7, p. 566–581, 2001. DOI: 10.1016/S0043-1648(01)00585-3.

WANG, S. W.; CHEN, L. D.; KANG, Y. S.; NIINO, M.; HIRAI, T. Effect of plasma activated sintering (PAS) parameters on densification of copper powder. **Materials Research Bulletin**, *[S. l.]*, v. 35, n. 4, p. 619–628, 2000. DOI: 10.1016/S0025-5408(00)00246-4.

WEGNER, Matthias; LEUTHOLD, Jörn; PETERLECHNER, Martin; SETMAN, Daria;

ZEHETBAUER, Michael; PIPPAN, Reinhard; DIVINSKI, Sergiy V.; WILDE, Gerhard. Percolating porosity in ultrafine grained copper processed by High Pressure Torsion. **Journal of Applied Physics**, *[S. l.]*, v. 114, n. 18, 2013. DOI: 10.1063/1.4829705.

WEN, Haiming; ZHAO, Yonghao; ZHANG, Zhihui; ERTORER, Osman; DONG, Shaoming; LAVERNIA, Enrique J. The influence of oxygen and nitrogen contamination on the densification behavior of cryomilled copper powders during spark plasma sintering. **Journal of Materials Science**, *[S. l.]*, v. 46, n. 9, p. 3006–3012, 2011. DOI: 10.1007/s10853-010-5178-9.

WILLIAMSON, G. K.; HALL, W. H. X-ray line broadening from filed aluminium and wolfram. **Acta Metallurgica**, *[S. l.]*, v. 1, n. 1, p. 22–31, 1953. DOI: 10.1016/0001-6160(53)90006-6.

XIAO, Jin Kun; ZHANG, Lei; ZHOU, Ke Chao; WANG, Xin Ping. Microscratch behavior of copper-graphite composites. **Tribology International**, *[S. l.]*, v. 57, p. 38–45, 2013. DOI: 10.1016/j.triboint.2012.07.004. Disponível em: http://dx.doi.org/10.1016/j.triboint.2012.07.004.

XIAO, Jin Kun; ZHANG, Wei; ZHANG, Chao. Microstructure evolution and tribological performance of Cu-WS2 self-lubricating composites. **Wear**, *[S. l.]*, 2018. DOI: 10.1016/j.wear.2018.07.024.

XIAO, Yelong; ZHANG, Zhongyi; YAO, Pingping; FAN, Kunyang; ZHOU, Haibin; GONG, Taimin; ZHAO, Lin; DENG, Minwen. Mechanical and tribological behaviors of copper metal matrix composites for brake pads used in high-speed trains. **Tribology International**, *[S. l.]*, v. 119, n. November 2017, p. 585–592, 2018. DOI: 10.1016/j.triboint.2017.11.038. Disponível em: https://doi.org/10.1016/j.triboint.2017.11.038.

XU, Ning; HAN, Weizhong; WANG, Yuchun; LI, Ju; SHAN, Zhiwei. Nanoscratching of copper surface by CeO2. **Acta Materialia**, *[S. l.]*, v. 124, p. 343–350, 2017. DOI: 10.1016/j.actamat.2016.11.008.

YAN, Y. D.; SUN, T.; DONG, S. Study on effects of tip geometry on AFM nanoscratching tests. **Wear**, *[S. l.]*, v. 262, n. 3–4, p. 477–483, 2007. DOI: 10.1016/j.wear.2006.06.017.

ZHANG, Dong; SUN, Yuan; GAO, Chenghui; LIU, Ming. Measurement of fracture toughness of copper via constant-load microscratch with a spherical indenter. **Wear**, *[S. l.]*, v. 444–445, n. October 2019, p. 203158, 2020. DOI: 10.1016/j.wear.2019.203158. Disponível em: https://doi.org/10.1016/j.wear.2019.203158.

ZHANG, Z. H.; WANG, F. C.; LEE, S. K.; LIU, Y.; CHENG, J. W.; LIANG, Y. Microstructure characteristic, mechanical properties and sintering mechanism of nanocrystalline copper

obtained by SPS process. **Materials Science and Engineering A**, *[S. l.]*, 2009. DOI: 10.1016/j.msea.2009.07.016.

ZHANG, Z. H.; WANG, F. C.; WANG, L.; LI, S. K.; SHEN, M. W.; OSAMU, S. Microstructural characteristics of large-scale ultrafine-grained copper. **Materials Characterization**, *[S. l.]*, v. 59, n. 3, p. 329–333, 2008. a. DOI: 10.1016/j.matchar.2007.06.014.

ZHANG, Zhao Hui; WANG, Fu Chi; WANG, Lin; LI, Shu Kui. Ultrafine-grained copper prepared by spark plasma sintering process. **Materials Science and Engineering A**, *[S. l.]*, 2008. b. DOI: 10.1016/j.msea.2007.04.107.

ZHAO, Wen min; BAO, Rui; YI, Jian hong. Enhancing the mechanical–electrical property simultaneously in pure copper composites by using carbonized polymer dots. **Journal of Materials Science**, *[S. l.]*, v. 56, n. 22, p. 12753–12763, 2021. DOI: 10.1007/s10853-021-06116-5. Disponível em: https://doi.org/10.1007/s10853-021-06116-5.

ZHAOHUI, Zhang; FUCHI, Wang; LIN, Wang; SHUKUI, Li; OSAMU, S. Sintering mechanism of large-scale ultrafine-grained copper prepared by SPS method. **Materials Letters**, *[S. l.]*, v. 62, n. 24, p. 3987–3990, 2008. DOI: 10.1016/j.matlet.2008.05.036.

ZHOU, Haibin et al. Friction and wear maps of copper metal matrix composites with different iron volume content. **Tribology International**, *[S. l.]*, v. 132, n. November 2018, p. 199–210, 2019. a. DOI: 10.1016/j.triboint.2018.11.027. Disponível em: https://doi.org/10.1016/j.triboint.2018.11.027.

ZHOU, Haibin; YAO, Pingping; GONG, Taiming; XIAO, Yelong; ZHANG, Zhongyi; ZHAO, Lin; FAN, Kunyang; DENG, Minwen. Effects of ZrO2 crystal structure on the tribological properties of copper metal matrix composites. **Tribology International**, *[S. l.]*, v. 138, n. March, p. 380–391, 2019. b. DOI: 10.1016/j.triboint.2019.06.005.

ZHOU, Ke Chao; PEI, Hai Long; XIAO, Jin Kun; ZHANG, Lei. Micro-scratch behavior of WC particle-reinforced copper matrix composites. **Rare Metals**, *[S. l.]*, 2015. DOI: 10.1007/s12598-015-0586-2.

ZHU, K. N.; GODFREY, A.; HANSEN, N.; ZHANG, X. D. Microstructure and mechanical strength of near- and sub-micrometre grain size copper prepared by spark plasma sintering. **Materials and Design**, *[S. l.]*, 2017. a. DOI: 10.1016/j.matdes.2016.12.042.

ZHU, K. N.; GODFREY, A.; HANSEN, N.; ZHANG, X. D. Microstructure and mechanical strength of near- and sub-micrometre grain size copper prepared by spark plasma sintering. **Materials and Design**, *[S. l.]*, v. 117, p. 95–103, 2017. b. DOI: 10.1016/j.matdes.2016.12.042. Disponível em: http://dx.doi.org/10.1016/j.matdes.2016.12.042.

ZHU, Linying; YI, Maozhong; WANG, Liming; CHEN, Shengan. Effects of foam copper on the mechanical properties and tribological properties of graphite/copper composites. **Tribology International**, *[S. l.]*, v. 148, n. January, p. 106164, 2020. DOI: 10.1016/j.triboint.2020.106164. Disponível em: https://doi.org/10.1016/j.triboint.2020.106164.

ZUM GAHR, Karl-Heinz. **Microstructure and Wear of Materials**. 1. ed. Siegen: Elsevier Science Publishers, 1987.

ANNEX A

Poster presented at the XXX International Materials Research Congress – IMRC202.

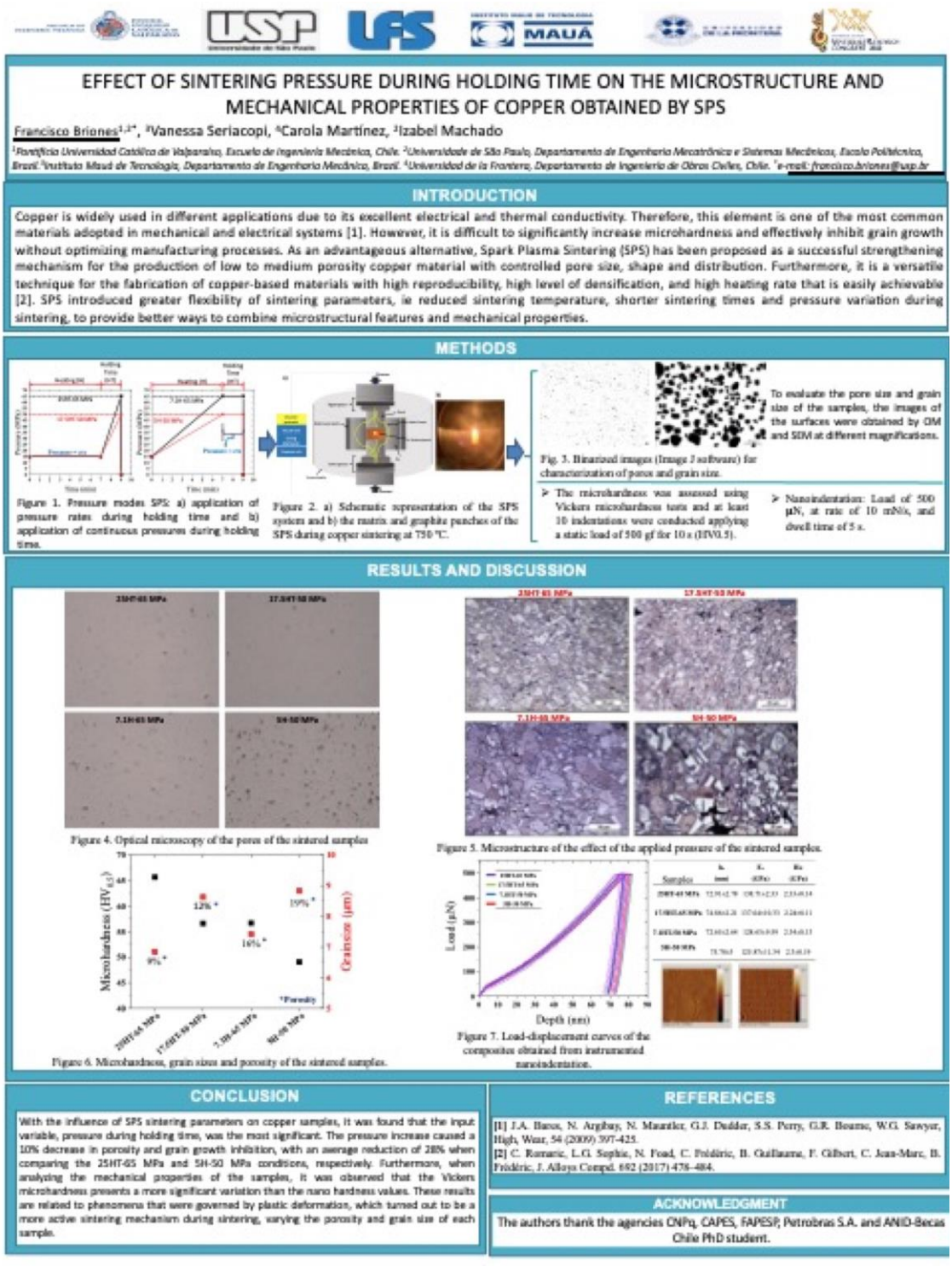

EFFECT OF SINTERING PRESSURE DURING HOLDING TIME ON THE MICROSTRUCTURE AND MECHANICAL PROPERTIES OF COPPER OBTAINED BY SPS

Francisco Briones[1,2*], [2]Vanessa Seriacopi, [3]Carola Martínez, [2]Izabel Machado

[1]Pontifícia Universidad Católica de Valparaíso, Escuela de Ingeniería Mecánica, Chile. [2]Universidade de São Paulo, Departamento de Engenharia Mecatrônica e Sistemas Mecânicos, Escola Politécnica, Brasil. [3]Instituto Mauá de Tecnologia, Departamento de Engenharia Mecânica, Brasil. [4]Universidad de la Frontera, Departamento de Ingeniería de Obras Civiles, Chile. *e-mail: francisco.briones@usp.br

INTRODUCTION

Copper is widely used in different applications due to its excellent electrical and thermal conductivity. Therefore, this element is one of the most common materials adopted in mechanical and electrical systems [1]. However, it is difficult to significantly increase microhardness and effectively inhibit grain growth without optimizing manufacturing processes. As an advantageous alternative, Spark Plasma Sintering (SPS) has been proposed as a successful strengthening mechanism for the production of low to medium porosity copper material with controlled pore size, shape and distribution. Furthermore, it is a versatile technique for the fabrication of copper-based materials with high reproducibility, high level of densification, and high heating rate that is easily achievable [2]. SPS introduced greater flexibility of sintering parameters, ie reduced sintering temperature, shorter sintering times and pressure variation during sintering, to provide better ways to combine microstructural features and mechanical properties.

METHODS

Figure 1. Pressure modes SPS: a) application of pressure rates during holding time and b) application of continuous pressures during holding time.

Figure 2. a) Schematic representation of the SPS system and b) the matrix and graphite punches of the SPS during copper sintering at 750 °C.

Fig. 3. Binarized images (Image J software) for characterization of pores and grain size.

To evaluate the pore size and grain size of the samples, the images of the surfaces were obtained by OM and SEM at different magnifications.

- The microhardness was assessed using Vickers microhardness tests and at least 10 indentations were conducted applying a static load of 500 gf for 10 s (HV0.5).
- Nanoindentation: Load of 500 μN, at rate of 10 mN/s, and dwell time of 5 s.

RESULTS AND DISCUSSION

Figure 4. Optical microscopy of the pores of the sintered samples

Figure 5. Microstructure of the effect of the applied pressure of the sintered samples.

Figure 6. Microhardness, grain sizes and porosity of the sintered samples.

Figure 7. Load-displacement curves of the composites obtained from instrumented nanoindentation.

CONCLUSION

With the influence of SPS sintering parameters on copper samples, it was found that the input variable, pressure during holding time, was the most significant. The pressure increase caused a 10% decrease in porosity and grain growth inhibition, with an average reduction of 28% when comparing the 25HT-65 MPa and SH-50 MPa conditions, respectively. Furthermore, when analyzing the mechanical properties of the samples, it was observed that the Vickers microhardness presents a more significant variation than the nano hardness values. These results are related to phenomena that were governed by plastic deformation, which turned out to be a more active sintering mechanism during sintering, varying the porosity and grain size of each sample.

REFERENCES

[1] J.A. Baros, N. Argibay, N. Mauntler, G.J. Dudder, S.S. Perry, G.R. Bourne, W.G. Sawyer, High, Wear, 54 (2009) 397-425.
[2] C. Romaric, L.G. Sophie, N. Foad, C. Frédéric, B. Guillaume, F. Gilbert, C. Jean-Marc, B. Frédéric, J. Alloys Compd. 692 (2017) 478–484.

ACKNOWLEDGMENT

The authors thank the agencies CNPq, CAPES, FAPESP, Petrobras S.A. and ANID-Becas Chile PhD student.